Probing Molecular Gas and its Physical Conditions in Disc Galaxies

Selçuk Topal
Christ Church College

A thesis submitted for the degree of Doctor of Philosophy

Trinity Term, 2015

Probing Molecular Gas and its Physical Conditions in Disc Galaxies

Selçuk Topal
Christ Church College
A thesis submitted for the degree of Doctor of Philosophy
Trinity Term, 2015

Abstract

New observations of multiple molecular gas tracers in nearby early- and late-types galaxies are presented and are used to study the physical conditions of the gas within different morphological structures. The CO Tully-Fisher relation is also constructed for a sample of star-forming galaxies at $z = 0.05-0.3$, probing their mass and size evolution.

First, using single-dish observations of multiple locations within the nearby spiral galaxy NGC 6946, extensive CO ladders are generated. The molecular line ratios reveal a large variety of physical conditions across the molecular gas complexes, depending primarily on the presence of current or recent star formation, itself compared with that in the centre of the galaxy and other galaxies.

Second, interferometric observations of CO and high density molecular tracers in the nearby edge-on early-type galaxies NGC 4710 and NGC 5866 are presented. The gas kinematics reveals that the galaxies are barred, with most of the gas contained within a nuclear disc and a distinct inner ring. Using the molecular line ratios to probe the physical conditions of the gas, the nuclear discs appear to have a more diffuse and hotter molecular medium than the inner rings, with more embedded dense clumps. This suggests that the conditions in the nuclear discs are similar to those in photo-dissociation regions, with intense UV radiation from young stars and few cosmic rays. Indeed, the observed molecular line ratios are also intermediate between those of spiral galaxies and starbursts, with even milder star formation in the inner rings.

Third, homogeneously measuring the line widths in the CO spectra of star-forming disc galaxies at $z = 0.05-0.3$, their K_s-band CO Tully-Fisher relation is constructed. A comparison to local star-forming galaxy TFRs from the literature provides mild evidence that our sample galaxies are ≈ 0.89 mag brighter than local ones at a given rotational velocity, a result entirely consistent with our stellar mass TFR, suggesting that our sample galaxies are more massive than local ones by ≈ 0.35 dex. While they deserve further scrutiny, we suspect that these results are due to our sample galaxies being more heavily star-forming (and thus brighter at a given mass) than the comparison sample galaxies.

Declaration

I hereby declare that no part of this thesis has been accepted, or is currently being submitted, for any degree or diploma or certificate or any other qualification in this University or elsewhere. This thesis is the result of my own work unless otherwise stated below.

All of the work presented in this thesis was completed under the supervision of Martin Bureau. The data reduction described in Chapter 2 and that in Chapter 3 was done in collaboration with Estelle Bayet and Tim A. Davis respectively.

The material in Chapter 2 was published in Topal et al., 2014, MNRAS, Volume: 437, pp. 1434-1455 and the material in Chapter 3 was submitted to MNRAS, while that in Chapter 4 is in preparation.

Each chapter begins with a *Wordle* image showing a cloud of words which acts as a summary of the contents of the following chapter. Figure 1.5 in Chapter 1 was also created using the same tool (www.wordle.net).

Acknowledgements

First and foremost, I would like to thank my supervisor, Martin Bureau, for all his tremendous efforts, help and guidance during my DPhil. As is true of all of his previous students, I will never forget his famous red pen. I would also like to thank to Estelle Bayet and Timothy A. Davis, for their useful comments and help on reduction and analysis of single-dish and interferometric data.

I would like to express my sincere gratitude to my college, Christ Church, and more importantly, to my college advisor Roger L. Davies, and to Phillip Wetton and his lovely wife Roswitha Wetton for generously supporting my research and for making my life more comfortable in Oxford.

I would like to give all my appreciation to my lovely family, my sisters and my brothers, and above all, to my mother who supported me in the worst situations and taught me that any difficulties could be overcome as long as I do my best. And my father. I believe you see me, although you passed away just one month before I got the scholarship to study for my PhD abroad. And my brand new little family, my wife Ayşegül and my light, my happiness, my little son Uzay Akay. God bless you! I love you! I am the luckiest and the happiest man on Earth since I've had you my son!

In addition, I'd like to thank all my friends and colleagues at the department. I also like to thank Ashling Morris, Vanessa Ferraro-Wood and Leanne O'Donnell for their excellent and prompt support. Special thanks go to the people who helped me by reading some parts of this manuscript: A. Crocker, A. Tiley and U. A. Yıldız - Thanks a lot!

Finally, I would like to express my deepest gratitude to the founder of the Republic of Turkey, M.K. Atatürk, who is also the founder of the scholarship that I receive. The world always needs such forward looking people when peace, freedom and science find themselves in times of moral crisis.

"Ne Mutlu Türk'üm Diyene!"

To the most precious ten billion billion billion atoms in my life...

to my son Uzay Akay
to my wife Ayşegül
..and to my mother 'The last rose'

Contents

Contents x

List of Figures xiv

List of Tables xxiv

1 Introduction 1

1.1 Evolution of galaxies and their classifications . . . 4

1.2 Interstellar Medium of Galaxies . . . 9

1.2.1 From the First Elements to Today's Complexity . . . 9

1.2.2 Phases of the ISM . . . 10

1.2.3 Molecular Clouds . . . 11

1.2.4 Molecular tracers of the ISM . . . 15

1.2.5 Radiative Transfer . . . 18

1.2.5.1 Radiative transfer code: RADEX . . . 18

1.3 CO as a kinematic tracer in galaxies . . . 21

2 GMC Complexes in the Spiral Galaxy NGC 6946 25

2.1 Introduction . . . 26

2.2 Observation and Data Reduction . . . 30

2.2.1 Observations . . . 30

2.2.2 Literature data . . . 32

2.2.3 Data reduction . . . 33

2.3 Modeling . . . 37

2.3.1 Radiative transfer code . . . 37

2.3.2 Best-fit models . . . 39

2.3.3 Likely models . . . 39

2.4 Results . . . 42

2.4.1 Empirical results . . . 42
2.4.2 Modeling results . . . 47
2.4.2.1 Molecular ISM physical conditions . . . 47
2.4.2.2 Spectral line energy distributions . . . 51
2.5 Discussion . . . 55
2.5.1 Star formation activity . . . 55
2.5.2 Regions 1, 2 and 3 . . . 58
2.5.3 Regions 4, 5 and 6 . . . 59
2.5.4 Regions 7 and 8 . . . 59
2.5.5 Spiral arms vs. galaxy centre . . . 59
2.5.6 Modeling methods . . . 60
2.6 Conclusions . . . 61
Appendices . . . 63
2.A Integrated spectra of the 8 regions studied . . . 63
2.B CSO detections . . . 68

3 Molecular Line Ratio Diagnostics in NGC 4710 and NGC 5866 73
3.1 Introduction . . . 74
3.2 Observations & Data Reduction . . . 77
3.2.1 Observations . . . 77
3.2.1.1 NGC 4710 . . . 77
3.2.1.2 NGC 5866 . . . 79
3.2.2 Data reduction . . . 80
3.2.2.1 CARMA data reduction . . . 80
3.2.2.2 PdBI data reduction . . . 81
3.3 Imaging & Analysis . . . 81
3.3.1 Emission regions and moment maps . . . 81
3.3.2 Position-velocity diagrams . . . 82
3.3.3 Comparisons with IRAM 30m data . . . 88
3.3.4 Continuum emission . . . 91
3.4 Line ratio diagnostics . . . 93
3.4.1 PVD ratios . . . 94
3.4.2 Integrated line intensity ratios as a function of projected radius . . . 98
3.4.3 Non-LTE LVG Modelling . . . 99
3.4.4 Best-fitting and most likely models . . . 105
3.4.5 General properties of the LVG model results . . . 106

3.5 Results and Discussion . . . 113
3.5.1 Moment maps . . . 117
3.5.2 PVDs . . . 117
3.5.3 Integrated spectra . . . 119
3.5.4 Molecular line ratios . . . 120
3.5.4.1 ^{12}CO (1–0) / ^{12}CO (2–1) ratio and tenous gas temperature . . . 120
3.5.4.2 ^{12}CO / ^{13}CO ratio and tenuous gas opacity . . . 121
3.5.4.3 HCN / HCO$^+$, HCN / HNC and HCN / HNCO ratios and dense gas excitation . . . 124
3.5.4.4 Ratios of CO to HCN, HCO$^+$, HNC and HNCO and dense gas fraction . . . 126
3.5.4.5 All ratios and gas physical conditions . . . 129
3.5.5 Line ratios and galaxy morphology . . . 129
3.6 Conclusions . . . 133
Appendices . . . 137
3.A Modeled line ratios in both galaxies . . . 137
3.B Ratios of CO to dense gas tracers . . . 139

4 The CO TFR of Star-forming Galaxies at $z = 0.05 - 0.3$ 145
4.1 Introduction . . . 146
4.2 Data . . . 147
4.2.1 EGNoG CO sample . . . 147
4.2.2 Additional CO data . . . 148
4.2.3 Near-infrared photometry . . . 149
4.2.4 Inclinations . . . 149
4.2.5 Stellar masses . . . 151
4.2.6 Absolute magnitudes and K corrections . . . 151
4.3 Sample selection . . . 152
4.3.1 Galaxy interactions . . . 152
4.3.2 AGN . . . 154
4.3.3 Inclination . . . 154
4.3.4 Integrated profile shape . . . 155
4.4 Velocity measurements and Tully-Fisher relations . . . 155
4.4.1 Velocity widths . . . 155
4.4.2 Tully-Fisher relation . . . 158
4.5 Results & Discussion . . . 160

4.5.1 Previous studies . . . 161
4.5.2 Evolution with redshift . . . 162
4.5.3 Intrinsic scatter . . . 164
4.5.4 Inclinations . . . 165
4.5.5 CO as a kinematic tracer . . . 165
4.6 Conclusions . . . 167
Appendices . . . 169
4.A Integrated CO profiles and best fits . . . 169

5 Conclusions **173**
5.1 Summary of the Main Results . . . 174
5.1.1 Molecular gas in the disc of NGC 6946 . . . 174
5.1.2 Extensive CO and high density gas in early-type galaxies . . . 176
5.1.3 The CO Tully-Fisher Relation of disc galaxies at $z = 0.05 - 0.3$ . . . 177
5.2 Ongoing work . . . 178
5.2.1 Molecular gas in the arms of NGC 0628 . . . 178
5.2.2 $M_\bullet$ - $\Delta V_{\rm CO}$ relation in galaxies . . . 180
5.3 Future Prospects . . . 181

References **183**

Publications **203**

Biography **207**

List of Figures

1.1 Hubble *tuning fork* morphological classification scheme [Hubble, 1936]. Image courtesy: Galaxy Zoo. Three galaxies studied in this thesis, the spiral galaxy NGC 6946 (see Chapter 2) and the lenticulars NGC 4710 and NGC 5866 (see Chapter 3), are overlaid on the image. 6

1.2 A revised parallel-sequence morphological classification of galaxies from Kormendy & Bender [2012] as presented in that work. 7

1.3 Morphology of galaxies from the ATLAS^{3D} survey. Image courtesy: Cappellari et al. [2011]. 8

1.4 Schematic of a photo-dissociation (or photon-dominated) region (PDR) from Hollenbach & Tielens [1999]. $T_{\rm gas}$ indicates gas temperature while $T_{\rm gr}$ represents the temperature of dust grains. 12

1.5 The molecules detected in the ISM or circumstellar shells as of May 2015. The H_2 and CO are intentionally shown bigger compared with the others since they are the most abundant molecules of the ISM. The dense gas tracers studied as part of this thesis are also shown bigger in the image compared with the rest of the detected molecules but with no indication for the relative abundances. 13

2.1 Regions studied and star formation-related features in NGC 6946. **Left**: Hα image of NGC 6946 [Knapen et al., 2004]. Overlaid green, yellow, blue and orange circles indicate respectively GMCs in the central 5 kpc [Donovan Meyer et al., 2012], GMCs in the eastern part [Rebolledo et al., 2012], CO (1–0) complexes in the eastern part [Rebolledo et al., 2012], and giant H II complexes [van der Kruit et al., 1977]. Red crosses and diamonds indicate supernova remnants identified in the radio [Lacey & Duric, 2001] and optical [Matonick & Fesen, 1997], respectively. **Right**: H I map of NGC 6946 [Braun et al., 2007]. Overlaid red circles and brown dots represent H I holes [Boomsma, 2007] and H II regions [Bonnarel et al., 1986], respectively. White circles with numbers in both images represent the 8 regions studied in this chapter, with our final common beam size of 31.5″, while the white "X" identifies the centre of the galaxy. The black square on the larger H I map shows our CO (2–1) pointings, covering a contiguous area of $510'' \times 510''$ centred on the galaxy. North is up and East to the left in all images. 28

2.2 NGC 6946 optical image (DSS), overlaid with the grid of CSO pointings for the CO (3–2) (blue), CO (4–3) (brown), CO (6–5) (yellow) and C I ($^3P_1$-$^3P_0$) (green) lines. The circles have a diameter equal to the beam size (FWHM) of each line. The CO (2–1) pointings cover a much larger contiguous area of $510'' \times 510''$ centred on the galaxy (see Fig. 2.1), so only a few representative pointings are shown in red along the major-axis. 31

2.3 **Top**: NGC 6946 CO (2–1) integrated line intensity map (green contours), overlaid on an optical image (DSS). **Bottom**: Same CO (2–1) integrated line intensity map (black contours), overlaid on the CO (2–1) mean velocity field. Contours are from 1 to 80 per cent of the peak integrated intensity of 100 K km s^{-1}, in steps of 5 per cent. The CO (2–1) beam of 31.5″ is shown in red in the bottom-left corner of each panel. 32

2.4 Radial distribution of the molecular gas in NGC 6946. The surface density profiles were obtained by taking a straight linear cut along the major-axis toward the East for each line. All surface density profiles decrease rapidly within $\approx$ 1 kpc and then remain nearly flat. Colours are as in Figure 2.2. 33

2.5 $\Delta\chi^2$ maps (contours and greyscales; see Section 2.3.2). For each region, $\Delta\chi^2$ is shown as a function of $T_{\rm K}$ and $n(H_2)$ for the best-fit N(CO) (indicated in the bottom-left corner of each panel). The model grid is indicated with red dots and the best-fit model with a red filled circle. Black dots represent bad models (e.g. unacceptably low opacity; see van der Tak et al. 2007a). $\Delta\chi^2$ contours indicate the 1 σ (darkest zone) to 5 σ (lightest zone) confidence levels in steps of 1 σ. For 3 line ratios (all regions except regions 1 and 2, 2 degrees of freedom), the levels are 2.3, 6.2, 11.8, 19.3 and 24.0. For 4 line ratios (region 1, 3 degrees of freedom), the levels are 3.5, 8.0, 14.2, 22.1 and 28.0. For 5 line ratios (region 2, 4 degrees of freedom), the levels are 4.7, 9.7, 16.3, 24.5 and 32.0. The reduced $\chi^2_{\rm min}$ ($\chi^2_{\rm r,min}$) values together with their corresponding degrees of freedom are also shown in each panel. 41

2.6 Marginalised probability distribution functions. For each region, the PDF of each model parameter marginalised over the other two is shown. The peak (most likely) and median values within the model grid are identified with dashed blue and solid black lines, respectively. The 68 per cent (1σ) confidence levels around the median are indicated by dotted black lines. The best-fit model from χ^2 minimisation is indicated by a solid red line. 43

2.6 Continued. 44

2.7 Beam-corrected line ratios as a function of radius in NGC 6946. The line ratios are color-coded and defined in the text (see Section 2.4.1). 47

2.8 **Top**: Correlations between the best-fit parameters ($T_{\rm K}$, $n(H_2)$ and N(CO)) of the 8 regions studied. **Middle**: Same physical parameters as a function of galacto-centric radius. **Bottom**: Same physical parameters as a function of the predicted $J_{\rm max}$. Red symbols show the results from the χ^2 analysis. Black symbols with error bars represent the median of the marginalised probability distribution function of each model parameter, along with the 68 per cent (1σ) confidence levels (see Table 2.5). . 50

2.9 Optical depth distributions. For each region (colour-coded), the optical depth of the CO line for the best-fit model is shown as a function of the upper J level of the transition (up to J=10-9). 51

2.10 Spectral line energy distributions. For each region, the integrated line intensity S (left) and beam-averaged total intensity per unit area I (right) are shown as a function of the upper J level of the transition (up to J=10-9). The solid red line shows the best-fit model, while the dotted red lines delineate the range of possible SLEDs encompassed by the 1σ confidence level on the best-fit model (the darkest zone in the $\Delta\chi^2$ contour maps of Fig. 2.5). The dashed black line shows the SLED corresponding to the most likely model. Blue circles with error bars are our observations. 53

2.10 Continued. 54

A.1 Integrated spectra used in the line ratio analysis for region 1. Gaussian fits are overlaid. The ^{12} CO (2–1) line integrated intensity and line width in each region was obtained by interpolating those of the two closest detections of the large-scale mapping. These are shown as dashed and solid lines in the ^{12}CO (2–1) panel. 63

A.1 (Continued.) Region 2 64

A.1 (Continued.) Regions 3 (left) and 4 (right). 65

A.1 (Continued.) Regions 5 (left) and 6 (right). 66

A.1 (Continued.) Regions 7 (left) and 8 (right). 67

3.1 NGC 4710 moment maps. **Left**: Moment 0 contour maps (white) of the detected lines overlaid on an optical image of the galaxy (greyscale) from the Sloan Digital Sky Survey (SDSS). Red circles show the primary beam of CARMA and/or PdBI at the respective frequency of each line. The beam sizes are also indicated. **Centre**: Moment 0 maps with overlaid isophotal contours. **Right**: Moment 1 maps with overlaid isovelocity contours. The large black circles on the moment maps show the IRAM 30 m telescope beam for comparison (HNC (1–0) was not observed; see Crocker et al. 2012). Contour levels on the moment 0 maps are from 10 to 100% of the peak integrated line intensity in steps of 10%. The moment 0 peaks are (from top to bottom) 59.8, 145.8, 10.8, 22.3, 3.0, 2.3, and 1.7 Jy beam^{-1} km s^{-1}. Contour levels on the moment 1 maps are spaced by 30 km s^{-1}. The array used, molecular line displayed, and synthesized beam are also indicated in each panel. 83

3.1 Continued. The large black circles on the moment maps show the IRAM 30 m telescope beam for comparison (HNC (1–0) and HNCO (4–3) were not observed; see Crocker et al. 2012). The moment 0 peaks are (from top to bottom) 3.7, 2.5, 1.9 and 1.0 Jy beam^{-1} km s^{-1}. Contour levels on the moment 1 maps are spaced by 30 km s^{-1}. The array used, molecular line displayed, and synthesized beam are also indicated in each panel. 84

3.2 Same as Figure 3.1 but for NGC 5866. The moment 0 peaks are (from top to bottom) 51.5, 5.5, 2.9, 1.4, 1.2, and 0.6 Jy beam^{-1} km s^{-1}. 85

3.3 PVDs of all the lines detected in NGC 4710. The PVDs are overlaid with contours (black lines) spaced by 3σ and starting at 3σ, while the colour scales start at 1σ. The rms noise for the CARMA observations of ^{12}CO (1–0), ^{13}CO (1–0), ^{12}CO (2–1), ^{13}CO (2–1), HCN (1–0), HCO$^+$ (1–0) and HNC (1–0) is 7.5, 3.7, 19.0, 19.0, 1.5, 1.6 and 1.2 mJy beam^{-1}, respectively, while that for the PdBI observations of HCN (1–0), HCO$^+$ (1–0), HNC (1–0) and HNCO (4–3) is 0.8, 0.9, 0.9 and 0.9 mJy beam^{-1}, respectively. The projected position numbers, as discussed in Section 3.4.2 and illustrated in Figure 3.11, are indicated on the top axes. The array used, molecular line displayed, and angular resolution along the major axis are also indicated in each panel. 87

3.4 Same as Figure 3.3 but for NGC 5866. The rms noise for the observations of ^{12}CO (1–0), ^{13}CO (1–0), HCN (1–0), HCO$^+$ (1–0), HNC (1–0) and HNCO (4–3) are 6.7, 0.9, 0.4, 0.4, 0.4 and 0.4 mJy beam^{-1}, respectively. 88

3.5 Comparison of integrated molecular line spectra for NGC 4710. Black solid lines show the integrated spectra of our CARMA and PdBI observations, with no spatial weighting nor limit. Black dotted lines show the IRAM 30m integrated spectra simulated from our CARMA and PdBI observations (with Gaussian spatial weighting; see Section 3.3.3). Red dashed lines show original IRAM 30m integrated spectra from the literature. The HNC (1–0) and HNCO (4–3) lines were never observed previously, so their integrated spectra are shown here for the first time. 90

3.6 Same as Figure 3.5 but for NGC 5866. 91

3.7 Spectral energy distribution of NGC 4710 and NGC 5866 from the radio to the infrared. Our measurements are shown in red. 93

3.8 PVD ratios of CO lines only and dense gas tracer lines only in NGC 4710. **Top row:** PVD ratios of CO lines only, with the relevant ^{12}CO (1–0) or ^{12}CO (2–1) PVD contours overlaid (black lines). **Bottom row:** PVD ratios of dense gas tracer lines only, with the HCN (1–0) PVD contours overlaid (black lines). Contour levels are spaced by 3σ starting at 3σ. Greyscales indicate lower limits to the line ratios (see Section 3.4.1). The projected position numbers, as discussed in Section 3.4.2 and illustrated in Figure 3.11, are indicated on the top axes. 95

3.9 Same as Figure 3.8 but for the ratios of CO to dense gas tracer lines in NGC 4710. . 96

3.10 Same as Figures 3.8 and 3.9 but for NGC 5866. 97

3.11 **Top:** Illustration of the projected positions along the major-axis of NGC 4710 (left) and NGC 5866 (right), where the line ratios are extracted and studied. **Bottom:** Corresponding 5-pixel (i.e. one beam width) slices in the PVDs. Red circles and associated numbers indicate positions where both kinematic components (nuclear disc and inner ring) are present along the line of sight, requiring a double-Gaussian fit (see Fig. 3.12, right). Black circles and associated numbers indicate positions where a single component (inner ring) is present, requiring a single Gaussian fit (see Fig. 3.12, left). The circle are one beam width (6.5″) in diameter. 99

3.12 Illustration of the spectrum extraction process using the NGC 4710 ^{12}CO (1–0) PVD. **Top left:** ^{12}CO (1–0) PVD and the spectrum extracted at position 2, in the outskirt of the disc where a single kinematic component (inner ring) is present along the line of sight. **Top right:** Same for position 4, where both kinematic components are present (nuclear disc and inner ring). **Bottom:** Same for position 6 (galaxy centre), where both kinematic components are again present. The red and blue solid lines overlaid on the spectra show the Gaussian profiles separately fitted to the emission of the inner ring and the nuclear disc, respectively, while the magenta solid lines show the sums of the multiple Gaussians. The red and blue dotted lines overlaid on the PVDs and spectra indicate velocities of ± FWHM with respect to the centre of the associated Gaussian (thus encompassing ≈ 95% of the total emission of each component). Black dotted lines overlaid on the PVDs and spectra indicate the galaxy heliocentric velocity. Turquoise solid lines overlaid on the PVDs show the (one beam) width of the spatial slice considered to extract the averaged spectrum at that position. 100

3.13 Ratios of CO lines only and dense gas tracer lines only as a function of projected radius in NGC 4710. **Top:** Ratios of CO lines only, along the inner ring (red), nuclear disc (blue) and intermediate region (black; position 9 only). **Bottom:** Ratios of dense gas tracer lines only, along the nuclear disc (blue). Upper and lower limits are indicated with arrows. The projected positions, as illustrated in Figure 3.11, are indicated on the top axis of each panel. 101

3.14 Same as Figure 3.13 but for the ratios of CO to dense gas tracer lines in NGC 4710. 102

3.15 Same as Figures 3.13 and 3.14 but for NGC 5866. 103

3.16 $\Delta\chi^2_{\rm r} \equiv \chi^2_{\rm r} - \chi^2_{\rm r,min}$ maps for the tenuous molecular gas in the nuclear disc of NGC 4710 (positions 5, 6, 7 and 8). For each region, $\Delta\chi^2_{\rm r}$ is shown as a function of $T_{\rm K}$ and $n(\rm H_2)$ for three values of $N(\rm CO)$ centred around the best-fit and indicated at the bottom of each panel. The models computed are indicated by red dots and the best-fit model with a red filled circle. Black dots represent bad models (e.g. unacceptably low opacity; see van der Tak et al. 2007b). The $\Delta\chi^2_{\rm r}$ contours show the 0.2σ (16% probability that the appropriate model is enclosed; darkest greyscale), 0.5σ (38%), and 1σ (68%) to 5σ (99.9%; lightest greyscale) confidence levels in steps of 1σ for 3 degrees of freedom (3 line ratios). The actual $\Delta\chi^2_{\rm r}$ levels from 0.2σ to 5σ are 0.8, 1.8, 3.5, 8.0, 14.2, 22.1 and 28.0, respectively. The confidence levels from 2σ to 5σ are separated by black lines, those from 0.2σ to 1σ by grey lines. The area containing models with $\leq 1\sigma$ confidence levels is much smaller than the best-fit model symbol at positions 5, 6 and 7. The $\chi^2_{\rm r,min}$ value, kinematic component and position along the galaxy disc are also indicated in each panel. 107

3.17 Same as Figure 3.16 but for the dense molecular gas in the nuclear disc of NGC 4710 (left) and NGC 5866 (right) (positions 5, 6 and 7). $N(\rm X)$ stands for the column number density of all four high density tracers. The area containing models with $\leq 1\sigma$ confidence levels is much smaller than the best-fit model symbol at positions 5 and 6 in NGC 4710 and at position 6 in NGC 5866. For positions with a line ratio lower limit, blue dots indicate models meeting the criterion for case (2) described in the text (Section 3.4.4). Associated $\Delta\chi^2_{\rm r}$ contours (confidence levels) are shown in colour: yellow (1σ), red (2σ), orange (3σ), green (4σ) and brown (5σ). 108

3.18 Same as Figures 3.16 and 3.17 but for the tenuous molecular gas in the inner ring of NGC 4710 (positions 2, 3, 6, 7, 8 and 10). The area containing models with $\leq 1\sigma$ confidence levels is much smaller than the best-fit model symbol at positions 2 and 7 in NGC 4710. 109

3.19 PDF of each model parameter marginalised over the other two, for the tenuous molecular gas in the nuclear disc of NGC 4710 (positions 5, 6, 7 and 8). In each PDF, the peak (most likely) and median value within the model grid are identified with a dashed blue and dashed-dotted black line, respectively. The 68% (1σ) confidence level around the median is indicated by dotted black lines. The best-fit model in a χ^2 sense is indicated by a solid red line. The PDFs for position 8 do not include the median value nor the 1σ confidence level, as at least one observed line ratio is a lower limit, resulting in PDF upper limits (blue dots with arrows). 113

3.20 Same as Figure 3.19 but for the dense molecular gas in the nuclear disc of NGC 4710 (left) and NGC 5866 (right) (positions 5, 6 and 7). N(X) stands for the column number density of all four high density tracers. The PDFs for positions 5 and 7 in NGC 5866 do not include the median value nor the 1σ confidence level, as at least one observed line ratio is a lower limit, resulting in PDF upper limits (blue dots with arrows). 114

3.21 Same as Figures 3.19 and 3.20 but for the tenuous molecular gas in the inner ring of NGC 4710 (positions 2, 3, 6, 7, 8 and 10). No PDF includes the median value or the 1σ confidence level, as at least one observed line ratio is a lower limit at each position, resulting in PDF upper limits (blue dots with arrows). 115

3.22 Molecular line ratio diagrams for NGC 4710, NGC 5866 and a variety of other galaxies. Our data for NGC 4710 and NGC 5966 are shown as filled circles and squares, respectively, while our data for the nuclear discs and inner rings are shown in blue and red, respectively (black for the intermediate region). Upper and lower limits are represented by arrows. Other lenticular galaxies are indicated by magenta filled stars [Crocker et al., 2012; Krips et al., 2010], starburst nuclei by dark green filled stars, Seyferts by brown filled stars, peculiar galaxies by red filled stars, Centaurus A by pale green filled stars (see Baan et al. 2008; Table 3 in Krips et al. 2010 and references therein), spiral arm GMCs by black circles with an X, NGC 6946 (starburst) GMCs by black circles with a cross [Topal et al., 2014], and M31 GMCs by orange circles with an X [Brouillet et al., 2005]. The data for NGC 1266 (a lenticular galaxy with a molecular outflow) are shown by magenta squares with a filled star [Alatalo et al., 2011]. The dark green dashed lines in panel *a* indicate the typical range of HCN (1–0)/^{12}CO (1–0) ratios in starbursts (see Table B2 in Baan et al. 2008). The range of I_{11} ratios in the nuclear disc and inner ring of NGC 5866 (this work) is indicated by grey solid lines in panel *b*, while the typical range in spirals [Paglione et al., 2001] is indicated by red dashed lines. In panels *a* and *b*, Crocker et al. [2012]'s single-dish observations of NGC 4710 and NGC 5866 are shown as an open black circle and an open black square, respectively (see Table 4 of Crocker et al. 2012). The HCN (1–0)/HCO$^+$ ratios for M31 GMCs [Brouillet et al., 2005] are indicated by red dashed lines in panel *c* and *d*. The vertical red dot-dashed lines in panel *d* indicate the typical range of ^{13}CO (1–0)/HCO$^+$ (1–0) ratios in the disc of M82 (starburst; Tan et al. 2011). The HCN (1–0)/^{12}CO (1–0) ratios in spirals [Gao & Solomon, 2004a] are indicated by red dashed lines in panels *a*, *e* and *f*, respectively. The black solid lines in a number of panels show the 1 : 1 relation and are there to guide the eye. Similarly, the black dashed lines show a ratio of 1 in panels *c*, *d* and *f*. 130

3.22 Continued. 131

4.1 **Top**: K_s-band CO TFR for the initial (left) and final (right) samples. The black solid lines show the reverse fits, while the red dashed (respectively blue long dashed) lines show the reverse fit with slope fixed to that of Tully & Pierce [2000] (resp. Tiley et al. 2015). The red solid lines show the H I TFR of local spirals from Tully & Pierce [2000]. The triple dot-dashed lines shows the CO TFR of local spirals [Tiley et al., 2015]. **Bottom**: As for the top panels, but for the $M_\star$ CO TFR. In panels (a) and (c), the data points shown as open red circles represent galaxies with a single Gaussian profile, while those shown as filled red circles represent galaxies with $i_{b/a} < 30°$. 159

A.1 Integrated CO profiles of the sample galaxies, taken from Bauermeister et al. [2013] and additional literature sources (see Section 4.2.2). For each plot, the red line shows the best parametric fit to the spectrum (see Section 4.4.1). The name of the galaxy as listed in Tables 4.1 and 4.2 is indicated in the top-left corner of each plot, and the reduced χ^2 value of the fit is indicated in the top-right corner. 169

A.1 Continued. 170

5.1 **Left**: The targeted regions in the spiral galaxy NGC 628 are overlaid on an optical image of the galaxy (SDSS). The red circles indicate the targeted positions with the IRAM 30m beam of 22 arcsec at 115 GHz, while the green circles indicate the H II regions detected by [Fathi et al., 2007]. **Right**: The targeted regions and the FUV emission are overlaid on the same optical image. Blue contours represent the FUV emission (GALEX). North is up and east to the left in both panels. The offsets are measured with respect to the galaxy centre of $\alpha = 1^h36^m41.770^s$ and $\delta = 15°47'00.40''$ 179

List of Tables

2.1 General properties of NGC 6946 . . . 27
2.2 CSO observational parameters. . . . 31
2.3 Beam-corrected line quantities. . . . 35
2.4 Beam-corrected line ratios. . . . 38
2.5 Model results for the two best-model identification methods. . . . 40
2.6 Total H_2 masses and beam-averaged H_2 column densities. . . . 45
B.1 CSO detections. . . . 68
B.1 Continued. . . . 69

3.1 General properties of NGC 4710 and NGC 5866. . . . 76
3.2 Main observational parameters for NGC 4710 and NGC 5866. . . . 79
3.3 Spectral energy distribution of NGC 4710 and NGC 5866. . . . 92
3.4 Model results for the tenuous and dense molecular gas in the nuclear disc and inner ring of NGC 4710. . . . 110
3.5 Model results for the dense gas in the nuclear disc of NGC 5866. . . . 111
A.1 Ratios of CO lines only and dense gas tracer lines only, in both the nuclear disc and inner ring of NGC 4710 and NGC 5866. . . . 137
A.1 Continued. . . . 138
B.1 Ratios of CO to dense gas tracer lines, in both the nuclear disc and inner ring of NGC 4710 and NGC 5866. . . . 139
B.1 Continued. . . . 140
B.1 Continued. . . . 141
B.2 Ratios of CO to dense gas tracer lines in the intermediate region of NGC 4710. 141

4.1 General galaxy parameters. . . . 150
4.2 TFR galaxy parameters. . . . 153
4.3 Best fit parameters for the K_s-band CO TFRs. . . . 160
4.4 Best-fit parameters for the $M_\star$ CO TFRs. . . . 160

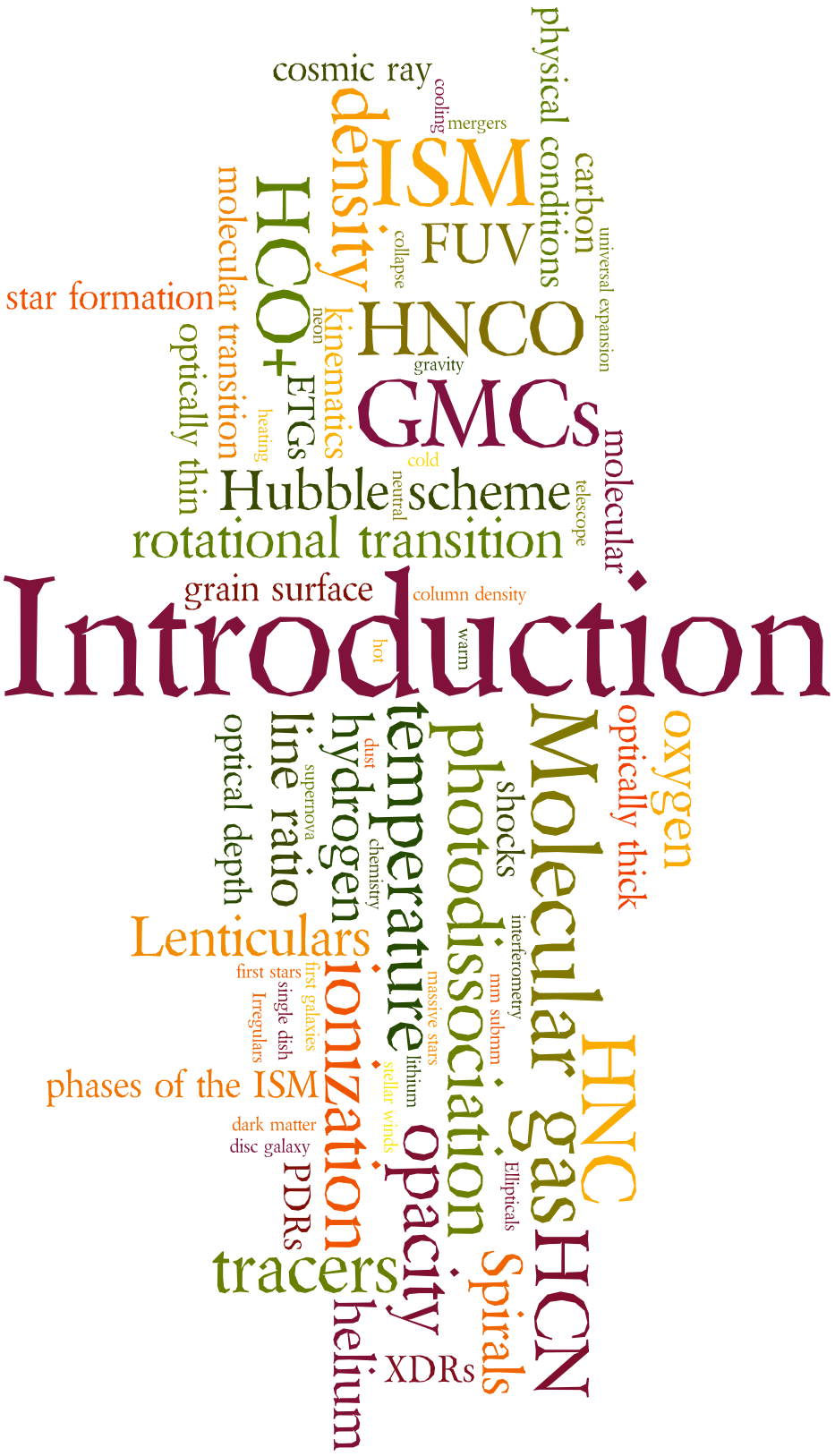
cosmic ray
cooling
mergers
physical conditions
carbon
universal expansion
density
ISM
FUV
collapse
molecular transition
HCO+
HNCO
star formation
kinematics
neon
gravity
optically thin
ETGs
GMCs
molecular
heating
cold
Hubble
scheme
neutral
telescope
rotational transition
grain surface
column density
Introduction
hot
warm
oxygen
optically thick
Molecular gas
HNC
photodissociation
temperature
hydrogen
shocks
dust
line ratio
supernova
chemistry
optical depth
Lenticulars
interferometry
first stars
first galaxies
mm submm
massive stars
single dish
Irregulars
lithium
phases of the ISM
stellar winds
dark matter
disc galaxy
Ellipticals
Spirals
opacity
PDRs
tracers
ionization
XDRs
helium

1

Introduction

"One day humans will walk on the skies, reach to the planets and maybe even send messages back to us from the Moon. There will be no need to wait until the year 2000 for this miracle to take place. The progress of technology gives us a glimpse of this even today. Our duty should be to ensure that we are not too far behind the West in this endeavour."

M. K. Atatürk, 1936, Eskişehir/Türkiye

When the telescope was *arguably*[1] used by Galileo Galilei for the first time for astronomical purposes in 1610, our endless journey through the heavens started. We finally realised that the planets were not revolving around the Sun, being pushed by angels with huge wings, Saturn did not actually have any ears, and most importantly, the Universe encompasses not only our own galaxy but billions of others also. William Herschel catalogued

[1] Although Galileo Galilei is credited as the first person who made the first use of an astronomical telescope and discovered that the Milky Way is made up of a myriad of stars, Leonard Digges, an Oxford-educated mathematician and surveyor, used a telescope (a theodolite pointed upwards) to look at the night sky and observed the band of light across the sky known as Milky Way in 1551. In fact, telescope was invented several times in north-west Europe before 1610 [Gribbin, 2008].

2500 nebulae and died in 1822 with the belief that these nebulae were nothing but diffuse clouds within our own Galaxy, although we now know that only some of them are actually stellar nebulae in our galaxy. Starting from early in the 20th century, paralleling improvements in telescopes, instruments and observational techniques, astronomers finally realised that most of these *diffuse clouds* are truly extragalactic, galaxies outside the Milky Way, spreading across the expanding Universe [Hubble, 1929; Lemaître, 1927, 1931a,b].

Moving forward by nearly a century, this thesis inserts itself in the same quest to understand our Universe. It aims to contribute to the multitude of efforts being made to solve some of the longest standing puzzles in astrophysics, such as the exact nature of star-forming gas and the links between gas chemistry and stellar feedback, the role of galaxy dynamics in the formation and destruction of molecules and gas clouds, and the mass-to-light ratio evolution of different types of galaxies across the Universe. This thesis aims to achieve these goals by seeking answers to many outstanding questions in the field. For example, what drives the physical conditions and the chemistry of molecular gas in galaxies? How does stellar feedback (supernova explosions, stellar winds and radiation from massive stars) affect the gas and its surroundings? Are there differences in the gas physical conditions between the arm and inter-arm regions of spiral galaxies, or between galaxies of different Hubble types? If so, what are the drivers of those differences? Why do some early-types galaxies still have a considerable amount of molecular gas, although they are known to be "red and dead"? Do the gas-rich lenticulars show similar characteristics as the spirals in terms of star formation processes, physical properties and kinematics of the gas? Can we better understand the star formation, gas kinematics and evolution of galaxies by applying line ratio diagnostics, that compare a multitude of molecular emission lines? Is the Tully-Fisher relation (TFR) also valid for higher-redshift disc galaxies, and what are the differences/similarities between high-redshift TFRs and those seen in the nearby Universe? Could carbon monoxide (CO) be used as an alternative to H I for studying the TFR of disc galaxies, particularly more distant galaxies?

One of the challenges to understand the physical properties of the gas in galaxies is that it comes in multiple phases, each having different physical characteristics, i.e. different temperatures and densities (and thus pressures and opacities). However, since each molecular emission line is the result of different physical processes in the gas, analysing multiple lines can help to better diagnose the gas physical conditions. In this thesis, we therefore invest much effort to probe the physical properties (e.g. temperature and density) and kinematics of the molecular gas in disc galaxies (i.e. spirals and lenticulars) in the local and distant universe (up to $z \approx 0.3$), this through observations of multiple transitions of molecular species tracing cold/warm and/or dense/tenuous gas, such as ^{12}CO, ^{13}CO, HCN, HCO$^+$, HNC and HNCO.

In Section 1.1 of this chapter, we briefly introduce the evolution of galaxies and their classification scheme. In Section 1.2, we draw an overall picture of the molecular structure of the interstellar medium (ISM) by giving a brief history of research on the molecular ISM. We start from the creation of the first elements in the Universe (Section 1.2.1), move to the multiple phases of the ISM (Section 1.2.2) and then to complex physics and chemistry (Sections 1.2.3 and 1.2.4), and finally use Section 1.2.5 to provide an overview of radiative transfer in molecular clouds. Finally, in Section 1.3, we discuss the advantages of using CO as a kinematic tracer in galaxies, particularly for the high redshift universe.

In Chapter 2, we present the first project of this thesis, in which giant molecular cloud complexes in the arms and inter-arms of a nearby flocculent spiral galaxy NGC 6946 are studied. For this project, we used single-dish observations of multiple lines of carbon monoxide (CO), i.e., ^{12}CO (1–0, 2–1, 3–2, 4–3, 6–5) and ^{13}CO (1–0, 2–1). In Chapter 3, we apply line ratio diagnostics along the disc of two nearby edge-on lenticular galaxies, NGC 4710 and NGC 5866, using the interferometric observations of not only multiple lines of CO but also some other dense gas tracers, i.e. HCN, HCO$^+$, HNC and HNCO. This work is the first attempt to study the physical properties and the kinematics of the gas along the disc of early-type galaxies using multiple lines of CO and dense gas tracers. Furthermore, we present the first detection of some particular dense gas tracers in both galaxies. In Chap-

ter 4, we present the CO Tully-Fisher (TF) relation constructed for CO rich disc galaxies at $z = 0.05 - 0.3$. We compare our results with that of recent and past TF studies. This work is the first attempt to construct the CO TFR for galaxies at high redshift, which provides a benchmark CO TFR for future higher redshift CO TFR studies.

Each chapter has its own introduction and methodology, where we review the literature, discuss current open questions and present the methods that we use to deal with these questions. Conclusions are made in Chapter 5, in which we summarise the key points drawn from this thesis, discuss ongoing work aiming to further study the properties of molecular gas in galaxies, and finally we share our opinions on some future prospects in the field.

1.1 Evolution of galaxies and their classifications

Evidence of the existence of 'dark matter' [Zwicky, 1933, 1937] led astronomers to propose a variety of models to explain the structure formation of today's Universe. Although the standard cold dark matter (CDM) model [Blumenthal et al., 1984] had been the most widely accepted until the '90s, it was shown that the model predicts less galaxy clustering on large scales than is observed [Efstathiou et al., 1990; Maddox et al., 1990]. Since it has been shown that the cosmic expansion is accelerating [Garnavich et al., 1998; Perlmutter et al., 1999] and the Universe is flat [de Bernardis et al., 2000], the final concordance model to explain the structure formation of the present-day Universe has been the lambda CDM (ΛCDM) model with a non-zero cosmological constant.

During the process of structure formation in the Universe, gravitational instabilities led to the formation of galaxies and stars. According to this scenario, the dark matter collapses in places where the density is slightly higher than the average density. Such clouds of matter attract other nearby clouds and stand against universal expansion to form galaxies, clusters and clusters of clusters and so on. Improvements in our understanding of the evolution and

formation of galaxies and advances made in cosmological computer simulations have enabled us to understand the structure of the Universe on ever larger scales. In this picture, galaxies and clusters of galaxies seem to follow filamentary structure [e.g. Aragón-Calvo et al., 2010; Colless et al., 2001], along which baryonic matter flows to form galaxies and stars.

Today, we are surrounded by many different types of galaxies with a variety of unique shapes and characteristics across the Universe. The still widely used Hubble scheme [Hubble, 1936] classifies galaxies in terms of the size of their bulge, and the structure of the disc. According to this morphological classification, galaxies with no disc are called *ellipticals* (or E0 - 7, where number from 0 to 7 indicates the ellipticity of the galaxy in 2-D, depending on the ratio of the galaxy's apparent major and minor axis), galaxies with a disc but no prominent spiral arms are called *lenticulars* (S0s), and galaxies with spiral arms are called *spirals* (S). Finally galaxies with no prominent shape are called *irregulars* (Irr).

Spirals have a large variety of sub-types, including both barred (SBa-d) and unbarred (SAa-d) systems. The letters a to d represent different classifications among spirals, according to the following criteria: (1) the openness of the spiral arms, (2) the degree of resolution of the arms into stars, (3) the size of the central spheroidal component or bar. Sa galaxies have tightly wound spiral arms and the central bulge or bar is dominant in these galaxies. Spiral arms in Sb galaxies are more open and central spheroidal component or bar is generally smaller than that of Sa types. Sc galaxies, however, have much more open, flocculent arms, which are resolved into star cluster and H II regions, and they have less prominent central spheroidal component or bar. Finally, Sd galaxies have broken, diffuse arms with very faint central component according to the extended Hubble classification scheme [de Vaucouleurs, 1974]. Additionally, spirals with a ring-like structure are denoted by letter 'r', while those without rings are indicated by the letter 's' and 'rs' for transition galaxies in between.

Ellipticals and lenticulars are called early-type galaxies (ETGs), whereas spirals and irregulars are called late-type galaxies. Since Hubble proposed an evolutionary sequence, where ellipticals collapse over time to form spiral discs, this naming was intended to reflect this

evolutionary sequence. Although current hierarchical scenarios suggest that this sequence is reversed, i.e. lower mass spirals merging to form ellipticals, the naming is, however, still used. Because of differences in their evolutionary pathway, galaxies show a variety of different morphologies and physical properties. Figure 1.1 shows this classification scheme via the famous diagram of Hubble.

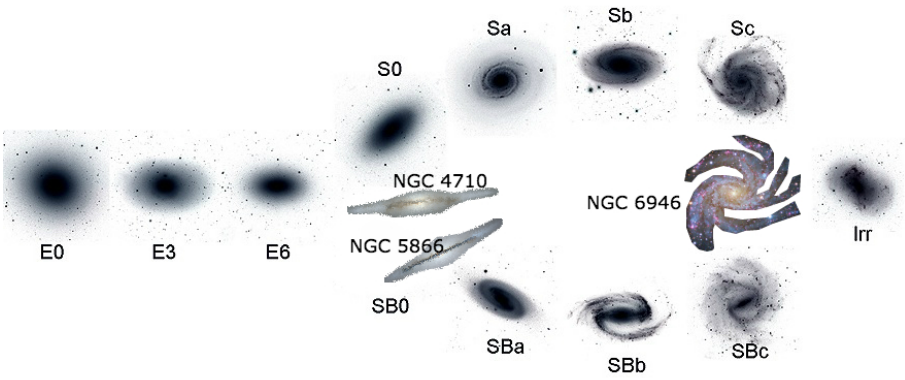

Figure 1.1: Hubble *tuning fork* morphological classification scheme [Hubble, 1936]. Image courtesy: Galaxy Zoo. Three galaxies studied in this thesis, the spiral galaxy NGC 6946 (see Chapter 2) and the lenticulars NGC 4710 and NGC 5866 (see Chapter 3), are overlaid on the image.

However, Kormendy & Bender [1996, 2012] published a revised parallel-sequence morphological classification scheme in which they extend the S0 types to spheroidal (Sph) galaxies that are positioned parallel to irregular galaxies in a similarly extended order: Sa-Sb-Sc-Irr. Kormendy & Bender [2012] suggest that Sph galaxies are transformed, *red and dead* Scd-Im[1] galaxies similar to S0 galaxies, which are transformed *red and dead* Sa-Sc galaxies. A revised parallel-sequence morphological classification of galaxies from Kormendy & Bender [2012] is shown in Figure 1.2.

A more physically motivated classification for S0s has been introduced by the ATLAS^{3D} team[2] by establishing a comb classification scheme [Cappellari et al., 2011]. The disc galaxies were separated into two groups; slow-rotators and fast-rotators (see Figure 1.3). The

[1]Im is a subtype of irregular galaxies without spiral structure
[2]http://www-astro.physics.ox.ac.uk/atlas3d/

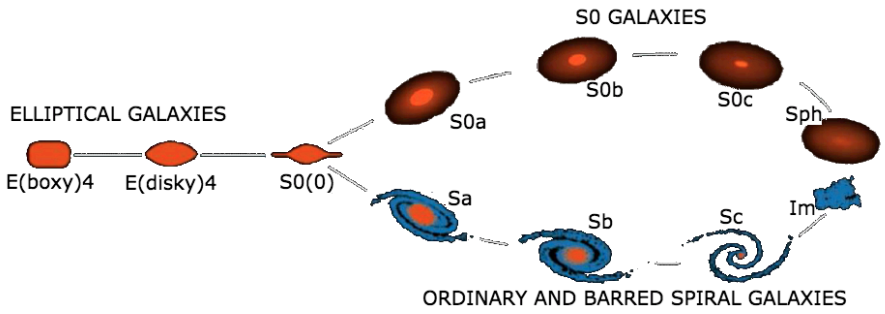

Figure 1.2: A revised parallel-sequence morphological classification of galaxies from Kormendy & Bender [2012] as presented in that work.

comb diagram suggests that lenticulars are evolved spiral galaxies with a smaller amount of molecular gas and a redder colour. Although the Hubble classification suggests an increase of bulge-to-disc ratio for earlier types, the ATLAS^{3D} classification does not imply such a dependence of the ratio on type.

Not only the appearance of galaxies but also their evolutionary paths are different. For instance, ETGs seem to form through mergers of smaller galaxies as the Universe expands and evolves [e.g. Toomre, 1977], while the formation and evolution of spiral galaxies is thought to follow a more secular path driven by the effects of central bar and spiral structure [e.g. Kormendy, 1979]. Additionally, small irregular galaxies are thought to be left over from the early days of the Universe, when there were many more small galaxies than we see around us today.

Since the ETGs follow a morphology-density relation, i.e., the fraction of ETGs increases as the environmental density increases, they are mostly found in clusters where the collisions, mergers, and/or interactions are more frequent than that in the field where spirals are dominant [e.g. Dressler, 1980]. Some simulations of disc galaxy mergers suggest that mergers between disc galaxies could create ellipticals [e.g. Barnes, 1988]. However, the transformation of spirals to ETGs, in other words the migration from the blue-cloud to the red sequence in the galaxy colour-colour diagram [e.g. Baldry et al., 2004; Strateva et al., 2001], is still a subject of much debate [e.g. Bell et al., 2004; Martin et al., 2007] and requires more observations

of both morphological types across the cosmic sea.

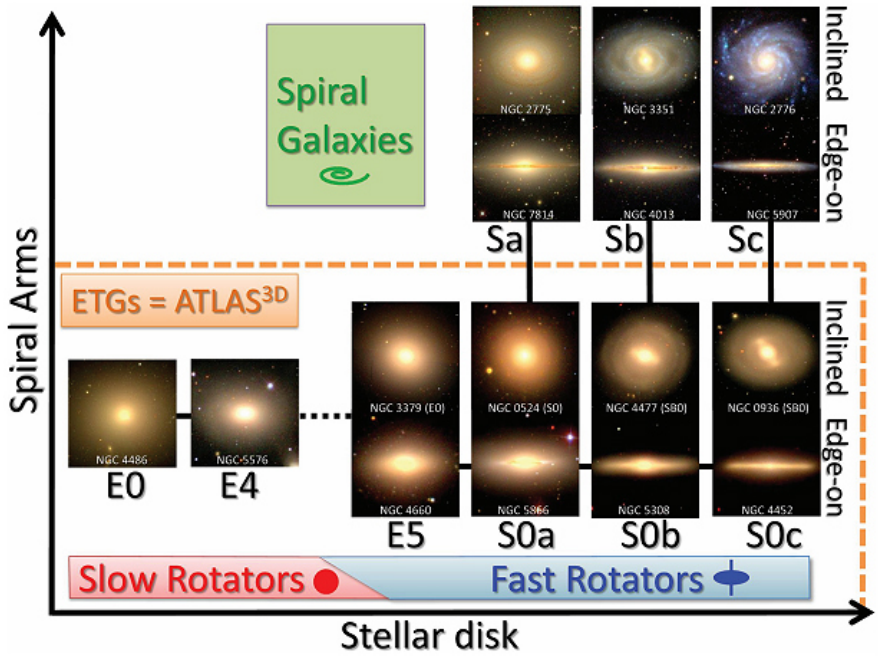

Figure 1.3: Morphology of galaxies from the ATLAS^{3D} survey. Image courtesy: Cappellari et al. [2011].

Although the Universe is full of galaxies with different appearances, they have/had something in common at some point throughout their evolutionary pathway: molecular gas. Since the molecular gas retains some memory of the violent past of its host galaxies as galaxies evolve, it is very important to study the nature of the ISM and the molecular gas in different types of galaxies throughout the expanding Universe. This will help us to better understand the fate of a galaxy, and ultimately the fate of the Universe.

Observations of molecules in galaxies during the last 40 years or so (see Section 1.2) have revealed that while spiral galaxies have a substantial amount of molecular gas —the fuel for star formation—, early-type galaxies appear to be either very poor in molecular gas or have no molecular gas at all. However, the ATLAS^{3D} CO survey of nearby ETGs has shown that about 22% of lenticular galaxies have a substantial amount of molecular gas in their ISM, with H_2 masses ranging from 10^7 to 10^9 $M_\odot$ (assuming a standard CO-to-H_2 conversion

factor; Young et al. 2011).

In the next section, we discuss the overall properties of the ISM and its constituents with more emphasis on the molecular gas. We also discuss some particularly important molecular tracers of the physical properties of the gas, such as its density, temperature and opacity.

1.2 Interstellar Medium of Galaxies

1.2.1 From the First Elements to Today's Complexity

Three minutes after the Big Bang, the Universe became cool enough for protons and neutrons to remain combined as nuclei for the first time. This period is called *nucleosynthesis* and led to the creation of the lightest three elements of the periodic table [i.e., hydrogen (H), helium (He), and very small amount of lithium (Li)]. When the Universe was only $300,000$ years old and much cooler, *'recombination'* occurred: electrons then joined the nuclei to make neutral atoms. At that time, the Universe had a very simple periodic table of only three elements compared with the today's more complex periodic table of over 118 elements[1].

This simple chemistry of the very early universe, with only H, He and Li, led to the creation of huge gas clouds, which were built up in dark matter halos, eventually forming the first stars and proto-galaxies. At the centre of star forming gas clouds, the temperature increased as gravitational energy was released, allowing the fusion of hydrogen into helium to begin. These were the first stars and consisted of only H and He, no heavier elements yet. The first stars were much more massive than the stars surrounding us today, due to their lack of cooling ingredients (i.e., atoms and molecules other than H and He). Thus these stars needed more mass to form. While the first stars evolve, the first heavier elements (up to iron) were fused at their centres and then even heavier elements (e.g. platinum and gold) were ejected into the ISM as the stars ended their lives by catastrophic supernova (SN) explosions [Cowan & Sneden, 2006]. The blast waves coming from these supernovae

[1] http://www.chem.qmul.ac.uk/iupac/AtWt/

caused even smaller clouds to collapse and the heavier elements were able to cool the clouds much more efficiently by collisional excitation/de-excitation processes. Because cooling of gas depends on its metallicity, more metal rich gas cools faster [Mo et al., 2010]. This process led to the formation of 2$^{\rm nd}$ generation stars, which are very similar to the ones in our own galaxy, like our own Sun. This interplay between *life* and *death* of stars has caused remarkable variations in the chemistry and physical properties of the ISM.

1.2.2 Phases of the ISM

After the discovery of the hot inter-cloud medium ($T \sim 10^6$ K), it has been shown that the ISM is not a quiescent place as previously thought [e.g. Burstein et al., 1977; Cox & Smith, 1974; Jenkins & Meloy, 1974]. The ISM is a complex mixture of gas, dust, interstellar radiation field (cosmic microwave background radiation, infrared emission from dust and starlight), and cosmic rays (CRs). The ISM has many phases: hot inter-cloud gas, warm neutral and ionized medium, cold neutral medium, molecular clouds and H II regions. Each one has its own physical characteristics. For instance, while the tenuous (with densities $n \sim 3 \times 10^{-3}$ cm^{-3}) hot inter-cloud gas can reach up to 10^6 K in temperature, the average temperature in the dense molecular clouds ($n > 200$ cm^{-3}), where stars actually begin their life, is only about 10 K. The cold neutral medium (diffuse H I clouds), however, has a temperature of about 100 K, whereas warm neutral medium can be as hot as ~ 8000 K.

The transition between warm, tenuous, and mostly atomic gas to cold, dense and fully molecular gas is driven by turbulent compression, large scale gravitational instabilities, the balance between heating and cooling processes, radiative processes, and magnetic fields. The physical conditions of the ISM can become very different when stellar feedback becomes dominant. For instance, even though the massive stars ($M_\star \sim 10 - 100\ M_\odot$) are rare compared to low mass stars, they have a substantial impact on physics and chemistry of the ISM. High-mass stars are also the main mechanical energy input for the ISM, through strong stellar winds, UV radiation and SN explosions. For instance, SN explosions have a direct

impact on the chemistry of the ISM as they are the main providers of heavy elements, such as iron, silicon, sulphur and calcium. Shock waves coming from SN explosions can quench star formation in the immediate vicinity of the explosion by dramatically increasing the temperature, while simultaneously the shocks could increase the density by accumulating material where star formation may thereafter be triggered. FUV photons and cosmic-rays, which are important heating, ionization and dissociation sources, are also controlled by massive stars in the ISM. For instance, FUV photons can be absorbed by dust grains which, as a result, eject energetic electrons into the ISM. This is one of the important heating mechanisms of the gas, known as *photoelectric heating*. CRs, however, can penetrate deeper into a gas cloud, where the density is too high for significant dissociation by interstellar UV radiation, and dissociate the molecules or ionise the neutral species. Young massive stars, even after their death, can therefore have dramatic effects on the physical properties of the ISM in galaxies (e.g. see Chapter 2).

The physics of the ISM is therefore a multi-scale and multi-physics problem which needs to be solved to understand the true nature of the life cycle of the ISM and ultimately the fate of its host galaxy.

1.2.3 Molecular Clouds

Stars form in regions of the ISM where the gas is extremely cold ($T_{\rm K} \sim 10$ K), dense ($n = 10^3$ - 10^7 cm^{-3}) and mostly molecular, called molecular clouds. The molecular clouds with very high mass ($M > 10^5$ M$_\odot$) are called giant molecular clouds (GMCs). The structure of individual GMCs can be investigated through the structure of photon-dominated regions (PDRs). The PDRs are the regions where far-ultraviolet (FUV, 6 eV $<$ hν $<$ 13.6 eV) photons radiated by young massive O and B stars dominate the medium (see Fig. 1.4). The PDRs form between H II regions and molecular clouds where the gas is mainly neutral. Even though PDRs are traditionally thought to be associated with atomic gas, substantial amount of molecular gas in our own galaxy and in external galaxies has also been found in PDRs

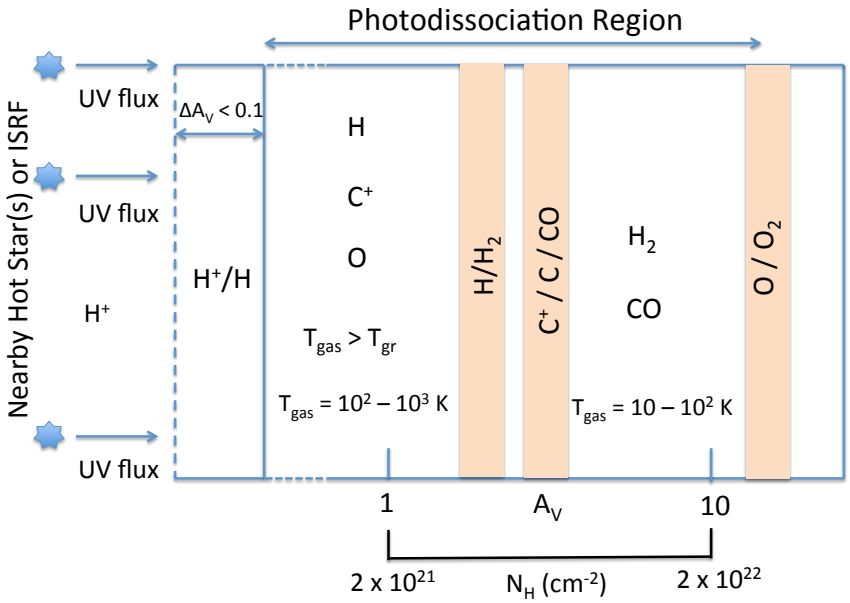

Figure 1.4: Schematic of a photo-dissociation (or photon-dominated) region (PDR) from Hollenbach & Tielens [1999]. $T_{\rm gas}$ indicates gas temperature while $T_{\rm gr}$ represents the temperature of dust grains.

[Hollenbach & Tielens, 1997a].

The first molecule detected in interstellar sight lines was CH [Swings & Rosenfeld, 1937]. The development of radio astronomy in the '50s led to the detection of H I via 21 cm emission [Ewen & Purcell, 1951]. Later, microwave lines of OH [Weinreb et al., 1963], NH_3 [Cheung et al., 1968] and water vapour [Cheung et al., 1969] were detected in the ISM. However, until the early '70s there were very few detected molecules and their abundance was very low. Therefore, it was thought that the ISM was mainly atomic and molecules were a trace abundance. At the time, people did not suspect that the dark clouds seen in the optical wavelength regime might actually be molecular. The development of mm astronomy starting in the '70s has enabled us to detect many other molecules, including the second most abundant molecule of the ISM, carbon monoxide ($^{12}C^{16}O$ hereafter CO), in our own galaxy [Wilson et al., 1970], in external spirals [Rickard et al., 1975; Solomon & de Zafra, 1975], and finally in ETGs [Phillips et al., 1987; Wiklind & Rydbeck, 1986]. Some higher density tracers were also detected, such as hydrogen cyanide (HCN), formyl cation (HCO^+), hydrogen isocyanide

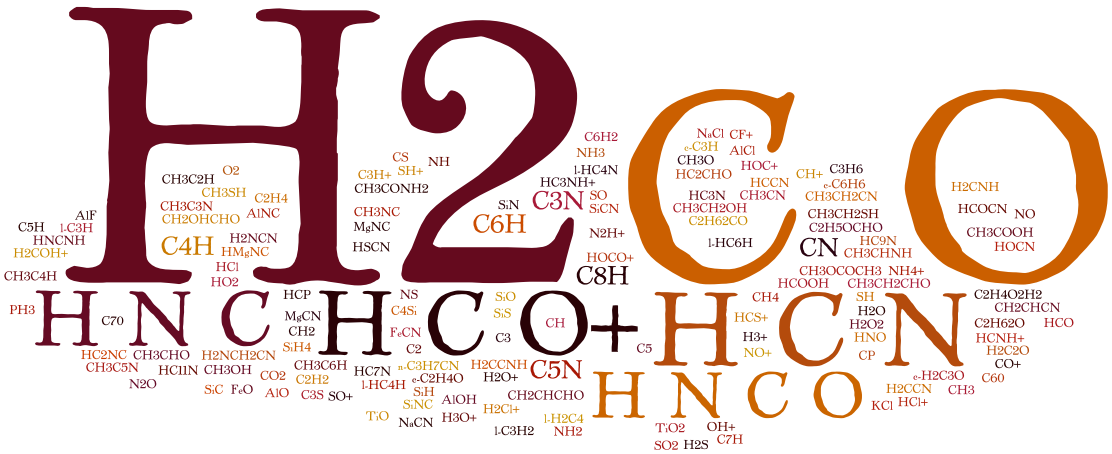

Figure 1.5: The molecules detected in the ISM or circumstellar shells as of May 2015. The H_2 and CO are intentionally shown bigger compared with the others since they are the most abundant molecules of the ISM. The dense gas tracers studied as part of this thesis are also shown bigger in the image compared with the rest of the detected molecules but with no indication for the relative abundances.

(HNC) and isocyanic acid (HNCO) [Buhl & Snyder, 1970; Snyder & Bhul, 1971; Snyder & Buhl, 1971, 1972].

The number of molecules detected in the ISM has dramatically increased since the '70s. From the first elements in the Universe to today's molecular complexity, more than 180 molecules have been identified in the ISM or in circumstellar shells[1], (see Fig. 1.5). Observations of molecules during the last 40 years or so have enlightened us on the physics of the molecular gas and its host ISM [e.g. Hollenbach & Tielens, 1997b, 1999; McKee & Hollenbach, 1980; van Dishoeck & Black, 1988].

The most abundant element in the Universe is H (75% by mass), followed by He (23%), Oxygen (O, 1%), Carbon (C, 0.5%) and Neon (Ne, 0.1%) respectively. However, as discussed previously, at high densities where stars form, H tends to be molecular, i.e., H_2, the most abundant molecule. H_2 cannot form by just combining two H atoms in space, since the collision time for two H atoms is too short ($\sim 10^{-13}$ seconds) to allow photons to radiate and thus remove the binding energy, making the system bound. Another scenario for forming H_2

[1]The data in Figure 1.5 were taken from http://www.astro.uni-koeln.de/cdms/molecules

molecules is three body collisions. In very dense environments [$n(H_2) \sim 10^{19}$ cm^{-3}], three body collisions can occur, forming a H_2 molecule with the binding energy carried out by the third body. However, in molecular clouds the density is too low [$n(H_2) \sim 10^2 - 10^{11}$ cm^{-3}] for this process. On the other hand, dust can act as a catalyst, allowing H_2 molecules to form on its surface, absorbing the binding energy itself. Dust therefore has a very important role in the formation of H_2 and many other simple/complex molecules (e.g. H_2O). Gas phase reactions (e.g. photodissociation, photoionisation, cosmic ray induced reactions) and grain surface reactions (i.e., accretion, surface migration, reaction and evaporation) lead the molecules to form, dissociate, ionise and/or neutralise. All these reactions depend on the density, temperature, and optical depth of the gas, which in turn depend on dominant forces driving the physical properties in and around the cloud (e.g. existence of young massive stars, supernova explosions, and turbulence).

Since H_2 is a homonuclear diatomic molecule, it does not have a permanent electric dipole moment. H_2 has its rotational quadrupole transitions in the far-IR (FIR) but they are very weak because they take such a long time to spontaneously decay (i.e., decay time is ~ 100 years). The lowest vibrational transitions are even less likely to occur with higher excitation energies [Bolatto et al., 2013]. H_2 can be detected via its UV absorption lines but there must be bright and hot background stars along the line of sight to observe this absorption; such examples are very rare. The most abundant molecule of the ISM, H_2, is therefore invisible for typical conditions in star forming clouds.

Unlike H_2, CO has a permanent dipole moment and its lowest rotational transition ($J = 1$–0) lies at an excitation energy of $h\nu/k \sim 5.53$ K corresponding to a wavelength of 2.6mm. This is readily observable from the ground. It is a relatively stable and massive molecule, almost 15 times heavier than H_2. Because of its large mass, it has a large moment of inertia, so its rotational energy levels are closely spaced and therefore easily excited at the very low temperatures seen in molecular clouds [Bolatto et al., 2013]. The CO transitions have therefore been widely used to study the physics of the ISM and to probe the physical

properties of H_2. For instance, using the relation between CO and H_2, called the conversion factor X_{CO}, one can calculate the beam-averaged molecular gas mass [e.g. Young & Scoville, 1991].

Molecules are important coolants of the GMCs which allow stars to form. The cooling is dominated by collisional excitation of rotational transitions of molecules, which then emit radiation in the mm/sub-mm wavelength of the electromagnetic spectrum. This is a very efficient cooling mechanism even at the low temperatures seen in star forming molecular clouds. Depending on the physical conditions of the surrounding medium, the gas chemistry on the surface of the gas cloud could be different than that deeper in the cloud. For example, the destruction of molecules in the outer PDR is driven by UV photons (e.g. HCN + $\nu \rightarrow$ CN + H), while at intermediate depths CRs dominate the destruction (e.g. HCN + CR $\rightarrow$ CN + H). In the dark core of the clouds, however, there may be additional removal processes by different species (e.g destruction of HCN by H^+ where $n \leq 10^3$ cm^{-3}) or by HCO^+ (e.g. HCN + $HCO^+ \rightarrow HCNH^+$ + CO, where $n \geq 10^3$ cm^{-3}). For example, the removal of HCN via HCO^+ is more frequent than that via H^+, leading to the creation of CO deeper in the cloud [e.g. Prasad & Huntress, 1980].

Since molecular clouds are complex places where stars live and die, multiple lines of some key molecules are necessary to diagnose their physical properties. In the following subsections, we briefly discuss some important molecular tracers, of which we present observations, analysis and discuss throughout this thesis, and also give a brief overview of radiative transfer in molecular clouds and the code used for the purpose of this thesis.

1.2.4 Molecular tracers of the ISM

In reality, density and temperature are not spatially uniform throughout a gas cloud. For example, some parts of the cloud, where star formation feedback is present, may have hot and relatively less dense gas compared with the rest of the cloud. This mixture of different densities and temperatures inside the cloud is seen in a single telescopic beam which

ultimately gives the average physical conditions of such a region. However, we can use molecular lines emitted in the mm/sub-mm regime to get a better idea of the physics inside a cloud and its vicinity. Ratios of molecular emission lines are particularly powerful diagnostics to probe temperature, density and kinematics of the gas.

Low-J rotational transitions of the CO can be excited where the temperature and density is relatively low ($T \sim 10$ K and $n_{\rm crit} \sim 10^3$ cm^{-3}). ^{13}CO usually exists as an optically thin gas compared to its parent molecule, CO. Measurements of the rare ^{13}C isotopes of CO indicate that CO emission is often optically thick except along very low column density lines-of-sight [Bolatto et al., 2013]. Additionally, highly turbulent gas motions (e.g. due to strong star formation feedback), or large velocity dispersions (e.g. stellar outflows), can diffuse the CO more efficiently and make its emission optically thin. ^{13}CO is a good tracer for the column density and optical depth of the molecular gas, since it allows us to see through the cloud.

In the optically thick case, the emission can only give information about the temperature at the surface of the gas, while in the optically thin limit we can see right through the cloud. The optical depth of a cloud (τ) has an important effect on critical density. The critical density is the density at which collisions are more frequent than radiative decay. If the critical density of a molecule is higher than the density of the host medium, emission is not likely to occur, and vice versa when the critical density of the molecule becomes less than the density of the medium. When the emitting gas gets optically thick ($\tau \gg 1$), radiative-trapping occurs, resulting in a reduction of the critical density by a factor $\sim 1/\tau$. As τ increases, the escape probability (β), i.e. the probability that a photon can escape the medium without any further interactions –first introduced by Sobolev [1960]–, decreases. In other words, trapping of photons within the cloud means that not every spontaneously-emitted photon escapes the cloud without any further interactions. This leads to higher excitation temperatures than those expected due to collisions with only H_2 [Scoville, 2013].

High density tracers with a higher critical density, such as HCN, HCO$^+$, HNC and HNCO, require a denser environment ($n_{\rm crit} \sim 10^5 - 10^6$ cm^{-3}) to be efficiently excited. HCN and

HCO^+ molecules are the most abundant H_2 mass tracers after CO with much higher dipole moments. HCN could trace gas with densities 100x higher than that traced by HCO^+ [Greve et al., 2009]. HNC, the isomer of HCN, is also an important density tracer and linked to the formation and destruction of many other important molecules of the ISM, while HNCO can trace the dense gaseous cores forming massive stars [Churchwell et al., 1986; Wilson et al., 1996; Zinchenko et al., 2000].

The ratios between the ground level transition of a molecule and its higher transitions, e.g. CO (1–0)/CO (2–1), can trace the temperature and density gradient through the medium. Higher transitions require higher densities and temperatures, as $n_{\mathrm{cr},J} \propto J^3$ and $\mathrm{E}_J \propto J^2$, where J indicates quantum energy levels. Additionally, the ratios of different species can give even more information about the physical properties of the gas and the ISM. For instance, ratios between CO and its isotopologue ^{13}CO trace the optical depth, while the ratios HCN/HCO^+ and HCN/HNC discriminate between PDRs and X-ray dominated regions, XDRs [e.g. Meijerink & Spaans, 2005a; Meijerink et al., 2007a]. Additionally, the HCN/HNC abundance ratio can increase with increasing temperature and density [e.g. Goldsmith et al., 1981; Schilke et al., 1992a]. In dense clouds, measurement of some species, such as HCO^+, relative to CO can be used to trace CRs in the medium [e.g. van der Tak & van Dishoeck, 2000; Williams et al., 1998]. HCO^+ is therefore one of the most important tracers of CRs, and thus SN explosions. Furthermore, HNC abundance can be used to probe the evolutionary stage of pre-stellar cores. Additionally, since HNCO abundances are enhanced in high velocity gas, its production may be related to shocks, similar to SiO [e.g. Meier & Turner, 2005, 2012; Zinchenko et al., 2000].

Line ratio diagnostics are therefore a powerful tool to investigate the physical properties of gas clouds, since every molecular transition requires a different density and temperature to be efficiently excited (see Chapter 2 and 3).

1.2.5 Radiative Transfer

The radiative transfer equation describes what happens to a beam of light that passes through a medium:

$$\frac{dI_\lambda}{d\tau_\lambda} = -I_\lambda + S_\lambda \ ,$$

where I_λ is the intensity of the radiation in the medium, S_λ is generally called the source function and is the ratio of the emission to the absorption coefficient, i.e. $S_\lambda = \varepsilon_\lambda/\kappa_\lambda$, and τ_λ is the optical depth, i.e. $\mathrm{d}\tau_\lambda \equiv \kappa_\lambda \mathrm{ds}$, where s is the path through the medium. The source function equals the Planck function ($S_\lambda = B_\lambda(T)$) when the medium is in local thermodynamical equilibrium (LTE).

We can write the formal solution as follows:

$$I_\lambda = I_{\lambda_0}\, \mathrm{e}^{-\tau_\lambda} \ + \ S_\lambda \left(1 - \mathrm{e}^{-\tau_\lambda}\right) \ .$$

The first term on the right-hand side describes the amount of radiation left over from the light entering the medium after it passes through an optical depth τ_λ. The second term on the right-hand side, on the other hand, gives the contribution of the radiation emitted along the path. To solve the radiative transfer equation, the level populations and radiation fields should be solved for separately.

1.2.5.1 Radiative transfer code: RADEX

RADEX is one of many radiative transfer codes that are publicly available. It uses the so-called escape probability method, i.e. the probability that a photon will escape the medium where it was created, first introduced by Sobolev [1960]. The escape probability depends on the source geometry and optical depth [see Sobolev, 1960]. RADEX estimates the collisional excitation and the radiation field in the following way. It first assumes optically thin emission (i.e. LTE) to calculate the level populations, thus allowing it to calculate the

optical depth and hence the escape probability, from which new level populations can in turn be calculated. The code iteratively calculates the level populations and optical depths until they converge (to a given tolerance level). RADEX then computes all line strengths for that solution. Finally, the program outputs the background-subtracted line intensity in units of the equivalent radiation temperature in the Rayleigh-Jeans limit. The inputs necessary for RADEX are as follows:

- the spectral range of the output;
- the equivalent black body temperature of the background radiation field, usually the cosmic microwave background radiation (T_{CMB});
- the kinetic temperature of the molecular cloud;
- the number density of H_2;
- the column density of the molecule of interest;
- the width of the molecular lines, i.e. the full width at half maximum (FWHM) of the line emission.

RADEX is an "intermediate-level" approach to line data, as compared to "basic-level" methods (i.e. the LTE assumption and rotation diagram method; e.g. Blake et al. 1987; Goldsmith & Langer 1999a; Helmich et al. 1994). RADEX offers three different medium geometries (uniform sphere, radially expanding sphere and homogeneous slab), but the differences between the geometries are generally small [see van der Tak et al., 2007b]. It has been shown that the expressions of the escape probability for the uniform sphere and the expanding sphere give solutions almost identical to those obtained by applying more advanced methods, e.g. Accelerated Lambda Iteration and Monte-Carlo type methods [van der Tak et al., 2007b].

RADEX assumes an isothermal and homogenous medium, which limits the number of free parameters and enables the rapid analysis of large sets of observational data. The program

can be used for any molecule for which collisional data exist, and it uses the collisional data from the Leiden Atomic and Molecular Database (LAMDA; Schöier et al. 2005a; Yang et al. 2010). RADEX does not consider the continuum (e.g. dust) opacity when calculating the escape probability, but continuum radiation from dust is generally negligible at longer wavelengths ($\gtrsim$ 1 mm). RADEX also assumes that the source is resolved. It is therefore necessary to correct for beam dilution or make sure that the source properly fills the telescope beam [van der Tak et al., 2007b].

RADEX cannot accurately calculate line intensities if the optical depth $\tau < -1$ (when masers, i.e. nonlinear amplification of the incoming radiation, saturate). Furthermore, in RADEX only one molecule is treated at a time, so the effects of possible line overlap from other molecules is not considered [van der Tak et al., 2007b]. Although these limitations are present, the performance of RADEX was tested by comparing it to other radiative transfer codes [van der Tak et al., 2007b]. RADEX produces results that are similar to those of full radiative transfer codes using the Monte-Carlo method [Hogerheijde & van der Tak, 2000; Schöier, 2000] and those of multi-zone escape probability codes [Poelman & Spaans, 2005].

Apart from RADEX, many radiative transfer codes have been developed over the years, e.g. Cloudy [Ferland et al., 1998; Shaw et al., 2005], UCL_PDR [Bell et al., 2005], Meijerink [Meijerink & Spaans, 2005b] and Meudon [Le Petit et al., 2006]. The codes are different in many aspects, such as chemistry (e.g. steady state vs. time dependent, chemical networks) and geometry used, treatment of dust, gas heating and cooling, range of input parameters, model output, and numerical treatment (see Röllig et al. 2007). Röllig et al. [2007] present a comparison study of 11 independent codes modeling the physics and chemistry of PDRs, and they conclude that there is overall agreement in the model results. If we had a complete knowledge of the local properties of a real gas cloud and the global observable properties, it would be easy to compare and calibrate many kinds of PDR models. However, this is not obtainable. Therefore none of the codes can reveal the complete physical properties of the gas in galaxies. While some of those codes are dedicated to study the physical conditions in great

detail at the cost of increased computing time, others (such as RADEX) aim at efficient and rapid calculations of large grids of models for comparison with large observational datasets. As a result, each code primarily takes into account some particular processes determining the gas physics and chemistry, while using only rough approximation for the other processes [Röllig et al., 2007].

For instance, the Cloudy and Meudon codes are known to be the most complex codes, accounting for the most physical effects, e.g. heating by cosmic rays, X-rays, turbulence, and photoelectric heating. These codes are therefore useful to study media with extreme conditions. The main features of the UCL_PDR code are a fully time-dependent treatment (similar to Cloudy) and its speed. Although these are advantages, the code is restricted to a plane parallel geometry. The Meijerink code also uses a plane parallel approximation, with more emphasis on XDRs. Meijerink, RADEX and most radiative transfer codes assume a homogeneous density medium, whereas Cloudy and UCL_PDR can also handle time-dependent density variations.

The aim of the studies presented in Chapters 2 and 3 is simply to provide a broad overview of the physical properties of the star-forming molecular gas in carefully-selected galaxies, this using low-J transitions of CO and some other dense gas tracers. Similarly, we are not aiming to study detailed chemistry (time-dependence, freeze-out on grains, etc), the physics of dust, nor the detailed physics of the heating mechanisms or internally generated radiation field. RADEX is thus well suited to our needs, and we adopt it for this thesis.

1.3 CO as a kinematic tracer in galaxies

CO emission is not only a good tracer of the physical properties of the molecular gas and the ISM but also of the kinematics in galaxies. CO also has some advantages compared with H I. For example, CO can be observed in more distant galaxies. Its observations have a smaller beam size which allows us to resolve individual galaxies in clusters at higher redshift.

Additionally, the CO gas is less sensitive to environment (e.g. tidal interactions). Furthermore, it has been shown that very little CO gas needs to lie in the flat part of the rotation curve to properly measure the rotational velocity properly even if CO is relatively centrally concentrated in galaxies compared with H I. These and some other advantages [Lavezzi & Dickey, 1998] make CO an attractive alternative to H I for the Tully-Fisher (TF) relation [Tully & Fisher, 1977a] studies in the nearby universe [e.g. Davis et al., 2011b; Tiley et al., 2015; Torii et al., 2015]. The TFR is a result of the connection between a galaxy's luminosity, i.e., stellar mass, and rotation velocity, i.e., the total mass including dark matter. The relation is therefore used to investigate the mass-to-light ratio (M/L) of galaxies and its evolution throughout the cosmic time. Taking advantage of using CO, particularly for the high-z universe, the TFR can be constructed for galaxies at different redshifts (see Chapter 4).

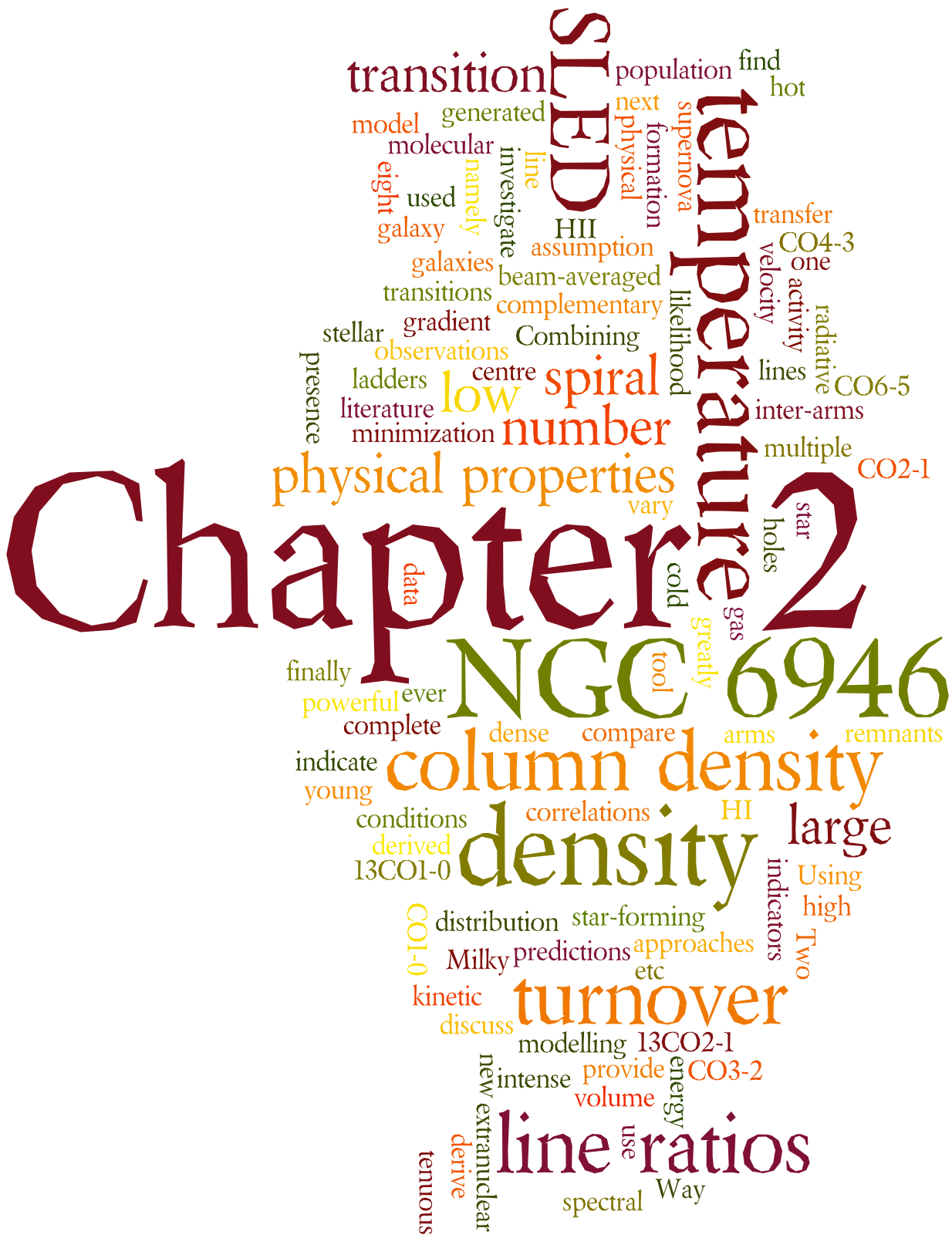
Chapter 2
NGC 6946
physical properties
column density
density
turnover
line ratios
temperature
SLED
transition
number
spiral
low
large
CO2-1
CO3-2
CO4-3
CO6-5
CO1-0
13CO1-0
13CO2-1
HII
HI
Two
Using
Way
Milky
etc
finally
powerful
complete
indicate
young
conditions
derived
distribution
star-forming
predictions
approaches
kinetic
discuss
modelling
intense
provide
volume
energy
new
extranuclear
derive
tenuous
spectral
use
dense
compare
arms
remnants
correlations
indicators
high
ever
tool
greatly
gas
cold
data
holes
star
vary
multiple
inter-arms
lines
radiative
activity
velocity
one
transfer
hot
find
population
next
physical
formation
supernova
line
investigate
namely
eight
used
galaxy
galaxies
transitions
beam-averaged
complementary
Combining
assumption
likelihood
gradient
stellar
observations
centre
ladders
literature
minimization
presence
model
generated
molecular

2

GMC Complexes in the Spiral Galaxy NGC 6946

"The time will come when diligent research over long periods will bring to light things which now lie hidden. A single lifetime, even though entirely devoted to the sky, would not be enough for the investigation of so vast a subject... And so this knowledge will be unfolded only through long successive ages. There will come a time when our descendants will be amazed that we did not know things that are so plain to them... Many discoveries are reserved for ages still to come, when memory of us will have been effaced."

Lucius Annaeus Seneca, Natural Questions, 65 AD

The material in this chapter has been published as "Molecular Gas Properties of the Giant Molecular Cloud Complexes in the Arms and Inter-arms of the Spiral Galaxy NGC 6946", Selçuk Topal, Estelle Bayet, Martin Bureau, Timothy A. Davis and Wilfred Walsh, 2014, MNRAS, Volume: 437, pp. 1434–1455.

2.1 Introduction

The interstellar medium (ISM) of galaxies has many phases, each one with its own temperature, density, chemical composition, etc. At high densities, molecular hydrogen (H_2) dominates and provides the reservoir for star formation (SF). Since its detection in the ISM by e.g. Wilson et al. [1970], Solomon et al. [1971] and Penzias et al. [1971], the ground-state rotational transition ($J = 1$–0) of the CO molecule (second most abundant in the ISM) has become the most widely used tracer of H_2, with an excitation temperature of $\approx$ 5 K and a wavelength of 2.6 mm readily observable from the ground.

Stars form in the densest parts of giant molecular clouds (GMCs), spanning tens of parsecs and weighting $\sim 10^4$–10^6 M_{sun} [Kirk, 2011]. The exact conditions under which star forms are however still poorly understood, and must ultimately depend on the local physical conditions in the dense gas. In this chapter, we thus aim to constrain the physical conditions in the star-forming regions of one particular galaxy, NGC 6946, in the hope of futhering our understanding of SF processes.

NGC 6946 is an almost face-on, nearby (5.5 Mpc; Tully 1988a) spiral galaxy whose basic properties are listed in Table 2.1. It has been intensively studied at all wavelengths, making it a particularly good target to study SF processes using a multitude of tracers. Figure 2.1 shows Hα and H I images of NGC 6946, along with the location of a number of features discussed below. In addition, the 8 key regions on which our analysis will focus are identified there.

The star formation rate (SFR) of NGC 6946 is higher than that of the Milky Way [Degioia-Eastwood et al., 1984; Karachentsev et al., 2005; Sauty et al., 1998]. Extensive CO (1–0) [Tacconi & Young, 1989; Walsh et al., 2002], CO (2–1) [Leroy et al., 2009a] and CO (3–2) [Walsh et al., 2002] observations of NGC 6946 are available in the literature, and we will present here new data comprising one of the most extensive CO (2–1) maps. More limited

Table 2.1: General properties of NGC 6946

Property	Value	Reference
Type	SABcd	1
RA (J2000)	$20^{h}34^{m}52.^{s}3$	2
Dec (J2000)	$60°09'13''$	2
Distance	5.5 Mpc	3
Major-axis diameter	$11'5$	1
Minor-axis diameter	$9'8$	1
Position angle	243°	4
Inclination	33°	4
M_{H_2}	$1.2 \pm 0.1 \times 10^{10}\ M_{\odot}$	5
$V_{\odot}$	40 km s^{-1}	6
SFR	3.12 $M_{\odot}$ yr^{-1}	7

References: (1) NASA/IPAC Extragalactic Database (NED); (2) Skrutskie et al. [2006a]; (3) Tully [1988a]; (4) de Blok et al. [2008]; (5) Tacconi & Young [1989]; (6) Epinat et al. [2008]; (7) Karachentsev et al. [2005].

mapping of the molecules HCN, HCO and CO also exist in the central regions [Ball et al., 1985; Bonnarel et al., 1988; Ishizuki et al., 1990; Levine et al., 2008; Nieten et al., 1999; Regan & Vogel, 1995; Weliachew et al., 1988], and the molecular gas physical properties have been studied in the centre [Bayet et al., 2006; Walsh et al., 2002] and one position in the arms [Walsh et al., 2002]. In this chapter, we will extend this analysis to all 8 regions defined in Figure 2.1.

As shown in Figure 2.1, NGC 6946 has prominent East/North-East spiral arms and more flocculent West/South-West arms [Arp, 1966], allowing us to probe possible differences in the gas physical properties as a function of radius in two physically different parts of the galaxy. Interestingly, NGC 6946 has hosted 9 recorded supernovae in the last 100 years (3 in the past 10 years alone), the highest number in any galaxy [Fridriksson et al., 2008; Schlegel, 1994]. The rate of supernova explosions at the centre of NGC 6946 is as high as 6×10^{-3} yr^{-1} [Engelbracht et al., 1996]. Radio-bright (35; Lacey & Duric 2001) and optically-selected (27; Matonick & Fesen 1997) supernova remnants (SNRs) have also been detected. Some of the regions probed in our study are associated with some of these SNRs (see Fig. 2.1). This SNR

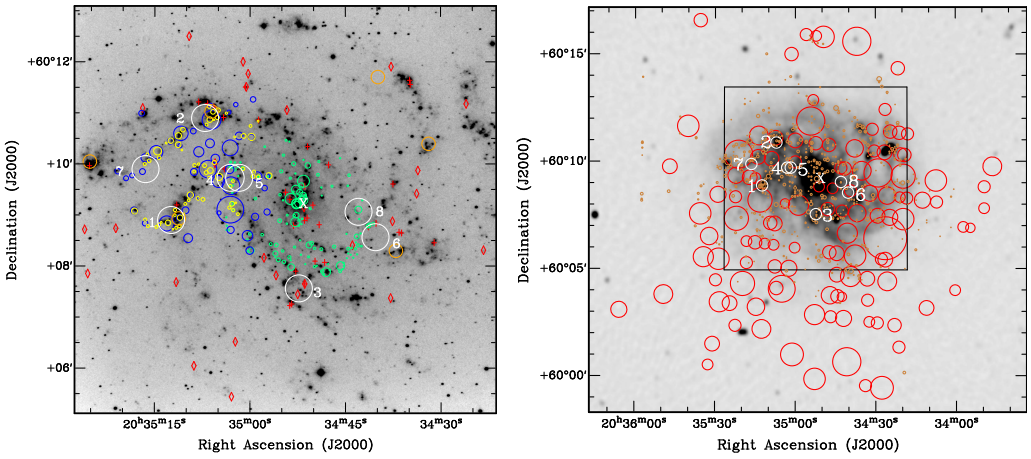

Figure 2.1: Regions studied and star formation-related features in NGC 6946. **Left**: Hα image of NGC 6946 [Knapen et al., 2004]. Overlaid green, yellow, blue and orange circles indicate respectively GMCs in the central 5 kpc [Donovan Meyer et al., 2012], GMCs in the eastern part [Rebolledo et al., 2012], CO (1–0) complexes in the eastern part [Rebolledo et al., 2012], and giant H II complexes [van der Kruit et al., 1977]. Red crosses and diamonds indicate supernova remnants identified in the radio [Lacey & Duric, 2001] and optical [Matonick & Fesen, 1997], respectively. **Right**: H I map of NGC 6946 [Braun et al., 2007]. Overlaid red circles and brown dots represent H I holes [Boomsma, 2007] and H II regions [Bonnarel et al., 1986], respectively. White circles with numbers in both images represent the 8 regions studied in this chapter, with our final common beam size of 31.5″, while the white "X" identifies the centre of the galaxy. The black square on the larger H I map shows our CO (2–1) pointings, covering a contiguous area of 510″ × 510″ centred on the galaxy. North is up and East to the left in all images.

richness implies the presence of a young stellar population, and it suggests an environment very rich in cosmic rays (CRs) produced during supernova explosions. This in turn allows us to probe for the first time in this source the possible relationship between supernovae and molecular gas physical conditions.

A catalogue of 643 H II regions was published by Bonnarel et al. [1986], who found that the H II regions on the eastern side of NGC 6946 are ≈ 30 per cent larger than those on western side. Many of these H II regions are associated with regions studied here, including two giant H II complexes (Fig. 2.1). Ten star-forming regions were studied in details by Murphy et al. [2010], who detected 33 GHz free-free emission and showed that it is as useful a tool to derive SFRs as any other standard diagnostic.

Over 100 H I holes have also been found in NGC 6946, most located in the inner regions where the gas density and SFR are high [Boomsma et al., 2008]. H I holes are thought to be

created by supernovae and stellar winds [Mac Low & McCray, 1988; McCray & Kafatos, 1987; Tenorio-Tagle & Bodenheimer, 1988; Tomisaka & Ikeuchi, 1986], and some of the regions we study directly coincide with holes, while others are located in their vicinity (see Fig. 2.1).

As for the fuel for star formation, Donovan Meyer et al. [2012] found more than 100 GMCs within the central 5 kpc of NGC 6946, with sizes ranging from 40 to 200 pc. Similarly, Rebolledo et al. [2012] studied a 6×6 kpc^2 area in the eastern part of NGC 6946 (where regions 1, 2 and 7 of this work are located) and found 45 CO complexes and 64 GMCs (see Fig. 2.1).

As the physical conditions and thus the SF processes of external galaxies may differ dramatically from those in the Milky Way, I specifically aim here to probe these SF processes in the presence of SNRs, stellar winds, H I holes, etc. All have the potential to significantly perturb both the dynamics and the thermal balance of GMCs. In this chapter, we therefore study in details 8 carefully-selected regions in the spiral arms and inter-arms of NGC 6946 (see Fig. 2.1). The molecular gas physical properties in these regions are probed through the large velocity gradient (LVG) method [de Jong et al., 1975; Goldreich & Kwan, 1974], using the non-local thermodynamic equilibrium (non-LTE) radiative transfer code RADEX [van der Tak et al., 2007a], and exploiting the flux ratios of multiple CO transitions. The specific goals are first to probe the gas physical conditions in various key regions of the galaxy, second to compare the conditions in the various regions (galaxy centre, spiral arms and inter-arms), and last to identify the main drivers of the gas physical conditions.

This chapter is set up as follows. Section 4.2 describes our own CO observations, the literature data we exploit, and their common data reduction. Section 2.3 presents the radiative transfer code adopted to model the molecular gas properties, and the two complementary methods used to identify the best models. In Section 2.4, we present the outcome of our own observations and the physical parameters of the best-fit models. A discussion of the derived parameters in relation to the characteristics and environment of each region is presented in Section 2.5. we conclude briefly in Section 2.6.

2.2 Observation and Data Reduction

2.2.1 Observations

Caltech Submillimeter Observatory (CSO) 10.4-m telescope observations of the CO (2–1), CO (3–2), CO (4–3), CO (6–5) and C I ($^3P_1$-$^3P_0$) lines were performed in 2003-2005 in atmospheric conditions varying from good to excellent ($\tau_{225\,\mathrm{GHz}} \leq 0.1$). The spatial coverage of the observations in each line is shown in Figure 2.2, overlaid on an optical image (Digitized Sky Survey, DSS). The CO (2–1) observations cover a $510'' \times 510''$ contiguous region centred on the galaxy, with a full-width at half-maximum (FWHM) beam size of $31.5''$. The CO (3–2) observations consist of clusters of pointings around the galaxy centre, region 1 and region 2, and a series of pointings along the major-axis toward the East (beam size $21''$). The CO (4–3) observations consist of a cluster of pointings around the galaxy centre, and a single pointing around region 1 and region 2 (beam size $15.7''$). The same applies to CO (6–5), although region 2 was not observed (beam size $10.5''$). The C I ($^3P_1$-$^3P_0$) observations have only a few pointings along the major-axis toward the East (beam size $14.7''$).

The main observational parameters of the CSO observations are listed in Table 2.2. All observations used the superconducting tunnel junction receivers operated in double side-band mode. A $3'$ chopping throw was adopted for the CO (2–1), CO (3–2), CO (4–3) and C I ($^3P_1$-$^3P_0$) lines, but a throw of only $1'$ for the CO (6–5) transition as its emission is more compact. The spectra were obtained with two acousto-optic spectrometers with effective bandwidths of 1000 and 500 MHz and spectral resolutions of ≈ 1.5 and 2 MHz, respectively. There was no sign of contamination by emission in the off beams in any spectrum. The pointing was checked using planets (Jupiter, Mars and Saturn) and evolved stars (IRC 10216 and R Hya), yielding a pointing accuracy of $\approx 5''$. The overall flux calibration is good to ≈ 20 per cent.

We show the spectra in Figure A.1 of and list our CSO detections (with a peak signal-to-noise ratio $S/N \geq 3$) in Table B.1 in Appendices. The CO (2–1) integrated intensity and

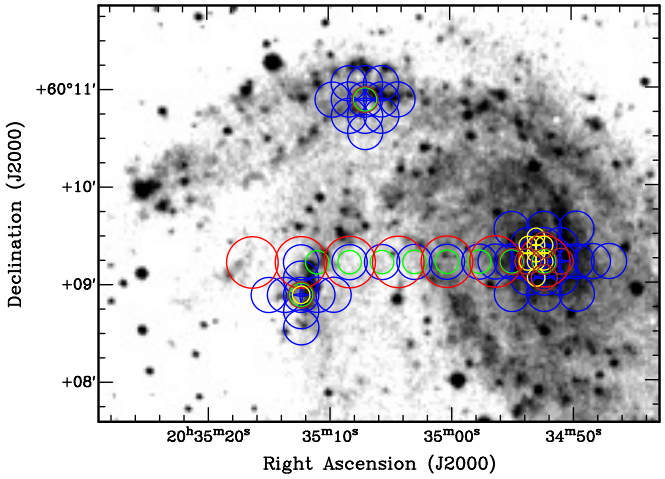

Figure 2.2: NGC 6946 optical image (DSS), overlaid with the grid of CSO pointings for the CO (3–2) (blue), CO (4–3) (brown), CO (6–5) (yellow) and C I ($^3P_1$-$^3P_0$) (green) lines. The circles have a diameter equal to the beam size (FWHM) of each line. The CO (2–1) pointings cover a much larger contiguous area of $510'' \times 510''$ centred on the galaxy (see Fig. 2.1), so only a few representative pointings are shown in red along the major-axis.

Table 2.2: CSO observational parameters.

Line	Rest frequency (GHz)	Beam size (arcsec)	Linear distance (kpc)	$\eta_{\rm mb}^{\rm a}$
CO (2–1)	230.538	31.5	0.84	0.70
CO (3–2)	345.795	21.0	0.56	0.75
CO (4–3)	461.040	15.7	0.42	0.50
CO (6–5)	691.473	10.5	0.28	0.50
C I ($^3P_1$-$^3P_0$)	492.160	14.7	0.39	0.53

[a]Main beam efficiency (http://www.submm.caltech.edu/cso/).

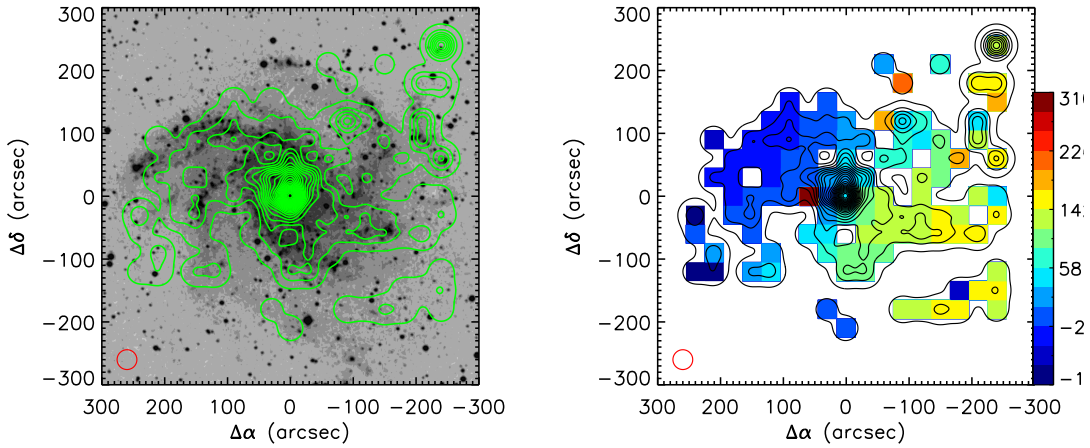

Figure 2.3: **Top**: NGC 6946 CO (2–1) integrated line intensity map (green contours), overlaid on an optical image (DSS). **Bottom**: Same CO (2–1) integrated line intensity map (black contours), overlaid on the CO (2–1) mean velocity field. Contours are from 1 to 80 per cent of the peak integrated intensity of 100 K km s^{-1}, in steps of 5 per cent. The CO (2–1) beam of 31.5″ is shown in red in the bottom-left corner of each panel.

mean velocity maps are presented in Figure 2.3, overlaid on an optical image (DSS). These are some of the largest CO (2–1) maps of NGC 6946 ever presented, with an average RMS noise level of $T_{mb} = 45$ mK. Finally, we also show in Figure 2.4 the radial distribution of the various molecular lines observed. As we do not have full spatial coverage for all lines (see above), standard azimuthal averages on ellipses are not possible, and we simply took linear cuts along the major-axis toward the East. We however also note a detection of CO (6–5) at a distance of ≈ 4 kpc from the centre toward the East (region 1; see Table 2.3).

2.2.2 Literature data

In addition to our own CSO observations described above [CO (2–1), CO (3–2), CO (4–3) and CO (6–5)], we use complementary data from Walsh et al. [2002]: CO (1–0) in region 1; CO (1–0), ^{13}CO (1–0) and ^{13}CO (2–1) in region 2; CO (1–0), CO (3–2) and ^{13}CO (2–1) in regions 3, 4, 5, 6 and 8; and CO (1–0), CO (3–2) and CO (4–3) in region 7. The CO (1–0) and ^{13}CO (1–0) observations were obtained at the Institut de Radioastronomie

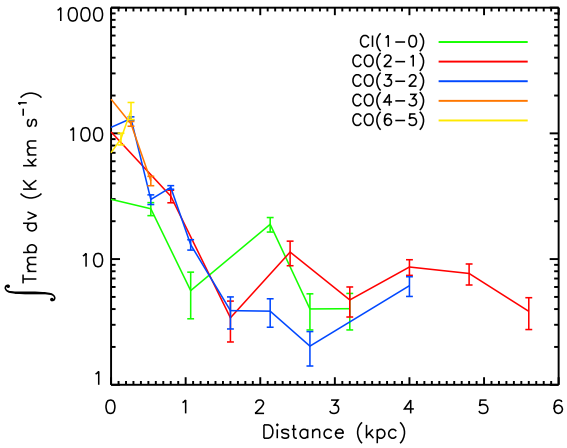

Figure 2.4: Radial distribution of the molecular gas in NGC 6946. The surface density profiles were obtained by taking a straight linear cut along the major-axis toward the East for each line. All surface density profiles decrease rapidly within ≈ 1 kpc and then remain nearly flat. Colours are as in Figure 2.2.

Millimetrique (IRAM) 30-m telescope with beam sizes of 21.8″ and 22.8″, respectively. The CO (3–2), CO (4–3) and ^{13}CO (2–1) observations were obtained at the Heinrich Hertz 10-m Telescope (HHT) with beam sizes of 21.8″, 16.4″ and 34.3″, respectively. We refer the reader to Walsh et al. [2002] for further information on these observations.

2.2.3 Data reduction

Both our own CSO data and the literature data from the IRAM 30-m telescope and HHT were consistently (re-)reduced using the Continuum and Line Analysis Single-Dish Software (CLASS) software package in the Grenoble Image and Line Analysis System (GILDAS). A baseline fit (polynomial of order 0 or 1, occasionally 2) was removed from each scan before averaging all integrations. Then, for each line in each region, a Gaussian was fit to the integrated spectrum to derive the velocity-integrated line intensity S (in K km s^{-1}). The fits are shown in Figure A.1 of Appendices, overlaid on the spectra. The integrated line intensity was then transformed from the antenna temperature scale ($T_{\rm A}^{*}$) to the main beam brightness temperature scale ($T_{\rm mb}$) by dividing by the main beam efficiency ($\eta_{\rm mb}$). The main

beam efficiencies for the IRAM 30-m telescope and HHT observations were taken from Walsh et al. [2002]. The velocity-integrated line intensities and velocity widths (full width at half maximum, FWHM) are listed in Table B.1.

To estimate the beam-averaged total intensities per unit area I and fluxes F, we used the standard expressions below (see also Bayet et al. 2004):

$$\frac{I}{\mathrm{W\,m^{-2}\,sr^{-1}}} = 1.02 \times 10^{-18} \left(\frac{\nu}{\mathrm{GHz}}\right)^{3} \left(\frac{S}{\mathrm{K\,km\,s^{-1}}}\right), \tag{2.1}$$

$$\frac{F}{\mathrm{W\,m^{-2}}} = \left(\frac{I}{\mathrm{W\,m^{-2}\,sr^{-1}}}\right) \left(\frac{\Omega_{\mathrm{B}}}{\mathrm{sr}}\right), \tag{2.2}$$

$$\frac{\Omega_{\mathrm{B}}}{\mathrm{sr}} = 1.133 \left(\frac{\theta_{\mathrm{B}}^{2}}{\mathrm{arcsec^{2}}}\right) \left(\frac{1}{206265^{2}}\right), \tag{2.3}$$

$$\frac{\theta_{\mathrm{B}}}{\mathrm{rad}} = 1.22\,\frac{\lambda}{D}, \tag{2.4}$$

where ν and λ are respectively the observed line frequency and wavelength, Ω_{B} is the solid angle sustained by the beam, θ_{B} is the beam size (FWHM) and D is the diameter of the telescope.

After calculating the integrated line intensity for each region and line on which our analysis focuses, using both our and literature data, we applied beam dilution corrections to all measured quantities to express them for a single, common spatial resolution, chosen here to be the CO (2–1) beam size of $31.5''$. Under the assumption that all the emission in each region comes from the same cloud, we have corrected our values for beam dilution assuming a fixed source size for each region. Similarly to Walsh et al. [2002] and Bayet et al. [2006], we used the highest spatial resolution map available for the size measurements. As no molecular gas map exists at sufficiently high resolution, we used instead the 24 μm image from the Spitzer Infrared Nearby Galaxies Survey (SINGS; Kennicutt et al. 2003).

Specifically, to calculate each source size, we first considered a circular zone equal to the

Table 2.3: Beam-corrected line quantities.

Region	Position ($\Delta\alpha(''), \Delta\delta('')$)	Radius[a] (kpc)	Line	k	$\int T_{\rm mb}\,{\rm d}v$[b] (K km s^{-1})	Intensity (W m^{-2} sr^{-1})	Flux (W m^{-2})	FWHM (km s^{-1})
1	$(150, -20)$	4.04	CO(1-0)	0.51	8.73 ± 0.37	$1.36 \pm 0.06 \times 10^{-11}$	$3.60 \pm 0.15 \times 10^{-19}$	24.9 ± 1.1
			CO(2-1)	1.00	9.16 ± 1.40	$1.14 \pm 0.18 \times 10^{-10}$	$3.02 \pm 0.46 \times 10^{-18}$	27.5 ± 4.6
			CO(3-2)	0.48	5.12 ± 0.70	$2.16 \pm 0.29 \times 10^{-10}$	$5.71 \pm 0.78 \times 10^{-18}$	26.8 ± 4.3
			CO(4-3)	0.29	3.90 ± 0.55	$3.89 \pm 0.55 \times 10^{-10}$	$1.03 \pm 0.14 \times 10^{-17}$	27.5 ± 5.1
			CO(6-5)	0.16	2.27 ± 0.78	$7.63 \pm 2.63 \times 10^{-10}$	$2.01 \pm 0.70 \times 10^{-17}$	20.2 ± 8.3
2	$(110, 100)$	3.96	CO(1-0)	0.52	8.25 ± 0.42	$1.29 \pm 0.07 \times 10^{-11}$	$3.41 \pm 0.18 \times 10^{-19}$	28.7 ± 1.7
			CO(2-1)	1.00	8.74 ± 1.48	$1.09 \pm 0.19 \times 10^{-10}$	$2.89 \pm 0.48 \times 10^{-18}$	44.6 ± 8.2
			CO(3-2)	0.49	5.49 ± 0.36	$2.31 \pm 0.15 \times 10^{-10}$	$6.12 \pm 0.40 \times 10^{-18}$	34.1 ± 2.4
			CO(4-3)	0.31	2.89 ± 0.39	$2.89 \pm 0.39 \times 10^{-10}$	$7.64 \pm 1.02 \times 10^{-18}$	27.1 ± 3.9
			^{13}CO(1-0)	0.56	1.05 ± 0.10	$1.42 \pm 0.13 \times 10^{-12}$	$3.77 \pm 0.35 \times 10^{-20}$	29.3 ± 3.1
			^{13}CO(2-1)	0.20	0.45 ± 0.06	$4.96 \pm 0.63 \times 10^{-12}$	$1.31 \pm 0.17 \times 10^{-19}$	28.1 ± 4.0
3	$(0, -100)$	2.67	CO(1-0)	0.63	7.54 ± 0.45	$1.18 \pm 0.07 \times 10^{-11}$	$3.11 \pm 0.19 \times 10^{-19}$	26.2 ± 1.9
			CO(2-1)	1.00	7.80 ± 1.78	$9.74 \pm 2.22 \times 10^{-11}$	$2.57 \pm 0.59 \times 10^{-18}$	36.2 ± 11.3
			CO(3-2)	0.63	6.76 ± 1.12	$2.85 \pm 0.47 \times 10^{-10}$	$7.53 \pm 1.24 \times 10^{-18}$	32.4 ± 6.9
			^{13}CO(2-1)	1.13	1.43 ± 0.26	$1.56 \pm 0.28 \times 10^{-11}$	$4.12 \pm 0.75 \times 10^{-19}$	30.6 ± 7.5
4	$(80, 30)$	2.28	CO(1-0)	0.58	4.75 ± 0.45	$7.42 \pm 0.70 \times 10^{-12}$	$1.96 \pm 0.18 \times 10^{-19}$	15.9 ± 1.7
			CO(2-1)	1.00	11.14 ± 1.76	$1.39 \pm 0.22 \times 10^{-10}$	$3.68 \pm 0.58 \times 10^{-18}$	39.4 ± 8.3
			CO(3-2)	0.58	2.53 ± 0.53	$1.07 \pm 0.23 \times 10^{-10}$	$2.82 \pm 0.59 \times 10^{-18}$	13.2 ± 3.6
			^{13}CO(2-1)	1.15	1.61 ± 0.39	$1.75 \pm 0.43 \times 10^{-11}$	$4.63 \pm 1.12 \times 10^{-19}$	17.3 ± 5.2
5	$(70, 30)$	2.03	CO(1-0)	0.65	5.73 ± 0.34	$8.95 \pm 0.53 \times 10^{-12}$	$2.36 \pm 0.14 \times 10^{-19}$	15.6 ± 1.1
			CO(2-1)	1.00	13.07 ± 1.98	$1.63 \pm 0.25 \times 10^{-10}$	$4.32 \pm 0.65 \times 10^{-18}$	53.5 ± 10.1
			CO(3-2)	0.65	3.90 ± 0.49	$1.65 \pm 0.21 \times 10^{-10}$	$4.35 \pm 0.55 \times 10^{-18}$	19.2 ± 3.0
			^{13}CO(2-1)	1.12	0.72 ± 0.12	$7.89 \pm 1.35 \times 10^{-12}$	$2.08 \pm 0.36 \times 10^{-19}$	20.9 ± 3.9
6	$(-90, -40)$	2.63	CO(1-0)	0.49	4.77 ± 0.43	$7.46 \pm 0.67 \times 10^{-12}$	$1.97 \pm 0.18 \times 10^{-19}$	24.1 ± 2.5
			CO(2-1)	1.00	7.95 ± 1.66	$9.93 \pm 2.08 \times 10^{-11}$	$2.63 \pm 0.55 \times 10^{-18}$	27.6 ± 7.3
			CO(3-2)	0.49	3.21 ± 0.51	$1.35 \pm 0.21 \times 10^{-10}$	$3.58 \pm 0.56 \times 10^{-18}$	37.9 ± 5.6
			^{13}CO(2-1)	1.18	1.24 ± 0.20	$1.35 \pm 0.22 \times 10^{-11}$	$3.58 \pm 0.58 \times 10^{-19}$	25.4 ± 4.3
7	$(180, 40)$	4.92	CO(1-0)	0.52	3.67 ± 0.43	$5.73 \pm 0.66 \times 10^{-12}$	$1.51 \pm 0.17 \times 10^{-19}$	22.3 ± 2.9
			CO(2-1)	1.00	8.42 ± 1.84	$1.05 \pm 0.23 \times 10^{-10}$	$2.78 \pm 0.61 \times 10^{-18}$	34.9 ± 9.9
			CO(3-2)	0.52	2.36 ± 0.61	$9.95 \pm 2.59 \times 10^{-11}$	$2.63 \pm 0.68 \times 10^{-18}$	17.7 ± 4.3
			CO(4-3)	0.33	1.07 ± 0.22	$1.07 \pm 0.22 \times 10^{-10}$	$2.83 \pm 0.59 \times 10^{-18}$	16.7 ± 4.9
8	$(-70, -10)$	1.89	CO(1-0)	0.62	7.32 ± 0.44	$1.14 \pm 0.07 \times 10^{-11}$	$3.02 \pm 0.18 \times 10^{-19}$	27.8 ± 1.9
			CO(2-1)	1.00	6.45 ± 1.22	$8.06 \pm 1.52 \times 10^{-11}$	$2.13 \pm 0.40 \times 10^{-18}$	22.6 ± 4.0
			CO(3-2)	0.62	3.87 ± 0.58	$1.63 \pm 0.25 \times 10^{-10}$	$4.31 \pm 0.65 \times 10^{-18}$	24.4 ± 4.5
			^{13}CO(2-1)	1.07	0.51 ± 0.12	$5.54 \pm 1.25 \times 10^{-12}$	$1.46 \pm 0.33 \times 10^{-19}$	18.7 ± 4.9

Notes: [a]Radii are calculated with respect to the galaxy centre. [b]The CO (2–1) integrated intensities and the line widths were obtained by interpolating the two closest detections of the large-scale mapping.

adopted beam (diameter 31.5″) centred on each region. We then calculated the total area with a flux above 50 per cent of the peak within this zone, and took the source size as the diameter of a circle with that same area. We thus measured source sizes of 7.8, 9.3, 22.1, 15.6, 5.9, 19.9, 9.7 and 19.5″ for regions 1 to 8, respectively. Although the area with a flux above 50 per cent of the peak is not contiguous in regions 3, 4 and 8, the secondary peaks are much smaller in both area and flux and should therefore have little impact on our modelling results. In any case, although this method of measuring source sizes is only approximate, all the lines in a given region are corrected to the same source size, so the method adopted only has a small effect on the final line ratios used in the modeling (see Section 2.3). Indeed, reducing the source sizes by 50 per cent (thus the source areas by a factor of 4) or increasing the source sizes by 50 per cent (thus the source areas by a factor of ≈ 2) only changes the line ratios by ≈ 12 per cent on average.

A beam dilution correction factor k was calculated for each line and each region using the source sizes calculated and a method similar to that described in Walsh et al. [2002] and Bayet et al. [2006]:

$$k = (\theta_{\rm line}^2 + \theta_{\rm source}^2) \,/\, (\theta_{\rm common}^2 + \theta_{\rm source}^2)\,, \tag{2.5}$$

where $\theta_{\rm line}$ is the beam size of the observations for the line considered, $\theta_{\rm common}$ is the common beam size adopted (here 31.5″) and $\theta_{\rm source}$ is the source size of the region considered. The correction factors obtained for all lines and all regions are listed in Table 2.3.

Following this, the beam dilution-corrected integrated line intensities (K km s^{-1}), beam-averaged total intensities (W m^{-2} sr^{-1}) and total fluxes (W m^{-2}) for the 8 regions studied were calculated and are also listed in Table 2.3. These are the values we will refer to and use in the rest of this paper, in particular for the line ratio analysis discussed in Section 2.3. The line ratios computed using these beam dilution-corrected values are listed in Table 2.4.

2.3 Modeling

2.3.1 Radiative transfer code

The radiative transfer equations need to be solved to probe the physical conditions of the molecular gas. This is achieved here applying RADEX [van der Tak et al., 2007a], a non-LTE radiative transfer code using the LVG approximation [de Jong et al., 1975; Goldreich & Kwan, 1974] and yielding line intensities as a function of a set of user-specified parameters: gas kinetic temperature $T_{\rm K}$, molecular hydrogen number volume density $n(\rm H_2)$ and CO number column density per unit line width $N(\rm CO)/\Delta v$. Here we take the FWHM of the Gaussian fit of each line as the line width Δv (see Table 2.3). We do not need to correct for the instrumental resolution, as it is always much smaller (≈ 2 km s^{-1}) than the observed line widths (see Table 2.3).

The LVG approximation assumes a one-dimensional (1D) isothermal ISM with a velocity gradient sufficiently large to ensure that the source function is locally defined. RADEX computes the first level populations using statistical equilibrium in the optically thin limit and considering a background radiation field (taken here to be a black body with temperature 2.73 K), and then calculates the optical depths of the lines. RADEX further calculates both the internally-generated radiation and the integrated intensity of the lines as background-subtracted Rayleigh-Jeans equivalent radiation temperatures. We assume here a uniform spherical geometry.

In our models, the range of parameters considered is: $T_{\rm K} = 10$ to 250 K in steps of 5 K, $n(\rm H_2) = 10^2$ to 10^7 cm^{-3} in steps of $10^{0.25}$ cm^{-3} and $N(\rm CO) = 10^{15}$ to 10^{21} cm^{-2} in steps of $10^{0.25}$ cm^{-2}. The collisional rate coefficients between the molecules $\rm H_2$, CO and ^{13}CO have been measured by several authors [e.g. Flower & Launay, 1985; Green & Thaddeus, 1976; Schinke et al., 1985] and we use here the Leiden Atomic and Molecular Database (LAMDA; Schöier et al. 2005b; Yang et al. 2010) for the most recent data. The ortho- to para-$\rm H_2$

Table 2.4: Beam-corrected line ratios.

Region	Line Ratio	Value
1	^{12}CO(2-1) / ^{12}CO(1-0)	1.05 ± 0.17
	^{12}CO(3-2) / ^{12}CO(1-0)	0.59 ± 0.08
	^{12}CO(4-3) / ^{12}CO(1-0)	0.45 ± 0.07
	^{12}CO(6-5) / ^{12}CO(1-0)	0.26 ± 0.09
2	^{12}CO(2-1) / ^{12}CO(1-0)	1.06 ± 0.19
	^{12}CO(3-2) / ^{12}CO(1-0)	0.66 ± 0.06
	^{12}CO(4-3) / ^{12}CO(1-0)	0.35 ± 0.05
	^{13}CO(1-0) / ^{12}CO(1-0)	0.13 ± 0.01
	^{13}CO(2-1) / ^{12}CO(2-1)	0.05 ± 0.01
3	^{12}CO(2-1) / ^{12}CO(1-0)	1.03 ± 0.24
	^{12}CO(3-2) / ^{12}CO(1-0)	0.90 ± 0.16
	^{13}CO(2-1) / ^{12}CO(2-1)	0.18 ± 0.05
4	^{12}CO(2-1) / ^{12}CO(1-0)	2.34 ± 0.43
	^{12}CO(3-2) / ^{12}CO(1-0)	0.53 ± 0.12
	^{13}CO(2-1) / ^{12}CO(2-1)	0.14 ± 0.04
5	^{12}CO(2-1) / ^{12}CO(1-0)	2.28 ± 0.37
	^{12}CO(3-2) / ^{12}CO(1-0)	0.68 ± 0.09
	^{13}CO(2-1) / ^{12}CO(2-1)	0.06 ± 0.01
6	^{12}CO(2-1) / ^{12}CO(1-0)	1.67 ± 0.38
	^{12}CO(3-2) / ^{12}CO(1-0)	0.67 ± 0.12
	^{13}CO(2-1) / ^{12}CO(2-1)	0.16 ± 0.04
7	^{12}CO(2-1) / ^{12}CO(1-0)	2.30 ± 0.57
	^{12}CO(3-2) / ^{12}CO(1-0)	0.64 ± 0.18
	^{12}CO(4-3) / ^{12}CO(1-0)	0.29 ± 0.07
8	^{12}CO(2-1) / ^{12}CO(1-0)	0.88 ± 0.17
	^{12}CO(3-2) / ^{12}CO(1-0)	0.53 ± 0.09
	^{13}CO(2-1) / ^{12}CO(2-1)	0.08 ± 0.02

ratio is assumed to be thermalised at the given kinetic temperature. The CO/^{13}CO isotopic abundance ratio is taken to be 40 [Bayet et al., 2006; Henkel & Mauersberger, 1993a; Israel & Baas, 2001] for the regions where ^{13}CO observations are available.

2.3.2 Best-fit models

We use a standard χ^2 approach to identify the best-fit model in each region. For each region and each set of model parameters ($T_{\rm K}$, $n(\rm H_2)$, $N(\rm CO)$), the χ^2 is defined as

$$\chi^2 \equiv \sum_i \left(\frac{R_{i,\rm mod} - R_{i,\rm obs}}{\Delta R_{i,\rm obs}} \right)^2 , \tag{2.6}$$

where $R_{\rm mod}$ is the modeled line ratio, $R_{\rm obs}$ is the observed line ratio with uncertainty $\Delta R_{\rm obs}$ (see Table 2.4), and the summation is over all independent line ratios i for that region (one fewer than the number of lines available for that region). The best-fit model parameters for each region are listed in Table 2.5 and are taken as the set of parameters yielding the smallest χ^2 ($\chi^2_{\rm min}$).

We also plot in Figure 2.5 the contours of $\Delta\chi^2 \equiv \chi^2 - \chi^2_{\rm min}$ in ($T_{\rm K}$, $n(\rm H_2)$, $N(\rm CO)$) space, to illustrate the uncertainties of the best-fit models and the usual degeneracies between the model parameters. The only way to break those degeneracies is to add observations of other lines coming from the same (or similar) gas phase as the current CO lines, e.g. low-J HCN lines (with similar critical densities; see e.g. Jansen 1995).

2.3.3 Likely models

We additionally applied the likelihood method to our models, calculating for each region the probability distribution function (PDF) of each model parameter. That is, for each possible value of a model parameter, we calculated the sum of the $e^{-\Delta\chi^2/2}$ for all possible values of the other two parameters. These PDFs are shown in Figure 2.6 along with their peak (most likely) and median values within the model grid, as well as the 68 per cent (1σ)

Table 2.5: Model results for the two best-model identification methods.

Region	Parameter	χ^2 minimisation	Likelihood	Region	Parameter	χ^2 minimisation	Likelihood
1	$T_{\rm K}$	250* K	153^{+69}_{-138} K	2	$T_{\rm K}$	250* K	211^{+27}_{-42} K
	$\log(n(\rm H_2))$	3.0 cm^{-3}	$3.0^{+2.4}_{-0.6}$ cm^{-3}		$\log(n(\rm H_2))$	2.3 cm^{-3}	$2.3^{+0.2}_{-0.2}$ cm^{-3}
	$\log(N(\rm CO))$	18.5 cm^{-2}	$19.2^{+0.9}_{-0.5}$ cm^{-2}		$\log(N(\rm CO))$	18.8 cm^{-2}	$18.8^{+0.2}_{-0.2}$ cm^{-2}
	$J_{\rm max}$	6			$J_{\rm max}$	5	
	CO cooling	3.30×10^{-9} W m^{-2} sr^{-1}			CO cooling	1.76×10^{-9} W m^{-2} sr^{-1}	
	$\tau_{\rm CO_{1-0}}$	0.3			$\tau_{\rm CO_{1-0}}$	4.7	
	$\tau_{\rm CO_{2-1}}$	4.3			$\tau_{\rm CO_{2-1}}$	13.7	
	$\tau_{\rm CO_{3-2}}$	8.2			$\tau_{\rm CO_{3-2}}$	22.9	
	$\tau_{\rm CO_{4-3}}$	10.3			$\tau_{\rm CO_{4-3}}$	24.5	
	$\tau_{\rm CO_{6-5}}$	8.1			$\tau_{\rm ^{13}CO_{1-0}}$	0.7	
					$\tau_{\rm ^{13}CO_{2-1}}$	1.9	
3	$T_{\rm K}$	175 K	139^{+76}_{-80} K	4	$T_{\rm K}$	15 K	105^{+94}_{-71} K
	$\log(n(\rm H_2))$	3.3 cm^{-3}	$2.9^{+0.9}_{-0.6}$ cm^{-3}		$\log(n(\rm H_2))$	7.0* cm^{-3}	$4.4^{+1.8}_{-1.7}$ cm^{-3}
	$\log(N(\rm CO))$	19.3 cm^{-2}	$19.5^{+0.6}_{-0.6}$ cm^{-2}		$\log(N(\rm CO))$	18.3 cm^{-2}	$19.6^{+0.7}_{-0.8}$ cm^{-2}
	$J_{\rm max}$	7			$J_{\rm max}$	2	
	CO cooling	6.77×10^{-9} W m^{-2} sr^{-1}			CO cooling	1.09×10^{-9} W m^{-2} sr^{-1}	
	$\tau_{\rm CO_{1-0}}$	1.5			$\tau_{\rm CO_{1-0}}$	8.5	
	$\tau_{\rm CO_{2-1}}$	6.8			$\tau_{\rm CO_{2-1}}$	8.0	
	$\tau_{\rm CO_{3-2}}$	14.5			$\tau_{\rm CO_{3-2}}$	22.1	
	$\tau_{\rm ^{13}CO_{2-1}}$	1.1			$\tau_{\rm ^{13}CO_{2-1}}$	0.4	
5	$T_{\rm K}$	15 K	41^{+108}_{-28} K	6	$T_{\rm K}$	15 K	111^{+95}_{-77} K
	$\log(n(\rm H_2))$	4.0 cm^{-3}	$3.7^{+1.9}_{-0.5}$ cm^{-3}		$\log(n(\rm H_2))$	4.3 cm^{-3}	$3.5^{+1.8}_{-0.9}$ cm^{-3}
	$\log(N(\rm CO))$	17.8 cm^{-2}	$17.9^{+0.6}_{-0.4}$ cm^{-2}		$\log(N(\rm CO))$	17.3 cm^{-2}	$18.6^{+1.1}_{-2.4}$ cm^{-2}
	$J_{\rm max}$	2			$J_{\rm max}$	3	
	CO cooling	5.24×10^{-10} W m^{-2} sr^{-1}			CO cooling	3.66×10^{-10} W m^{-2} sr^{-1}	
	$\tau_{\rm CO_{1-0}}$	3.1			$\tau_{\rm CO_{1-0}}$	0.6	
	$\tau_{\rm CO_{2-1}}$	2.4			$\tau_{\rm CO_{2-1}}$	1.4	
	$\tau_{\rm CO_{3-2}}$	5.5			$\tau_{\rm CO_{3-2}}$	0.9	
	$\tau_{\rm ^{13}CO_{2-1}}$	0.2			$\tau_{\rm ^{13}CO_{2-1}}$	$\ll 1$	
7	$T_{\rm K}$	35 K	65^{+99}_{-43} K	8	$T_{\rm K}$	35 K	140^{+76}_{-81} K
	$\log(n(\rm H_2))$	3.8 cm^{-3}	$4.1^{+1.8}_{-0.8}$ cm^{-3}		$\log(n(\rm H_2))$	3.5 cm^{-3}	$2.9^{+0.4}_{-0.7}$ cm^{-3}
	$\log(N(\rm CO))$	15.0* cm^{-2}	$17.8^{+2.5}_{-2.1}$ cm^{-2}		$\log(N(\rm CO))$	17.8 cm^{-2}	$18.2^{+0.7}_{-0.7}$ cm^{-2}
	$J_{\rm max}$	3			$J_{\rm max}$	4	
	CO cooling	3.82×10^{-10} W m^{-2} sr^{-1}			CO cooling	5.58×10^{-10} W m^{-2} sr^{-1}	
	$\tau_{\rm CO_{1-0}}$	$\ll 1$			$\tau_{\rm CO_{1-0}}$	0.6	
	$\tau_{\rm CO_{2-1}}$	$\ll 1$			$\tau_{\rm CO_{2-1}}$	3.5	
	$\tau_{\rm CO_{3-2}}$	$\ll 1$			$\tau_{\rm CO_{3-2}}$	4.2	
	$\tau_{\rm CO_{4-3}}$	$\ll 1$			$\tau_{\rm ^{13}CO_{2-1}}$	0.2	

Notes: χ^2 minimisation results list the best-fit models, defined as having the smallest χ^2. Likelihood results list the median value and 68 per cent (1σ) confidence levels of the marginalised probability distribution function of each model parameter. A star (*) indicates a value lying at the edge of the model grid. See Section 2.3 for more details.

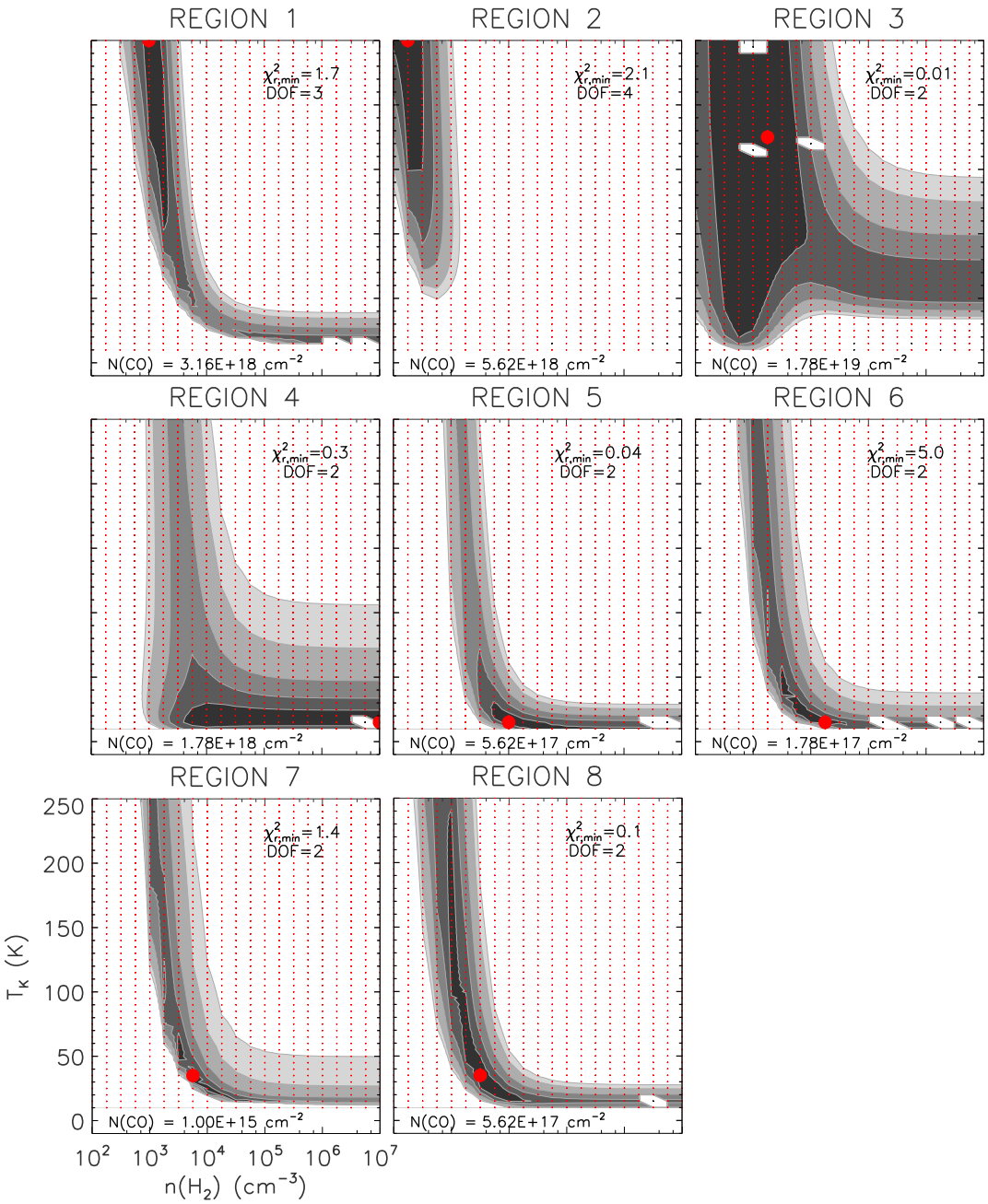

Figure 2.5: $\Delta\chi^2$ maps (contours and greyscales; see Section 2.3.2). For each region, $\Delta\chi^2$ is shown as a function of $T_{\rm K}$ and $n(\rm H_2)$ for the best-fit $N(\rm CO)$ (indicated in the bottom-left corner of each panel). The model grid is indicated with red dots and the best-fit model with a red filled circle. Black dots represent bad models (e.g. unacceptably low opacity; see van der Tak et al. 2007a). $\Delta\chi^2$ contours indicate the 1 σ (darkest zone) to 5 σ (lightest zone) confidence levels in steps of 1 σ. For 3 line ratios (all regions except regions 1 and 2, 2 degrees of freedom), the levels are 2.3, 6.2, 11.8, 19.3 and 24.0. For 4 line ratios (region 1, 3 degrees of freedom), the levels are 3.5, 8.0, 14.2, 22.1 and 28.0. For 5 line ratios (region 2, 4 degrees of freedom), the levels are 4.7, 9.7, 16.3, 24.5 and 32.0. The reduced $\chi^2_{\rm min}$ ($\chi^2_{\rm r,min}$) values together with their corresponding degrees of freedom are also shown in each panel.

confidence levels around the median (following Kaviraj et al. 2007). The latter values are listed in Table 2.5.

2.4 Results

2.4.1 Empirical results

Figure 2.3 shows our new CO (2–1) integrated intensity and mean velocity maps of NGC 6946, some of the most extensive in the literature. Molecular gas traced by CO (2–1) emission is pervasive in NGC 6946, albeit concentrated along the spiral arms, and the velocity field is regular. Although our coverage is patchy, CO (3–2) emission (tracing slightly more excited gas) is particularly strong around regions 1 and 2, located in the prominent East/North-East spiral arms. These two regions are also very bright at Hα [Knapen et al., 2004], 24 μm [Kennicutt et al., 2003], 850 μm [Bianchi et al., 2000] and 6.2 cm [Beck & Hoernes, 1996], suggesting intense SF in a dusty ISM. Regions 4, 5, 6 and 7 have weaker H I emission than that of the other regions (see Fig. 2.1).

Figure 2.4 shows the radial distribution of the molecular gas using the multiple tracers available. Two different components dominate: a highly concentrated central molecular core with a radius ≤ 1 kpc, and a nearly flat lower surface brightness disc extending to large radii.

Of the 134 GMC candidates identified by Donovan Meyer et al. [2012] in the central 5 kpc of NGC 6946, only 30 are fully resolved in their data, and the others could be blends of GMCs smaller than the beam. Donovan Meyer et al. [2012] found that the most massive clouds ($> 10^7$ $M_\odot$) are located at the very centre of NGC 6946, and that clouds with masses $> 5 \times 10^5$ $M_\odot$ are preferentially found where the cloud density is highest (i.e. in the spiral arms). They also showed that the GMC sizes range from 40 to 200 pc in the central 5 kpc, similar to the sizes found by Rebolledo et al. [2012] for 64 GMCs in the eastern part of the galaxy (50 to 150 pc). As our adopted common beam size of 31.5″ corresponds to a linear diameter of ≈ 840 pc at the distance of NGC 6946, our beam will usually encompass

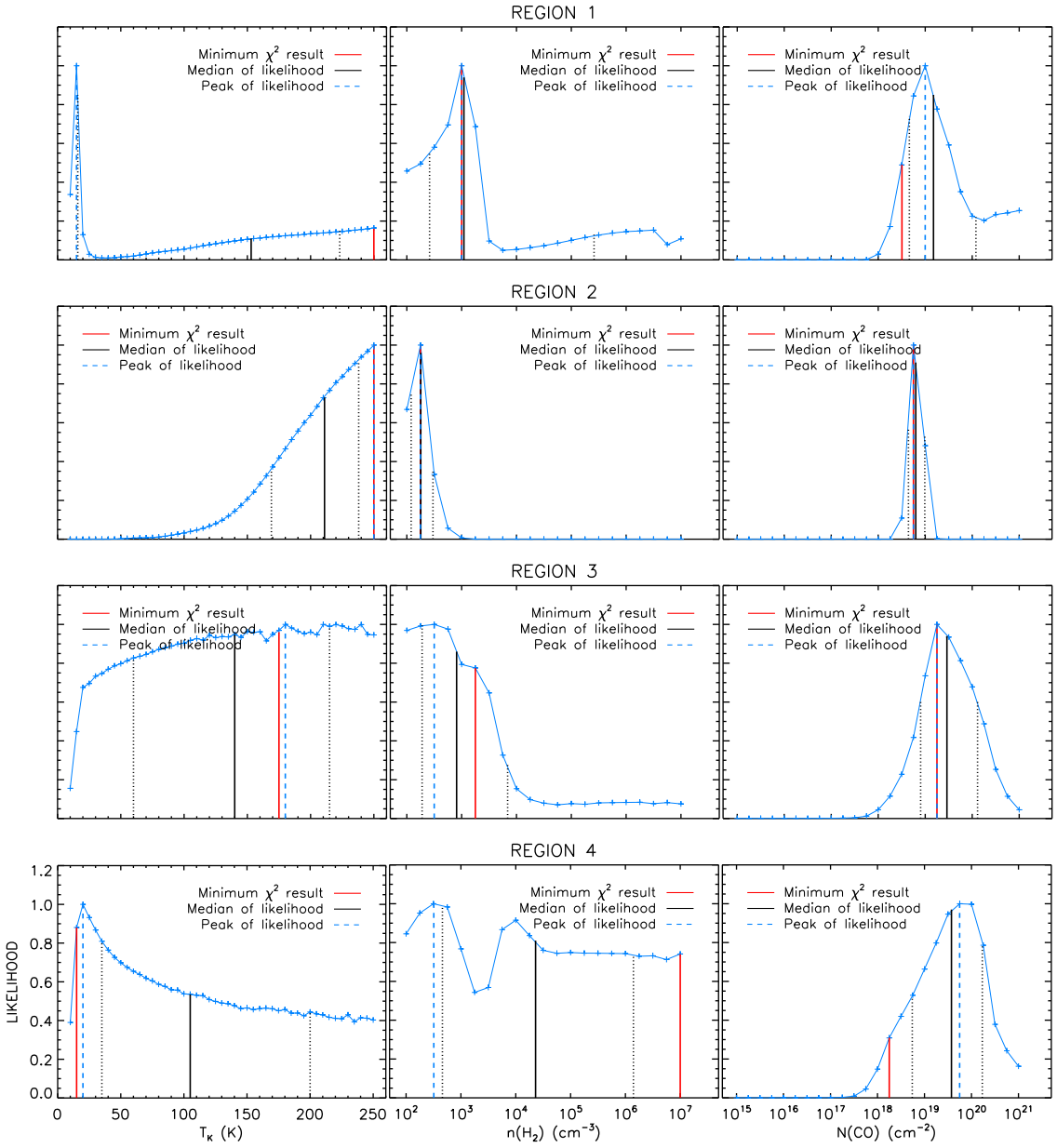

Figure 2.6: Marginalised probability distribution functions. For each region, the PDF of each model parameter marginalised over the other two is shown. The peak (most likely) and median values within the model grid are identified with dashed blue and solid black lines, respectively. The 68 per cent (1σ) confidence levels around the median are indicated by dotted black lines. The best-fit model from χ^2 minimisation is indicated by a solid red line.

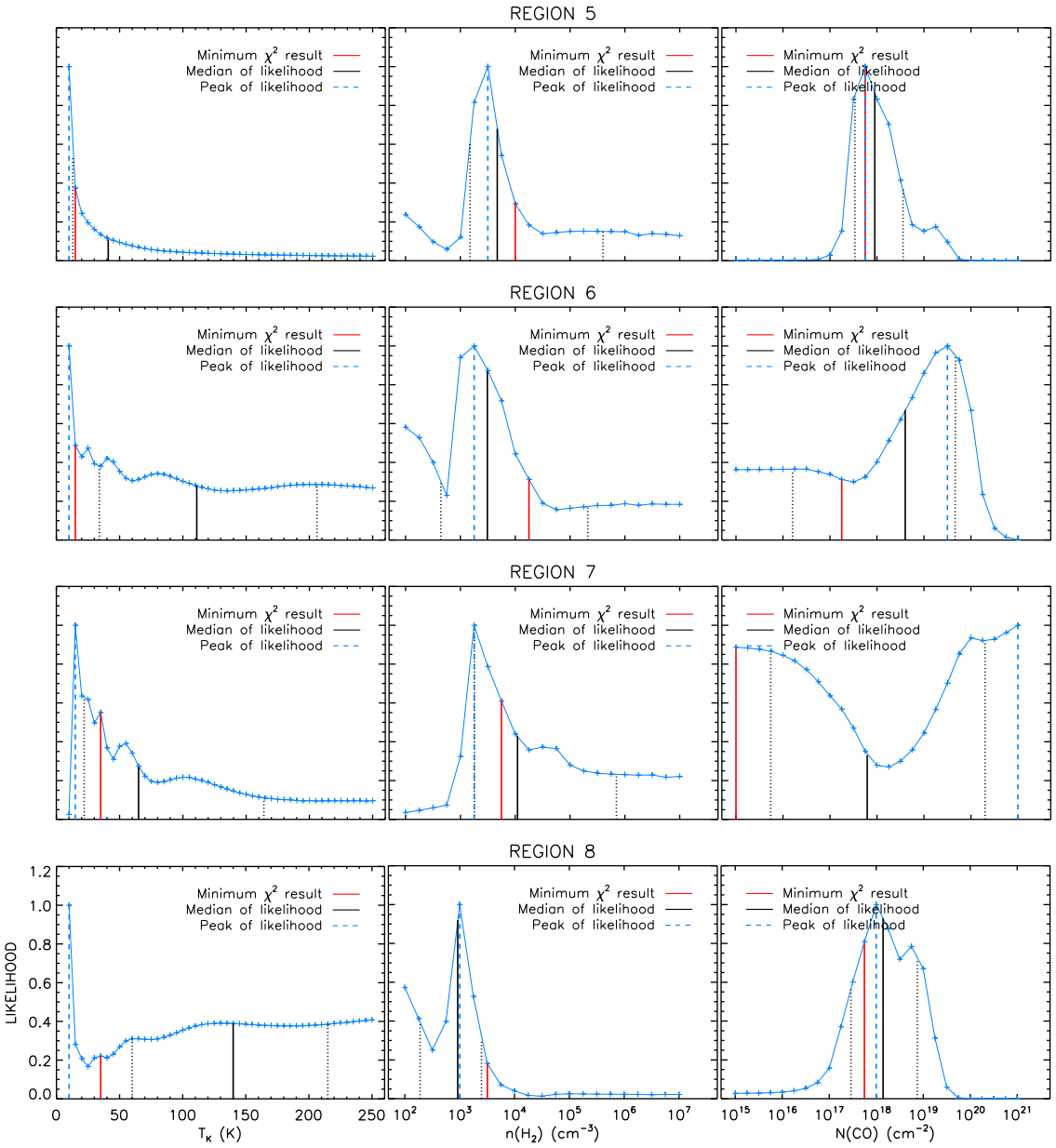

Figure 2.6: Continued.

Table 2.6: Total H_2 masses and beam-averaged H_2 column densities.

Region	M_{H_2} ($M_\odot$)	$N(H_2)$ (cm^{-2})
1	$3.1 \pm 0.1 \times 10^6$	$1.1 \pm 0.1 \times 10^{21}$
2	$2.9 \pm 0.2 \times 10^6$	$9.9 \pm 0.5 \times 10^{20}$
3	$2.7 \pm 0.2 \times 10^6$	$9.0 \pm 0.5 \times 10^{20}$
4	$1.7 \pm 0.2 \times 10^6$	$5.7 \pm 0.5 \times 10^{20}$
5	$2.1 \pm 0.1 \times 10^6$	$6.9 \pm 0.4 \times 10^{20}$
6	$1.7 \pm 0.2 \times 10^6$	$5.7 \pm 0.5 \times 10^{20}$
7	$1.3 \pm 0.2 \times 10^6$	$4.4 \pm 0.5 \times 10^{20}$
8	$2.6 \pm 0.2 \times 10^6$	$8.8 \pm 0.5 \times 10^{20}$

an ensemble of (giant) molecular clouds. For each region, I thus estimate the total H_2 mass enclosed within our beam (M_{H_2}) using the CO-to-H_2 conversion factor ($X_{CO} = N(H_2)$ / S_{1-0}) calculated by Donovan Meyer et al. [2012] from their 30 spatially-resolved GMCs in the centre of NGC 6946 (see Fig. 2.1): $X_{CO} = 1.2 \times 10^{20}$ cm^{-2} (K km s^{-1})$^{-1}$, consistent with the value assumed for the eastern GMCs by Rebolledo et al. [2012] and the average for the NGC 6946 disc reported by Sandstrom et al. [2013]. Sandstrom et al. [2013] do report a depression of the X_{CO} value in the very centre of NGC 6946 (i.e. within a radius of 1.2 kpc), but since all our regions are well outside of this our calculations should be unaffected. Considering the adopted beam, distance, and X_{CO} factor, we thus obtain

$$\frac{M_{H_2}}{M_\odot} = 3.6 \times 10^5 \left(\frac{S_{1-0}}{\mathrm{K\,km\,s^{-1}}} \right). \tag{2.7}$$

The resulting total H_2 mass and beam-averaged H_2 column density of each region are listed in Table 2.6. The gas complex in region 1 has the highest CO (1–0) flux and thus total H_2 mass ($3.1 \pm 0.1 \times 10^6$ $M_\odot$), while the gas in the inter-arm region 7 (farthest from the galaxy centre) has the lowest mass ($1.3 \pm 0.2 \times 10^6$ $M_\odot$). Having said that, the total gas mass does not vary much from region to region (factor ≈ 3), and for the 8 regions studied it does not vary linearly with distance from the galaxy centre (as hinted from Fig. 2.4). All regions have total H_2 masses $> 5 \times 10^5$ $M_\odot$.

As shown in Table 2.4, the beam-corrected velocity-integrated line intensity of the CO (2–1) transition is higher than that of all other transitions observed in all regions (including region 8 within the uncertainties). While R_{21} (the CO (2–1) / CO (1–0) line ratio) is higher than unity in all regions, all other line ratios considered (with respect to the ground state) are less than unity. Interestingly, R_{31} (the CO (3–2) / CO (1–0) line ratio) is the only line ratio that is very similar in all regions. Where there are measurements, the isotopologue transitions ^{13}CO (1–0) and ^{13}CO (2–1) are 5–20 times fainter than their parent lines. The line ratios of regions 1, 2 and 3, those of regions 4, 5, and 6, and lastly those of regions 7 and 8 are similar (although not identical) to each other, suggesting similar molecular gas physical conditions in each group of regions.

Figure 2.7 shows the beam-corrected velocity-integrated line ratios (as listed in Table 2.4) as a function of radius, from $\approx$ 2 (region 8) to 5 kpc (region 7). The well-sampled radial profiles of R_{31}, R_{41} (the CO (4–3) / CO (1–0)) line ratio) and R_{22} (the ^{13}CO (2–1) / CO (2–1) line ratio) show little variation with radius ($R_{31} \approx 0.7$, $R_{41} \approx 0.4$ and $R_{22} \approx 0.1$). R_{61} (the CO (6–5) / CO (1–0) line ratio) and R_{11} (the ^{13}CO (1–0) / CO (1–0) line ratio) were measured in two different regions only (see Fig.2.7). R_{31} is less than that at the centre of our own Galaxy, but higher than in the Milky Way arms [Oka et al., 2007].

The R_{21} ratio does vary across the radial range probed ($R_{21} \approx$ 1.0–2.5), but it is always greater than 1.0. Koda et al. [2012] studied the spatial variations of R_{21} in both the arms and inter-arm regions of M 51 (with a spatial resolution comparable to ours), and found that $R_{21} > 0.7$ in the spiral arms (often 0.8–1.0). They also showed that R_{21} generally increases with SF activity (as traced by $f_{24\mu m}$ and $f_{24\mu m}/S_{CO(1-0)}$). However, Koda et al. [2012] do note that high values of R_{21} are also present with low $f_{24\mu m}$, $S_{CO(1-0)}$ and $f_{24\mu m}/S_{CO(1-0)}$ values, at the upstream edges of the 24 μm spiral arms (indicating dense gas that could potentially form massive OB stars). As regions 4, 5, 6 and 7 in NGC 6946 are located in the more flocculent spiral arms and inter-arm regions, the CO (1–0) velocity-integrated line intensity is lower there compared to other regions, and this could be the cause of the high

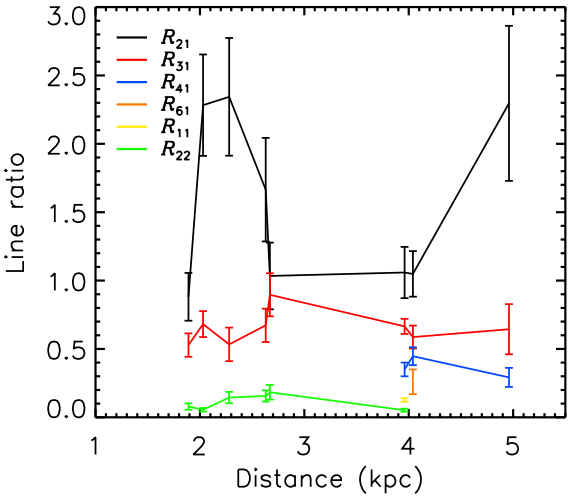

Figure 2.7: Beam-corrected line ratios as a function of radius in NGC 6946. The line ratios are color-coded and defined in the text (see Section 2.4.1).

R_{21} ratios observed. These regions may therefore have dense but not very warm pre-SF gas.

2.4.2 Modeling results

2.4.2.1 Molecular ISM physical conditions

The physical parameters estimated for each region are listed in Table 2.5, from both the χ^2 minimisation and likelihood methods. Overall, across the 8 regions considered, the modeled beam-averaged kinetic temperature $T_{\rm K}$ ranges from 15 to 250 K (the whole range of models considered), while the molecular hydrogen number volume density $n(\rm H_2)$ and the CO number column density $N(\rm CO)$ vary by a factor of ≈ 100 (although regions 4 and 7 possibly have more extreme values of $n(\rm H_2)$ and $N(\rm CO)$, respectively). In some regions, one of the best-fit model parameters lies at the edge of the model grid (temperature in regions 1 and 2, $\rm H_2$ number density in region 4 and CO column density in region 7; see Fig. 2.5 and Table 2.5). Those parameters are thus simply ill-constrained.

As shown in Figure 2.8, the best-fit CO column density and total volume density are not

correlated. If anything, excluding region 4, there is a marginal anti-correlation. Another weak anti-correlation may be present between $T_{\rm K}$ and $n(\rm H_2)$ (again excluding region 4), implying a weak correlation between $N(\rm CO)$ and $T_{\rm K}$. These trends, if they were confirmed, would suggest a slight decrease of the CO abundance when the temperature decreases and the volume density increases. Although speculative, this could be interpreted as the effects of depletion processes and freeze-out onto dust grains during cloud collapse. However, without confirmation from additional molecules such as $\rm N_2H^+$ and/or methanol, known to be good tracers of gas phases experiencing or having experienced freeze-out, and given the size of the error bars in Figure 2.8, this is rather speculative at this point.

As each region is located at a different distance from the galactic centre, radial variations of the three main derived physical parameters could in principle be probed in NGC 6946 (Fig. 2.8). However, given the large uncertainties on the most likely model results, no clear trend emerges.

Having said that, irrespective of the significance of the trends discussed above between different molecular gas physical parameters, as only particular star-forming regions in the spiral arms and inter-arms of NGC 6946 (where observations of multiple lines of CO are available) were probed, these trends can not be generalised to the entire disc of NGC 6946, even less to spirals in the nearby universe generally. Only a high-quality homogeneous survey of multiple molecular gas tracers across the entire disc of NGC 6946 could provide demonstratively unbiased results.

As hinted above, it is interesting to compare the probability distribution functions of the three main physical parameters (marginalised over the other two) with the simple χ^2 minimisation results, as done in Figure 2.6. $N(\rm CO)$ is generally the best constrained parameter, with single-peaked Gaussian PDFs and thus good agreement between the peak and median of the likelihood. Similarly, the best-fit model (in a χ^2 sense) is generally contained within the 68 per cent (1σ) confidence levels (it is in all but one region at the 2σ level). The situation is less satisfactory for $n(\rm H_2)$ and particularly for $T_{\rm K}$, due to their degeneracy (i.e. the

characteristic "banana"-shaped $\Delta\chi^2$ contours or inverse $n(H_2)$–T_K relationship; see Fig. 2.5 and Appendix C of van der Tak et al. 2007a). The PDFs for $n(H_2)$ and T_K typically have a small peak within a rather broad and flat likelihood distribution. Unsurprisingly, the best-fit model is thus again generally contained within the 68 per cent confidence levels (except in a few cases where the best-fit model is at the edge of the grid and thus unreliable). However, this also highlights the fact that, although generally well-defined, the best-fit model is often only slightly more likely (i.e. better fitting) than a host of other models spanning a wide range of physical parameters. We stress that this questions the wisdom of considering the best-fit model alone as a reasonable approximation of the true physical conditions, a practice adopted in many studies. The confidence intervals listed in Table 2.5 are a first step at concisely quantifying the uncertainties.

In Fig. 2.9, we show the modelled optical depth τ of the CO lines as a function of the upper J level of the transition J_{up}, this for the best-fit model of each region. All regions except region 7 (which also has the lowest best-fit CO number column density) have $\tau > 1$ for at least one transition, indicating that we only see the outermost layers of the clouds in those transitions. The optical depth distributions are qualitatively similar to the beam-averaged total intensity distributions, in the sense that both peak at roughly the same transitions. Indeed the optical depth is maximum at $J_{up} = 5$–7 in regions 1, 2 and 3, while it peaks at $J_{up} = 2$–4 in the other regions. A similar trend has also been observed for high density tracers by Goldsmith & Langer [1999b].

The beam-averaged total CO cooling rate of each region was also estimated from the best-fit model, summing all CO transition intensities up to $J_{up} = 10$. The results are listed in Table 2.5. As expected, regions 1, 2 and 3 have CO cooling rates ≈ 10 times higher than those of the other regions. They are the most powerful emitting regions, encompassing the highest number of H II regions and GMCs (regions 1 and 2) and the highest number of SNRs (region 3), all indicating young stellar populations (see Fig. 2.1). However, the other regions have lower CO cooling rates, which may indicate colder and denser ISM there.

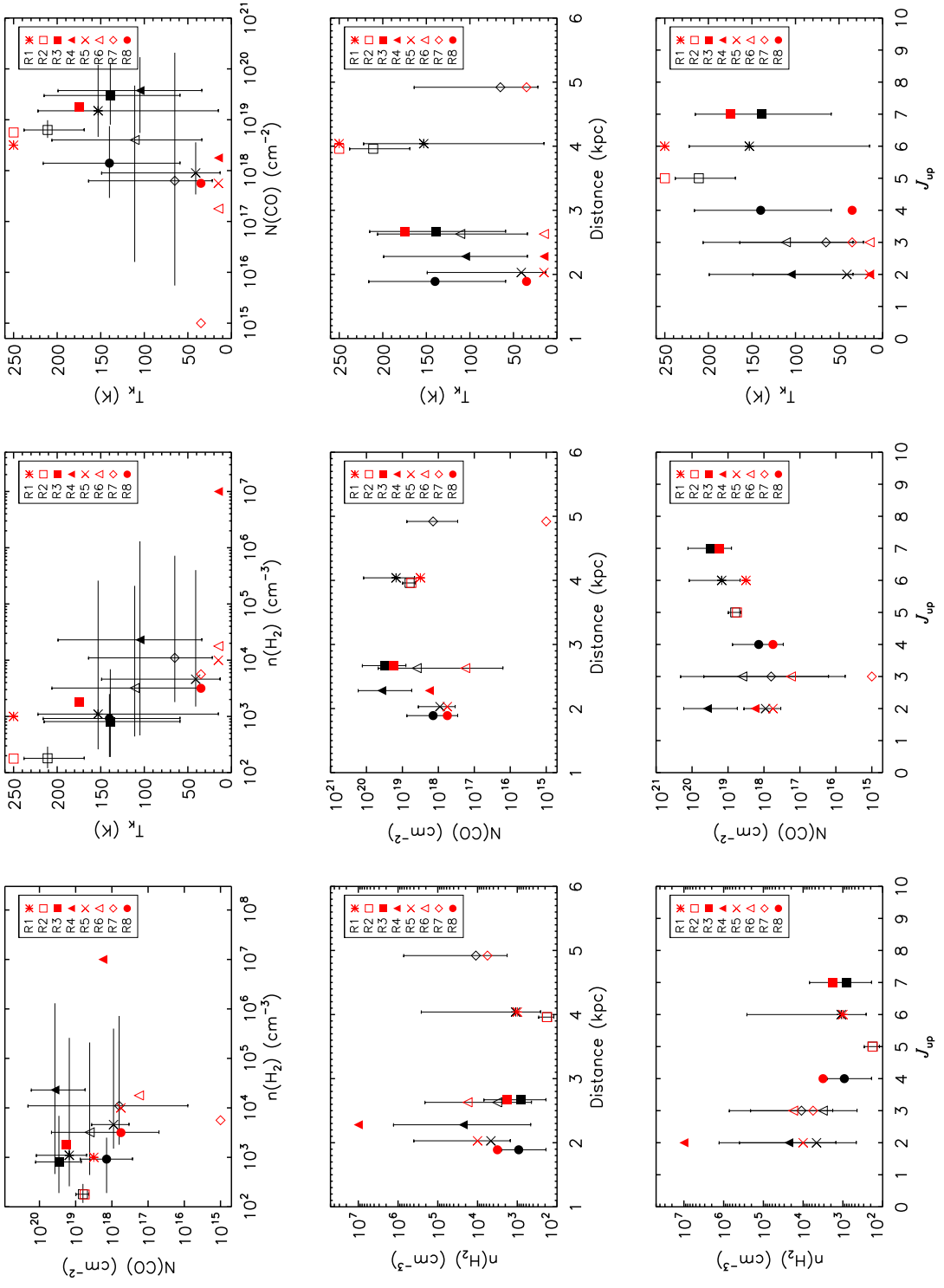

Figure 2.8: **Top**: Correlations between the best-fit parameters ($T_{\rm K}$, $n({\rm H_2})$ and $N({\rm CO})$) of the 8 regions studied. **Middle**: Same physical parameters as a function of galacto-centric radius. **Bottom**: Same physical parameters as a function of the predicted $J_{\rm max}$. Red symbols show the results from the χ^2 analysis. Black symbols with error bars represent the median of the marginalised probability distribution function of each model parameter, along with the 68 per cent (1σ) confidence levels (see Table 2.5).

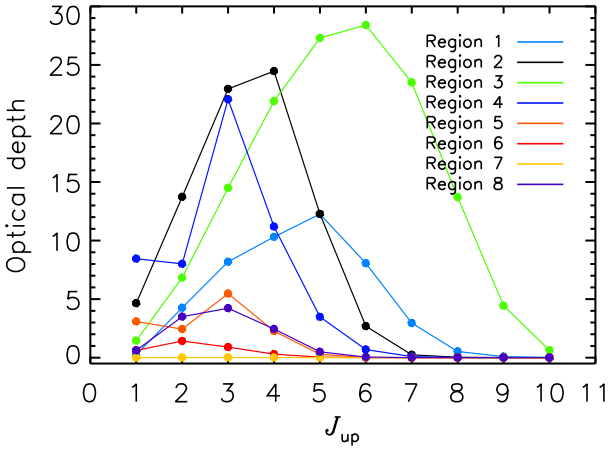

Figure 2.9: Optical depth distributions. For each region (colour-coded), the optical depth of the CO line for the best-fit model is shown as a function of the upper J level of the transition (up to J=10-9).

2.4.2.2 Spectral line energy distributions

We plot the CO spectral line energy distribution (SLED) of the best-fit model of each region in Figure 2.10, overlaid with the observed data points. Also shown are the SLED ranges allowed by the 1σ confidence level on the best-fit model, as well as the SLED of the most likely model. By construction, the models are in good agreement with the data. The modelled integrated line intensities generally decrease with increasing upper energy level $J_{\rm up}$, but the beam-averaged total intensities peak at intermediate transitions. The location of the SLED turnover ($J_{\rm max}$) is particularly interesting, as when well constrained it provides information on the SF activity level. It is listed in Table 2.5 for each region.

In the heavily star-forming galaxy APM 08279+5255 at redshift $z \approx 4$, $J_{\rm max} = 9$ [Weiss et al., 2007]. In the centre of local starbursting galaxies such as Henize 2-10, NGC 253 and M 82, $J_{\rm max} \approx 6$–7 [Bayet et al., 2004; Weiß et al., 2005a], while it is ≈ 3 in molecular streamers/outflows around M 82's central molecular disc [Weiß et al., 2005a]. $J_{\rm max} \approx 4$ in the centre of our own Galaxy, whereas it is ≈ 3 in the Galactic plane at longitudes $2.5^\circ < l < 32.5^\circ$, where CO emission is much weaker than in the central regions [Fixsen

et al., 1999]. On the other hand, the Orion Bar photodissociation region in the Milky Way disc shows extreme star formation activity, with $J_{\rm max} \approx 13$ [Habart et al., 2010]. All these results are consistent with an increasing $J_{\rm max}$ with increasing star formation activity.

Using the Spectral and Photometric Imaging Receiver (SPIRE) Fourier Transform Spectrometer (FTS) onboard *Herschel*, Rangwala et al. [2011], Kamenetzky et al. [2012] and Schirm et al. [2014] obtained CO SLEDs extending to much higher energy levels than possible from the ground, up to $J = 13 - 12$, for the starburst galaxies Arp 220, M 82 and the Antennae (NGC 4038/39), respectively. They also used RADEX for radiative transfer modeling and found that the CO SLEDs required a two-component molecular ISM (cold $T_{\rm K} < 100$ K, and warm $T_{\rm K} > 100$ K). They found that the CO SLEDs peak at $J = 6 - 5$ and then fall off at the higher J transitions. Since we do not have higher J transitions of CO (i.e. $J > 6 - 5$), we are not able to study or indeed assess the presence of cold and warm gas components separately (nor derive the CO SLED peak of each gas component; see Figure 2.10). We return to this point in the Discussion (Section 2.5).

As visible in Figure 2.10, an inflection point is present at $J_{\rm up} = 3$ in the SLED of region 4, where the CO (3–2) integrated line intensity is slightly smaller than that of both CO (2-1) and CO (4–3). Although we refer the reader to van der Tak et al. [2007a] for more details on the relation between opacity and line intensity, we note that the opacity in region 4 peaks at $J_{\rm up} = 3$ and is more than twice that for $J_{\rm up} = 2$ and 4 (see Fig. 2.9), causing the apparent reduction of the CO (3–2) integrated line intensity. Since the low-J trend is more consistent with the observed lines and the best-fit physical parameters (see Fig. 2.10), we adopt $J_{\rm max} = 2$ for region 4.

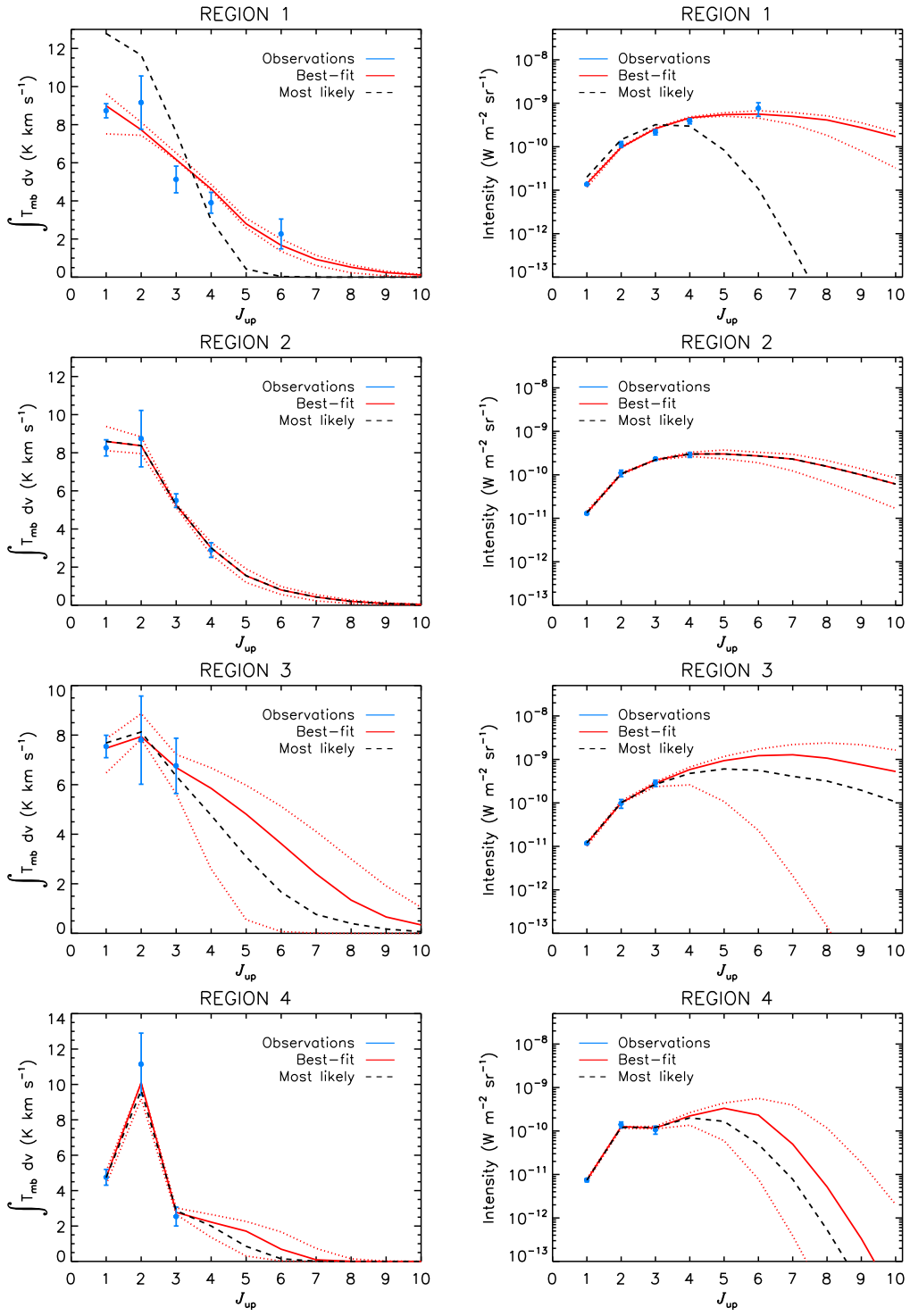

Figure 2.10: Spectral line energy distributions. For each region, the integrated line intensity S (left) and beam-averaged total intensity per unit area I (right) are shown as a function of the upper J level of the transition (up to J=10-9). The solid red line shows the best-fit model, while the dotted red lines delineate the range of possible SLEDs encompassed by the 1σ confidence level on the best-fit model (the darkest zone in the $\Delta\chi^2$ contour maps of Fig. 2.5). The dashed black line shows the SLED corresponding to the most likely model. Blue circles with error bars are our observations.

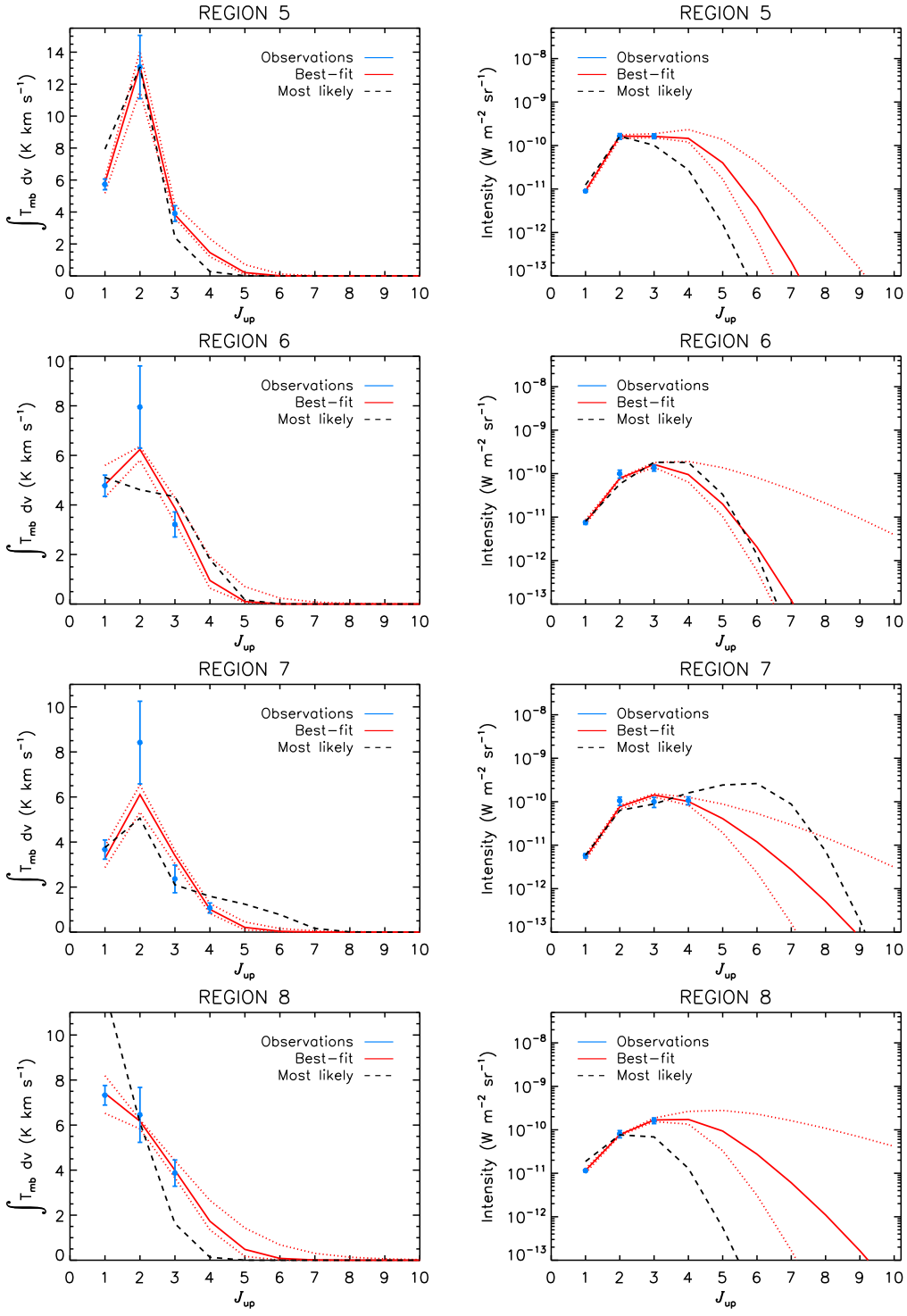

Figure 2.10: Continued.

2.5 Discussion

2.5.1 Star formation activity

A variety of heating mechanisms of the molecular ISM is present in galaxies, including far-ultraviolet (FUV) radiation (from massive stars and active galactic nuclei), dust-gas collisions, cosmic rays, mechanical heating (e.g. turbulence) and chemical heating [see, e.g., Röllig et al., 2007]. But which heating mechanisms dominate in the regions studied? More specifically, how does SF feedback regulate the physical conditions of the ISM? From both observational and theoretical arguments, there must be a connection between the gas physical conditions and the immediate environment of the regions, such as the presence SNRs, H II regions, and H I holes.

Overlaid on Hα and H I images, some of the features present in NGC 6946 were illustrated in Figure 2.1: H I holes [Boomsma et al., 2008], GMCs [Donovan Meyer et al., 2012; Rebolledo et al., 2012], H II regions [Bonnarel et al., 1986], giant H II complexes [van der Kruit et al., 1977], CO complexes [Rebolledo et al., 2012] and SNRs [Lacey & Duric, 2001; Matonick & Fesen, 1997]. All the regions studied here are associated with one or more of these features.

Of the 62 SNRs detected in NGC 6946 (both optically and in the radio), 40 are associated with spiral arms while 22 are located in inter-arm regions. Lacey & Duric [2001] argued that the arm SNRs (mostly radio-bright) have massive progenitors (Population I stars) and explode as Type II/Ib/Ic supernovae. Indeed, with short lifetimes, many of the progenitors will explode inside or close to their parent molecular cloud. Lacey & Duric [2001] in fact showed that the radio-bright SNRs are likely associated with H II and star-forming regions, an association borne out by Figure 2.1. On the other hand, the inter-arm SNRs (mostly optically-selected) are thought to have Population II progenitors [Lacey & Duric, 2001].

In the galaxy M33, most radio-emitting SNRs have a diameter ranging from 20 to 80 pc [Duric et al., 1995]. In the Galaxy, the bulk of the 47 SNRs with a distance determination in

the catalogue of Green [2012] have a diameter between 10 and 100 pc[1]. However, stellar winds and/or diffuse ionised gas can help create shells with diameters $\geq$ 100 pc [Matonick & Fesen, 1997]. As cosmic rays produced by SN explosions and shocks can travel large distances in low density environments (weak absorption), where they heat up their surroundings [Meijerink et al., 2011], we can expect that the average temperature will be higher in low density environments than in high density ones.

Of course, UV radiation from short-lived massive stars is generally believed to be the main stellar feedback mechanism affecting GMCs (e.g. Colín et al. 2013 and references therein). Indeed, simulations show that massive stars ($M_\star \geq$ 20 $M_\odot$) can locally disrupt their surrounding clouds via photoionisation, creating H II regions and potentially triggering SF at new locations in the clouds.

Spiral arms clearly lead to an increase in the number of cloud collisions [Dobbs, 2008]. Classical grand-design spiral structures are thought to form from perturbations due to bars or companions, while flocculent structures develop from local gravitational instabilities (see; e.g., Dobbs & Bonnell 2008). NGC 6946 is a flocculent galaxy, with characteristic broken spiral arms. For the formation of GMCs, and thus of stars, the local gravitational instabilities seen in flocculent galaxies are therefore likely to be more important than global spiral dynamics.

The CO SLED is a useful tool to investigate SF activity in the ISM. There are many studies in the literature probing the gas physical conditions based on low-J CO transitions only, i.e. up to $J = 3 - 2$ [e.g. Petitpas & Wilson, 2000; Walsh et al., 2002; Weiß et al., 2005b]. In this study, however, we present modeling results based on the highest number of CO transitions in NGC 6946 so far (up to $J = 6 - 5$; see Figure 2.10). This is a significant improvement. However, more recent studies such as van der Werf & Spaans [2009] have demonstrated the importance of higher J transitions (only available from space) to truly discriminate between SF-dominated regions and either X-ray-dominated regions (XDRs) or dense PDRs (see also Kamenetzky et al. 2012; Rangwala et al. 2011; Schirm et al. 2014).

[1] http://www.mrao.cam.ac.uk/projects/surveys/snrs/

A peak in the CO SLED at mid-J lines accompanied by a decrease at higher J lines could indicate a SF-dominated region, whereas a flat SLED beyond the peak suggests the presence of XDRs, (e.g. Mrk 231; van der Werf et al. 2010). If these trends identified for starbursting (and often interacting) galaxies hold true for galaxies with more quiescent SF, however, this suggests that we can not reliably assess what the dominant excitation mechanism in the molecular ISM of our eight regions is (i.e. XDR, PDR or SF). The improvement in coverage of the CO SLED we have achieved may simply not be enough. Although this is unfortunate, it also puts into question many results reported in the literature based on relatively few low-J CO transitions.

Given the large uncertainties in the most likely model results, the physical properties of the gas across the eight regions studied are arguably very similar, and often (but not always) indistinguishable within the uncertainties (see Table 2.5). As can be seen from Figure 2.6, the $T_{\rm K}$ and $n(\rm H_2)$ PDFs generally show a peak followed by a flat distribution, causing the high uncertainties in the most likely results (i.e. the 68 per cent or 1σ confidence levels around the median of the PDFs). In the literature, similarly flat $T_{\rm K}$ and $n(\rm H_2)$ PDFs are seen in some studies based on RADEX modeling [e.g., Kamenetzky et al., 2012; Rangwala et al., 2011].

Nevertheless, the eight selected regions can still be divided into three different groups based on the presence of young stellar population indicators and the location of each region within the galaxy disc (i.e. arm vs. inter-arm region). It is then possible to check whether some trends emerge from the rather noisy modeling results. While regions 1 and 2 have the highest numbers of H II regions and GMCs among the regions studied, region 3 has the highest number of SNRs, all indicating high SF activity (see Fig. 2.1). Interestingly, Rebolledo et al. [2012] concluded that while the clouds located in the eastern part of NGC 6946 have properties independent of their location in the disc, some arm clouds have a higher SFR. In particular, they found three such clouds located within our regions 1 and 2 (regions 6, 7 and 11 in their work; see also their Fig. 2). Regions 4, 5 and 6 are located in the more flocculent arms, and include fewer young stellar population indicators compared to regions 1,

2 and 3. Finally, regions 7 and 8 are located between the arms, while all other regions are located within the (flocculent) arms. Therefore three different groups of regions emerge, i.e. regions 1, 2 and 3, regions 4, 5 and 6, and regions 7 and 8. It is interesting to note that despite their limitations, the best-fit model results do reflect these groupings.

In the following sub-sections, we therefore discuss the physical properties of the ISM in view of the presence of young stellar population indicators, grouping regions with similar characteristics. Specifically, we consider regions 1, 2 and 3 (highest numbers of H II regions, GMCs and SNRs), regions 4, 5 and 6 (fewer young stellar population indicators), and regions 7 and 8 (inter-arm regions).

2.5.2 Regions 1, 2 and 3

As shown in Figure 2.1, regions 1 and 2 are associated with giant H II complexes, encompassing many H II regions that each indicate the presence of OB stars and thus FUV radiation. In particular, as mentioned before, region 1 has the highest number of H II regions of all the regions studied. The H I hole associated with region 2 may well have been created by supernova explosions, as three SNRs are located near the centre of the hole. Regions 1 and 2 are also associated with some of the main star-forming regions previously studied by Murphy et al. [2011, 2010] using 33 GHz free-free emission, a standard tracer of SF. Although not part of a catalogued giant H II complex, region 3 nevertheless lies in an important spiral arm and harbours many H II regions and SNRs (see Fig. 2.1).

The environment and features present in regions 1, 2 and 3 are thus similar, both indicating a high level of SF activity (slightly higher in region 1 than 2, and in region 2 than 3). The presence of young stellar population indicators indicate significant heating of the molecular ISM in all three regions, presumably from FUV radiation and stellar winds associated with OB stars (and potentially cosmic rays from supernovae).

2.5.3 Regions 4, 5 and 6

Regions 4 and 5 are very close to each other and overlap significantly (see Fig. 2.1). All three regions are located in rather similar environments (flocculent spiral arms; see Fig. 2.1). Regions 4 and 5 do encompass some H II regions (and region 4 has one catalogued SNR), but not as many as regions 1–3. Similarly, region 6 has a small number of H II regions, SNRs and GMCs at its edge, but none within our adopted beam (see Fig. 2.1). It is also largely co-spatial with a large H I hole ($\approx$ 900 pc diameter). It is thus likely that, while SF likely took place in the past and the potential for future SF is high, current SF activity is relatively mild in regions 4–6 (compared to regions 1–3).

2.5.4 Regions 7 and 8

Regions 7 and 8 are located in the inter-arm regions of NGC 6946, respectively to the NE and SW of the galaxy centre (see Fig. 2.1). Region 7 lies at the edge of a major spiral arm and has some H II regions and GMCs, while region 8 harbours one particularly large GMC (spatially) and a few H II regions (at the centre of the GMC; see Fig. 2.1). As there is no SNR in either region, it is possible that the SF activity in those regions is likely to be lower or is just beginning compared to the other regions studied. However, SF activity in regions 7 and 8 may well be higher by construction than naive expectations for the general inter-arm medium, as the regions studied here were necessarily chosen to contain some molecular clouds.

2.5.5 Spiral arms vs. galaxy centre

Many studies have probed the molecular gas physical conditions at the centre of NGC 6946, where there is a small bar [Ball et al., 1985; Bonnarel et al., 1988; Ishizuki et al., 1990; Regan & Vogel, 1995; Weliachew et al., 1988] and starburst activity [Engelbracht et al., 1996]. Israel & Baas [2001] concluded that there are at least two molecular components in the central region, a warm ($T_{\rm K}$ = 30–60 K) and dense ($n(H_2)$= 3–10 $\times 10^3$ cm^{-3}) component and a more

tenuous ($n(H_2) \leq 10^3$ cm^{-3}) and hotter (T_K = 100–150 K) component. Walsh et al. [2002] and Bayet et al. [2006] also probed the gas physical properties at the centre using LVG modeling. Walsh et al. [2002] found T_K = 40 K for the gas kinetic temperature at the centre, while Bayet et al. [2006] found T_K = 130 K. The higher temperature found by Bayet et al. [2006] may be caused by the high-J transition of CO used [CO (6–5)], requiring a higher temperature to be excited. The densities derived are however very similar ($n(H_2) = 10^{3.2}$–$10^{3.3}$ cm^{-3}).

Given the large uncertainties on the most likely model parameters of our regions, a comparison to past studies of the galaxy centre is unfortunately of little use. Our regions have temperatures and densities that encompass those quoted above for the galaxy centre.

2.5.6 Modeling methods

Overall, our study provides a more complete CO ladder for NGC 6946 (up to $J = 6-5$) than previous studies. However, as recent studies with much more extensive CO SLEDs (e.g. up to $J = 13-12$) and higher S/N have shown, this is often not enough to properly constrain the full shape of a SLED and thus reliably identify its peak (J_{max}). Only limited information on the relative intensity of SF across our eight selected regions could thus be gleaned from the SLED-predicted J_{max}.

More importantly, many previous studies of the physical conditions of the molecular gas exploiting emission line ratios (as done here) have relied exclusively on best-fit models identified in a χ^2 manner (see Section 2.3.2). However, we have shown here that model uncertainties derived considering the most likely models (and thus marginalised PDFs; see Section 2.3.3) are much larger than usually assumed. As a result, the discriminating power of the models (here RADEX) in terms of the physical properties of the gas (T_K, $n(H_2)$, N(CO)) is in practice very limited. Here, the physical properties of the eight regions of NGC 6946 studied are largely consistent with each other, and any trend identified is therefore at best weak.

While this result is disappointing, it is nevertheless important. First, it questions the

robustness of past results based on χ^2 analyses only (often quoting only the best-fit model without any uncertainty). Second, it raises the bar for future studies, that should properly quantify their uncertainties before making any claim.

2.6 Conclusions

In this chapter, we have described the most complete CO survey of the nearby spiral galaxy NGC 6946 ever performed, including for each of 8 regions studied at least 4 transitions of CO. The data presented in Figure A.1 and Table B.1 further cover a much broader area, and should be useful for diverse projects investigating the SF activity of NGC 6946. The main results of this work can be summarised as follows.

1. The CO (2–1) map indicates that molecular gas is ubiquitous across NGC 6946 but is concentrated along the spiral arms, with a regular velocity field. The CO (3–2) data reveal two compact "hotspots" (very active star-forming regions) in the eastern spiral arms (regions 1 and 2), where the gas is also bright at Hα, 24 μm, 850 μm and 6.2 cm.

2. The radial profiles of the different CO transitions probed (eastward from the centre up to $\approx$ 4 kpc) reveal the likely presence of two components: a centrally concentrated molecular core and a nearly flat lower surface brightness extended disc.

3. While the beam-corrected line ratio R_{21} varies significantly across NGC 6946 (from $\approx$ 1 to 2.5), the other ratios are more constant: $R_{31} \approx 0.7$, $R_{41} \approx 0.4$ and $R_{22} \approx 0.1$.

4. Although the eight regions studied can naturally be divided into three broad groups based on the presence of recent star formation indicators at other wavelengths (presence of SNRs, H I holes, H II regions/complexes and GMCs), the most likely RADEX model results do not indicate any significant differences between the regions, i.e. most physical parameters ($T_{\rm K}$, $n(\rm H_2)$, $N(\rm CO)$) are consistent within the uncertainties. This is in

contrast to results relying on the best-fit model results only.

5. This last result raises doubts on the robustness of past results relying on χ^2 analyses and fewer CO transitions, and suggests that future studies should quantify their uncertainties more carefully.

2.A Integrated spectra of the 8 regions studied

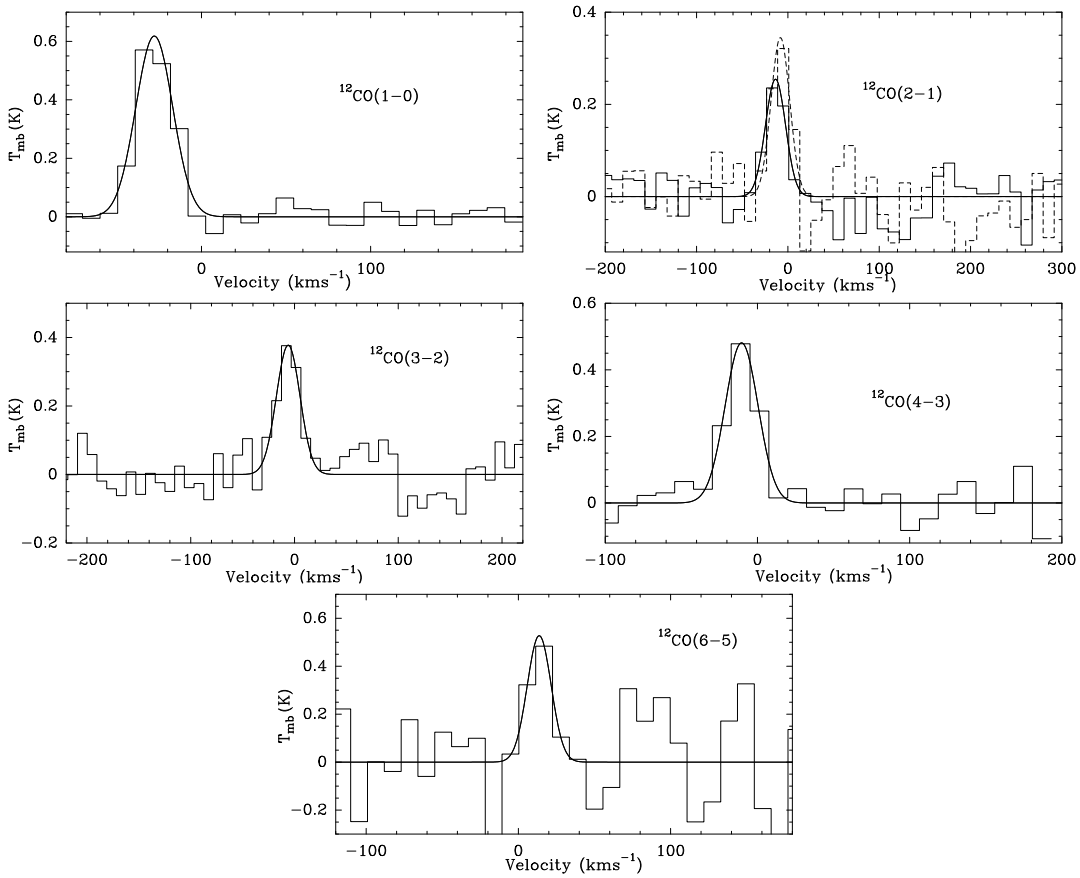

Figure A.1: Integrated spectra used in the line ratio analysis for region 1. Gaussian fits are overlaid. The ^{12} CO (2–1) line integrated intensity and line width in each region was obtained by interpolating those of the two closest detections of the large-scale mapping. These are shown as dashed and solid lines in the ^{12}CO (2–1) panel.

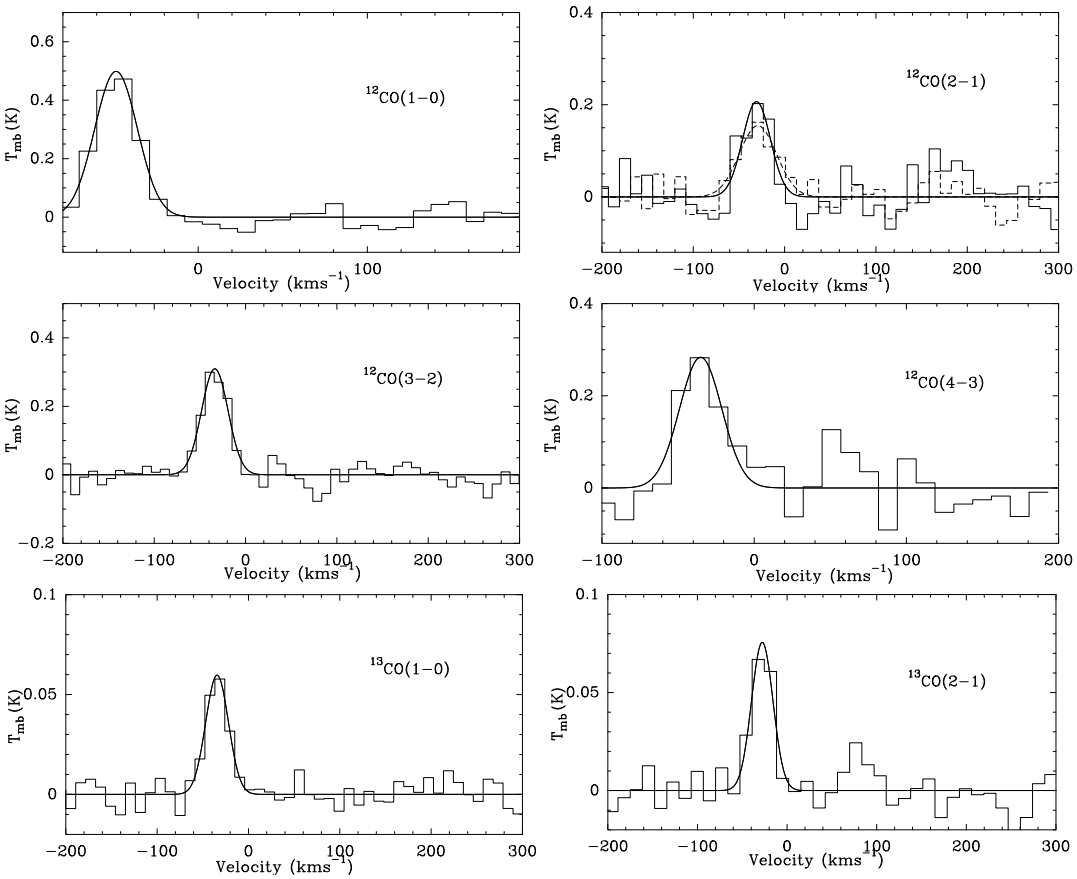

Figure A.1: (Continued.) Region 2

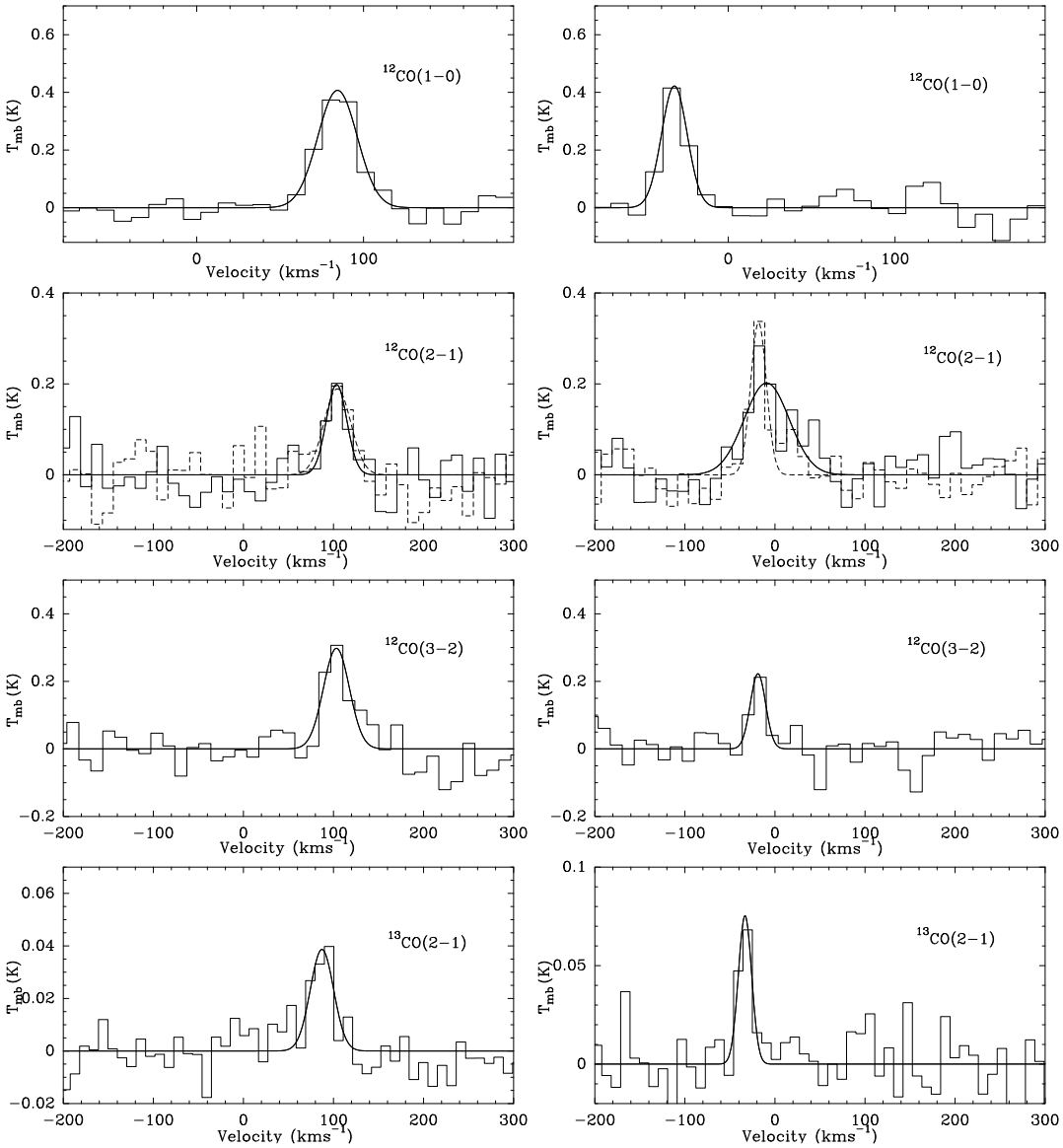

Figure A.1: (Continued.) Regions 3 (left) and 4 (right).

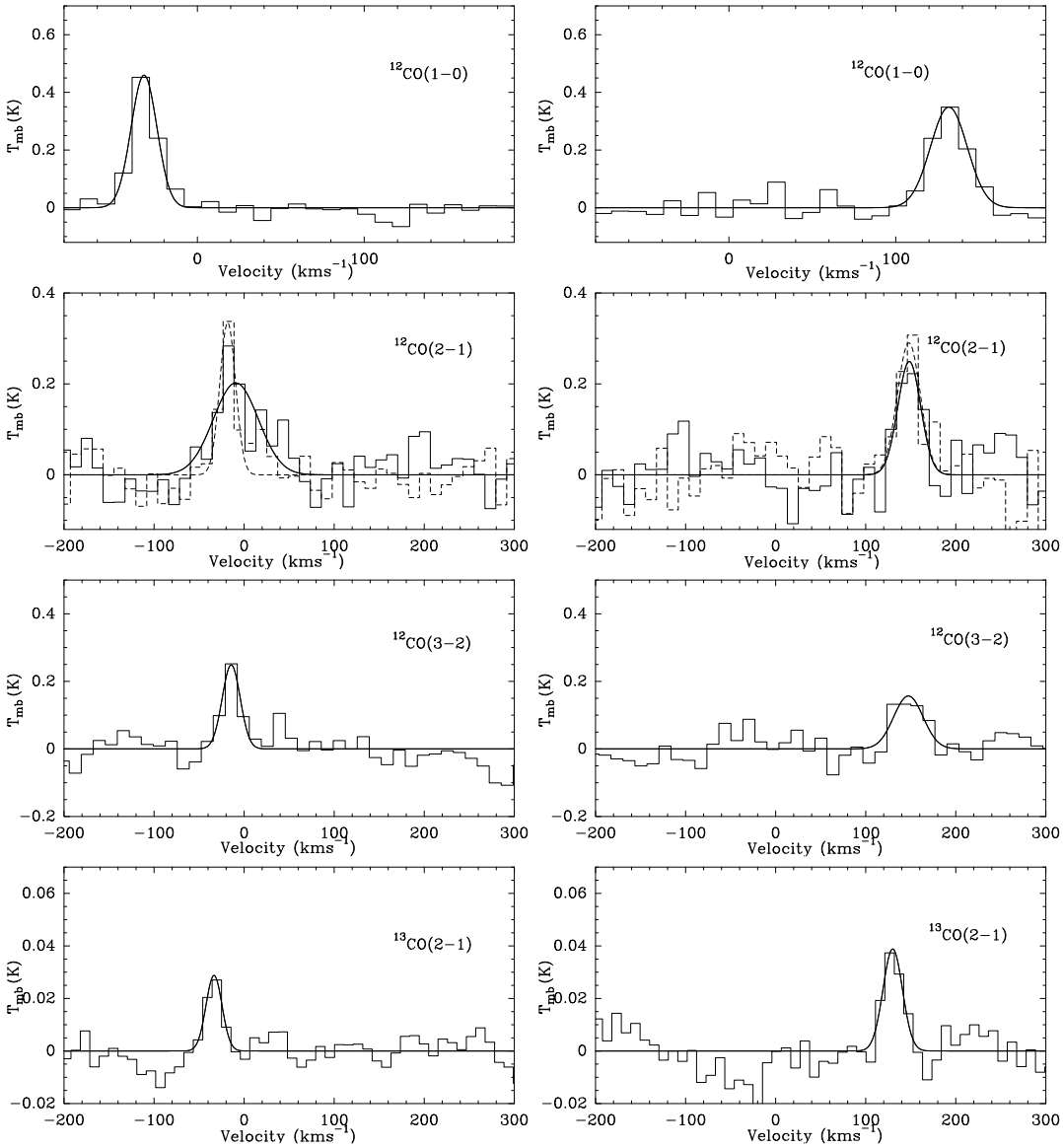

Figure A.1: (Continued.) Regions 5 (left) and 6 (right).

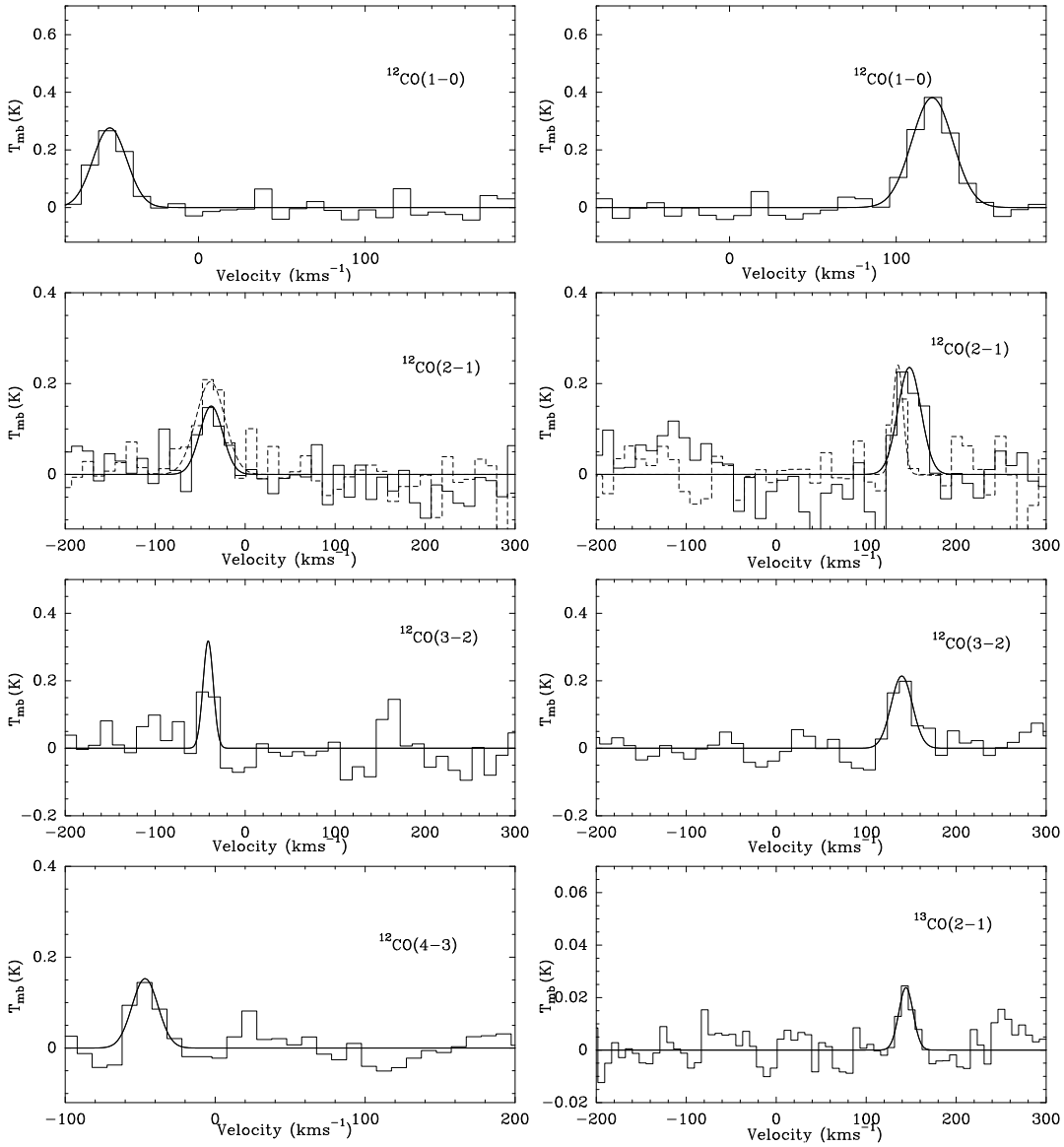

Figure A.1: (Continued.) Regions 7 (left) and 8 (right).

2.B CSO detections

Table B.1: CSO detections.

Transition	Offset (arcsec)	$\int T_{\rm mb}\,{\rm d}v$ (K km s^{-1})	FWHM (km s^{-1})	Transition	Offset (arcsec)	$\int T_{\rm mb}\,{\rm d}v$ (K km s^{-1})	FWHM (km s^{-1})
CI (^{3}P$_1$-^{3}P$_0$)	(0, 0)	29.9 ± 2.8	148.5 ± 15.2	CO (2–1)	(-90, -30)	7.9 ± 1.5	29.8 ± 5.4
	(20, 0)	25.1 ± 2.9	87.3 ± 11.9		(-90, -60)	7.9 ± 1.8	25.4 ± 8.6
	(40, 0)	5.6 ± 2.3	37.9 ± 27.3		(-120, 0)	2.5 ± 0.9	14.4 ± 5.3
	(80, 0)	18.9 ± 2.5	155.8 ± 22.6		(-120, 120)	6.5 ± 1.3	25.1 ± 6.4
	(100, 0)	4.1 ± 1.3	93.3 ± 38.2		(-120, -30)	8.6 ± 1.4	30.3 ± 5.3
	(110, 100)	4.4 ± 0.9	29.9 ± 5.7		(-120, -60)	10.8 ± 2.6	46.6 ± 17.0
	(120, 0)	4.0 ± 1.3	41.7 ± 18.7		(-150, 30)	3.2 ± 0.8	12.1 ± 5.5
	(150, -20)	3.8 ± 0.9	20.2 ± 4.7		(-150, 60)	3.9 ± 1.5	18.6 ± 14.1
CO (2–1)	(0, 0)	102.7 ± 3.0	155.5 ± 4.8		(-150, 90)	6.0 ± 1.6	41.6 ± 12.7
	(0, 30)	43.7 ± 2.4	106.6 ± 6.3		(-150, 120)	11.1 ± 2.6	73.8 ± 26.2
	(0, 60)	20.3 ± 2.7	88.9 ± 14.3		(-150, -30)	5.7 ± 1.5	30.6 ± 8.5
	(0, 90)	6.6 ± 1.9	49.5 ± 17.2		(-150, -60)	8.9 ± 2.0	57.8 ± 17.8
	(0, 120)	5.5 ± 0.9	35.2 ± 7.4		(-180, -30)	4.4 ± 1.2	25.9 ± 8.1
	(0, -30)	18.4 ± 2.5	87.2 ± 12.8		(-210, 0)	3.0 ± 1.1	18.4 ± 11.1
	(0, -90)	7.0 ± 1.5	31.8 ± 9.1		(-210, 90)	6.5 ± 2.6	43.6 ± 27.7
	(0,-120)	9.4 ± 2.4	44.9 ± 15.7		(-210, 120)	16.2 ± 2.7	114.1 ± 18.8
	(30, 0)	31.7 ± 3.6	98.6 ± 17.7		(-210, 180)	13.1 ± 2.3	94.8 ± 17.5
	(30, 30)	31.4 ± 2.4	96.6 ± 9.2		(-210, -60)	8.4 ± 2.2	64.6 ± 19.3
	(30, 90)	10.9 ± 1.7	48.3 ± 11.3		(-240, 60)	3.6 ± 1.1	23.6 ± 8.2
	(30, 120)	4.6 ± 1.3	30.5 ± 10.3		(-240, 180)	11.8 ± 2.5	93.9 ± 20.4
	(30, -30)	13.2 ± 2.7	81.3 ± 18.2		(-240, 240)	34.6 ± 4.2	217.5 ± 28.2
	(30, -60)	7.9 ± 1.4	39.1 ± 7.3	CO (3–2)	(0, 0)	111.6 ± 2.5	151.0 ± 3.7
	(30, -90)	4.3 ± 1.2	29.5 ± 9.1		(0, 10)	100.8 ± 2.2	155.9 ± 3.6
	(60, 30)	15.0 ± 2.2	67.6 ± 11.9		(0, 20)	66.7 ± 5.2	138.0 ± 12.3
	(60, 60)	9.5 ± 1.7	47.7 ± 11.1		(0, -10)	89.1 ± 3.0	133.1 ± 5.3
	(60, 90)	7.9 ± 1.2	25.5 ± 4.4		(10, 0)	131.2 ± 4.2	155.0 ± 5.3
	(60, 120)	4.5 ± 1.2	24.9 ± 7.3		(10, 10)	54.9 ± 7.9	107.3 ± 26.6
	(60, -60)	3.7 ± 1.0	20.7 ± 6.5		(10, -10)	79.5 ± 5.8	169.9 ± 13.6
	(90, 0)	11.4 ± 2.5	61.4 ± 22.5		(20, 0)	29.8 ± 2.6	75.1 ± 9.7
	(90, 30)	9.2 ± 1.5	25.3 ± 6.5		(20, -20)	7.3 ± 1.9	20.1 ± 5.1
	(90, 60)	5.6 ± 1.2	22.2 ± 6.3		(40, 0)	13.0 ± 1.2	57.2 ± 9.2
	(90, 90)	12.4 ± 1.6	46.4 ± 7.8		(60, 0)	3.9 ± 1.1	20.8 ± 6.6
	(90, 120)	8.4 ± 1.3	36.8 ± 5.6		(80, 0)	3.9 ± 0.9	11.4 ± 3.7
	(90, 150)	5.1 ± 1.5	31.9 ± 11.1		(90, 100)	9.2 ± 1.7	35.9 ± 8.5
	(120, 0)	4.7 ± 1.3	24.0 ± 6.9		(100, 0)	2.0 ± 0.6	14.3 ± 3.7
	(120, 30)	7.8 ± 1.4	25.4 ± 4.9		(100, 90)	7.0 ± 1.4	25.0 ± 5.2
	(120, 60)	6.5 ± 1.1	22.4 ± 3.9		(100, 110)	6.7 ± 1.3	14.7 ± 3.6
	(120, 90)	9.1 ± 1.6	52.4 ± 10.7		(110, 100)	11.2 ± 0.7	34.1 ± 2.4
	(120,-120)	6.6 ± 2.2	42.5 ± 21.8		(110, 110)	3.4 ± 0.9	16.5 ± 4.5
	(150, 0)	8.7 ± 1.2	29.8 ± 5.1		(120, 90)	2.8 ± 0.9	8.4 ± 3.4
	(150, 60)	9.3 ± 2.1	43.4 ± 15.0		(140, -20)	8.8 ± 0.8	25.2 ± 2.3
	(150, 90)	8.4 ± 1.8	43.0 ± 12.9		(150, 0)	6.1 ± 0.6	27.9 ± 3.1
	(150, -30)	9.7 ± 1.6	25.2 ± 4.1		(150, -10)	6.6 ± 0.6	22.1 ± 2.4
	(150, -60)	3.4 ± 1.1	23.4 ± 7.9		(150, -20)	10.8 ± 1.5	26.8 ± 4.3
	(180, 0)	7.7 ± 1.5	38.8 ± 9.2		(150, -30)	6.2 ± 0.7	21.1 ± 2.5

Notes: Offsets are measured with respect to the galaxy centre.

Table B.1: Continued.

Transition	Offset (arcsec)	$\int T_{\rm mb}\,{\rm d}v$ (K km s^{-1})	FWHM (km s^{-1})	Transition	Offset (arcsec)	$\int T_{\rm mb}\,{\rm d}v$ (K km s^{-1})	FWHM (km s^{-1})
CO (2–1)	(180, 30)	5.6 ± 1.5	28.8 ± 9.3	CO (3–2)	(150, -40)	3.7 ± 0.6	14.4 ± 2.4
	(180, 60)	7.7 ± 2.4	44.7 ± 17.6		(160, -20)	9.2 ± 1.6	23.5 ± 4.7
	(180, -30)	7.3 ± 1.9	32.5 ± 8.9		(-10, 0)	70.3 ± 2.9	129.8 ± 6.2
	(210, 30)	5.9 ± 1.4	34.9 ± 9.8		(-10, 10)	37.9 ± 2.9	125.9 ± 11.0
	(240, -30)	9.4 ± 2.3	76.8 ± 22.9		(-10, -10)	36.9 ± 3.7	116.0 ± 15.9
	(-30, 0)	13.1 ± 2.7	97.7 ± 26.2		(-20, 0)	8.9 ± 2.7	14.2 ± 6.0
	(-30, 30)	25.1 ± 2.9	170.1 ± 21.6		(-20, 20)	3.0 ± 1.7	14.5 ± 6.2
	(-30, 90)	12.1 ± 1.9	86.2 ± 14.1		(-40, 0)	5.0 ± 0.4	36.1 ± 3.5
	(-30, -60)	11.7 ± 2.2	54.1 ± 13.3	CO (4–3)	(0, 0)	187.1 ± 5.5	144.9 ± 4.6
	(-30, -90)	8.6 ± 1.4	31.6 ± 5.9		(0, 10)	40.0 ± 7.9	105.2 ± 21.7
	(-30,-120)	9.1 ± 2.1	68.3 ± 21.2		(10, 0)	167.4 ± 9.9	137.4 ± 8.8
	(-60, 0)	11.4 ± 1.8	39.5 ± 8.6		(20, 0)	41.9 ± 3.6	141.3 ± 13.0
	(-60, 60)	10.2 ± 1.7	46.9 ± 9.5		(110, 100)	9.4 ± 1.3	27.1 ± 3.9
	(-60, -30)	9.5 ± 1.4	33.2 ± 4.7		(150, -20)	13.4 ± 1.9	27.5 ± 5.1
	(-60, -60)	7.3 ± 1.6	30.2 ± 9.9		(-110, -30)	6.5 ± 1.1	19.0 ± 4.6
	(-60,-150)	7.1 ± 1.9	56.4 ± 19.0	CO (6–5)	(0, 0)	70.1 ± 10.4	101.1 ± 18.5
	(-90, 60)	5.6 ± 1.5	31.3 ± 9.2		(5, 0)	90.7 ± 9.8	129.5 ± 13.9
	(-90, 90)	4.3 ± 1.3	30.0 ± 8.1		(10, 0)	152.4 ± 23.7	191.3 ± 30.8
	(-90, 120)	19.2 ± 3.8	136.0 ± 37.0		(150, -20)	13.9 ± 4.8	20.2 ± 8.3
	(-90, 0)	3.3 ± 1.0	12.1 ± 3.3				

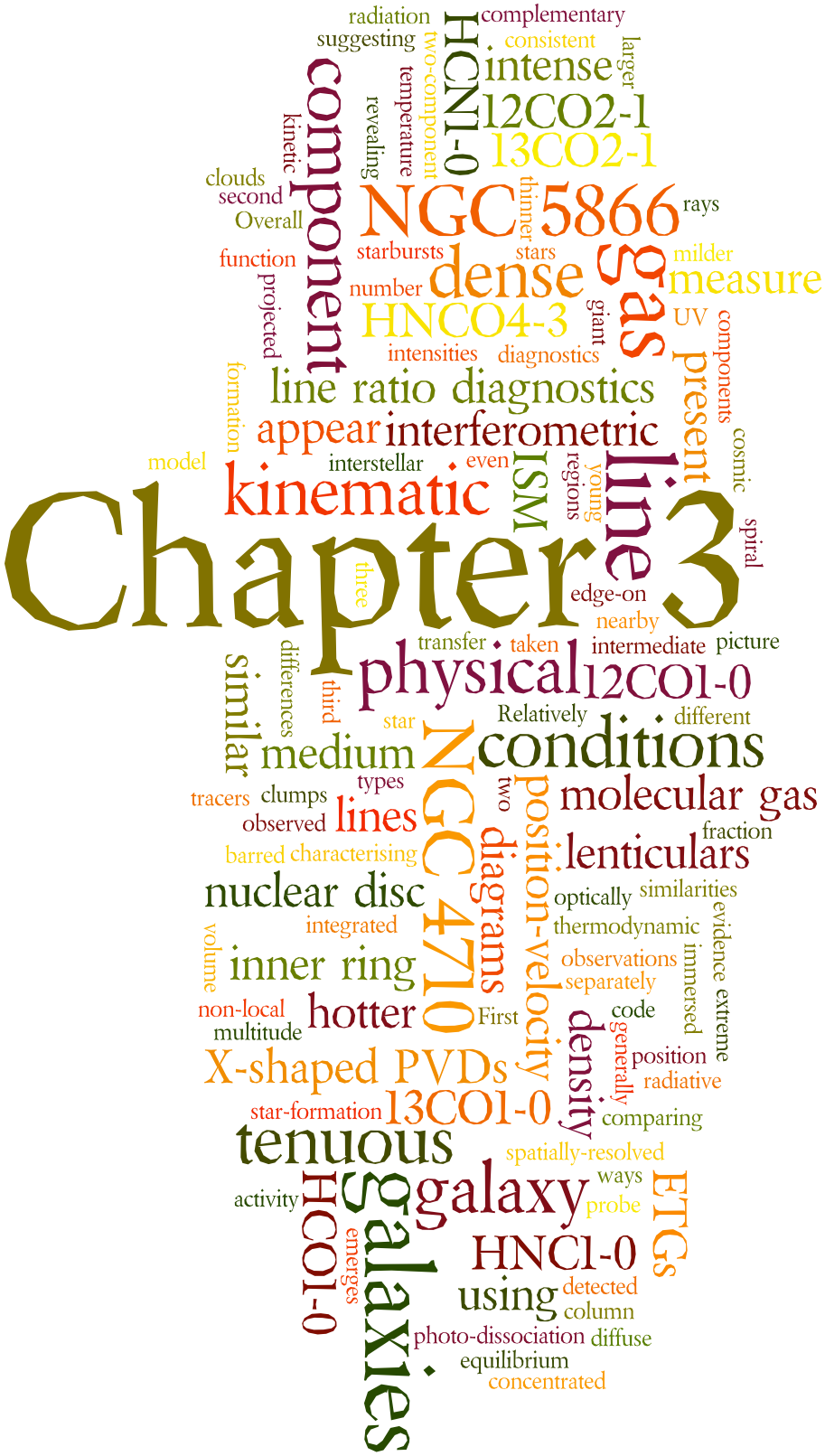
Chapter3
kinematic
line
physical
conditions
component
gas
NGC5866
dense
intense
HCN1-0
12CO2-1
13CO2-1
HNCO4-3
line ratio diagnostics
appear
interferometric
present
measure
molecular gas
lenticulars
medium
similar
lines
NGC4710
diagrams
position-velocity
nuclear disc
inner ring
hotter
X-shaped PVDs
tenuous
galaxy
galaxies
ETGs
HNC1-0
using
HCO1-0
12CO1-0
13CO1-0
density
ISM
radiation
suggesting
complementary
consistent
larger
two-component
temperature
revealing
kinetic
clouds
second
Overall
thinner
rays
starbursts
stars
milder
function
number
projected
giant
UV
components
intensities
diagnostics
formation
model
interstellar
even
young
regions
cosmic
spiral
three
edge-on
nearby
transfer
taken
intermediate
picture
differences
third
star
Relatively
different
tracers
clumps
types
two
observed
fraction
barred
characterising
optically
similarities
integrated
thermodynamic
evidence
extreme
volume
observations
immersed
separately
non-local
multitude
First
code
generally
position
radiative
star-formation
comparing
spatially-resolved
activity
ways
probe
emerges
detected
column
photo-dissociation
diffuse
equilibrium
concentrated

3

Molecular Line Ratio Diagnostics in NGC 4710 and NGC 5866

"Some piously record 'In the beginning God', but I say 'In the beginning hydrogen'."

Harlow Shapley

The material in this chapter has been submitted to MNRAS as "Molecular Gas Kinematics and Line Diagnostics in Early-type Galaxies: NGC 4710 & NGC 586", Selçuk Topal, Martin Bureau, Timothy A. Davis, Melanie Krips, Lisa M. Young, Alison F. Crocker

3.1 Introduction

Molecular clouds are the stellar nurseries of galaxies, and probing their physical properties in different galaxy types has the potential to answer many important open questions regarding star formation processes and galaxy evolution. Actively star-forming spiral galaxies, including our own Milky Way, are rich in cold gas and their molecular gas reservoirs have been studied for many years. However, since so-called 'red and dead' early-type galaxies (ETGs; lenticulars and ellipticals) are generally thought to be very poor in molecular gas, star formation within them is thought to have largely stopped. Nevertheless, roughly 10 years after the first detection of molecular gas in external spiral galaxies [Rickard et al., 1975; Solomon & de Zafra, 1975], different phases of the interstellar medium (ISM) of ETGs were also studied, through observations of X-rays [e.g. Forman et al., 1985], optical emission lines [e.g. Caldwell, 1984], H I [e.g. Knapp et al., 1985] and CO lines [e.g. Sage et al., 2007; Welch & Sage, 2003; Wiklind & Rydbeck, 1986].

Young et al. [2011] carried out the most extensive survey of molecular gas [^{12}CO (1–0)] in ETGs so far, in the 260 galaxies of the volume-limited ATLAS^{3D} sample[1] [Cappellari et al., 2011]. They obtained a 22% detection rate, with H_2 masses ranging from 10^7 to 10^9 $M_\odot$. The CO-rich ETGs in the ATLAS^{3D} sample were further studied to probe the molecular gas properties in more details. Interferometric observations of ^{12}CO (1–0) in 40 objects were presented in Alatalo et al. [2013], revealing a variety of CO morphologies (discs, rings, bars, and spiral arms), with sizes smaller than in spirals in absolute terms but similar when compared to their optical extent [Davis et al., 2013a]. The molecular gas kinematics is generally regular [Davis et al., 2013a], allowing one to easily probe the Tully-Fisher (luminosity-rotational velocity; Tully & Fisher 1977b) relation of ETGs [Davis et al., 2011b]. However, gas-star kinematic misalignments indicate that the molecular gas has an external origin in at least

[1] http://www-astro.physics.ox.ac.uk/atlas3d/

one third of the systems, with significant field–cluster environmental differences [Davis et al., 2011a].

The molecular gas can also be used to study the physical conditions (temperature, density, column density, opacity, excitation mechanism, etc) within the dense cold gas of ETGs, where star formation takes place. For example, different transitions of a given molecule are good proxies for the gas temperature (e.g. ^{12}CO (2–1)/ ^{12}CO (1–0)), isotopologues probe the gas optical depth and column density (e.g. ^{13}CO/ ^{12}CO), and complex molecules (e.g. HCN, HCO$^+$, HNC, and HNCO) require much larger critical densities (up to $n_{\rm crit} \approx 10^6$ cm^{-3}) to be excited compared to simpler ones (typically $n_{\rm crit} \approx 10^3$ cm^{-3}). More subtle effects also exist. HCN and its isotopomer HNC trace respectively the warm-dense and cool-slightly less dense parts of a cloud, while HCO$^+$ traces even more tenuous regions [Huettemeister et al., 1995]. HCO$^+$ can also be enhanced in shocks associated with young supernova remnants (SNRs), due to cosmic rays (CRs) in the shocked material [Dickinson et al., 1980; Elitzur, 1983; Wootten, 1981], and is therefore also an important tracer of CR-dominated regions of the ISM. HNCO, on the other hand, is a good tracer of shocked gas [Meier & Turner, 2005, 2012; Ott et al., 2014; Rodríguez-Fernández et al., 2010], and it correlates well with SiO, a well-known shock tracer [Zinchenko et al., 2000].

Focusing on the physical conditions of the ISM through single-dish observations of several ^{12}CO transitions, the ^{13}CO isotopologue, and other molecules, Krips et al. [2010] and later Crocker et al. [2012] (see also Davis et al. 2013c) found that the molecular line ratios of ETGs are generally similar to those of spirals and Seyferts, but different from those of starbursts and (ultra-) luminous infrared galaxies ((U)LIRGs). Interestingly, the line ratios are statistically correlated with several other ISM and stellar properties, e.g. the molecular-to-atomic gas ratio, dust temperature, dust morphology, K-band absolute magnitudes and stellar population age [Crocker et al., 2012]. The ^{13}CO (1–0)/ ^{12}CO (1–0) ratio of ETGs also seems to depend on environment [Alatalo et al., 2015].

Here, we conduct interferometric (i.e. spatially-resolved) observations of two CO-bright

Table 3.1: General properties of NGC 4710 and NGC 5866.

Galaxy	Property	Value	Reference
NGC 4710	Type	$S0_3(9)$	a
	RA (J2000)	$12^h49^m38.8^s$	b
	Dec (J2000)	$15^d09^m56^s$	b
	Distance (Mpc)	16.8	c
	$\log(M_{H_2}/M_\odot)$	8.72 ± 0.01	d
	$SFR_{22\mu m}$ ($M_\odot$ yr^{-1})	0.11 ± 0.02	e
	V_{sys} (km s^{-1})	1102	f
	Major diameter	$4.9'$	c
	Minor diameter	$1.2'$	c
	Inclination	86°	h
NGC 5866	Type	$S0_3(8)$	a
	RA (J2000)	$15^h06^m29.5^s$	b
	Dec (J2000)	$55^d45^m48^s$	b
	Distance (Mpc)	15.3	c
	$\log(M_{H_2}/M_\odot)$	8.47 ± 0.01	f
	$SFR_{22\mu m}$ ($M_\odot$ yr^{-1})	0.21 ± 0.04	e
	V_{sys} (km s^{-1})	755	f
	Major diameter	$4.7'$	c
	Minor diameter	$1.9'$	c
	Inclination	89°	h

References: [a] Sandage & Bedke [1994]; [b]Nasa/Ipac Extragalactic Database (NED); [c] Tully [1988b]; [d] Young et al. [2011]; [e] Davis et al. [2014]; [f] Cappellari et al. [2011]; [g] Welch & Sage [2003]; [h] Davis et al. [2011b].

edge-on ETGs (lenticulars), NGC 4710 and NGC 5866. NGC 4710 is located in the outskirts of the Virgo Cluster [Kraan-Korteweg, 1982] at a distance of 16.8 Mpc [Tully, 1988b], while NGC 5866 is in a small group including two spirals at a distance of 15.3 Mpc [Tully, 1988b]. The general properties of the galaxies are listed in Table 3.1. We map the entire discs of NGC 4710 and NGC 5866 in HCN (1–0), HCO^+ (1–0), HNC (1–0) and HNCO (4–3) (the latter two lines being detected for the first time in those galaxies), thus probing relatively dense gas, as well as some other more common low-J CO lines such as ^{12}CO (1–0), ^{12}CO (2–1), ^{13}CO (1–0) and ^{13}CO (2–1), thus probing more tenuous gas.

The most abundant tracers reveal an X-shaped position-velocity diagram (PVD) in both

galaxies, indicating the presence of an edge-on barred disc [see Athanassoula & Bureau, 1999; Bureau & Athanassoula, 1999; Bureau & Freeman, 1999], with gas concentrated in a nuclear disc within the inner Lindblad resonance and in an inner ring around the end of the bar (corotation) and possibly farther out. Variations of the molecular line ratios along the galaxy discs (as a function of projected radius and velocity) allow us to study the physical properties of the molecular gas in each of those two dynamical components independently. We do this by modeling the molecular line ratios with a non-local thermodynamic equilibrium (non-LTE) code (RADEX; van der Tak et al. 2007b). The observed line ratios are also compared with those at the centre of spirals, starbursts, Seyferts and lenticulars, as well as with some giant molecular clouds (GMCs) in the spiral arms and inter-arm regions of nearby galaxies [Baan et al., 2008; Brouillet et al., 2005; Crocker et al., 2012; Krips et al., 2010; Sorai et al., 2002].

This chapter is divided as follows. Section 3.2 describes the observations and data reduction, while Section 3.3 presents the results and a basic analysis of the data. We discuss the line ratio diagnostics in Section 3.4, both empirically and through modelling. A detailed discussion is presented in Section 3.5 and we conclude briefly in Section 3.6.

3.2 Observations & Data Reduction

3.2.1 Observations

3.2.1.1 NGC 4710

NGC 4710 was primarily observed using the Combined Array for Research in Milimeter-wave Astronomy (CARMA), which includes 15 antennae (6×10.4 m, 9×6.1 m) and thus 105 baselines. The ^{12}CO (1–0) and ^{13}CO (1–0) observations were carried out in April 2009, with 3 spectral windows per line (186 MHz or ≈ 450 km s^{-1} bandwidth, with 1 MHz or ≈ 2.5 km s^{-1} channels), in the D configuration (maximum baseline of 150 m, yielding a synthesized beam and thus angular resolution of $\approx 3.8''$ at 115 GHz). The CO (2–1) obser-

vations were carried out in January 2011, with 3 spectral windows per line (1500 MHz or ≈ 2100 km s^{-1} bandwidth, with 5 MHz or ≈ 7 km s^{-1} channels), using the E configuration (maximum baseline of 66 m, yielding a resolution of $\approx 4.2''$ at 230 GHz). The ^{12}CO (2–1) and ^{13}CO (2–1) observations were obtained with a mosaic of 7 pointings, a central pointing surrounded by 6 pointings in an hexagonal pattern (see Fig. 3.1). Simultaneous observations of HCN (1–0), HCO$^+$ (1–0), HNC (1–0) and HNCO (4–3) were obtained in October 2011. For each of HCN (1–0) and HCO$^+$ (1–0), 3 spectral windows per line were used (375 MHz or ≈ 1100 km s^{-1} bandwidth, with 0.4 MHz or ≈ 1.3 km s^{-1} channels), using the D configuration (yielding an average resolution of $\approx 5.5''$ for these lines). Observations of HNC (1–0) and HNCO (4–3) used a single spectral window for each line (500 MHz or ≈ 1600 km s^{-1} bandwidth, with 5 MHz or ≈ 16 km s^{-1} channels). All the lines except HNCO (4–3) were detected with a signal-to-noise ratio $S/N \geq 3$.

All four dense gas tracers, namely HCN (1–0), HCO$^+$ (1–0), HNC (1–0) and HNCO (4–3), were also observed using the Institut de Radio Astronomie Millimetrique (IRAM) Plateau de Bure Interferometer (PdBI), with six 15 m antennae and thus 15 baselines in the 6ant-Special configuration (yielding an average resolution of $\approx 6.0''$ for these lines). A 3.6 GHz or ≈ 12500 km s^{-1} bandwidth with a spectral resolution of 2 MHz or ≈ 7 km s^{-1} was used. The observations of the dense gas tracers were obtained with a mosaic of 2 pointings, centred at offsets $(+5.3'', +11.3'')$ and $(-5.3'', -11.3'')$ with respect to the galaxy centre (and thus along the galaxy major axis; see Fig. 3.1).

At the distance of NGC 4710, $1''$ corresponds to ≈ 81 pc. The resolution of the CARMA observations thus corresponds to a linear scale of ≈ 300 and ≈ 450 pc for the tenuous (CO) and dense gas tracers, respectively, while that of the PdBI observations corresponds to ≈ 480 pc. The main observational parameters for NGC 4710 are listed in Table 3.2.

Table 3.2: Main observational parameters for NGC 4710 and NGC 5866.

Galaxy	Transition	Rest Freq. (GHz)	Obs. Date	Total Obs. Time (hours)	Interferometer	Beam (arcsec)	Conversion factor (K Jy^{-1} beam)	Noise (mJy beam^{-1})
NGC 4710	^{12}CO (1–0)	115.271	02 APR 2009	6.42	CARMA	3.9×3.2	7.3	9
	^{13}CO (1–0)	110.201				4.4×3.9	5.8	5
	^{12}CO (2–1)	230.538	30/31 JAN 2011	5.03	CARMA	4.1×3.5	1.6	28
	^{13}CO (2–1)	220.398				4.6×3.9	1.4	23
	HCN (1–0)	88.633				5.1×4.6	6.7	
	HCO$^+$ (1–0)	89.188	15/18/23/24/25 OCT 2011	16.62	CARMA	5.5×4.8	5.8	2
	HNC (1–0)	90.663				5.1×4.6	6.3	
	HCN (1–0)	88.633				6.1×5.3	4.9	
	HCO$^+$ (1–0)	89.188	30 NOV 2011, 19 JAN 2012	7.90	PdBI	6.1×5.2	4.9	1
	HNC (1–0)	90.663				5.7×5.0	5.2	
	HNCO (4–3)	87.925				6.3×5.4	4.7	
NGC 5866	^{12}CO (1–0)	115.271	12/13/16 AUG 2010	6.67	CARMA	3.6×2.9	8.7	11
	^{13}CO (1–0)	110.201	28/30 APR & 03 MAY 2011	11.55	PdBI	4.9×3.6	5.8	1
	HCN (1–0)	88.633				6.3×5.2	4.8	
	HCO$^+$ (1–0)	89.188	03/04 MAY 2011	11.33	PdBI	6.3×5.2	4.7	0.5
	HNC (1–0)	90.663				6.2×5.1	4.8	
	HNCO (4–3)	87.925				6.3×5.2	4.8	

3.2.1.2 NGC 5866

NGC 5866 was primarily observed with PdBI. Observations of ^{13}CO (1–0) and the dense gas tracers HCN (1–0), HCO$^+$ (1–0), HNC (1–0) and HNCO (4–3), were carried out using the 6Dq configuration during April–May 2011, yielding a resolution of $\approx 4.9''$ at 110 GHz and $\approx 6.5''$ for the dense gas tracers. The total bandwidth was 3.6 GHz or ≈ 12500 km s^{-1}, with a spectral resolution of 2 MHz or ≈ 7 km s^{-1}. ^{12}CO (1–0) observations were obtained at CARMA in the D configuration, yielding a resolution of $\approx 3.8''$ at 115 GHz. Three spectral windows were used (375 MHz or ≈ 1000 km s^{-1} bandwidth, with a spectral resolution of 0.4 MHz or ≈ 1 km s^{-1})

At the distance of NGC 5866, $1''$ corresponds to ≈ 74 pc. The resolution of the PdBI observations thus corresponds to a linear scale of ≈ 360 and ≈ 480 pc for ^{13}CO (1–0) and the dense gas tracers, respectively, while that of the CARMA observations corresponds to ≈ 280 pc. The main observational parameters for NGC 5866 are listed in Table 3.2.

3.2.2 Data reduction

3.2.2.1 CARMA data reduction

The CARMA data were reduced using the Multichannel Image Reconstruction, Image Analysis and Display (MIRIAD) package [Sault et al., 1995]. First, for each track, initial data corrections were applied (i.e. line-length calibration, baseline and rest frequency corrections). The temporal behaviour of the phase calibrator was then checked to flag de-correlations when necessary. Second, the bandpass and phase calibrations were performed using a bright calibrator, usually a quasar (3C273, 1224+213 or 1419+513), within 20° of the source. The gain solutions were then derived and applied to the source. Flux calibration was carried out using the latest calibrator flux catalog maintained at CARMA (typically using a planet). After successfully calibrating the source data for each track and each observed line, all data for a given line were combined into one visibility file and imaged using the MIRIAD task *invert*. As CARMA is a heterogeneous array, *invert* was run with the mosaicking option, to take into account the different primary beams. All data cubes were created with a pixel size of $1'' \times 1''$ and $1.5'' \times 1.5''$ for the CO lines and dense gas tracers, respectively, typically yielding ≈ 4 pixels across the synthesized beam major axis. The dirty cubes were cleaned to a threshold equal to the rms noise of the dirty channels in regions devoid of emission. The cleaned components were then added back and re-convolved using a Gaussian beam of full-width at half-maximum (FWHM) equal to that of the dirty beam. A fully calibrated and reduced data cube was thus obtained for each molecular line.

Note that to simplify the discussion, the fully-calibrated and cleaned data cubes were also rotated using the MIRIAD task *regrid* with the keyword *rotate* and the molecular gas position angle [Davis et al., 2011a], this so that the emission (galaxy major-axis) is horizontal. The data presented therefore do not represent the true orientation of the galaxies on the sky.

3.2.2.2 PdBI data reduction

The PdBI data were reduced using the Grenoble Image and Line Analysis System (GILDAS) packages Continuum and Line Interferometer Calibration (CLIC) and MAPPING[1]. CLIC was used for the initial data reduction, including the bandpass, phase and flux calibrations, and the creation of the *uv* tables. MAPPING was then used to create fully calibrated and cleaned cubes, with the same procedure and pixel sizes as above. Those cubes were then converted into Flexible Image Transport System (FITS) files for further analysis in MIRIAD and Interactive Data Language (IDL) environments.

3.3 Imaging & Analysis

3.3.1 Emission regions and moment maps

To derive the moment maps of NGC 4710 and NGC 5866, the spatial extent of the emission must first be defined in the fully-calibrated and cleaned cube of each line. The data cubes were therefore first Hanning-smoothed spectrally and Gaussian-smoothed spatially with a FWHM equal to that of the beam. The smoothed cubes were then clipped (in three dimensions) at a 3σ threshold ($3\times$ rms in smoothed cube) and (smoothed) moment maps created. A region of contiguous emission for each line was then defined using the IDL region-growing algorithm *label_region* and the (smoothed) moment 0 map, creating a two-dimensional (2D) mask that was then used to derive the moment maps of the original (unsmoothed and unclipped) cubes, shown in Figures 3.1 and 3.2.

As the ^{12}CO (1–0) is the most spatially extended line in both galaxies, the contiguous emission region for the other lines cannot be more extended than this. Furthermore, as all ^{12}CO (1–0) emission lies along the major axis of the galaxies, it was assumed here that this must be the case for the other lines as well. These two criteria were thus also used to define

[1] http://www.iram.fr/IRAMFR/GILDAS

the real extent of the line emission when this emission is discontinuous, typically in the centre (nuclear disc) and nearly symmetric regions farther along the disc on either side (inner ring edges) (see, e.g., the ^{13}CO (1–0) emission in Fig. 3.1).

The rms noise levels ($\sigma_{\rm rms}$) in the original cubes were calculated using all pixels outside of the identified emission regions.

3.3.2 Position-velocity diagrams

To create a PVD for each molecular line detected, we simply took a slice along the major axis of the galaxies in the fully-calibrated and cleaned data cubes, averaging 5 pixels in the perpendicular direction (i.e. along the galaxy minor axis; slightly larger than the synthesised beam, maximising S/N as the emission is generally not resolved perpendicular to the disc). The PVDs of all the lines detected in NGC 4710 and NGC 5866 are shown in Figures 3.3 and 3.4, respectively. The spatial resolution of each PVD, i.e. the size of the beam along the major axis of the galaxy, was calculated by taking into account the synthesised beam position angle, major axis and minor axes, as well as the position angle of the emission itself (see Davis et al. 2013a).

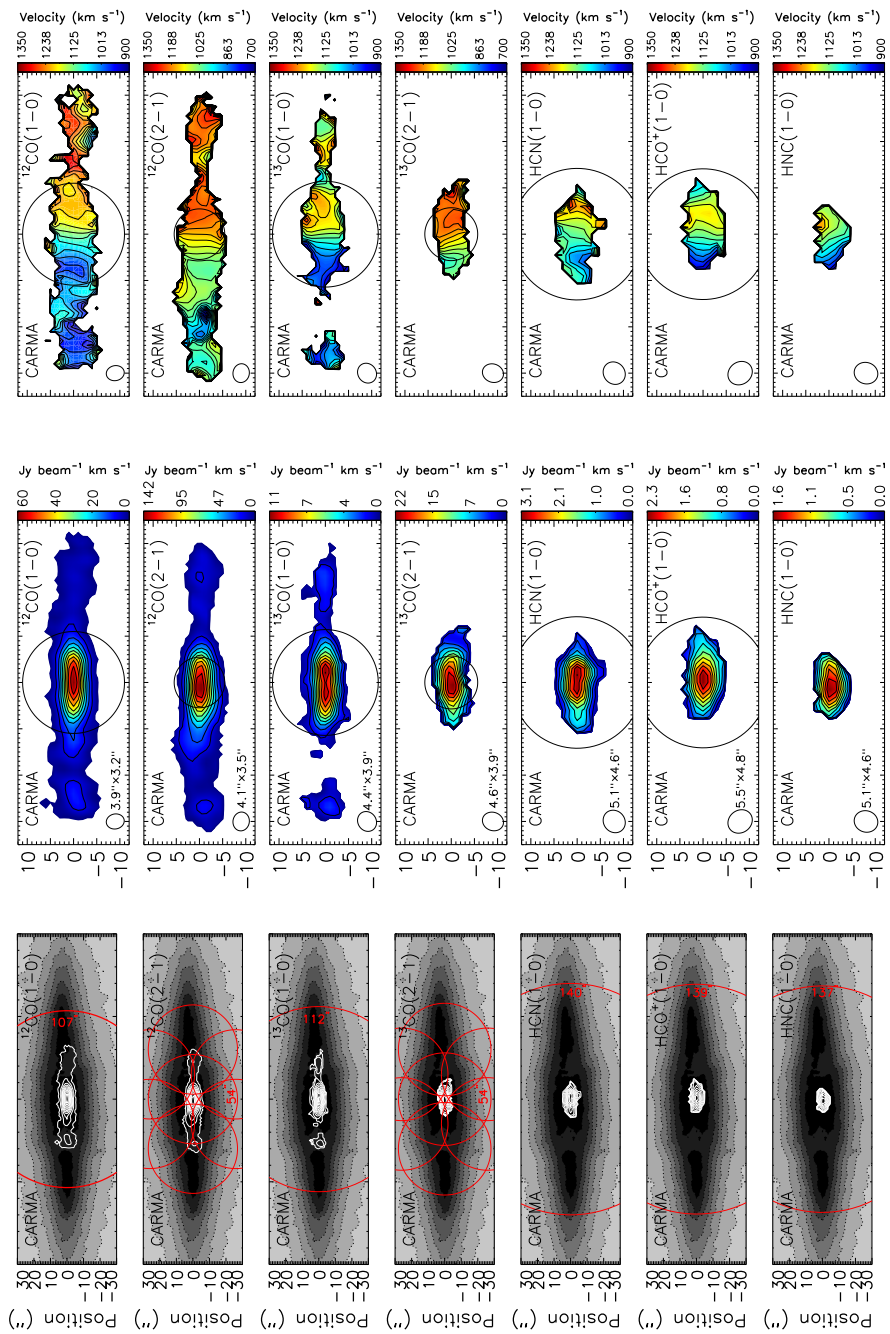

Figure 3.1: NGC 4710 moment maps. **Left**: Moment 0 contour maps (white) of the detected lines overlaid on an optical image of the galaxy (greyscale) from the Sloan Digital Sky Survey (SDSS). Red circles show the primary beam of CARMA and/or PdBI at the respective frequency of each line. The beam sizes are also indicated. **Centre**: Moment 0 maps with overlaid isophotal contours. **Right**: Moment 1 maps with overlaid isovelocity contours. The large black circles on the moment maps show the IRAM 30 m telescope beam for comparison (HNC (1–0) was not observed; see Crocker et al. 2012). Contour levels on the moment 0 maps are from 10 to 100% of the peak integrated line intensity in steps of 10%. The moment 0 peaks are (from top to bottom) 59.8, 145.8, 10.8, 22.3, 3.0, 2.3, and 1.7 Jy beam^{-1} km s^{-1}. Contour levels on the moment 1 maps are spaced by 30 km s^{-1}. The array used, molecular line displayed, and synthesized beam are also indicated in each panel.

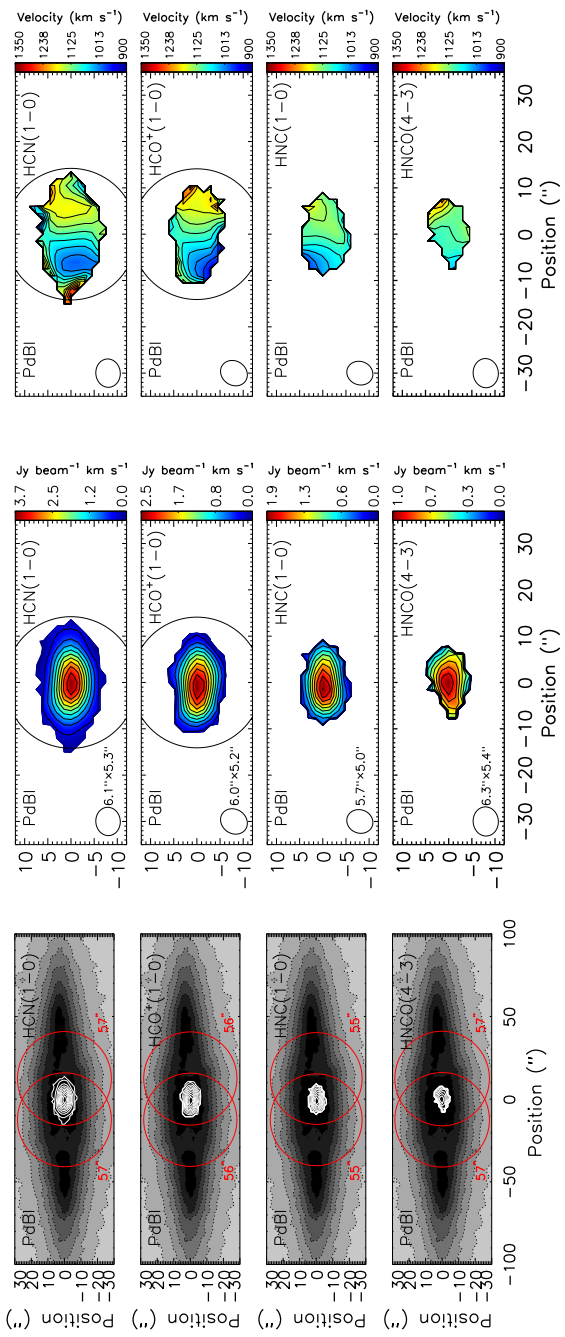

Figure 3.1: Continued. The large black circles on the moment maps show the IRAM 30 m telescope beam for comparison (HNC (1–0) and HNCO (4–3) were not observed; see Crocker et al. 2012). The moment 0 peaks are (from top to bottom) 3.7, 2.5, 1.9 and 1.0 Jy beam^{-1} km s^{-1}. Contour levels on the moment 1 maps are spaced by 30 km s^{-1}. The array used, molecular line displayed, and synthesized beam are also indicated in each panel.

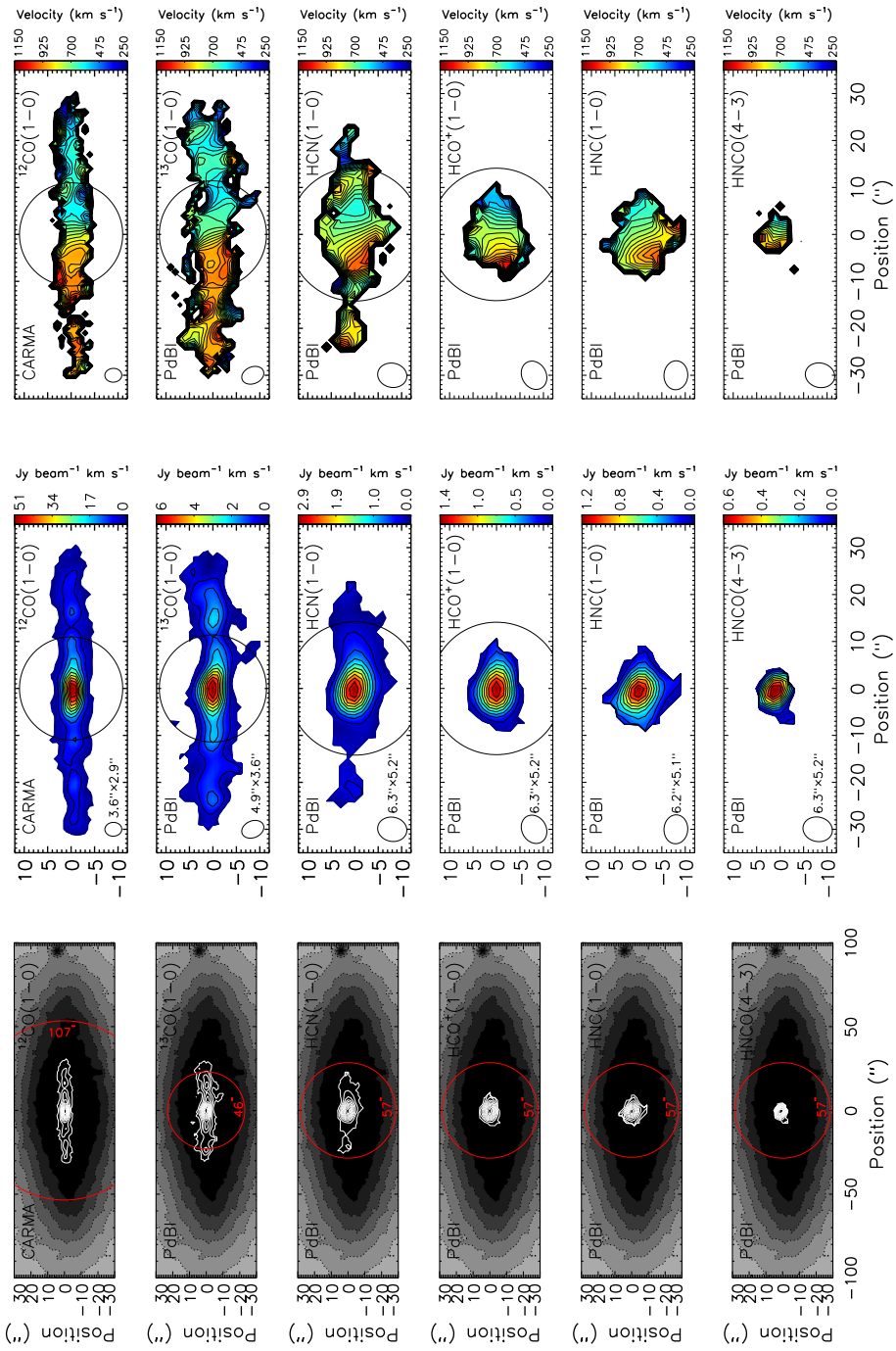

Figure 3.2: Same as Figure 3.1 but for NGC 5866. The moment 0 peaks are (from top to bottom) 51.5, 5.5, 2.9, 1.4, 1.2, and 0.6 Jy beam^{-1} km s^{-1}.

As seen in Figures 3.3 – 3.4, the PVDs of the CO lines in both galaxies (except ^{13}CO (2–1) in NGC 4710) and the PVD of HCN (1–0) in NGC 5866 reveal X-shape patterns, with two distinct velocity components: a central rapidly-rising velocity component (hereafter nuclear disc) and an outer slowly-rising velocity component (hereafter inner ring). Both can easily be understood in the context of barred galaxy dynamics (see Sellwood & Wilkinson 1993 for a general review; Bureau & Athanassoula 1999, Athanassoula & Bureau 1999 and Bureau & Freeman 1999 for the observed kinematics of edge-on systems). Bar-driven inflows cause gas to accumulate on x_2 orbits (elongated perpendicular to the bar) within the inner Lindblad resonance (ILR; when present) at the centre of the galaxy, creating a feature known as a nuclear disc (or ring), and giving rise to the central rapidly-rising velocity component seen in the PVDs. Gas also accumulates just beyond the end of the bar near corotation (and possibly beyond), creating a feature known as an inner ring, and giving rise to the outer slowly-rising velocity component of the PVDs. The intermediate region occupied by x_1 orbits (elongated parallel to the bar) is swept free of gas, creating a gap between the nuclear disc and inner ring (both morphologically and in the PVDs). However, there is some material there, at least in NGC 4710, where the X shape of the ^{12}CO (1–0) PVD resembles a figure of eight at positive projected radii (see position 9 in Fig. 3.11; less so for other tenuous gas transitions). The emission coming from the intermediate region is less clear at position 8 and 10 since higher S/N emission coming from the central disc and inner ring mostly contributes to the flux at these positions respectively. These three morphological and kinematic features generally constitute reliable bar signatures.

The boxy/peanut-shaped bulge of NGC 4710 confirms that it is barred, while the dominant classical bulge of NGC 5866 makes the characteristic kinematic bar signatures observed somewhat surprising (see the optical images in Figs. 3.1 and 3.2). The X-shaped PVD (and thus kinematic bar signature) was first observed in NGC 4710 by Wrobel & Kenney [1992] and in NGC 5866 by Alatalo et al. [2013], both from ^{12}CO (1–0) observations.

The nuclear disc has a radial extent of $\approx 12''$ (≈ 1 kpc) in NGC 4710 and $\approx 8''$ (≈ 0.6 kpc)

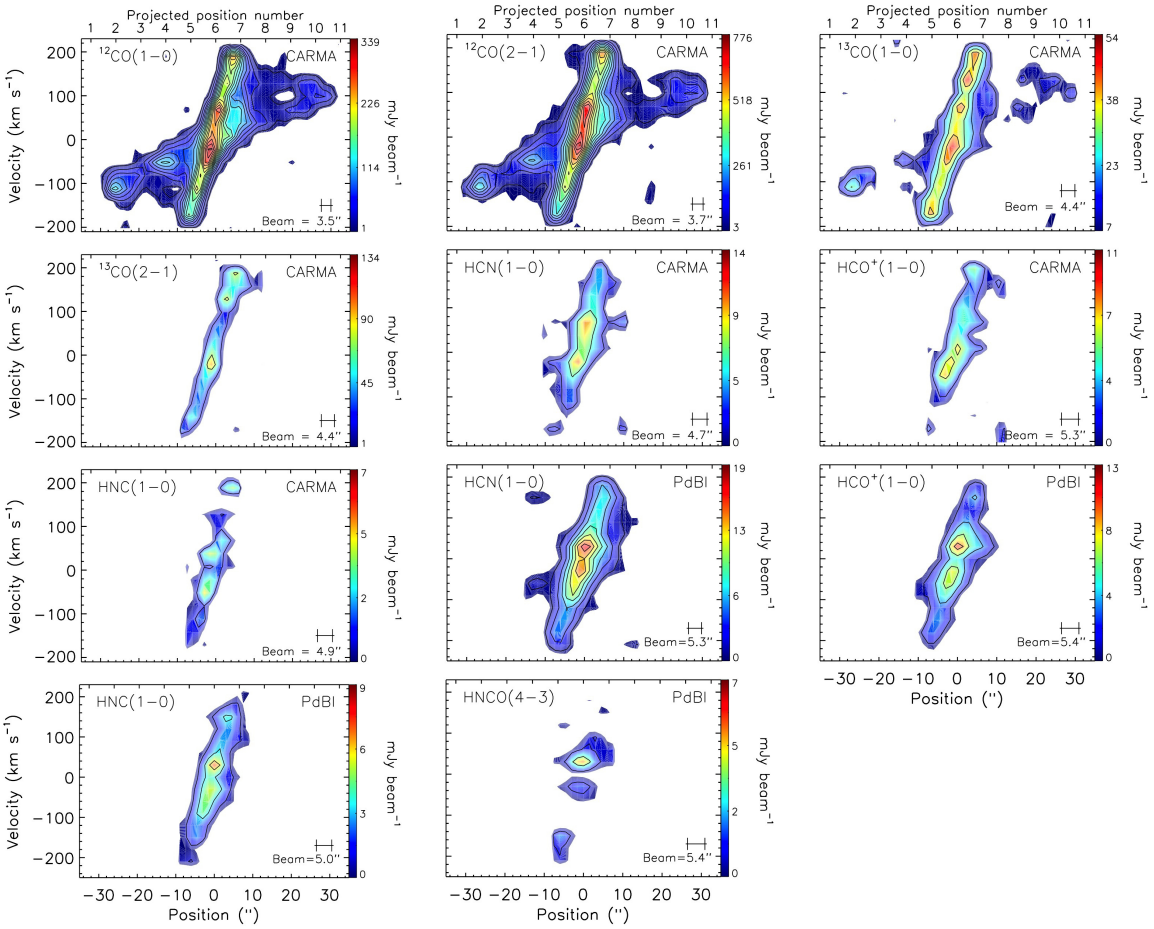

Figure 3.3: PVDs of all the lines detected in NGC 4710. The PVDs are overlaid with contours (black lines) spaced by 3σ and starting at 3σ, while the colour scales start at 1σ. The rms noise for the CARMA observations of ^{12}CO (1–0), ^{13}CO (1–0), ^{12}CO (2–1), ^{13}CO (2–1), HCN (1–0), HCO$^+$ (1–0) and HNC (1–0) is 7.5, 3.7, 19.0, 19.0, 1.5, 1.6 and 1.2 mJy beam^{-1}, respectively, while that for the PdBI observations of HCN (1–0), HCO$^+$ (1–0), HNC (1–0) and HNCO (4–3) is 0.8, 0.9, 0.9 and 0.9 mJy beam^{-1}, respectively. The projected position numbers, as discussed in Section 3.4.2 and illustrated in Figure 3.11, are indicated on the top axes. The array used, molecular line displayed, and angular resolution along the major axis are also indicated in each panel.

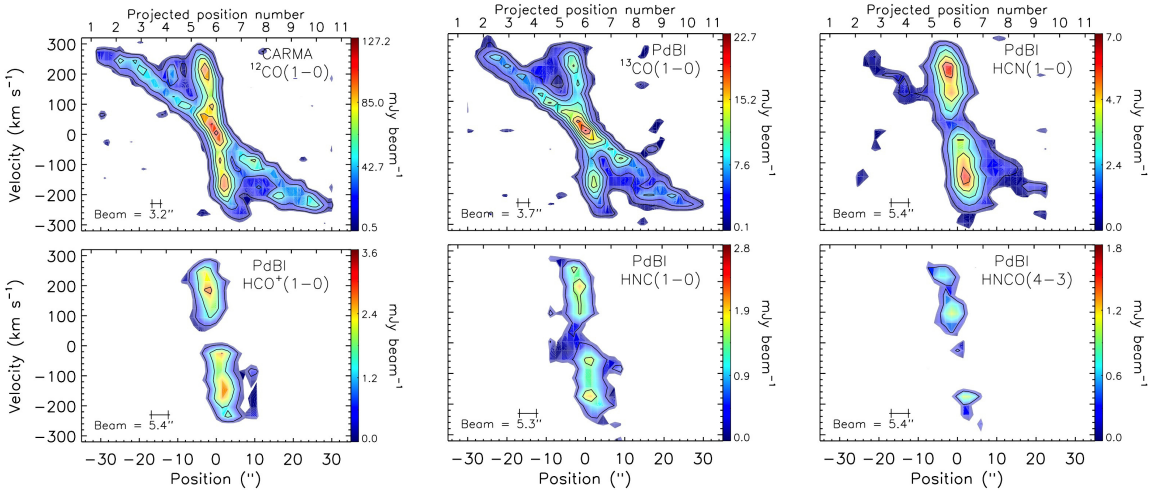

Figure 3.4: Same as Figure 3.3 but for NGC 5866. The rms noise for the observations of ^{12}CO (1–0), ^{13}CO (1–0), HCN (1–0), HCO$^+$ (1–0), HNC (1–0) and HNCO (4–3) are 6.7, 0.9, 0.4, 0.4, 0.4 and 0.4 mJy beam^{-1}, respectively.

in NGC 5866, while the inner ring has a radius of $\approx 32''$ (≈ 2.6 kpc) in NGC 4710 and $\approx 32''$ (≈ 2.4 kpc) in NGC 5866 (see Figs. 3.3 and 3.4).

3.3.3 Comparisons with IRAM 30m data

Some lines detected with CARMA and PdBI in this work were also previously detected with the IRAM 30m single-dish telescope. For NGC 4710, the relevant lines are ^{12}CO (1–0), ^{12}CO (2–1) [Young et al., 2011], ^{13}CO (1–0), ^{13}CO (2–1), HCN (1–0) and HCO$^+$ (1–0) [Crocker et al., 2012], while those for NGC 5866 are ^{12}CO (1–0) [Welch & Sage, 2003], ^{13}CO (1–0), HCN (1–0) and HCO$^+$ (1–0) [Crocker et al., 2012]. As the IRAM 30m beam is smaller than the primary beams of CARMA and PdBI at any frequency (see Figs. 3.1 and 3.2), CARMA and PdBI are better able to recover the true integrated molecular gas content of the galaxies (as long as the interferometer did not filter out diffuse, extended emission).

To check the consistency of the datasets from the IRAM 30m single-dish telescope and the interferometers, we simulated IRAM 30m integrated spectra using our CARMA and PdBI interferometric data cubes. To do this, for each line we summed the flux in our cubes spatially

using a Gaussian weighting function of FWHM equal to that of the single-dish beam at the given frequency (and centred on the galaxies, thus assuming no 30m pointing error). The IRAM 30m beam size adopted for the ^{12}CO (1–0), ^{13}CO (1–0), ^{12}CO (2–1) and ^{13}CO (2–1) line was 22″, 23″, 11″ and 11.5″, respectively, while that for the HCN (1–0), HCO$^+$ (1–0), HNC (1–0) and HNCO (4–3) lines was 28″. When the IRAM 30m fluxes were listed in Kelvin (either antenna temperature T_a^* or main beam temperature T_{mb}), we converted the fluxes using the conversion factors given in the associated papers or listed on the IRAM website[1]. For values at frequencies not specified there, we linearly interpolated between the two nearest values.

The true IRAM 30m spectra, simulated IRAM 30m spectra and spatially-integrated CARMA and PdBI spectra (the latter with no weighting nor spatial limit, thus recovering more flux if the emission extends beyond the 30m beam) are shown in Figure 3.5 and 3.6 for NGC 4710 and NGC 5866, respectively (see also Section 3.5.3).

[1] http://www.iram.es/IRAMES/mainWiki/Iram30mEfficiencies

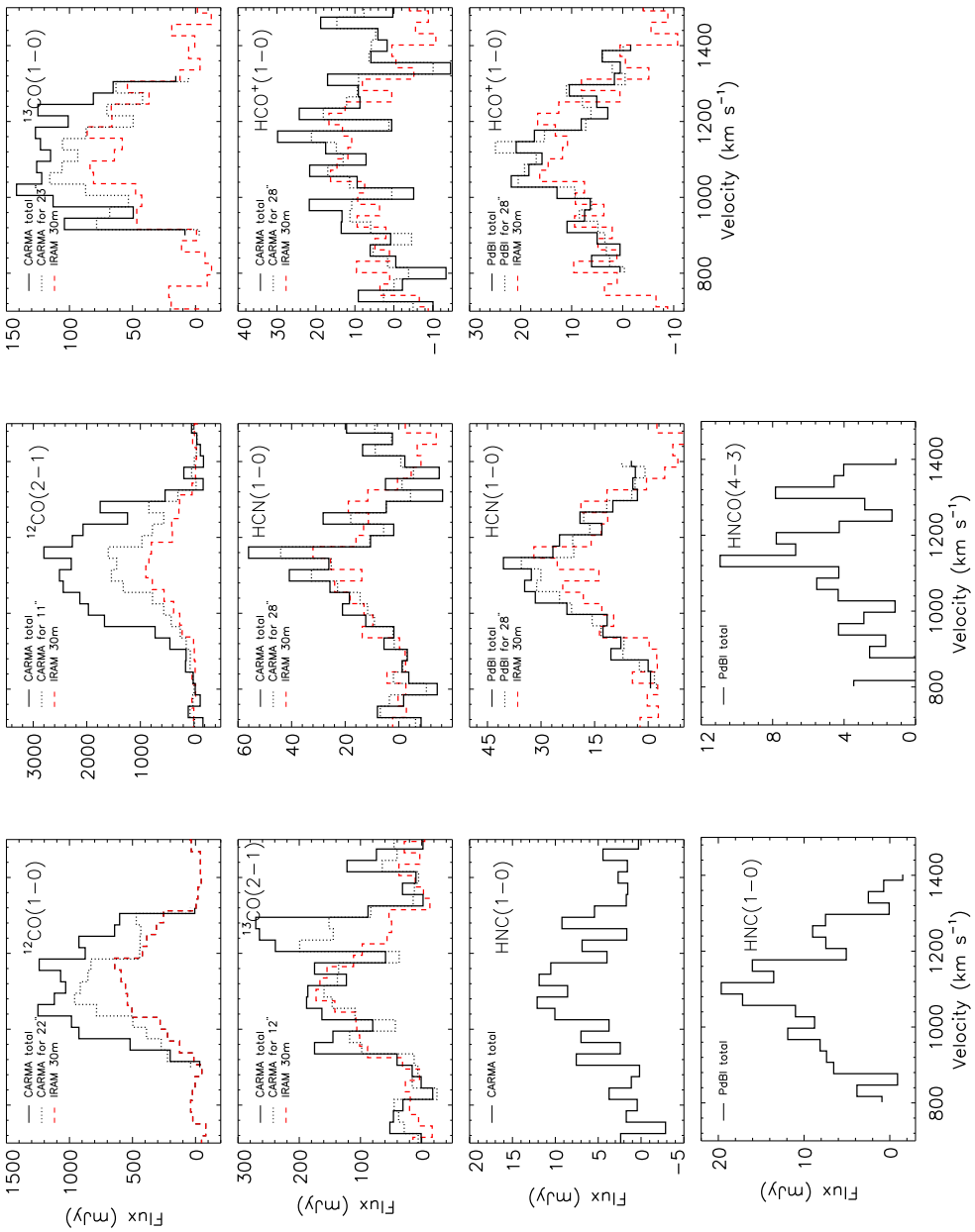

Figure 3.5: Comparison of integrated molecular line spectra for NGC 4710. Black solid lines show the integrated spectra of our CARMA and PdBI observations, with no spatial weighting nor limit. Black dotted lines show the IRAM 30m integrated spectra simulated from our CARMA and PdBI observations (with Gaussian spatial weighting; see Section 3.3.3). Red dashed lines show original IRAM 30m integrated spectra from the literature. The HNC (1–0) and HNCO (4–3) lines were never observed previously, so their integrated spectra are shown here for the first time.

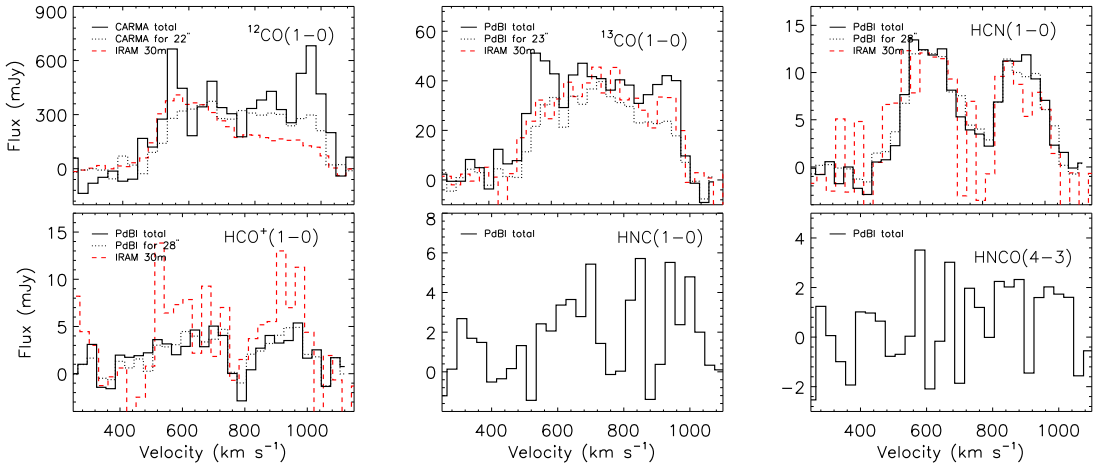

Figure 3.6: Same as Figure 3.5 but for NGC 5866.

3.3.4 Continuum emission

NGC 4710 and NGC 5866 do not reveal spatially extended continuum emission, but they do harbour a continuum point source at their respective centre. We thus measured the continuum flux of each galaxy by fitting a point source model in the *uv* plane, using only channels free of emission. To do this, for PdBI data we used the *MAPPING* task *uv_fit*, and for CARMA data we used the *Miriad* task *uvfit*.

In NGC 4710, we found a continuum flux of 3.23 ± 0.88 mJy at 230 GHz and 3σ upper limits of 2.46 and 3.80 mJy at 220 and 90 GHz, respectively. We were not able to estimate a continuum flux at 115 and 110 GHz, as there is no emission free channel, but Alatalo et al. [2013] list a 3σ upper limit of 5.20 mJy at 115 GHz. In NGC 5866, we found a continuum flux of 5.99 ± 1.28 mJy at 115 GHz, 3.71 ± 0.07 mJy at 110 GHz and 3.55 ± 0.04 mJy at 90 GHz. The spectral energy distribution of each galaxy is shown in Figure 3.7 and the flux values are listed in Table 3.3.

Table 3.3: Spectral energy distribution of NGC 4710 and NGC 5866.

Galaxy	Instrument	Frequency (GHz)	Flux (mJy)	Reference
NGC 4710	VLA	1.4	19	1
	PdBI	90	< 3.8	2
	CARMA	115	< 5.2	3
	CARMA	220	< 2.5	2
	CARMA	230	3.2	2
	IRAS	3000	13.2	4
	IRAS	5000	5.9	4
	IRAS	12500	0.5	4
	IRAS	25000	0.4	4
NGC 5866	VLA	1.4	22	1
	VLA	5	12.7	5
	VLA	15	9.3	5
	PdBI	90	3.6	2
	PdBI	110	3.7	2
	CARMA	115	5.9	2
	SCUBA	347	173	6
	MIPS	1875	17740	7
	IRAS	3000	16980	4
	MIPS	4286	8710	7
	IRAS	5000	5260	4
	MIPS	12500	200	8
	IRAS	25000	350	4
	IRAC	38100	310	7
	IRAC	84400	660	7

References: [1] Brown et al. [2011]; [2] this paper; [3] Alatalo et al. [2013]; [4] Sanders et al. [2003a]; [5] Nagar. et al. [2001]; [6] Doi et al. [2005]; [7] Dale et al. [2007]; [8] Dale et al. [2005]

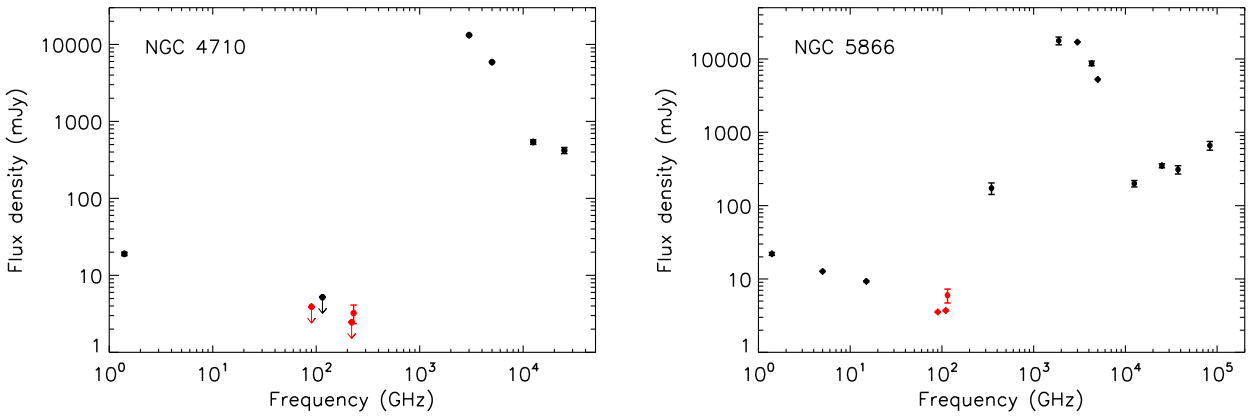

Figure 3.7: Spectral energy distribution of NGC 4710 and NGC 5866 from the radio to the infrared. Our measurements are shown in red.

3.4 Line ratio diagnostics

Different molecular lines require different physical conditions to be excited, so a multitude of line ratios are required to probe complex media. In this work, we perform three types of line ratio analyses, providing complementary information on the physical conditions of the gas along the disc (major-axis) of NGC 4710 and NGC 5866. First, we analyse direct ratios of the major-axis PVDs (see Section 3.4.1), providing a qualitative view of the physical conditions in both kinematic components of the galaxies (nuclear disc and inner ring). Second, we calculate the ratios of integrated line intensities as a function of projected radius along the galaxy discs, by extracting integrated spectra as a function of position for each kinematic component separately (see Section 3.4.2). Third, we model these line ratios using a non-LTE radiative transfer code, thus estimating a number of physical parameters describing a two-component molecular ISM (see Section 3.4.3 – 3.4.5).

When the density exceeds a given molecular transition critical density $n_{\rm crit}$, collisions become the dominant excitation and de-excitation mechanism. In dense clouds, gas excitation

is thus dominated by collisions with H_2, by far the most abundant species. Low-J CO lines, such as ^{12}CO (1–0) and its isotopologue ^{13}CO (1–0), have $n_{\rm crit} \approx 10^3$ cm^{-3}, whereas high density tracers, such as HCN (1–0), HCO$^+$ (1–0), HNC (1–0) and HNCO (4–3), have critical densities up to $n_{\rm crit} \approx 10^6$ cm^{-3}. In this work, we therefore separate our line ratios in three different groups, to better probe the physical conditions of different phases of the molecular ISM. The three groups are: i) ratios of low-J CO lines only, tracing the temperature, opacity and column density of the relatively tenuous molecular gas; ii) ratios of dense gas tracers only, tracing the density, chemical state and dominant excitation/ionisation mechanisms of the dense molecular gas (e.g. UV and X-ray radiation, stellar winds and supernova explosions); and iii) ratios of CO to dense gas tracers, tracing the dense gas fraction. As our PdBI observations of HCN (1–0), HCO$^+$ (1–0), HNC (1–0) and HNCO (4–3) in NGC 4710 are roughly twice as deep as our CARMA observations of the same lines, we will exclusively use the PdBI data of those lines for the line ratio analyses of this galaxy.

3.4.1 PVD ratios

We start all line ratio analyses by first creating identical data cubes for all molecular lines. These identical cubes have the same number of channels, channel width, start and end velocities, and pixel size. They are also convolved to a common circular beam size of 6.5″, the largest synthesised beam in our dataset (i.e. the beam of the high density tracers observed at PdBI; see Table 3.2). The pixel size of these data cubes was chosen to be 1.3″, yielding 5 pixels across the beam. We then converted our fluxes from Jy beam^{-1} to Kelvin (K) using the conversion factors calculated by the MIRIAD task *imstat* (see Table 3.2), so that by convention and throughout this paper we take the ratio of integrated line intensities expressed in K km s^{-1}.

For our first approach to line ratio analysis, PVDs were created from these identical cubes as before, and ratios of these PVDs were calculated for relevant line pairs in each of the three aforementioned line ratio groups (CO lines only, dense gas tracers only, and CO

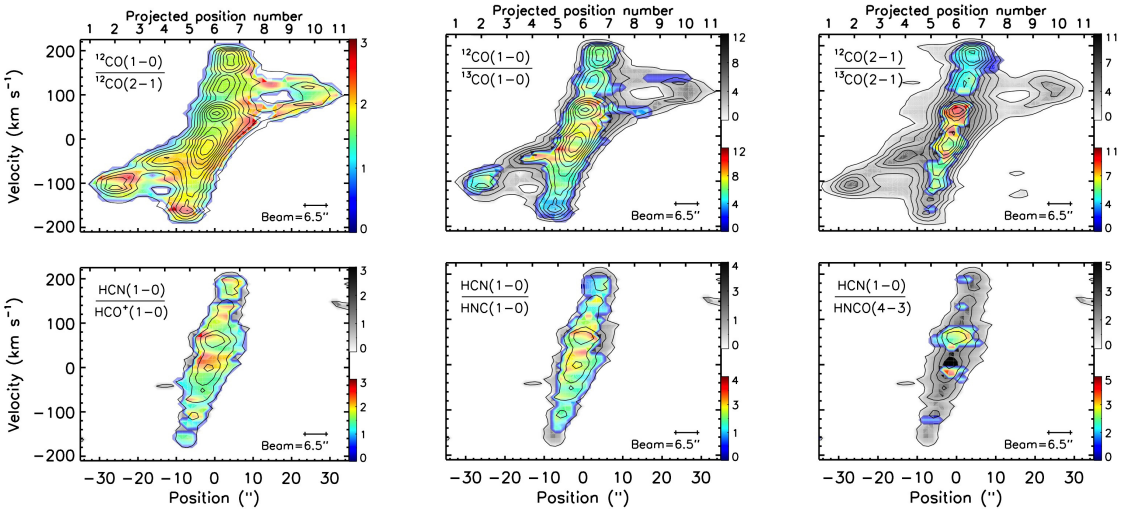

Figure 3.8: PVD ratios of CO lines only and dense gas tracer lines only in NGC 4710. **Top row:** PVD ratios of CO lines only, with the relevant ^{12}CO (1–0) or ^{12}CO (2–1) PVD contours overlaid (black lines). **Bottom row:** PVD ratios of dense gas tracer lines only, with the HCN (1–0) PVD contours overlaid (black lines). Contour levels are spaced by 3σ starting at 3σ. Greyscales indicate lower limits to the line ratios (see Section 3.4.1). The projected position numbers, as discussed in Section 3.4.2 and illustrated in Figure 3.11, are indicated on the top axes.

versus dense gas tracers). For the high density tracer and ^{13}CO lines that remain undetected in some regions of the discs, a 3σ flux upper limit was adopted, yielding a lower limit on the line ratios considered. The PVD ratios are shown in Figures 3.8, 3.9 and 3.10, where the greyscales indicate lower limits.

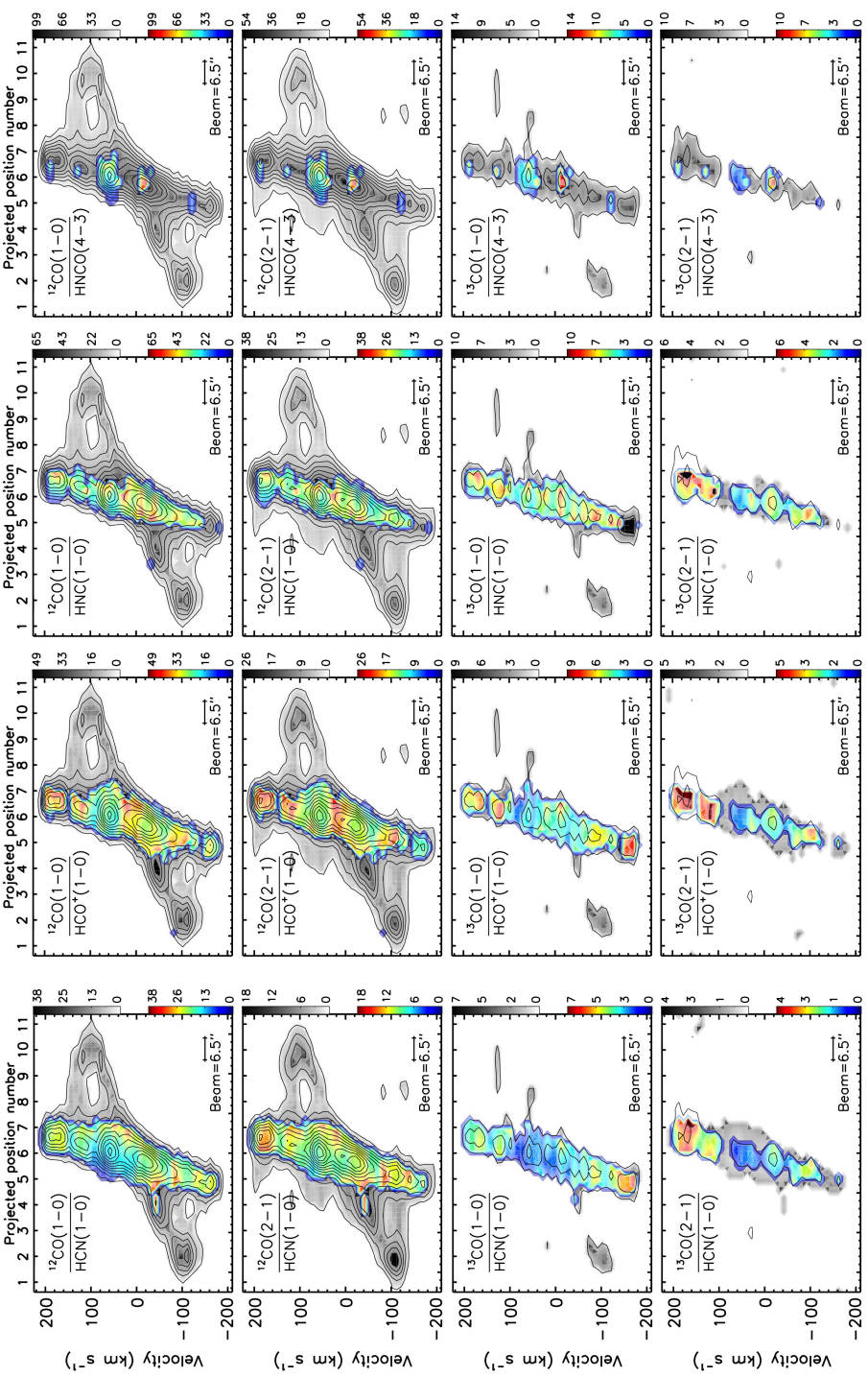

Figure 3.9: Same as Figure 3.8 but for the ratios of CO to dense gas tracer lines in NGC 4710.

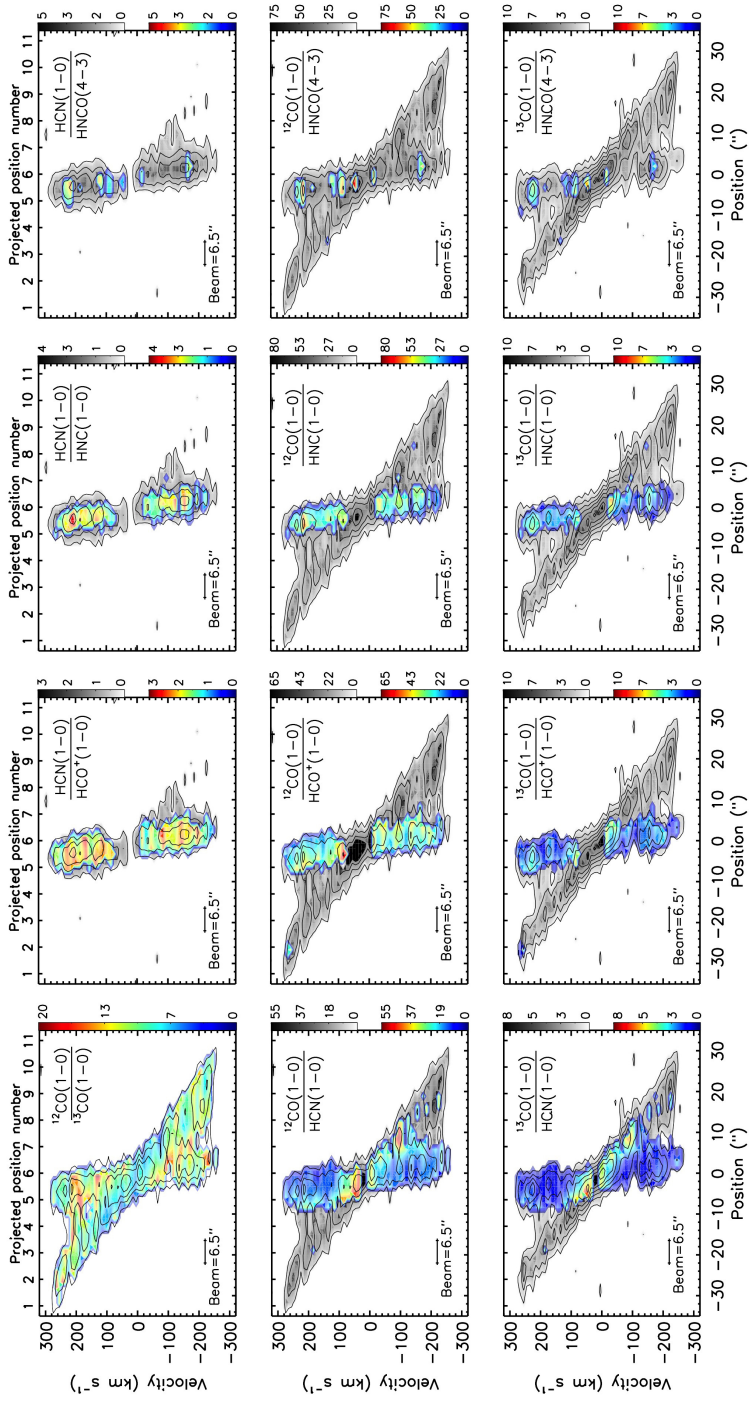

Figure 3.10: Same as Figures 3.8 and 3.9 but for NGC 5866.

3.4.2 Integrated line intensity ratios as a function of projected radius

Using the PVDs created from the identical data cubes, for our second approach we attempted to disentangle the spectra of the two kinematic components seen in the PVDs (nuclear disc and inner ring; see Section 3.3.2), this as a function of projected position along the disc. First, we extracted "integrated" spectra at a number of positions along the discs, each separated by one beam width, by taking averages of subsequent 5-pixel (i.e. one beam width) slices, as illustrated in Figure 3.11. Second, we calculated the integrated line intensity (i.e. $\int T_{\rm mb}\,{\rm d}v$ in K km s^{-1}) of each kinematic component at each position by fitting a single or double Gaussian to the extracted spectrum at each position, depending on whether a single or both kinematic components were present along the line of sight (see Fig. 3.12). The package *MPFIT* was used to optimize the fits [Markwardt, 2009a]. When both components are detected, a single Gaussian was normally sufficient in the outer parts (inner ring), while a double Gaussian was normally required in the inner parts (nuclear disc and inner ring). When a single component is detected in the inner parts (nuclear disc), a single Gaussian is of course always sufficient. The ratios of the integrated line intensities were then calculated as a function of projected radius along the discs. The corresponding line ratio profiles are shown in Figures 3.13 – 3.15 and are tabulated in Tables A.1 – B.2.

At the projected positions where there is at least one undetected line ($\int T_{\rm mb}\,{\rm d}v < 3\sigma$, where σ is the uncertainty in the integrated line intensity), we assigned an upper limit to the integrated line intensity of $3\sigma_{\rm rms}\times$FWHM, where $\sigma_{\rm rms}$ is the noise in the spectrum of the undetected line and FWHM is the FWHM of the (other) detected line used to define the line ratio at that position. The error on this integrated line intensity upper limit was estimated using the noise in the spectrum and the error on the FWHM. As listed in Table A.1, the integrated line intensity ratios of interest are $I_{12} \equiv {}^{12}$CO (1–0)/^{12}CO (2–1), $I_{11} \equiv {}^{12}$CO (1–0)/^{13}CO (1–0) and $I_{22} \equiv {}^{12}$CO (2–1)/^{13}CO (2–1) for the low-J CO lines only, and $I_{\rm D1} \equiv$ HCN (1–0)/HCO$^+$ (1–0), $I_{\rm D2} \equiv$HCN (1–0)/HNC (1–0) and $I_{\rm D3} \equiv$HCN (1–0)/HNCO (4–3)

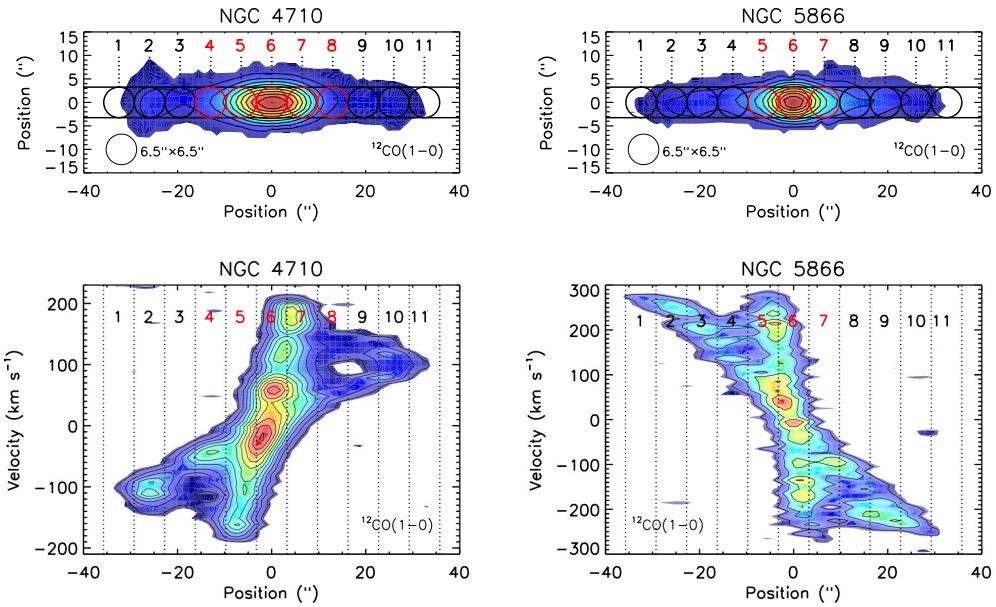

Figure 3.11: **Top:** Illustration of the projected positions along the major-axis of NGC 4710 (left) and NGC 5866 (right), where the line ratios are extracted and studied. **Bottom:** Corresponding 5-pixel (i.e. one beam width) slices in the PVDs. Red circles and associated numbers indicate positions where both kinematic components (nuclear disc and inner ring) are present along the line of sight, requiring a double-Gaussian fit (see Fig. 3.12, right). Black circles and associated numbers indicate positions where a single component (inner ring) is present, requiring a single Gaussian fit (see Fig. 3.12, left). The circle are one beam width (6.5″) in diameter.

for the dense gas tracer lines only. The ratios of CO to dense gas tracer lines are listed in Tables B.1 and B.2.

3.4.3 Non-LTE LVG Modelling

For our third approach, we probe the physical conditions of the molecular gas quantitatively by modeling the observed line ratios using the non-LTE radiative transfer code RADEX (please see Chapter 2 for more details on RADEX).

As the critical densities of the high density tracers are ≈ 3 orders of magnitude larger than those of the low-J CO lines, the two sets of lines trace different phases of the ISM and are not directly comparable. We therefore assume a two-component molecular ISM (at each projected position and for each kinematic component) and accordingly run models for the

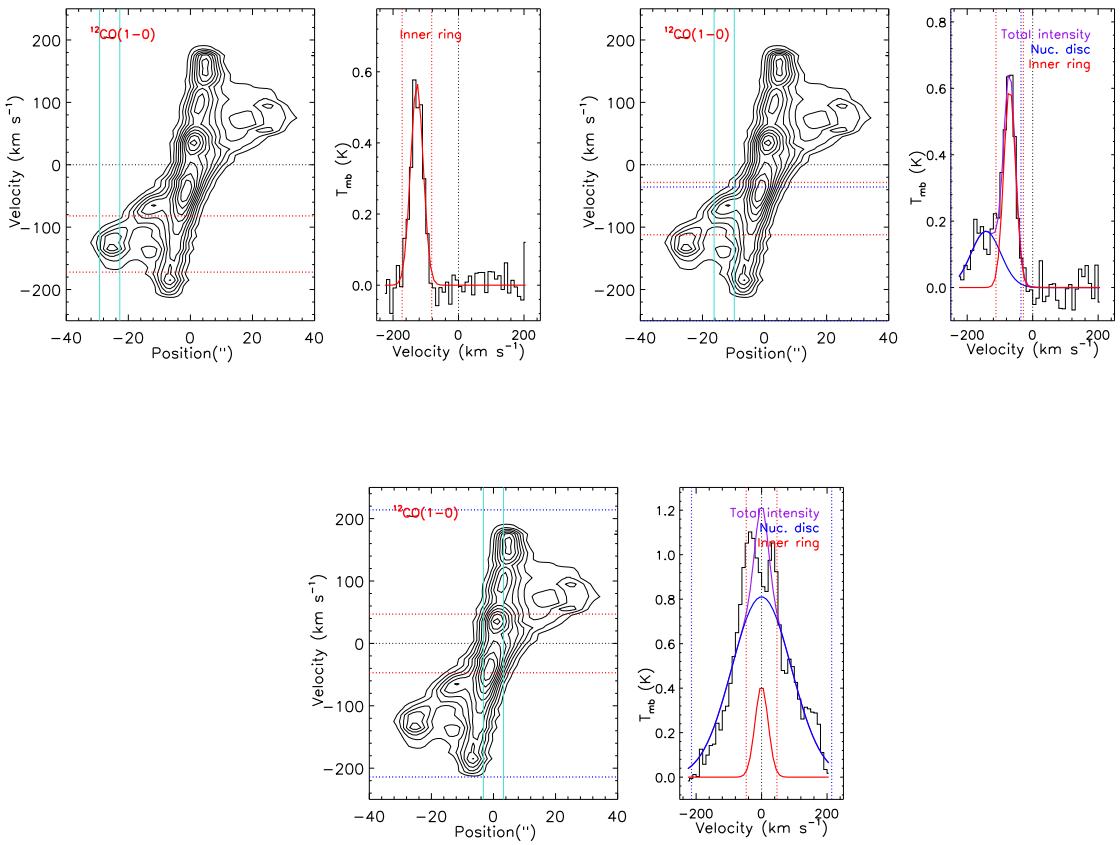

Figure 3.12: Illustration of the spectrum extraction process using the NGC 4710 ^{12}CO (1–0) PVD. **Top left:** ^{12}CO (1–0) PVD and the spectrum extracted at position 2, in the outskirt of the disc where a single kinematic component (inner ring) is present along the line of sight. **Top right:** Same for position 4, where both kinematic components are present (nuclear disc and inner ring). **Bottom:** Same for position 6 (galaxy centre), where both kinematic components are again present. The red and blue solid lines overlaid on the spectra show the Gaussian profiles separately fitted to the emission of the inner ring and the nuclear disc, respectively, while the magenta solid lines show the sums of the multiple Gaussians. The red and blue dotted lines overlaid on the PVDs and spectra indicate velocities of ± FWHM with respect to the centre of the associated Gaussian (thus encompassing ≈ 95% of the total emission of each component). Black dotted lines overlaid on the PVDs and spectra indicate the galaxy heliocentric velocity. Turquoise solid lines overlaid on the PVDs show the (one beam) width of the spatial slice considered to extract the averaged spectrum at that position.

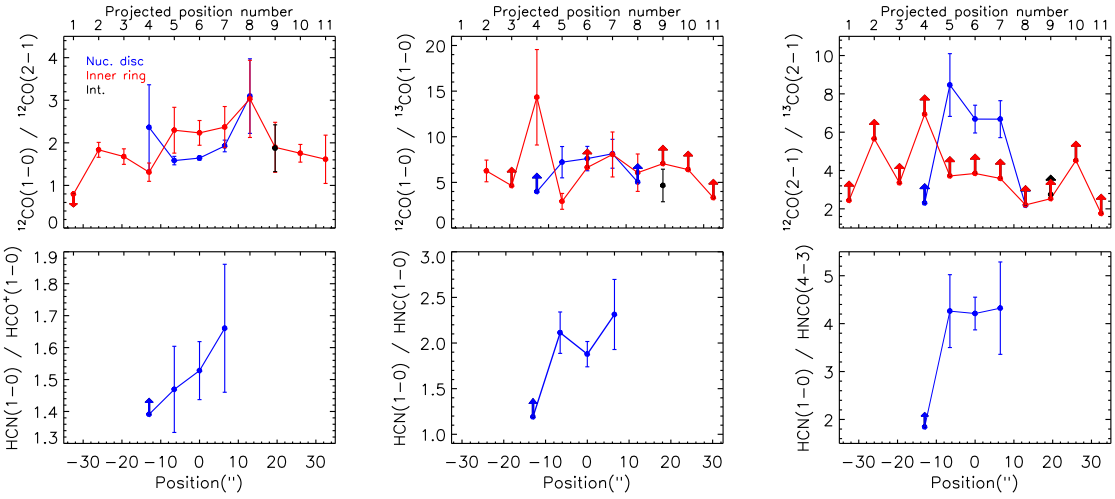

Figure 3.13: Ratios of CO lines only and dense gas tracer lines only as a function of projected radius in NGC 4710. **Top:** Ratios of CO lines only, along the inner ring (red), nuclear disc (blue) and intermediate region (black; position 9 only). **Bottom:** Ratios of dense gas tracer lines only, along the nuclear disc (blue). Upper and lower limits are indicated with arrows. The projected positions, as illustrated in Figure 3.11, are indicated on the top axis of each panel.

two groups of lines separately. Hereafter, we will refer to the molecular gas traced by the low-J CO lines as the tenuous molecular gas and that traced by the high density tracers as the dense molecular gas.

The model grids were created as follows. $T_{\rm K}$, $n({\rm H_2})$, and $N({\rm mol})$ are kept as free parameters to be fit for. $T_{\rm K}$ grid ranges from 10 to 250 K in steps of 5 K, $n({\rm H_2})$ ranges from 10^2 to 10^7 cm^{-3} in steps of 0.25 dex, and $N({\rm mol})$ ranges from 10^{13} to 10^{21} cm^{-2} in steps of 0.25 dex. As the widths of all the lines are similar, we adopt a single (average) line width for each kinematic component and each group of lines (rather than, e.g., using the exact width of each line in each kinematic component at each position).

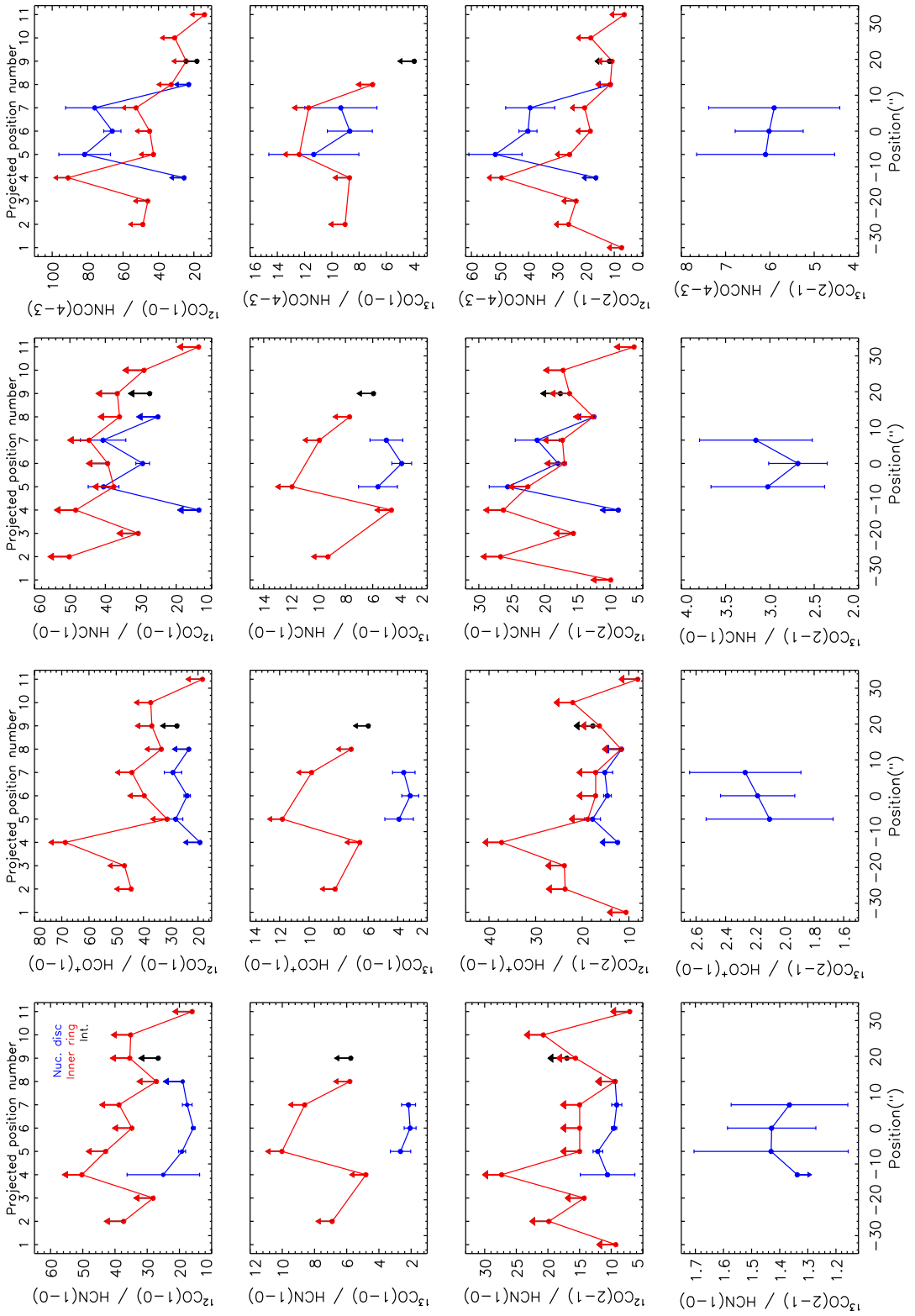

Figure 3.14: Same as Figure 3.13 but for the ratios of CO to dense gas tracer lines in NGC 4710.

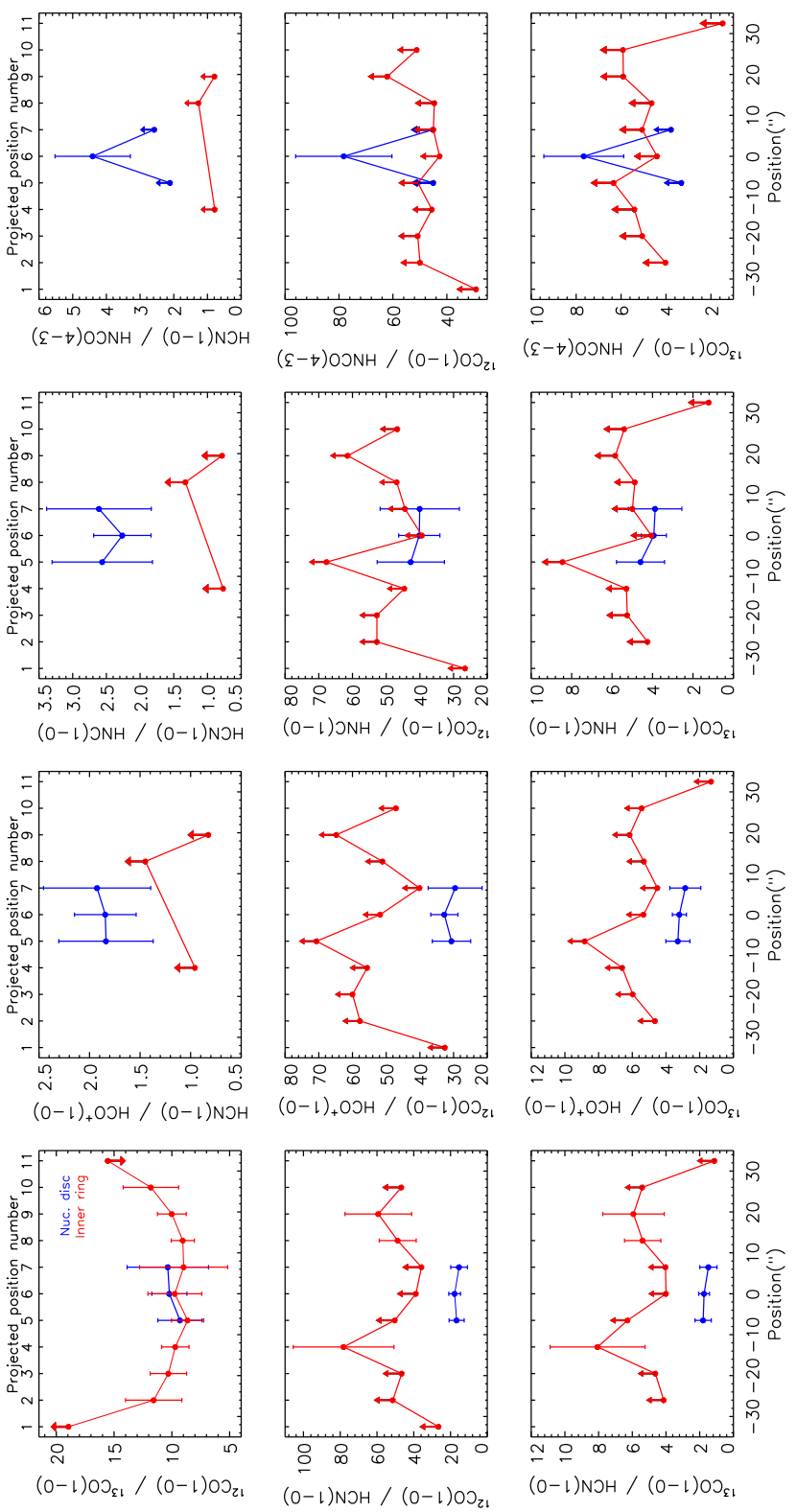

Figure 3.15: Same as Figures 3.13 and 3.14 but for NGC 5866.

The intrinsic abundance ratios of different molecules are also important inputs to the model calculations and must therefore be chosen carefully. Roberts et al. [2011] state that the ratios of velocity-integrated line intensities are not good proxies for intrinsic abundance ratios, while the ratios of column densities are better. We therefore take here the ratios of the column densities as the ratios of the intrinsic abundances. This indicates that changes in the abundance ratios affect the column densities linearly, i.e. a 50% change in an intrinsic abundance ratio will change the associated column densities by 50%. The [^{12}C] / [^{13}C] ratio is $\approx$ 20 at the centre of the Milky Way, $\approx$ 50 in the 4 kpc molecular ring, $\approx$ 70 in the local ISM and $\approx$ 90 in the Solar System [Anders & Grevesse, 1989; Wilson & Rood, 1994]. In the active nuclear regions of nearby starburst galaxies, the [^{12}C] / [^{13}C] ratio is $\geq$ 40 [Henkel & Mauersberger, 1993b; Henkel et al., 1993; Martín et al., 2010]. There is thus much variation in the intrinsic [^{12}C] / [^{13}C] ratio. The situation is even less satisfactory for the abundance ratios of high density tracers, since they have been much less studied in external galaxies. The [HCN] / [HCO$^+$] and [HCN] / [HNC] ratios vary widely from source to source [Goldsmith et al., 1986, 1981; Roberts et al., 2011; Wootten et al., 1978] and there is a lack of information in the literature about the [HCN] / [HNCO] ratio. These ratios also vary from region to region within galaxies, as molecular clouds located in different regions of galactic discs may well have different physical conditions and processes at play. For example, HCO$^+$ is enhanced by shocks, and the [HCN] / [HNC] ratio is known to vary with temperature (it increases with increasing temperature, although the abundance of each species decreases with increasing temperature and density; Goldsmith et al. 1986, 1981; Schilke et al. 1992b). Roberts et al. [2011] suggest that [HCN] / [HNC] and [HCN] / [HCO$^+$] range from 0.2 to 100 and 50 to 0.02, respectively (at $n(\mathrm{H_2}) = 10^6$ cm^{-3} and T_K = 10–200 K). However, both abundance ratios are about 1 at $\approx$ 30 K. In this work, we therefore assume an intrinsic ratio of 70 for [^{12}C] / [^{13}C] and 1 for the dense gas tracers (i.e. [HCN] / [HCO$^+$], [HCN] / [HNC] and [HCN] / [HNCO]).

Overall, this thus yields 4 possible sets of models for each position in each galaxy: models

for the tenuous molecular gas only (i.e. ^{12}CO (1–0), ^{12}CO (2–1), ^{13}CO (1–0) and ^{13}CO (2–1)) and for the dense molecular gas only (i.e. HCN, HCO^+, HNC and HNCO), this for both the nuclear disc and the inner ring separately (adopting an average Δv for each group of lines separately).

The positions along the disc of the galaxies where we apply the radiative transfer modelling are the same as those discussed in Section 3.4.2 and illustrated in Figure 3.11. However, since only 2 low-J CO lines were observed in NGC 5866, these sets of models for the tenuous molecular gas would be unconstrained and are thus not computed. Similarly, the dense gas tracer lines are generally not detected in the inner ring, so these sets of models are not computed either. Overall, we thus need models for the tenuous and dense molecular gas in the nuclear disc of NGC 4710, for the tenuous gas in the inner ring of NGC 4710, and for the dense gas in the nuclear disc of NGC 5866.

3.4.4 Best-fitting and most likely models

Following the method described in Chapter 2 [Topal et al., 2014], we use two methods to characterise the models (i.e. the physical parameters $T_{\rm K}$, $n(\rm H_2)$ and $N(\rm mol)$ of a two-component molecular ISM) best representing the data at each position illustrated in Figure 3.11. First we use a χ^2 method identifying the best-fitting model, and second a likelihood method identifying the most likely model.

For each set of model parameters, the χ^2 is defined as

$$\chi^2 \equiv \sum_i \left(\frac{R_{i,\rm mod} - R_{i,\rm obs}}{\Delta R_{i,\rm obs}} \right)^2 , \tag{3.1}$$

where $R_{\rm mod}$ is the modeled line ratio, $R_{\rm obs}$ is the observed line ratio with uncertainty $\Delta R_{\rm obs}$, and the summation is over all independent line ratios i at that position (one fewer than the number of lines available at that position).

For positions where 4 lines are detected, so 3 line ratios are available, the χ^2 is well-defined

and the models are well constrained. However, for positions where at least one observed line ratio is a lower limit, we calculate the χ^2 following one of two procedures. (1) For models with a line ratio larger than or equal to the observed lower limit, the χ^2 is taken as 1, thus ensuring that all models meeting this criterion are equally likely. (2) For models with a line ratio smaller than the observed lower limit, the χ^2 is calculated in the usual way, but the resultant reduced χ^2 value then indicates a lower limit only, leading to an upper limit on the likelihood (see below).

Contours and grey scales of reduced χ^2 (formally $\Delta\chi^2_{\rm r} \equiv \chi^2_{\rm r} - \chi^2_{\rm r,min}$, where $\chi^2_{\rm r,min}$ is the minimum reduced χ^2) in $T_{\rm K}$, $n({\rm H_2})$ and $N({\rm CO})$ space are shown in Figures 3.16 – 3.18. These illustrate the uncertainties of the best-fit model parameters and exhibit the usual degeneracies between physical parameters. The best-fit models ($\chi^2_{\rm r,min}$) are listed in Tables 3.4 and 3.5. For positions with a line ratio lower limit where a model meets the criterion for case (2) above, the contours and greyscales are instead shown in colour, indicating a $\Delta\chi^2_{\rm r}$ lower limit. If $\chi^2_{\rm r,min}$ lies in such a region of parameter space, the best-fit model is then ill defined.

We also estimate the likelihood of our models, calculating at each position the probability distribution function (PDF) of each model parameter marginalised over the other two. That is, for each possible value of a model parameter within our grid, we calculated the sum of the $e^{-\Delta\chi^2/2}$ terms for all possible values of the other two parameters. These PDFs are shown in Figures 3.19 – 3.21, along with their peaks (most likely values), medians and 68% (1σ) confidence levels around the median (the latter also listed in Tables 3.4 and 3.5). Again, for positions with a line ratio lower limit where a model meets the criterion for case (2) above, the likelihoods represent upper limits. If the peak of the PDFs is an upper limit, the most likely model is then ill defined.

3.4.5 General properties of the LVG model results

The best-fit model results generally agree well with those obtained from the likelihood analysis, in the sense that the three best-fit model parameters ($T_{\rm K}$, $n({\rm H_2})$ and $N({\rm CO})$) are

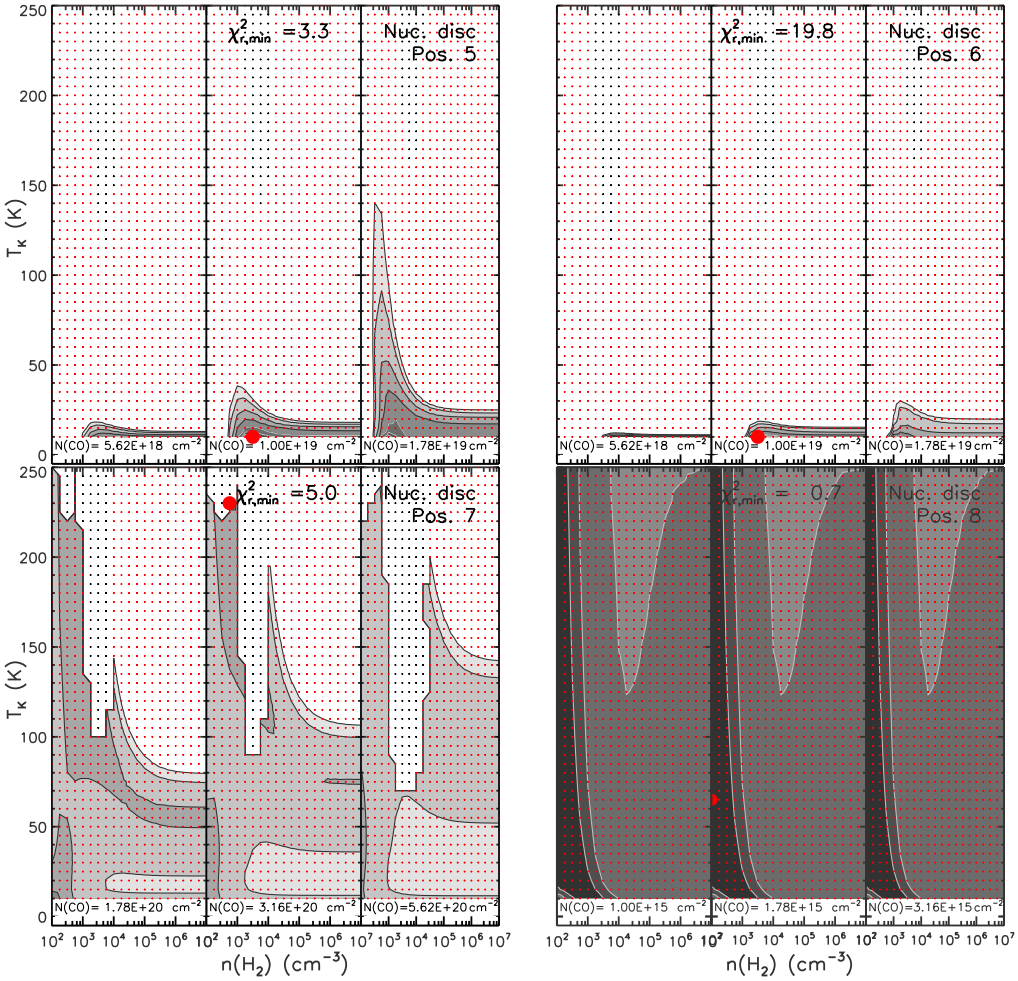

Figure 3.16: $\Delta\chi^2_{\rm r} \equiv \chi^2_{\rm r} - \chi^2_{\rm r,min}$ maps for the tenuous molecular gas in the nuclear disc of NGC 4710 (positions 5, 6, 7 and 8). For each region, $\Delta\chi^2_{\rm r}$ is shown as a function of $T_{\rm K}$ and $n({\rm H_2})$ for three values of $N({\rm CO})$ centred around the best-fit and indicated at the bottom of each panel. The models computed are indicated by red dots and the best-fit model with a red filled circle. Black dots represent bad models (e.g. unacceptably low opacity; see van der Tak et al. 2007b). The $\Delta\chi^2_{\rm r}$ contours show the 0.2σ (16% probability that the appropriate model is enclosed; darkest greyscale), 0.5σ (38%), and 1σ (68%) to 5σ (99.9%; lightest greyscale) confidence levels in steps of 1σ for 3 degrees of freedom (3 line ratios). The actual $\Delta\chi^2_{\rm r}$ levels from 0.2σ to 5σ are 0.8, 1.8, 3.5, 8.0, 14.2, 22.1 and 28.0, respectively. The confidence levels from 2σ to 5σ are separated by black lines, those from 0.2σ to 1σ by grey lines. The area containing models with $\leq 1\sigma$ confidence levels is much smaller than the best-fit model symbol at positions 5, 6 and 7. The $\chi^2_{\rm r,min}$ value, kinematic component and position along the galaxy disc are also indicated in each panel.

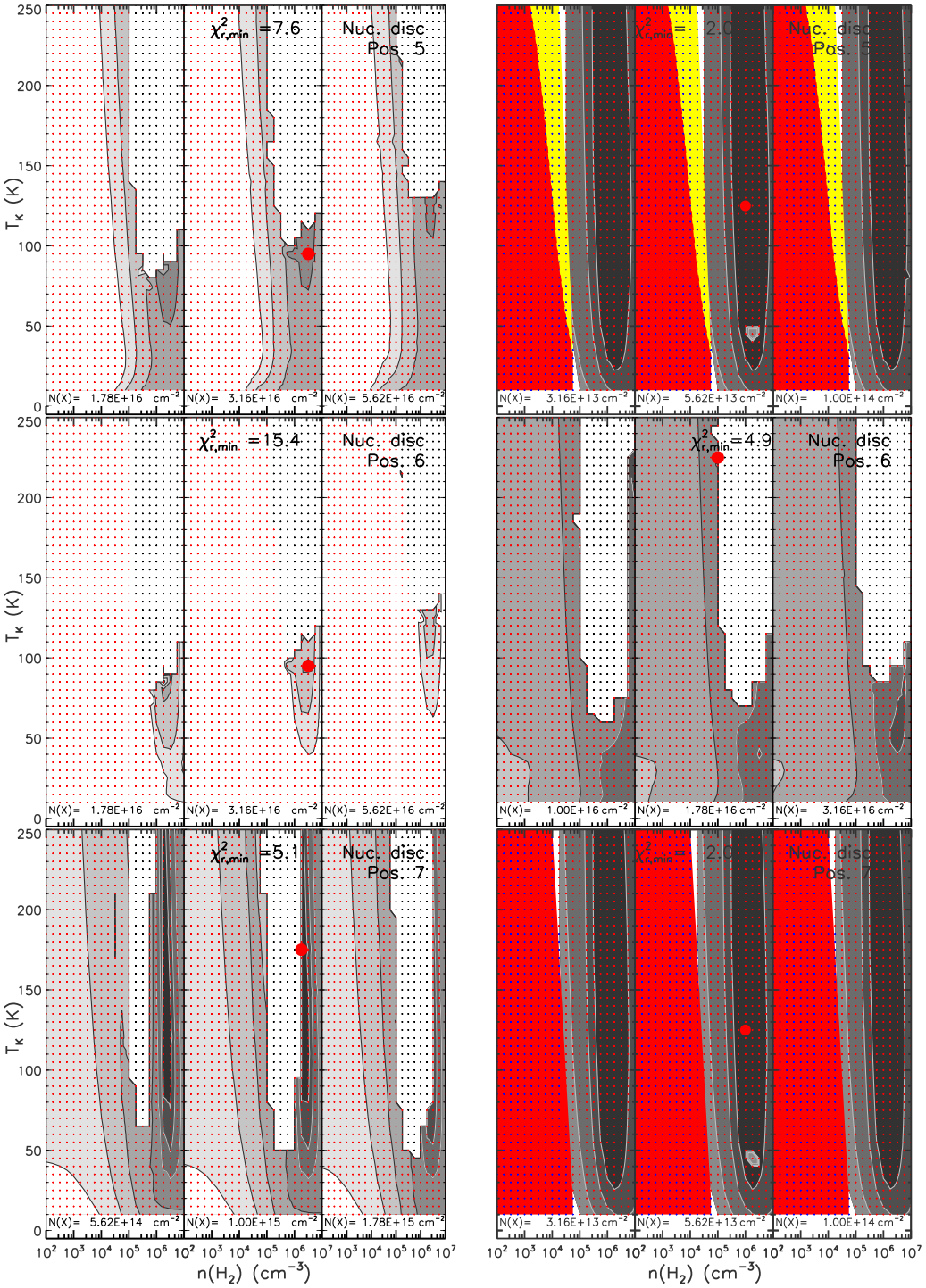

Figure 3.17: Same as Figure 3.16 but for the dense molecular gas in the nuclear disc of NGC 4710 (left) and NGC 5866 (right) (positions 5, 6 and 7). N(X) stands for the column number density of all four high density tracers. The area containing models with $\leq 1\sigma$ confidence levels is much smaller than the best-fit model symbol at positions 5 and 6 in NGC 4710 and at position 6 in NGC 5866. For positions with a line ratio lower limit, blue dots indicate models meeting the criterion for case (2) described in the text (Section 3.4.4). Associated $\Delta\chi^2_{\rm r}$ contours (confidence levels) are shown in colour: yellow (1σ), red (2σ), orange (3σ), green (4σ) and brown (5σ).

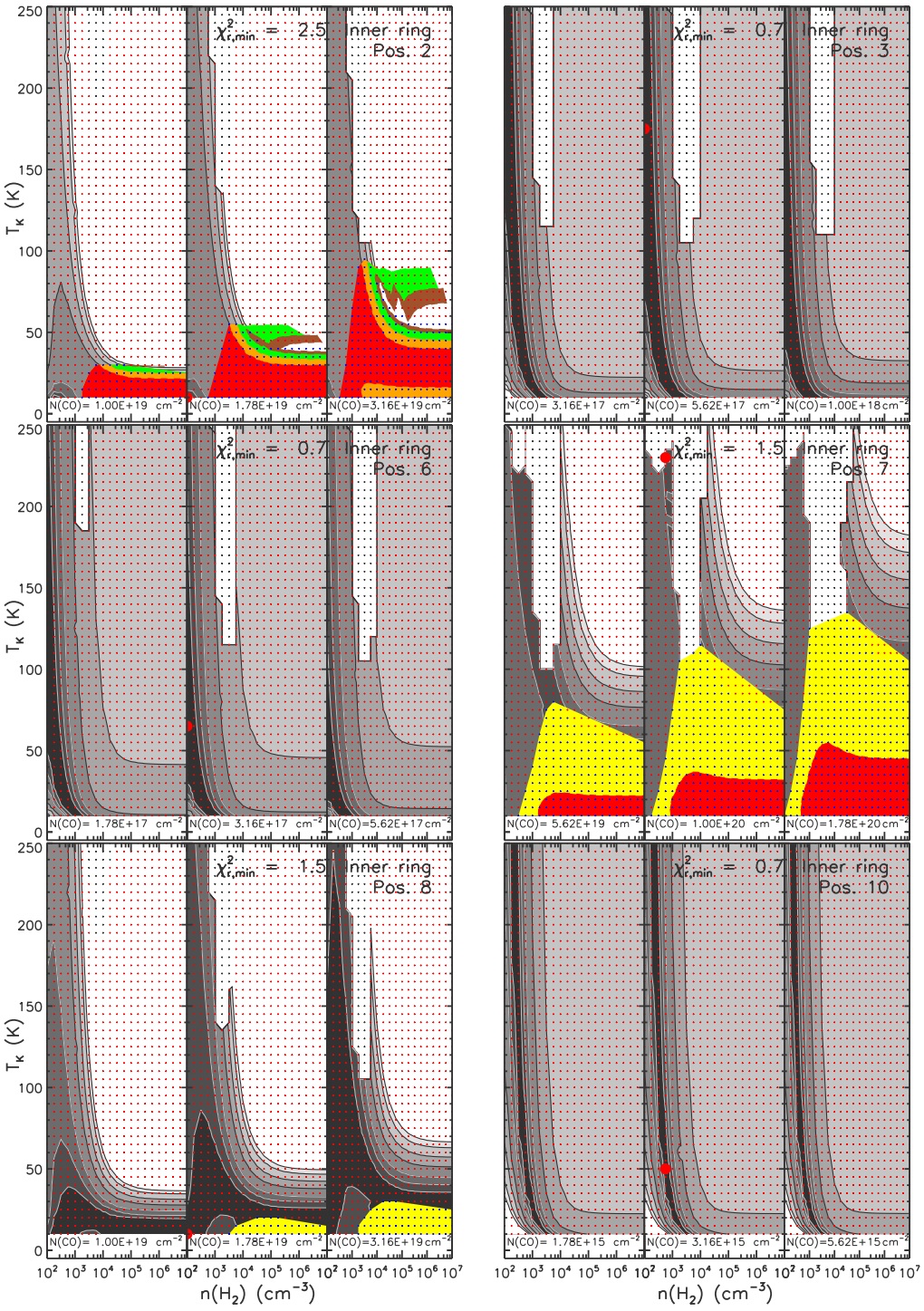

Figure 3.18: Same as Figures 3.16 and 3.17 but for the tenuous molecular gas in the inner ring of NGC 4710 (positions 2, 3, 6, 7, 8 and 10). The area containing models with $\leq 1\sigma$ confidence levels is much smaller than the best-fit model symbol at positions 2 and 7 in NGC 4710.

Table 3.4: Model results for the tenuous and dense molecular gas in the nuclear disc and inner ring of NGC 4710.

			Tenuous gas			Dense gas		
Component	Position	Offset ($''$)	Parameter	χ^2	Likelihood	Parameter	χ^2	Likelihood
(1)	(2)	(3)	(4)	(5)	(6)	(7)	(8)	(9)
nuclear disc	5	$-6.5''$	$T_{\rm K}$	10* K	25^{+119}_{-14} K	$T_{\rm K}$	95 K	135^{+73}_{-63} K
			$\log(n(\rm H_2))$	3.5 cm^{-3}	$3.3^{+1.9}_{-0.7}$ cm^{-3}	$\log(n(\rm H_2))$	6.5 cm^{-3}	$6.4^{+0.2}_{-0.2}$ cm^{-3}
			$\log(N(\rm CO))$	19.0 cm^{-2}	$19.6^{+0.6}_{-0.6}$ cm^{-2}	$\log(N(\rm X))$	16.5 cm^{-2}	$14.3^{+0.8}_{-0.9}$ cm^{-2}
	6	$0''$	$T_{\rm K}$	10* K	11^{+2}_{-1} K	$T_{\rm K}$	95 K	153^{+67}_{-58} K
			$\log(n(\rm H_2))$	3.7 cm^{-3}	$3.7^{+1.7}_{-1.0}$ cm^{-3}	$\log(n(\rm H_2))$	6.5 cm^{-3}	$6.4^{+0.2}_{-0.2}$ cm^{-3}
			$\log(N(\rm CO))$	19.0 cm^{-2}	$19.1^{+0.6}_{-0.2}$ cm^{-2}	$\log(N(\rm X))$	16.5 cm^{-2}	$14.3^{+0.7}_{-0.9}$ cm^{-2}
	7	$+6.5''$	$T_{\rm K}$	230 K	57^{+169}_{-45} K	$T_{\rm K}$	175 K	134^{+75}_{-70} K
			$\log(n(\rm H_2))$	2.7 cm^{-3}	$3.3^{+2.1}_{-0.6}$ cm^{-3}	$\log(n(\rm H_2))$	6.3 cm^{-3}	$6.4^{+0.3}_{-0.2}$ cm^{-3}
			$\log(N(\rm CO))$	20.5 cm^{-2}	$19.7^{+0.7}_{-0.7}$ cm^{-2}	$\log(N(\rm X))$	15.0 cm^{-2}	$14.4^{+1.1}_{-0.9}$ cm^{-2}
	8	$+13.0''$	$T_{\rm K}$	65 K	≤ 250 K			
			$\log(n(\rm H_2))$	2.0* cm^{-3}	≤ 7 cm^{-3}			
			$\log(N(\rm CO))$	15.3 cm^{-2}	≤ 21 cm^{-2}			
inner ring	2	$-26.0''$	$T_{\rm K}$	10* K	≤ 250 K			
			$\log(n(\rm H_2))$	2.0* cm^{-3}	≤ 7 cm^{-3}			
			$\log(N(\rm CO))$	19.3 cm^{-2}	≤ 21 cm^{-2}			
	3	$-19.5''$	$T_{\rm K}$	175 K	≤ 250 K			
			$\log(n(\rm H_2))$	2.0* cm^{-3}	≤ 7 cm^{-3}			
			$\log(N(\rm CO))$	17.8 cm^{-2}	17.8 cm^{-2}			
	6	$0''$	$T_{\rm K}$	65 K	≤ 250 K			
			$\log(n(\rm H_2))$	2.0* cm^{-3}	≤ 7 cm^{-3}			
			$\log(N(\rm CO))$	17.5 cm^{-2}	16.5 cm^{-2}			
	7	$+6.5''$	$T_{\rm K}$	230 K	≤ 250 K			
			$\log(n(\rm H_2))$	2.8 cm^{-3}	≤ 7 cm^{-3}			
			$\log(N(\rm CO))$	20.0 cm^{-2}	≤ 21 cm^{-2}			
	8	$+13.0''$	$T_{\rm K}$	10* K	≤ 250 K			
			$\log(n(\rm H_2))$	2.0* cm^{-3}	≤ 7 cm^{-3}			
			$\log(N(\rm CO))$	19.3 cm^{-2}	≤ 21 cm^{-2}			
	10	$+26.0''$	$T_{\rm K}$	50 K	≤ 250 K			
			$\log(n(\rm H_2))$	2.8 cm^{-3}	≤ 7 cm^{-3}			
			$\log(N(\rm CO))$	15.5 cm^{-2}	17.5 cm^{-2}			

Notes: Likelihood results list the median values and 68% (1σ) confidence levels. A star (*) indicates a physical parameter lying at the edge of the model grid.

Table 3.5: Model results for the dense gas in the nuclear disc of NGC 5866.

Position (1)	Offset (″) (2)	Parameter (3)	χ^2 (4)	Likelihood (5)
5	$-6.5''$	$T_{\rm K}$	125 K	≤ 250 K
		$\log(n(\rm H_2))$	6.0 cm^{-3}	≤ 7 cm^{-3}
		$\log(N(\rm X))$	13.8 cm^{-2}	≤ 21 cm^{-2}
6	$0''$	$T_{\rm K}$	225 K	102^{+103}_{-75} K
		$\log(n(\rm H_2))$	5.0 cm^{-3}	$6.6^{+0.3}_{-1.7}$ cm^{-3}
		$\log(N(\rm X))$	16.3 cm^{-2}	$16.3^{+1.7}_{-1.9}$ cm^{-2}
7	$6.5''$	$T_{\rm K}$	125 K	≤ 250 K
		$\log(n(\rm H_2))$	6.0 cm^{-3}	≤ 7 cm^{-3}
		$\log(N(\rm X))$	13.8 cm^{-2}	≤ 21 cm^{-2}

Notes: Likelihood results list the median values and 68% (1σ) confidence levels.

generally contained within the 68% (1σ) confidence level around the median of the PDF (or are just outside of it; see Figs. 3.19 – 3.21 and Tables 3.4 – 3.5). However, because of the flatness of the PDFs, the uncertainties in the most likely model results are rather large (particularly for $T_{\rm K}$). Significant differences are found between the tenuous and dense gas components for certain parameters ($n(\rm H_2)$ and $N(\rm CO)$), but perhaps unsurprisingly the different positions within a single kinematic component are generally statistically indistinguishable.

Looking at the results for NGC 4710 in more details, the $\rm H_2$ volume density $n(\rm H_2)$ is generally well constrained (with frequent single-peaked PDFs) for both the tenuous and dense molecular gas components, at least in the nuclear disc. Unsurprisingly, the model results indicate that $n(\rm H_2)$ is larger and $N(\rm CO)$ smaller in the dense gas component than in the tenuous gas component. The kinetic temperature $T_{\rm K}$ of the tenuous gas component in the nuclear disc always has a peak at 10 K (at the low-temperature edge of the model grid) in the PDFs, with a monotonic decreases at higher temperatures, causing the large uncertainties seen in the most likely model results. However, the most likely $T_{\rm K}$ model results in the inner ring are just upper limits (i.e. all models are equally likely). $T_{\rm K}$ for the dense gas component

(nuclear discs only) shows single-peaked PDFs with much higher temperatures, but again the uncertainties are large. Overall, while there seems to be a clear trend for the dense gas component to have a higher $T_{\rm K}$, higher $n(H_2)$ and smaller N(CO), the $T_{\rm K}$ trend is not significant given the uncertainties (see Table 3.4).

For NGC 5866, only the dense gas in the nuclear disc was modeled. At the central projected position (i.e. position 6), the model results indicate a similar dense gas volume density, column density and temperature as those in the nuclear disc of NGC 4710. And again, the uncertainties for $T_{\rm K}$ are proportionally higher than those for $n(H_2)$ and N(CO). However, as two positions in the nuclear disc of NGC 5866 have at least one line ratio that is a lower limit, the model results at those positions are just upper limits (and thus unconstrained; see Table 3.5).

In the nuclear discs, the line widths used for the modeling were 150 km s^{-1} for the CO lines of NGC 4710, 180 km $^{-1}$ for the dense gas lines of NGC 4710, and 300 km s^{-1} for the dense gas lines of NGC 5866. These line widths are similar to the values used for RADEX modeling of other external galaxies in the literature [e.g. Kamenetzky et al., 2012; Rangwala et al., 2011]. However, the observed line widths in the nuclear discs are combinations of the intrinsic widths of the lines and the range of rotational velocities contained within the synthesized beams. The latter effect could be dominant in the nuclear discs (while it is negligible in the inner rings), as the molecular gas rotation is increasing rapidly in those regions, but it is not related to the physical conditions in the molecular clouds. The true intrinsic widths of the lines in the nuclear discs should thus lie between the observed line widths in the inner rings (i.e. $\approx$ 50 km s^{-1}) and those observed in the nuclear discs. To test whether our modeling results are sensitive to the line widths adopted, we ran the nuclear disc models again using the line widths measured in the inner rings and the average line widths of the nuclear discs and inner rings. The best-fit model results are formally different in a few positions only (and generally only the CO column densities), and the results from the three different line widths tested always agree within the uncertainties. As expected [van der Tak

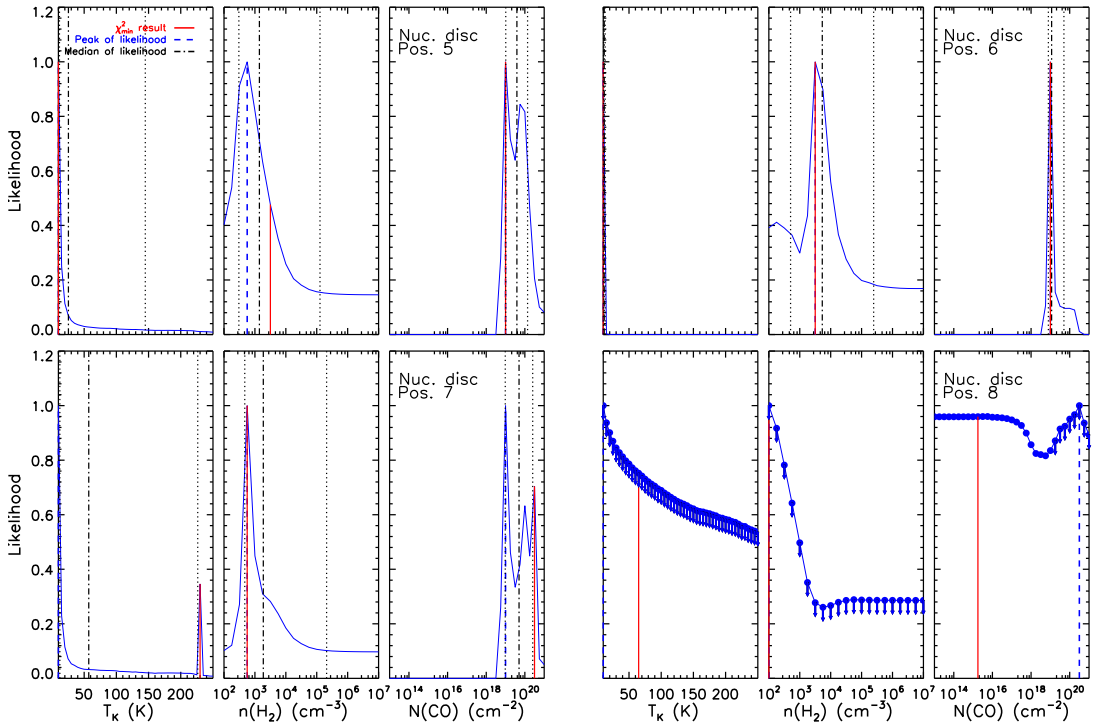

Figure 3.19: PDF of each model parameter marginalised over the other two, for the tenuous molecular gas in the nuclear disc of NGC 4710 (positions 5, 6, 7 and 8). In each PDF, the peak (most likely) and median value within the model grid are identified with a dashed blue and dashed-dotted black line, respectively. The 68% (1σ) confidence level around the median is indicated by dotted black lines. The best-fit model in a χ^2 sense is indicated by a solid red line. The PDFs for position 8 do not include the median value nor the 1σ confidence level, as at least one observed line ratio is a lower limit, resulting in PDF upper limits (blue dots with arrows).

et al., 2007b], the RADEX results are therefore only minimally affected by the line widths assumed, and possible beam smearing effects on the line widths adopted in the nuclear discs does not have a significant impact on our modeling results.

3.5 Results and Discussion

In the previous sections, we quantified the physical conditions of a two-component molecular ISM, i.e. tenuous and dense gas components, along the discs of the edge-on early-type

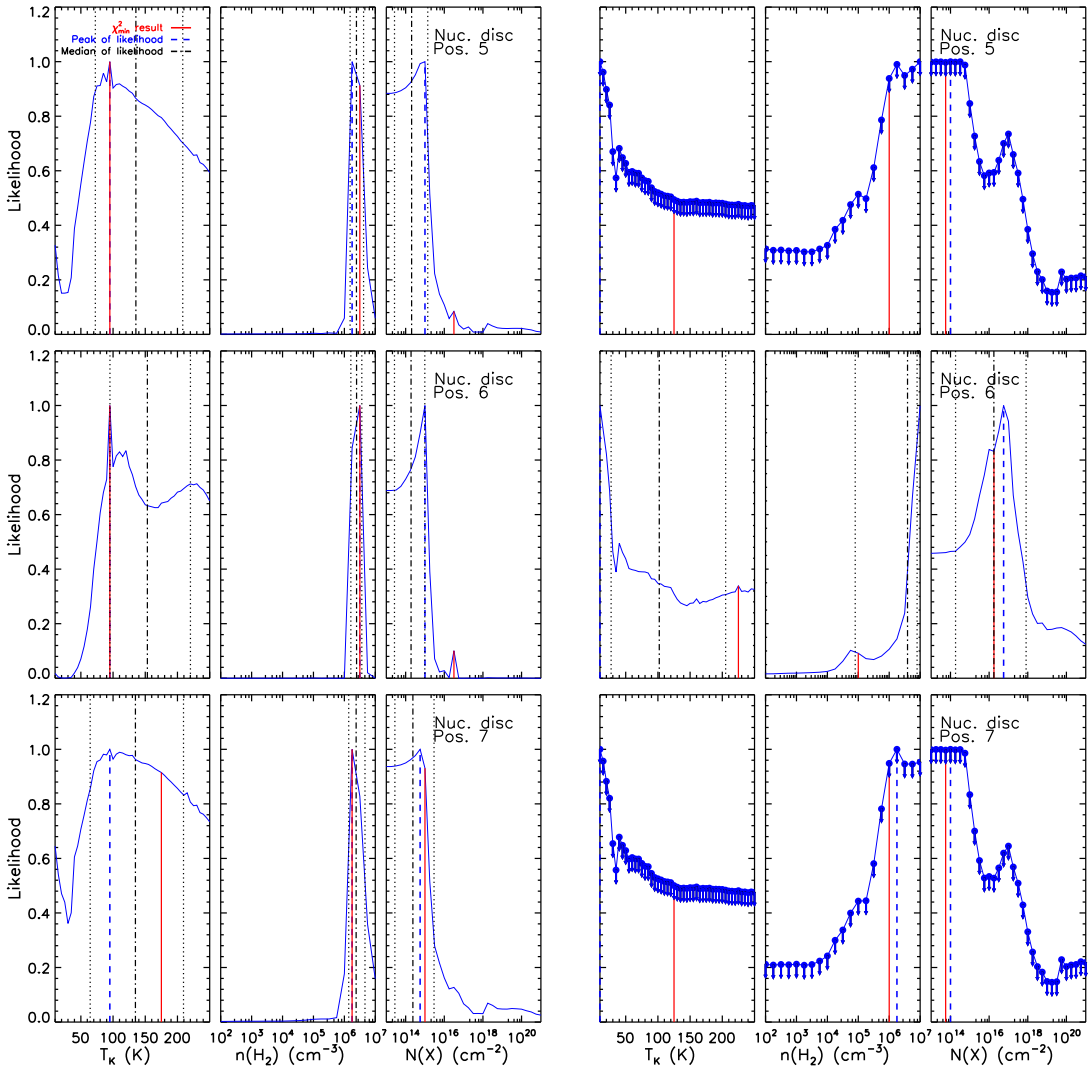

Figure 3.20: Same as Figure 3.19 but for the dense molecular gas in the nuclear disc of NGC 4710 (left) and NGC 5866 (right) (positions 5, 6 and 7). N(X) stands for the column number density of all four high density tracers. The PDFs for positions 5 and 7 in NGC 5866 do not include the median value nor the 1σ confidence level, as at least one observed line ratio is a lower limit, resulting in PDF upper limits (blue dots with arrows).

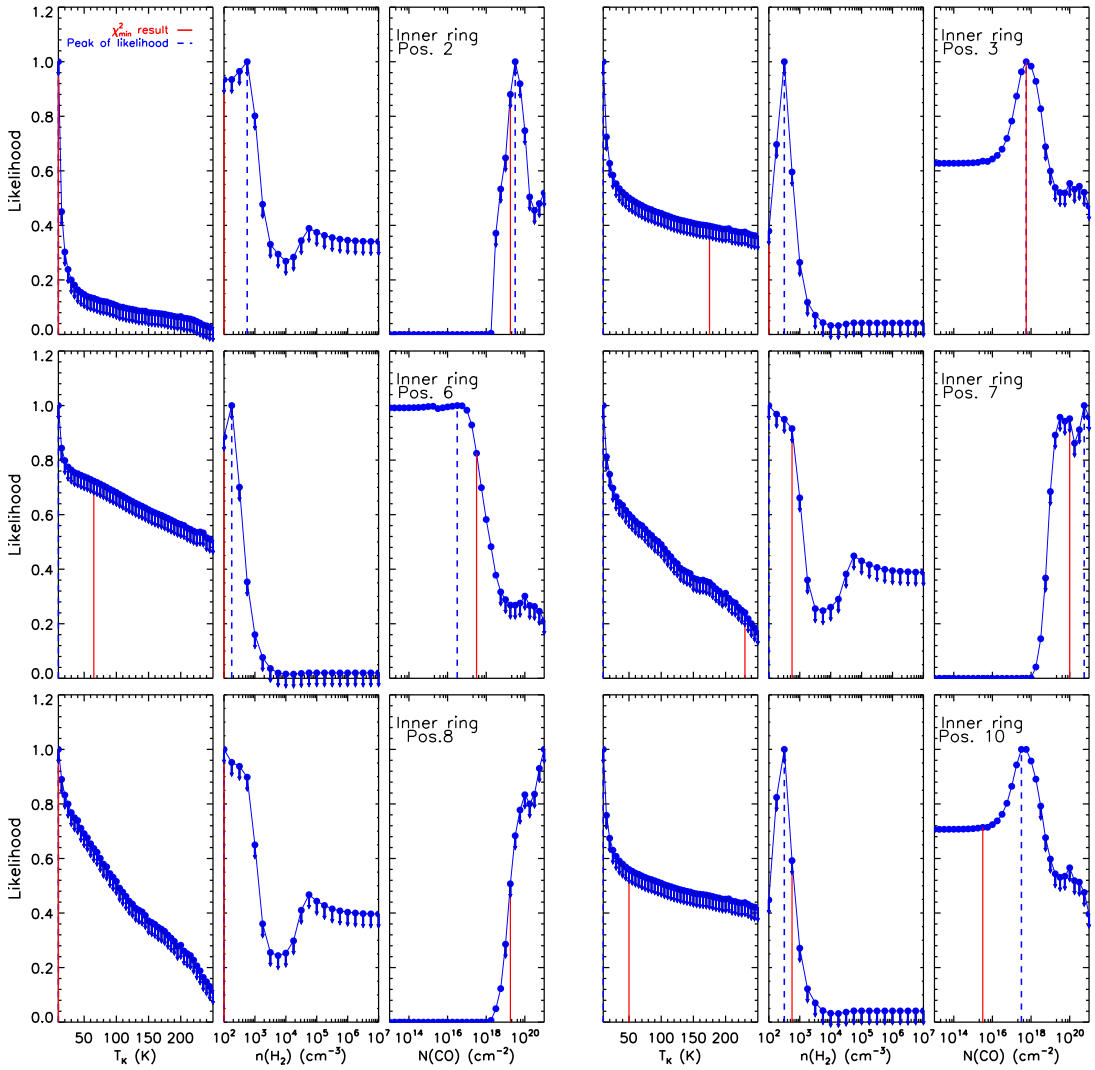

Figure 3.21: Same as Figures 3.19 and 3.20 but for the tenuous molecular gas in the inner ring of NGC 4710 (positions 2, 3, 6, 7, 8 and 10). No PDF includes the median value or the 1σ confidence level, as at least one observed line ratio is a lower limit at each position, resulting in PDF upper limits (blue dots with arrows).

galaxies NGC 4710 and NGC 5866. This was achieved by probing the variations of molecular line ratios as a function of projected radius along the galaxy discs, and by performing radiative transfer modeling of these multiple molecular gas tracers. Both galaxies are fast rotators and their ionised gas is kinematically-aligned with the stellar kinematics, indicating that the gas is likely supplied by internal processes (e.g. stellar mass loss; Davis et al. 2011a) or is left over from the galaxy formation event itself. NGC 4710 is a member of the Virgo Cluster and NGC 5866 is a member of a small group containing two spirals. However, since NGC 4710 is located in the outskirts of the cluster and the distance between NGC 5866 and its nearest companion is rather large, both galaxies are unlikely to have had recent significant interactions with other galaxies, interactions that could have affected their molecular gas content. Therefore, the physical conditions of the tenuous and dense gas components in NGC 4710 and NGC 5866 should not have been affected by galaxy interactions/mergers or other environmental effects [see, e.g., Alatalo et al., 2015].

Both galaxies are also edge-on and show X-shaped PVDs (i.e. two-component line-of-sight velocity distributions), indicating that the molecular gas is primarily confined within a nuclear disc and a distinct inner ring within the large-scale barred stellar disc of each galaxy (see Section 3.4.1). Infrared observations also support a nuclear disc surrounded by a ring-like structure in the disc of NGC 5866. Indeed, Xilouris et al. [2004] found that the 6.75 and 15 μm emission in NGC 5866 peaks in the centre and at $\approx$ 4 kpc on either side of it (see their Fig. 10). The barred nature of NGC 4710 is consistent with its box/peanut-shaped bulge, but that of NGC 5866 is more surprising given its classical bulge. Should the ring-like structure in NGC 5866 have a different origin, however, the barred nature of NGC 5866 would have to be revisited. Nevertheless, we discuss our empirical and model results in light of these facts in the following sub-sections.

3.5.1 Moment maps

As our interferometric maps show (see Fig. 3.1 and 3.2), the tenuous molecular gas extends to $\approx 30''$ on either side of the centre in both galaxies. The tenuous gas is brighter in the nuclear disc than in the inner ring of NGC 4710, but while this is also the case in NGC 5866, its inner ring is clearly more prominent (relative to the nuclear disc). As expected, the tenuous gas is more extended than the dense gas along the galaxy discs (at least given the roughly comparable noise levels in most cubes), the latter being generally centrally concentrated and restricted to the nuclear disc only (HCN (1–0) emission in the outskirts of NGC 5866 again suggests a more prominent inner ring). Already, the integrated molecular gas maps therefore suggest that different physical conditions are likely to prevail in the nuclear discs and inner rings.

In addition, the mean velocity maps reveal surprisingly complex behaviour beyond the nuclear disc in both galaxies, already hinting at multiple velocity components along the line of sight in these edge-on discs, a characteristic confirmed by the galaxies' PVDs (see Section 3.5.2 below).

3.5.2 PVDs

As discussed in Section 3.3.2, the PVDs of NGC 4710 and NGC 5866 show a characteristic X shape (see Figs 3.3 and 3.4). This is easily understood in the context of barred galaxy dynamics, whereby the central rapidly-rising PVD component is associated with a nuclear disc within the ILR, while the outer slowly-rising PVD component can be associated with an inner ring near corotation.

In both NGC 4710 and NGC 5866, it is obvious that both ^{12}CO and ^{13}CO (i.e. the tenuous gas) have similar distributions and kinematics, although as hinted from the moment 0 maps the inner ring in NGC 5866 is more prominent. In fact, separating the nuclear disc from the inner ring in the PVD, the integrated ^{12}CO (1–0) (and ^{13}CO (1–0)) flux of the inner ring in

NGC 5866 is larger than that of the nuclear disc (opposite in NGC 4710). There does not seem to be any molecular gas beyond the inner ring (i.e. beyond corotation) in either galaxy, where the rotation curve (i.e. the high-velocity envelope of the PVD) would be expected to be flat. The particularly strong emission at the edges of the inner rings (especially in NGC 4710) is simply due to edge brightening (as the rings are seen edge-on). However, other local emission maxima are observed along the nuclear discs and inner rings in the PVDs (see Figs 3.3 and 3.4), indicating that the molecular gas in both of these components is clumpy. The molecular gas peaks likely trace individual giant molecular cloud complexes, and they should be associated with regions of increased star formation.

The gap between the nuclear disc and inner ring in the PVDs is easily understood by a lack of gas on x_1 orbits, as they are swept free of gas by the shocks on the leading edge of the bar. However, the feature seen at the intermediate region in ^{12}CO (1–0) PVD (see Section 3.3.2 and Fig. 3.11) is not fully understood, but Athanassoula & Bureau [1999] speculated based on hydrodynamical simulations that this emission originates in secondary enhancements of gas in front of the leading edges of particularly strong (and sharp) bars.

Overall, it is clear that the molecular gas in the barred edge-on galaxies NGC 4710 and NGC 5866 is primarily concentrated in two distinct but clumpy kinematic components, a nuclear disc and an inner ring. As the dense gas tracers (HCN (1–0), HCO$^+$ (1–0), HNC (1–0) and HNCO (4–3)) are not detected outside the nuclear discs (except HCN (1–0) in NGC 5866), their PVDs do not show the characteristic X shape. It is thus natural to expect the ISM physical conditions to be similar within each kinematic component (with possibly small variations between clumps, especially if they are star-forming), but for the conditions to be different across the two components. The clumpy nature of the two kinematic components is confirmed by the observed line ratios, as local emission maxima in the PVDs (i.e. clumps) seem to correlate with local variations in the line ratios (particularly the ratios of CO to dense gas tracer lines; see Figs. 3.13 – 3.15).

Lastly, we note that unlike the behaviour of the other lines in both galaxies, there is

almost no dense gas detected at the very centre of the PVDs in NGC 5866. The same effect, if present at all, is much weaker in NGC 4710 (see Figs. 3.3 and 3.4). This suggests that a different excitation mechanism (or possibly gas distribution) dominates in the very centre of NGC 5866 (e.g. active galactic nucleus or nuclear starburst activity), unless the local emission minimum is in fact due to absorption against a nuclear continuum source. The latter possibility however seems unlikely, since while there is a continuum source in NGC 5866 (see Section 3.3.4), no absorption is seen in the spectra.

3.5.3 Integrated spectra

Except for HNC (1–0) and HNCO (4–3) (shown here for the first time), all the molecular lines discussed were previously observed with the IRAM 30m telescope (see Young et al. 2011 and Crocker et al. 2012). As illustrated in the moment maps (Figs. 3.1 and 3.2), where we overlaid the corresponding IRAM 30m beam sizes, the CO extent (at all transitions) is covered entirely only by the interferometric observations (with larger primary beams). The single-dish beams systematically cover the nuclear discs only, thus missing out much of the tenuous molecular gas (this is not a problem for the dense gas tracers, that are not detected in the inner rings).

In Figures 3.5 and 3.6, the integrated CARMA and PdBI spectra, simulated (i.e. integrated with a spatial Gaussian weighting) IRAM 30m spectra, and observed IRAM 30m spectra are overlaid with each other (see Section 3.3.3). As expected given the comments above, the integrated interferometric CO (i.e. tenuous molecular gas) fluxes are systematically larger than the single-dish fluxes (simulated and observed). However, again as expected given their spatially compact emission (nuclear discs only), the integrated and single-dish dense gas tracer spectra are consistent with each other. Slight differences are probably due to flux calibration uncertainties and possible single-dish pointing errors. Differences in the shapes of the spectra from line to line can further indicate different gas physical conditions along the discs of the galaxies (and thus a slightly different spatial distribution for each

tracer). Interestingly, only the dense gas tracers of NGC 5866 show clearl double-peaked integrated line profiles (and to a lesser extent ^{12}CO (1–0); see Figs. 3.5 and 3.6).

The only discordant note in relation to the integrated spectra is the fact that the simulated IRAM 30m spectra of the tenuous molecular gas in NGC 4710 are significantly brighter than the true IRAM 30m spectra (see the top three panels of Fig. 3.5). We double-checked the data reduction and analysis and did not find any problem. The relatively large offset between the simulated and observed spectra is thus most likely due to a combination of single-dish pointing errors (possibly supported by the slight asymmetry of the true IRAM 30m spectra, not present in the CARMA data) and flux calibration uncertainties (20% is standard for millimetric observations flux-calibrated using planetary models; see e.g. Alatalo et al. 2013).

3.5.4 Molecular line ratios

The ratios of the PVDs from different lines are shown in Figures 3.8 – 3.10, while Figures 3.13 – 3.15 show the ratios of the integrated line intensities as a function of projected radius for each kinematic component separately (nuclear disc and inner ring; the values are listed in Tables A.1, B.1 and B.2). Similarly, the LVG modeling results for the tenuous and dense molecular gas components, in the nuclear discs and inner rings, are listed in Tables 3.4 and 3.5.

We recall here that for rings, the different projected positions simply correspond to different azimuthal positions (i.e. angles) within the rings, so we do not expect significant gradients with projected position. The nuclear disc, as its name suggests, may well however be filled in.

3.5.4.1 ^{12}CO (1–0) / ^{12}CO (2–1) ratio and tenous gas temperature

In NGC 4710, the ratio of the PVDs of the ^{12}CO (1–0) and ^{12}CO (2–1) lines shows that the ratio is greater than unity everywhere, but is slightly smaller in the nuclear disc than the inner ring (see Fig. 3.8), suggesting a higher temperature in the tenuous molecular gas of the

nuclear disc. This is confirmed by the ratio of the integrated line intensities along the two kinematic components (see Fig. 3.13), clearly showing that $I_{12} \equiv {}^{12}\mathrm{CO}\,(1\text{–}0)/{}^{12}\mathrm{CO}\,(2\text{–}1)$ at the central three projected positions along the nuclear disc (i.e. projected positions 5, 6 and 7) is smaller than that at the same positions in the inner ring. This trend appears marginal at the edges of the nuclear disc (projected positions 4 and 8), but this is simply due to the very weak emission (and associated large uncertainties) there.

Ideally, the temperature difference between the tenuous gas in the nuclear disc and inner ring of NGC 4710 would be confirmed by our LVG modeling, but the results are inconclusive. This is perhaps unsurprising, as we have only two CO transitions ($J = 1 \rightarrow 0,\ 2 \rightarrow 1$) to constrain the temperature, but it is nevertheless disappointing. Within each kinematic component, the best-fit temperatures of the tenuous gas cover nearly the entire range allowed by the models. This is probably because the $\Delta\chi^2_\mathrm{r}$ contours at each position are often shallow and extended (see Figs. 3.16 and 3.18), so that the best-fit model results should be taken with a grain of salt. Due to the large uncertainties in the most likely model results (see Table 3.4), the apparent kinetic temperature differences between the tenuous and dense molecular gas in the nuclear disc are not statistically significant (and no useful constraint can be derived for the inner ring, due to some line ratio lower limits).

Although ^{12}CO (2–1) and its isotopologue were not observed interferometrically in NGC 5866, single-dish observations of these lines in the central regions of NGC 5866 show that I_{12} is larger there than in the central regions of NGC 4710 [Crocker et al., 2012]. This suggests that the CO gas at the centre of NGC 5866 is colder than that in NGC 4710. However, since the single-dish observations cannot disentangle the emission from the nuclear disc and inner ring, this should be verified with interferometric data.

3.5.4.2 ^{12}CO / ^{13}CO ratio and tenuous gas opacity

As shown in Figure 3.8, the ratio of ^{12}CO to its isotopologue ^{13}CO is larger in the central regions of the nuclear disc of NGC 4710 than in all other regions (external parts of the nuclear

disc and the few positions in the inner ring where a measurement is possible). This is true of both the $1 \rightarrow 0$ and $2 \rightarrow 1$ transitions. If confirmed, this behaviour would indicate optically thinner tenuous molecular gas in the central regions of the nuclear disc (assuming that all of the ^{13}CO is optically thin but only some of the ^{12}CO). However, the emission in the central regions includes contributions from the inner rings as well (in projection).

Looking at the ratios of the integrated line intensities of CO and its isotopologue ($I_{11} \equiv$ ^{12}CO (1–0)/^{13}CO (1–0) and $I_{22} \equiv$ ^{12}CO (2–1)/^{13}CO (2–1)) as a function of projected radius (Fig. 3.13), the above behaviour seems confirmed. Indeed, the I_{11} and I_{22} ratios at positions 5, 6 and 7 of the nuclear disc of NGC 4710 (the central three projected positions) are slightly larger than those at the same projected positions in the inner ring. We note however that the I_{22} ratios in the inner ring of NGC 4710 are all lower limits (the same applies to some positions for I_{11}). Similarly, since as before the fluxes are much smaller there than in the three central positions, the I_{11} and I_{22} ratios at positions 4 and 8 of the nuclear disc are also lower limits.

Interestingly, the I_{11} ratio of the inner ring of NGC 4710 shows a significant maximum at projected position 4, that clearly corresponds to a clump (see Fig. 3.11), while the I_{11} minimum at position 5 has no obvious clump associated with it.

While a χ^2 (and thus likelihood) analysis of the opacity is not possible, since it is not a model parameter, each model computed does return the optical depths of the associated lines. The optical depths of the ^{12}CO (1–0) and ^{12}CO (2–1) lines for the best-fit models are thus known. In addition, one would expect the CO column number density to correlate with its optical depth. Looking at the model results (Table 3.4), the ^{12}CO (1–0) optical depth, ^{12}CO (2–1) optical depth, and CO column number density in the nuclear disc are generally slightly larger than those in the inner ring, contrary to our expectations based on the empirical ^{12}CO/^{13}CO ratios. However, as the best-fit models are not representative of the $\Delta\chi^2_{\rm r}$ geometry and most lie at the edge of the model grid, the associated opacities and column number densities are questionable.

Unlike NGC 4710, the ^{12}CO (1–0)/^{13}CO (1–0) ratio in NGC 5866 appears smaller in the central regions (compared with all other regions in the ratio PVD; see Fig. 3.10). However, the effect is weak and seems to be associated with a generally slightly smaller ratio in the inner ring compared to the nuclear disc (if more marked in the central regions). Looking at the ratio of the integrated line intensities (I_{11} only), the I_{11} ratios of the nuclear disc and inner ring are consistent in the central regions, although the ratios do increase at larger projected radii in the inner ring. The effect is marginal at best however, as all I_{11} ratios measured are consistent within the uncertainties.

Crocker et al. [2012] also measured the I_{11} and I_{22} ratios in the central regions of both galaxies (without disentangling the two kinematic components). While our average values along the nuclear disc and the inner ring of NGC 4710 agree with the ratios reported by Crocker et al. [2012] (within the uncertainties), our average I_{11} ratio for both the nuclear disc and the inner ring of NGC 5866 is larger than that found by Crocker et al. [2012].

As hinted above, as ^{13}CO is less abundant then its parent molecule ^{12}CO and is generally considered optically thin, ^{12}CO/^{13}CO variations largely reflect variations in the ^{12}CO optical depth. The larger the ratio, the thinner the ^{12}CO gas (and vice-versa). The general behaviour in NGC 4710 and NGC 5866 (but more prominent in NGC 4710) is thus that the CO gas is optically thinner in the nuclear disc than in the inner ring, although the trend is weak and may be restricted to the inner parts of the nuclear disc in NGC 5866. Variations within each kinematic component (e.g. local maximum in the inner ring of NGC 4710 and projected radius trend in NGC 5866) likely indicate azimuthal variations of the physical conditions (i.e. clumpiness) within them.

High I_{11} and I_{22} ratios tracing diffuse gas are probably the result of stellar feedback, and therefore indicate more active current and/or recent star formation. Radial I_{11} gradients are indeed seen in spirals [Paglione et al., 2001], and the ratio can have local maxima in star-forming regions along spiral arms [Tan et al., 2011]. This thus suggests that star formation is more intense in the nuclear discs of our galaxies then their inner rings (at least in NGC 4710), a

behaviour entirely consistent with the general behaviour of barred disc galaxies, particularly early-type spirals [e.g. Kormendy & Kennicutt, 2004]. This also agrees with the higher temperatures inferred for the molecular gas in the nuclear discs (compared to that in the inner rings) in the previous sub-section (Section 3.5.4.1). Higher S/N ^{13}CO observations would however help to strengthen this result.

On a different note, the average I_{11} ratios in the nuclear disc and inner ring of NGC 5866 ($\approx 9-10$) are larger than those in NGC 4710 ($\approx 7-8$, excluding lower limits), suggesting that the CO gas is thinner and the star formation activity more intense in NGC 5866 than NGC 4710 (or that it has a different intrinsic [^{12}C] / [^{13}C] abundance ratio).

3.5.4.3 HCN / HCO$^+$, HCN / HNC and HCN / HNCO ratios and dense gas excitation

The ratios of the PVDs of the dense gas tracers only are shown in Figures 3.8 and 3.10 for NGC 4710 and NGC 5866, respectively (where grey scales represent lower limits, where HCN was detected but not the other lines). The ratios of the integrated line intensity ratios, namely $I_{\rm D1} \equiv$HCN (1–0)/HCO$^+$ (1–0), $I_{\rm D2} \equiv$HCN (1–0)/HNC (1–0) and $I_{\rm D3} \equiv$HCN (1–0)/HNCO (4–3) are shown as a function of projected radius in Figures 3.13 and 3.15. Generally, the dense gas tracers are detected only in the nuclear discs (typically projected positions 5, 6 and 7). The only exception to this is the detection of HCN (1–0) in the inner ring of NGC 5866 (with significant detections at projected positions 4, 8 and 9).

The $I_{\rm D1}$, $I_{\rm D2}$ and $I_{\rm D3}$ ratios are larger than 1 at all projected positions, and they do not show any evidence of a gradient with projected position (and thus azimuthal angle). $I_{\rm D1} < I_{\rm D2} < I_{\rm D3}$, indicating that HCN (1–0) is the brightest line among the dense gas tracers, followed by respectively HCO$^+$ (1–0), HNC (1–0) and HNCO (4–3). Crocker et al. [2012] also detected HCN (1–0) and HCO$^+$ (1–0) in the central regions of both galaxies, finding $I_{\rm D1} \approx 1.5$, consistent with the values found here for the nuclear discs.

UV radiation from young massive (O and B) stars, X-rays from active galactic nuclei

(AGN) and CRs from supernova explosions all have distinct characteristic effects on the molecular gas physical conditions, and each plays an important role in the dissociation and ionisation of molecules, thus changing the chemistry of the ISM and affecting the molecular line ratios observed. UV radiation primarily affects the outermost layers of clouds (photon dissociation regions or PDRs; e.g. Blake et al. 1987; Tielens & Hollenbach 1985a,b), while X-rays penetrate deeper and form X-ray dissociation regions (XDRs; Lepp & Dalgarno e.g. 1996; Maloney et al. e.g. 1996). Both UV and X-ray radiation can enhance HCN, but since X-rays can affect the gas chemistry much deeper into clouds, they can do so more efficiently [e.g. Krips et al., 2008].

The theoretical results of Meijerink et al. [2007b] suggest that if the volume density exceeds a value 10^5 cm^{-3}, then $I_{\rm D1} > 1$ in PDRs, while $I_{\rm D1} < 1$ in XDRs. Our LVG modelling results for a two-component molecular ISM indicate that for the dense gas component $n(\rm H_2)\geq$ 10^5 cm^{-3} for both galaxies (see Tables 3.4 and 3.5). Combined with the fact that $I_{\rm D1} > 1$ everywhere in both galaxies, this therefore indicates that PDRs are most likely dictating the physical conditions (and thus the observed line ratios) of the molecular ISM in the nuclear discs of both galaxies. Reassuringly, those densities are also much larger than those obtained for the tenuous molecular gas component (typically by 3 orders of magnitude).

Our results are also consistent with the absence of any substantial AGN activity (and thus X-rays) in NGC 4710 and NGC 5866. However, since $I_{\rm D1} > 1$, supernova explosions are also unlikely to be significant, and young massive OB stars are likely responsible for the HCN enhancement. If supernova explosions were a dominant force in the ISM, $\rm HCO^+$ would have been enhanced by CRs (with respect to HCN), leading to $I_{\rm D1} < 1$ as seen in starbursts, although not all starbursts and spiral galaxies have $I_{\rm D1} < 1$ (see Section 3.5.5). Overall, the high $I_{\rm D1}$ ratio observed thus suggests a low-CR PDR-dominant environment in the nuclear disc of both galaxies, but there could be some impact from supernova explosions as seen in starbursts/spirals that have similar $I_{\rm D1}$ ratios.

We note briefly that, assuming the $I_{\rm D1}$, $I_{\rm D2}$ and $I_{\rm D3}$ upper limits in the inner ring of

NGC 5866 are not too far off the mark, these ratios are then larger in the nuclear disc than in the inner ring, indicating different dissociation and ionisation mechanisms in the two kinematic components. The HCN would need to be suppressed or HCO^+, HNC and HNCO enhanced in the inner ring. More sensitive observations of HCN, HCO^+, HNC and HNCO in the inner ring of both galaxies are however necessary to clearly contrast the physical conditions of their dense molecular ISM.

3.5.4.4 Ratios of CO to HCN, HCO^+, HNC and HNCO and dense gas fraction

The ratios of CO PVDs to high density tracer PVDs (hereafter I_{CD}) are shown in Figures 3.9 and 3.10 (where greyscales represent lower limits, where CO was detected but not the high density lines), while the ratios of the integrated line intensities as a function of projected radius are shown in Figures 3.14 and 3.15 (see also Tables B.1 and B.2).

As seen from all those figures, there is a clear difference of the CO to high density tracer ratios between the nuclear disc and inner ring, for both NGC 4710 and NGC 5866. Indeed, the I_{CD} ratios are significantly larger in the inner rings, and the true differences are likely to be even greater than that hinted by Figures 3.9, 3.10, 3.14 and 3.15 as the I_{CD} ratios in the inner rings are all lower limits (except for a few positions in HCN in NGC 5866). This contrast is incontrovertible for the HCN, HCO^+ and HNC lines, but may well also hold true for HNCO (where some inner ring lower limits are smaller than the corresponding nuclear disc ratios). As the I_{CD} ratios essentially trace the fraction of dense molecular gas (see below), these results strongly suggest that the fraction of dense gas is larger in the nuclear discs of the galaxies than in their inner rings. This is consistent with dense gas being generally centrally-concentrated in galaxies, and with the more intense star formation activity (with hotter and optically thinner CO gas) inferred in the previous sub-sections (Section 3.5.4.1 – 3.5.4.3) for NGC 4710 and NGC 5866 specifically.

The average ^{12}CO (1–0)/HCN (1–0), ^{12}CO (1–0)/HCO^+ (1–0), ^{13}CO (1–0)/HCN (1–0) and ^{13}CO (1–0)/HCO^+ (1–0) ratios along the nuclear disc of NGC 4710 are consistent with those

found by Crocker et al. [2012] for the central regions of the galaxy, while the average ^{12}CO (2–1)/HCN (1–0), ^{12}CO (2–1)/HCO$^+$ (1–0), ^{13}CO (2–1)/HCO$^+$ (1–0) and ^{13}CO (2–1)/HCO$^+$ (1–0) ratios in the nuclear disc are slightly smaller. Similarly, the average ^{12}CO (1–0)/HCN (1–0), ^{12}CO (1–0)/HCO$^+$ (1–0) and ^{13}CO (1–0)/HCO$^+$ (1–0) ratios along the nuclear disc of NGC 5866 are consistent with those found by Crocker et al. [2012], but the average ^{13}CO (1–0)/HCN (1–0) ratio in the nuclear disc is slightly smaller.

It is generally agreed that CO (1–0) traces the total molecular gas content of galaxies, due to its low critical density ($n_{\rm crit} \approx 10^3$ cm^{-3}). Some of the gas traced by CO (1–0) may therefore not be involved in star formation [Scoville, 2012]. However, transitions of more complex molecules such as HCN (1–0), HCO$^+$ (1–0), HNC (1–0) and HNCO (4–3) have higher critical densities (up to $n_{\rm crit} \approx 10^6$ cm^{-3}) because of their larger dipole moments. These molecules are therefore generally taken as tracers of high-density molecular gas, more closely related to star-forming regions than CO itself [e.g. Gao & Solomon, 2004b; Scoville, 2012]. As hinted above, the ratios of CO to these dense gas tracers therefore trace the dense gas fraction of the ISM (larger for smaller ratios), underlying our statement that the nuclear discs have a larger fraction of dense gas than the inner rings.

Nevertheless, another possible reason specifically for the low CO/HCO$^+$ ratios observed in the nuclear discs is an enhancement of HCO$^+$ via supernova explosions (as the CRs generated can ionize H_2, producing H_3^+ that reacts with CO to form HCO$^+$). However, as discussed in the previous sub-section (Section 3.5.4.3), the CRs ionisation rates are not likely to be as high as what is normally inferred in starbursts (enhancing HCO$^+$ with respect to HCN and other molecules), so the role of CRs in the ISM ionisation and gas chemistry is probably limited.

In parallel to the discussion in the previous sub-section (Section 3.5.4.3), the low ^{12}CO (1–0)/HCN (1–0) ratios observed in the nuclear discs can further be driven by the chemical enhancement of HCN via UV radiation from young stars. Meijerink et al. [2007b] claims that at high densities ($n_{\rm crit} > 10^5$ cm^{-3}), PDRs produce lower CO (1–0)/HCN (1–0) ratios

than XDRs, similar to the low ratios found in the nuclear disc of both galaxies. This thus suggests again that PDRs with relatively few CRs but strong UV radiation are the most likely mechanism to explain the low $I_{\rm CD}$ ratios (and $I_{\rm D1}$, $I_{\rm D2}$ and $I_{\rm D3}$ ratios greater than unity) observed in the nuclear disc of both galaxies.

In the Milky Way, M31 and some other spirals, the ^{12}CO/HCN ratio increases with radius [Brouillet et al., 2005; Gao & Solomon, 2004b; Helfer & Blitz, 1997], in turn indicating a decrease of the dense gas fraction with radius. Our results in NGC 4710 and NGC 5866 are similar, as the $I_{\rm CD}$ ratios in their inner rings (with radii of ≈ 2.6 and ≈ 2.4 kpc, respectively) are larger than those in the nuclear discs (with radii of ≈ 1 and ≈ 0.6 kpc). Given the geometries we have argued for, however, we are only sampling possible dense gas fraction gradients at two discrete locations in the galaxies (nuclear disc and inner ring radii).

Helfer & Blitz [1997] also argued that the CO/HCN ratio is directly related to the hydrostatic pressure, the ratio decreasing as the pressure increases. The results in this work thus suggest that the ambient pressure is higher in the nuclear discs than in the inner rings. This is as expected for the central regions of galaxies, as the nuclear discs of NGC 4710 and NGC 5866 are located well within their bulges, and is consistent with the idea that higher pressures lead to larger dense gas fractions. In fact, the ^{12}CO (1–0)/HCN and ^{12}CO (1–0)/HCO$^+$ ratios of the nuclear discs of both galaxies are similar (similarly for ^{13}CO (1–0)), indicating that the dense gas fraction and/or the ionisation mechanisms of the gas in the nuclear discs of both galaxies are similar.

Finally, we note that if the low $I_{\rm CD}$ ratios observed in the nuclear discs of both galaxies were the result of chemical enhancement of HCN via X-rays from an AGN, then that could also explain the smaller CO/HCN ratios observed in the nuclear discs compared with the inner rings. However, as we mentioned previously, there is no significant AGN activity in NGC 4710 and NGC 5866. It is therefore more likely that the other mechanisms highlighted above are dominant.

Unfortunately, as the tenuous (CO) and dense (HCN, HCO$^+$, HNC and HNCO) gas

tracers have been separately considered for our LVG modeling, it does not inform on the dense gas fraction.

3.5.4.5 All ratios and gas physical conditions

Overall, considering the empirical line ratios, our results seem to suggest that while the nuclear discs and inner rings of NGC 4710 and NGC 5866 have similar molecular gas physical conditions, the nuclear discs have a slightly larger dense gas fraction with a hot and optically thinner molecular gas than their inner rings. Physically, this in turn suggests that compared to the inner rings, the nuclear discs have a more inhomogeneous ISM, with more dense clumps bathed in a more diffuse molecular medium. Conversely, the inner rings have a more homogeneous ISM, with fewer clumps immersed in optically thicker molecular gas. This may indicate a dominant PDR-like environment with few CRs but intense UV radiation in the nuclear discs. However, we must caution that the large uncertainties associated with the most likely model results indicate that those differences between the nuclear discs and inner rings are not always statistically significant.

3.5.5 Line ratios and galaxy morphology

In Figure 3.22, we compare the ratios of the integrated line intensities obtained along the equatorial plane of NGC 4710 and NGC 5866 with those obtained in the central regions of a variety of galaxies (ellipticals, lenticulars, spirals, starbursts, Seyferts and peculiars) as well as spatially-resolved spiral galaxy GMCs. The figure caption describes all the symbols and overlaid lines in detail.

In Figure 3.22*a*, the I_{12} ratio is shown as a function of ^{12}CO (1–0)/HCN (1–0) for the nuclear disc and inner ring of NGC 4710 only, as ^{12}CO (2–1) was not observed in NGC 5866. However, the single-dish data for the centre of NGC 5866 and NGC 4710 are also shown for comparison. While the range of ^{12}CO (1–0)/HCN (1–0) ratios in lenticulars and particularly starbursts is larger than that in NGC 4710, the striking feature of this figure is that the I_{12}

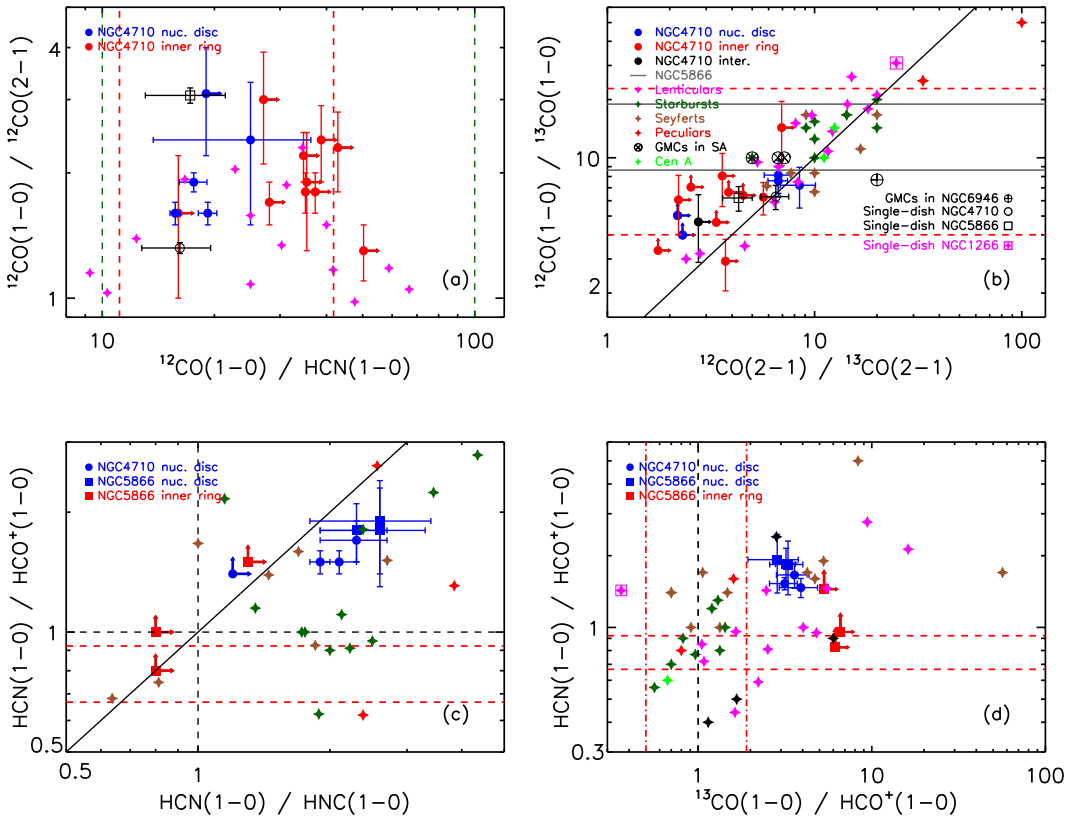

Figure 3.22: Molecular line ratio diagrams for NGC 4710, NGC 5866 and a variety of other galaxies. Our data for NGC 4710 and NGC 5966 are shown as filled circles and squares, respectively, while our data for the nuclear discs and inner rings are shown in blue and red, respectively (black for the intermediate region). Upper and lower limits are represented by arrows. Other lenticular galaxies are indicated by magenta filled stars [Crocker et al., 2012; Krips et al., 2010], starburst nuclei by dark green filled stars, Seyferts by brown filled stars, peculiar galaxies by red filled stars, Centaurus A by pale green filled stars (see Baan et al. 2008; Table 3 in Krips et al. 2010 and references therein), spiral arm GMCs by black circles with an X, NGC 6946 (starburst) GMCs by black circles with a cross [Topal et al., 2014], and M31 GMCs by orange circles with an X [Brouillet et al., 2005]. The data for NGC 1266 (a lenticular galaxy with a molecular outflow) are shown by magenta squares with a filled star [Alatalo et al., 2011]. The dark green dashed lines in panel *a* indicate the typical range of HCN (1–0)/^{12}CO (1–0) ratios in starbursts (see Table B2 in Baan et al. 2008). The range of I_{11} ratios in the nuclear disc and inner ring of NGC 5866 (this work) is indicated by grey solid lines in panel *b*, while the typical range in spirals [Paglione et al., 2001] is indicated by red dashed lines. In panels *a* and *b*, Crocker et al. [2012]'s single-dish observations of NGC 4710 and NGC 5866 are shown as an open black circle and an open black square, respectively (see Table 4 of Crocker et al. 2012). The HCN (1–0)/HCO$^+$ ratios for M31 GMCs [Brouillet et al., 2005] are indicated by red dashed lines in panel *c* and *d*. The vertical red dot-dashed lines in panel *d* indicate the typical range of ^{13}CO (1–0)/HCO$^+$ (1–0) ratios in the disc of M82 (starburst; Tan et al. 2011). The HCN (1–0)/^{12}CO (1–0) ratios in spirals [Gao & Solomon, 2004a] are indicated by red dashed lines in panels *a*, *e* and *f*, respectively. The black solid lines in a number of panels show the 1 : 1 relation and are there to guide the eye. Similarly, the black dashed lines show a ratio of 1 in panels *c*, *d* and *f*.

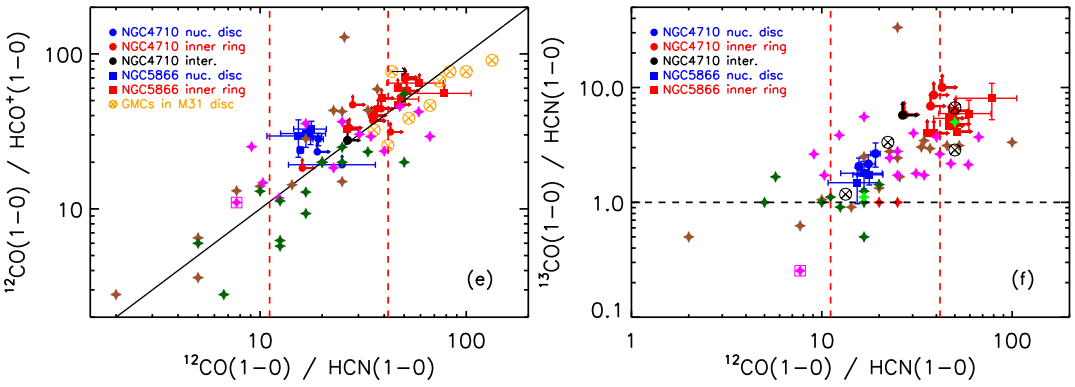

Figure 3.22: Continued.

ratio in NGC 4710 appears much larger than that in most lenticulars, suggesting that the molecular gas temperature in most lenticulars is higher than that in NGC 4710.

As seen in Figure 3.22*b*, the I_{11} ratio is larger than I_{22} in a majority of sources of all kinds, including NGC 4710 and NGC 5866. However, the range of I_{11} ratios in NGC 5866 is smaller ($9 \leq I_{11} \leq 20$) than that in lenticulars and spirals ($3 \leq I_{11} \leq 30$; Crocker et al. 2012; Krips et al. 2010; Paglione et al. 2001), and it is located toward the upper end of the distribution, similarly to starbursts. The I_{11} ratios in NGC 4710 are smaller (mostly $3 \leq I_{11} \leq 8$) and occupy the lower end of the spiral range. This indicates that the CO gas is optically thinner in NGC 5866 and starbursts than in NGC 4710, supporting the idea that strong star formation feedback in starbursts (both radiative via UV light from OB stars and mechanical via supernova explosions) leads to diffuse gas. The difference between NGC 4710 and NGC 5866 is however consistent with the wide range of I_{11} and I_{22} ratios observed in lenticular galaxies, analogous to the significant variations observed in their CO to dense gas tracer ratios (Figs. 3.22*a*, *d*–*f*).

As seen from Figure 3.22*c*, the HCN (1–0)/HNC (1–0) ratios in the nuclear discs of NGC 4710 and NGC 5866 are greater than 1 and similar to those in starbursts, while some Seyferts have much smaller ratios. The behaviour is similar for the HCN (1–0)/HCO^+ (1–0) ratio, although many starbursts also then have smaller ratios. As hinted by the 1 : 1 line, the

HCO^+/HNC ratio is essentially always larger than 1 in the nuclear discs of NGC 4710 and NGC 5866, as for all starbursts (except one), while many Seyferts cluster around the 1 : 1 relation. The ratios may be different in the inner rings of NGC 4710 and NGC 5866, but this is unclear as all ratios are lower limits.

As shown in Figure 3.22*d*, there is a clear difference between the ^{13}CO (1–0)/HCO^+ and HCN (1–0)/HCO^+ (1–0) ratios of NGC 4710 and NGC 5866 and those of starbursts (including M82) in particular, while both Seyferts and other lenticulars have broad ranges of ratios encompassing those of NGC 4710 and NGC 5866. As discussed in Section 3.5.4.4, the ^{13}CO (1–0)/HCO^+ ratio is smaller in the nuclear discs than the inner rings of NGC 4710 and NGC 5866, but now it also appears that this ratio is smaller in all starbursts than in either component, suggesting that starbursts have a larger fraction of dense molecular gas than either the nuclear discs or inner rings of NGC 4710 and NGC 5866 (in that order). As usual, NGC 1266 stands out, here with an exceptionally high dense gas fraction. The HCN (1–0)/HCO^+ (1–0) ratios in the nuclear discs of NGC 4710 and NGC 5866 are also larger than those in starbursts or the GMCs of M31, indicating less HCO^+ and thus fewer CRs from supernova explosions in NGC 4710 and NGC 5866. Observations of both ^{13}CO and high density tracers in the outskirts of our galaxies and normal star-forming (i.e. not star-bursting) spirals would help to establish a better comparison sample for all galaxy types.

As can be seen from Figure 3.22*e*, while the ^{12}CO (1–0)/HCN (1–0) ratios in the inner rings of NGC 4710 and NGC 5866 are at the upper end of the range for spirals, and are entirely consistent with the ratios in M31 GMCs, the ^{12}CO (1–0)/HCN (1–0) ratios in their nuclear discs are smaller and in the middle of the spiral range. While overlapping slightly with the nuclear discs, the ratios for starbursts are generally even smaller, suggesting again a sequence of dense gas fraction (increasing from the GMCs of M31, to the inner rings and nuclear discs of NGC 4710 and NGC 5866, to starbursts). However, the ^{12}CO (1–0)/HCO^+ (1–0) ratios in NGC 4710 and NGC 5866 are larger than those in starbursts, this both for the nuclear discs and inner rings (although more so for the latter and M31 GMCs). While the M31

GMCs and most starbursts lie below the 1 : 1 lines, indicating an HCO^+ enhancement, the opposite is true in both the nuclear discs and inner rings of NGC 4710 and NGC 5866 (see also Figs. 3.22*c* and *d*). This indicates that while the aforementioned dense gas fraction sequence may dominate both ratios, the enhancement of HCO^+ via CRs is strongest in starbursts, less so in M31 GMCs, and is weakest in NGC 5866 and NGC 4710.

The behaviour shown in Figure 3.22*f* largely mimics that in Figure 3.22*e*, although being unaffected by optical depth effects, the ^{13}CO (1–0) line is arguably a better tracer of the total molecular gas content, thus introducing additional scatter. NGC 1266 remains the only lenticular with ^{13}CO (1–0)/HCN (1–0) significantly smaller than 1.

3.6 Conclusions

Interferometric observations of tenuous [^{12}CO (1–0), ^{12}CO (2–1), ^{13}CO (1–0) and ^{13}CO2-1)] and dense [HCN (1–0), HCO^+ (1–0), HNC (1–0) and HNCO (4–3)] molecular gas tracers were presented for the edge-on lenticular galaxies NGC 4710 and NGC 5866. The main conclusions are:

1. The PVDs of the CO lines are X-shaped and reveal that the gas is constrained to two bar-driven kinematic components in both galaxies, a nuclear disc (contained within the inner Lindblad resonance) and an inner ring (around corotation). Although brighter in the nuclear discs, the tenuous molecular gas is clearly detected in both kinematic components and is radially more extended than the dense gas, generally detected in the nuclear discs only. However, as suggested by the HCN (1–0) detection in the inner ring of NGC 5866, it is likely that the inner rings also contain dense gas below our detection thresholds. Both components appear clumpy, and no molecular gas is detected beyond the inner rings.

2. A comparison of our interferometric data with published single-dish data (with much

smaller primary beams) reveal that the latter were missing significant flux associated with the CO lines in the radially-extended inner rings.

3. Molecular line ratios were probed empirically by studying the ratios of the PVDs of CO lines only, dense gas tracer lines only, and CO to dense gas tracer lines, as well as by extracting the integrated line intensity ratios of these same lines as a function of projected position along the galaxy discs, this for each kinematic component separately. The CO (1–0)/CO (2–1) ratios are smaller in the nuclear discs than the inner rings, suggesting that they have higher tenuous molecular gas kinetic temperatures. The ^{12}CO/^{13}CO ratios are slightly larger in the nuclear discs, suggesting that the tenuous gas there has slightly smaller optical depths and column densities (at the very least in NGC 4710). The line ratios of the dense gas tracers only (detected only in the nuclear discs) are all larger than 1 and HCN (1–0)/HCO$^+$ (1–0) $<$ HCN (1–0)/HNC (1–0) $<$ HCN (1–0)/HNCO (4–3), suggesting that the environment is similar to PDRs, with a chemical enhancement of HCN via UV radiation from young massive OB stars and relatively few (supernova explosion-related) CRs. The ratios of CO to dense gas tracers (e.g. ^{12}CO/HCN (1–0) or ^{13}CO/HCN (1–0)) are significantly lower in the nuclear discs than in the inner rings, suggesting a higher fraction of dense gas there, possibly linked to a higher ambient pressure. Overall, the picture that emerges is that of nuclear discs that have a more inhomogeneous ISM, with more dense clumps immersed in a hotter and optically thinner molecular gas medium, consistent with a more intense star formation activity (conversely for the inner rings).

4. LVG (RADEX) modeling was also carried out, considering a two-component molecular ISM traced by the CO lines only (tenuous component) and dense gas tracer lines only (dense component). The results are however inconclusive. The best-fit models within a single kinematic component often cover the entire range of parameters allowed by the models and are often driven to the edge of the model grid, presumably as a result

of the shallowness and extent of the χ^2 contours. The most likely model parameters have very large uncertainties (particularly for $T_{\rm K}$), due to the shape of the marginalised probability distribution functions. As such, they do not reveal clear differences between the inner rings and nuclear discs. This is exacerbated by the facts that most model results are upper limits in the inner ring of NGC 4710, and that we are unable to model the tenuous gas component in the disc of NGC 5866.

5. The line ratios measured in NGC 4710 and NGC 5866 were compared with those obtained in other galaxy types, revealing interesting contrasts. The CO (1–0)/CO (2–1) ratio is larger and thus the tenuous molecular gas temperature lower in NGC 4710 than in most other lenticular galaxies. The ^{12}CO/^{13}CO ratios in NGC 5866 are larger than those in NGC 4710 and similar to those in starbursts, suggesting an optically thinner tenuous component similar to that in starbursts. The range of ratios in other lenticulars and Seyferts is however much larger than that in either NGC 4710 or NGC 5866. While the ^{12}CO (1–0)/HCN (1–0) ratios in the nuclear discs of NGC 4710 and NGC 5866 are similar to those of starbursts near the lower end of the range for spirals, the ratios in the inner rings are larger and rather similar to those observed in some Seyferts and lenticulars near the upper end of the spiral range (where M31 GMCs are found). The ^{13}CO (1–0)/HCN (1–0) ratios of both the inner rings and nuclear discs are however larger than those of starbursts (in that order), indicating smaller dense gas fractions. The HCN (1–0)/HCO$^+$ (1–0) ratio is greater than unity everywhere in NGC 4710 and NGC 5866, as in most starbursts, while it is smaller than unity in spatially-resolved GMCs. High ^{13}CO (1–0)/HCO$^+$ (1–0) ratios in NGC 4710 and NGC 5866 further indicate relatively low HCO$^+$ enhancement (few CRs from supernova explosions) compared to that seen in starbursts and GMCs. Overall, the molecular line ratios in the nuclear discs of NGC 4710 and NGC 5866 thus suggest that the physical conditions of the molecular gas are intermediate between those of spiral galaxies and starbursts, with intense but not extreme star-formation activity, while the inner rings host even milder

star formation.

In summary, based on empirical line ratios, star formation feedback is likely to be stronger in the nuclear discs of NGC 4710 and NGC 5866 than in their inner rings, leading to hotter and optically thinner CO gas with a higher fraction of dense gas clumps. However, due to their large uncertainties, the most likely model results do not support this apparent dichotomy. As the resolution of our observations ($\approx$ 300 pc for the CO lines) is not enough to resolve individual GMCs ($<$ 80 pc), the physical conditions estimated either empirically or via LVG modeling are only averages over GMC associations. Higher angular resolution observations of high-J CO lines and dense gas tracers with ALMA will ultimately resolve the GMCs, and therefore allow us to verify and expand these statements with much greater accuracy.

3.A Modeled line ratios in both galaxies

Table A.1: Ratios of CO lines only and dense gas tracer lines only, in both the nuclear disc and inner ring of NGC 4710 and NGC 5866.

Galaxy (1)	Position (2)	Ratio (3)	Nuclear disc (4)	Inner ring (5)	Galaxy (6)	Position (7)	Ratio (8)	Nuclear disc (9)	Inner ring (10)
NGC 4710	1	I_{12}	-	$\leq 0.8 \pm 0.3$	NGC 5866	1	I_{11}	-	$\geq 18.9 \pm 7.8$
		I_{22}	-	$\geq 2.4 \pm 1.1$					
	2	I_{12}	-	1.8 ± 0.2		2	I_{11}	-	11.6 ± 2.4
		I_{11}	-	6.3 ± 1.2					
		I_{22}	-	$\geq 5.7 \pm 1.9$					
	3	I_{12}	-	1.7 ± 0.2		3	I_{11}	-	10.3 ± 1.6
		I_{11}	-	$\geq 4.6 \pm 1.6$					
		I_{22}	-	$\geq 3.4 \pm 1.2$					
	4	I_{12}	2.4 ± 0.9	1.3 ± 0.2		4	I_{11}	-	9.7 ± 1.2
		I_{11}	$\geq 4.0 \pm 2.2$	14.3 ± 5.2			I_{D1}	-	$\geq 1.0 \pm 0.5$
		I_{22}	$\geq 2.3 \pm 1.1$	$\geq 6.9 \pm 2.5$			I_{D2}	-	$\geq 0.8 \pm 0.4$
		I_{D1}	$\geq 1.4 \pm 0.7$	-			I_{D3}	-	$\geq 0.8 \pm 0.4$
		I_{D2}	$\geq 1.2 \pm 0.6$	-					
		I_{D3}	$\geq 1.8 \pm 0.9$	-					
	5	I_{12}	1.6 ± 0.1	2.3 ± 0.5		5	I_{11}	9.3 ± 1.9	8.6 ± 1.4
		I_{11}	7.2 ± 1.7	2.9 ± 0.9			I_{D1}	1.8 ± 0.5	-
		I_{22}	8.5 ± 1.6	$\geq 3.7 \pm 1.5$			I_{D2}	2.6 ± 0.7	-
		I_{D1}	1.5 ± 0.1	-			I_{D3}	$\geq 2.1 \pm 0.9$	-
		I_{D2}	2.1 ± 0.2	-					
		I_{D3}	4.3 ± 0.8	-					

Notes: (1),(6) Galaxy name. (2),(7) Projected position number as illustrated in Figure 3.11. (3),(8) The line ratio (see the text). (4),(9) The value of the line ratio in the nuclear disc with its error. (5),(10) The value of the line ratio in the inner ring with its error. The errors are based on the statistical uncertainties of integrated line intensities and can be calculated from the error transfer formula. For instance, for transitions a and b the formula for the error on the ratio of a / b is $\sigma(I_{\rm ab}) = I_{\rm ab} \times ([\frac{\sigma_{I_{\rm a}}}{I_{\rm a}}]^2 + [\frac{\sigma_{I_{\rm b}}}{I_{\rm b}}]^2)^{1/2}$

Table A.1: Continued.

Galaxy (1)	Position (2)	Ratio (3)	Nuclear disc (4)	Inner ring (5)	Galaxy (6)	Position (7)	Ratio (8)	Nuclear disc (9)	Inner ring (10)
	6	I_{12}	1.6 ± 0.1	2.2 ± 0.3		6	I_{11}	10.2 ± 1.5	9.7 ± 2.3
		I_{11}	7.6 ± 1.3	≥ 6.6 ± 2.2			I_{D1}	1.8 ± 0.3	-
		I_{22}	6.7 ± 0.7	≥ 3.8 ± 1.4			I_{D2}	2.3 ± 0.4	-
		I_{D1}	1.5 ± 0.1	-			I_{D3}	4.4 ± 1.1	-
		I_{D2}	1.9 ± 0.1	-					
		I_{D3}	4.2 ± 0.3	-					
	7	I_{12}	1.9 ± 0.1	2.4 ± 0.5		7	I_{11}	10.4 ± 3.5	8.9 ± 3.8
		I_{11}	8.1 ± 1.6	8.1 ± 2.5			I_{D1}	1.9 ± 0.5	-
		I_{22}	6.7 ± 0.9	≥ 3.6 ± 1.4			I_{D2}	2.6 ± 0.8	-
		I_{D1}	1.7 ± 0.2	-			I_{D3}	≥ 2.6 ± 1.7	-
		I_{D2}	2.3 ± 0.4	-					
		I_{D3}	4.3 ± 0.9	-					
	8	I_{12}	3.1 ± 0.9	3.0 ± 0.9		8	I_{11}	-	9.0 ± 1.0
		I_{11}	≥ 5.0 ± 2.1	6.1 ± 2.1			I_{D1}	-	≥ 1.5 ± 0.6
		I_{22}	≥ 2.2 ± 1.0	≥ 2.2 ± 1.0			I_{D2}	-	≥ 1.3 ± 0.5
							I_{D3}	-	≥ 1.3 ± 0.5
	9*	I_{12}	-	1.9 ± 0.6		9	I_{11}	-	10.0 ± 1.3
		I_{11}	-	≥ 7.1 ± 2.8			I_{D1}	-	≥ 0.8 ± 0.4
		I_{22}	-	≥ 2.5 ± 1.2			I_{D2}	-	≥ 0.8 ± 0.4
							I_{D3}	-	≥ 0.8 ± 0.4
	10	I_{12}	-	1.8 ± 0.2		10	I_{11}	-	11.8 ± 2.4
		I_{11}	-	≥ 6.4 ± 2.2					
		I_{22}	-	≥ 4.5 ± 1.6					
	11	I_{12}	-	1.6 ± 0.6		11	I_{11}	-	15.5 ± 6.5
		I_{11}	-	≥ 3.3 ± 1.5					
		I_{22}	-	≥ 1.8 ± 0.8					

Notes: *The ratios between the CO lines were also obtained at the intermediate region in NGC 4710, the position 9 (see Fig. 3.11). The ratios at the intermediate region are 1.9 ± 0.6, 4.7 ± 1.8 and ≥ 2.7 ± 1.3 for I_{12}, I_{11} and I_{22} respectively.

3.B Ratios of CO to dense gas tracers

Table B.1: Ratios of CO to dense gas tracer lines, in both the nuclear disc and inner ring of NGC 4710 and NGC 5866.

Galaxy (1)	Position (2)	Ratio (3)	Nuclear disc (4)	Inner ring (5)	Galaxy (6)	Position (7)	Ratio (8)	Nuclear disc (9)	Inner ring (10)
NGC 4710	1	^{12}CO (2–1) / HCN (1–0)	-	$\geq$ 9.3 ± 4.1	NGC 5866	1	^{12}CO (1–0) / HCN (1–0)	-	$\geq$ 26.5 ± 13.9
		^{12}CO (2–1) / HCO$^+$ (1–0)	-	$\geq$ 10.6 ± 4.6			^{12}CO (1–0) / HCO$^+$ (1–0)	-	$\geq$ 32.6 ± 17.1
		^{12}CO (2–1) / HNC (1–0)	-	$\geq$ 9.9 ± 4.3			^{12}CO (1–0) / HNC (1–0)	-	$\geq$ 26.6 ± 14.0
		^{12}CO (2–1) / HNCO (4–3)	-	$\geq$ 7.4 ± 3.2			^{12}CO (1–0) / HNCO (4–3)	-	$\geq$ 29.2 ± 15.3
	2	^{12}CO (1–0) / HCN (1–0)	-	$\geq$ 37.3 ± 12.8		2	^{12}CO (1–0) / HCN (1–0)	-	$\geq$ 51.4 ± 19.5
		^{12}CO (1–0) / HCO$^+$ (1–0)	-	$\geq$ 44.5 ± 15.3			^{12}CO (1–0) / HCO$^+$ (1–0)	-	$\geq$ 57.8 ± 21.9
		^{12}CO (1–0) / HNC (1–0)	-	$\geq$ 50.2 ± 17.3			^{12}CO (1–0) / HNC (1–0)	-	$\geq$ 52.8 ± 20.1
		^{12}CO (1–0) / HNCO (4–3)	-	$\geq$ 48.8 ± 16.8			^{12}CO (1–0) / HNCO (4–3)	-	$\geq$ 49.9 ± 18.9
		^{13}CO (1–0) / HCN (1–0)	-	$\geq$ 6.9 ± 2.8			^{13}CO (1–0) / HCN (1–0)	-	$\geq$ 4.1 ± 1.6
		^{13}CO (1–0) / HCO$^+$ (1–0)	-	$\geq$ 8.2 ± 3.3			^{13}CO (1–0) / HCO$^+$ (1–0)	-	$\geq$ 4.7 ± 1.8
		^{13}CO (1–0) / HNC (1–0)	-	$\geq$ 9.3 ± 3.7			^{13}CO (1–0) / HNC (1–0)	-	$\geq$ 4.3 ± 1.6
		^{13}CO (1–0) / HNCO (4–3)	-	$\geq$ 9.0 ± 3.6			^{13}CO (1–0) / HNCO (4–3)	-	$\geq$ 4.0 ± 1.5
		^{12}CO (2–1) / HCN (1–0)	-	$\geq$ 19.8 ± 6.8			I_{11}	-	11.6 ± 2.4
		^{12}CO (2–1) / HCO$^+$ (1–0)	-	$\geq$ 23.7 ± 8.1					
		^{12}CO (2–1) / HNC (1–0)	-	$\geq$ 26.7 ± 9.2					
		^{12}CO (2–1) / HNCO (4–3)	-	$\geq$ 26.0 ± 8.9					
	3	^{12}CO (1–0) / HCN (1–0)	-	$\geq$ 28.1 ± 9.7		3	^{12}CO (1–0) / HCN (1–0)	-	$\geq$ 46.5 ± 16.8
		^{12}CO (1–0) / HCO$^+$ (1–0)	-	$\geq$ 47.0 ± 16.2			^{12}CO (1–0) / HCO$^+$ (1–0)	-	$\geq$ 60.0 ± 21.7
		^{12}CO (1–0) / HNC (1–0)	-	$\geq$ 30.7 ± 10.5			^{12}CO (1–0) / HNC (1–0)	-	$\geq$ 52.8 ± 19.1
		^{12}CO (1–0) / HNCO (4–3)	-	$\geq$ 46.0 ± 15.8			^{12}CO (1–0) / HNCO (4–3)	-	$\geq$ 50.8 ± 18.3
		^{12}CO (2–1) / HCN (1–0)	-	$\geq$ 14.3 ± 5.0			^{13}CO (1–0) / HCN (1–0)	-	$\geq$ 4.6 ± 1.7
		^{12}CO (2–1) / HCO$^+$ (1–0)	-	$\geq$ 23.8 ± 8.4			^{13}CO (1–0) / HCO$^+$ (1–0)	-	$\geq$ 6.0 ± 2.1
		^{12}CO (2–1) / HNC (1–0)	-	$\geq$ 15.6 ± 5.5			^{13}CO (1–0) / HNC (1–0)	-	$\geq$ 5.3 ± 1.9
		^{12}CO (2–1) / HNCO (4–3)	-	$\geq$ 23.3 ± 8.2			^{13}CO (1–0) / HNCO (4–3)	-	$\geq$ 5.1 ± 1.8
	4	^{12}CO (1–0) / HCN (1–0)	25.0 ± 11.3	$\geq$ 50.3 ± 18.7		4	^{12}CO (1–0) / HCN (1–0)	-	78.2 ± 27.4
		^{12}CO (1–0) / HCO$^+$ (1–0)	$\geq$ 19.3 ± 10.8	$\geq$ 68.6 ± 25.6			^{12}CO (1–0) / HCO$^+$ (1–0)	-	$\geq$ 55.6 ± 19.6
		^{12}CO (1–0) / HNC (1–0)	$\geq$ 13.6 ± 7.6	$\geq$ 48.3 ± 18.0			^{12}CO (1–0) / HNC (1–0)	-	$\geq$ 44.6 ± 15.7
		^{12}CO (1–0) / HNCO (4–3)	$\geq$ 25.5 ± 14.3	$\geq$ 91.0 ± 33.9			^{12}CO (1–0) / HNCO (4–3)	-	$\geq$ 45.6 ± 16.0
		^{13}CO (1–0) / HCN (1–0)	-	$\geq$ 4.8 ± 2.6			^{13}CO (1–0) / HCN (1–0)	-	8.1 ± 2.8
		^{13}CO (1–0) / HCO$^+$ (1–0)	-	$\geq$ 6.6 ± 3.6			^{13}CO (1–0) / HCO$^+$ (1–0)	-	$\geq$ 6.6 ± 2.3
		^{13}CO (1–0) / HNC (1–0)	-	$\geq$ 4.6 ± 2.5			^{13}CO (1–0) / HNC (1–0)	-	$\geq$ 5.3 ± 1.9
		^{13}CO (1–0) / HNCO (4–3)	-	$\geq$ 8.7 ± 4.7			^{13}CO (1–0) / HNCO (4–3)	-	$\geq$ 5.4 ± 1.9
		^{12}CO (2–1) / HCN (1–0)	10.6 ± 4.3	$\geq$ 27.3 ± 9.7					
		^{12}CO (2–1) / HCO$^+$ (1–0)	$\geq$ 12.4 ± 6.0	$\geq$ 37.3 ± 13.2					
		^{12}CO (2–1) / HNC (1–0)	$\geq$ 8.7 ± 4.2	$\geq$ 26.3 ± 9.3					
		^{12}CO (2–1) / HNCO (4–3)	$\geq$ 16.4 ± 8.0	$\geq$ 49.4 ± 17.5					
		^{13}CO (2–1) / HCN (1–0)	$\leq$ 1.3 ± 1.0	-					

Notes: The uncertainties on the line ratios are calculated from the uncertainties on the integrated line intensities using the standard error propagation formula.

Table B.1: Continued.

Galaxy (1)	Position (2)	Ratio (3)	Nuclear disc (4)	Inner ring (5)	Galaxy (6)	Position (7)	Ratio (8)	Nuclear disc (9)	Inner ring (10)
NGC 4710	5	^{12}CO (1–0) / HCN (1–0)	19.2 ± 1.1	≥ 42.9 ± 16.3	NGC 5866	5	^{12}CO (1–0) / HCN (1–0)	16.7 ± 4.1	≥ 50.3 ± 18.4
		^{12}CO (1–0) / HCO$^+$ (1–0)	28.2 ± 2.6	≥ 31.4 ± 11.9			^{12}CO (1–0) / HCO$^+$ (1–0)	30.6 ± 5.7	≥ 70.7 ± 25.9
		^{12}CO (1–0) / HNC (1–0)	40.5 ± 4.3	≥ 37.6 ± 14.3			^{12}CO (1–0) / HNC (1–0)	42.7 ± 10.0	≥ 67.7 ± 24.8
		^{12}CO (1–0) / HNCO (4–3)	81.7 ± 14.6	≥ 42.8 ± 16.2			^{12}CO (1–0) / HNCO (4–3)	≥ 45.0 ± 7.4	≥ 50.7 ± 18.6
		^{13}CO (1–0) / HCN (1–0)	2.7 ± 0.6	≥ 10.0 ± 4.7			^{13}CO (1–0) / HCN (1–0)	1.8 ± 0.5	≥ 6.3 ± 2.3
		^{13}CO (1–0) / HCO$^+$ (1–0)	3.9 ± 1.0	≥ 11.8 ± 5.5			^{13}CO (1–0) / HCO$^+$ (1–0)	3.3 ± 0.7	≥ 8.8 ± 3.2
		^{13}CO (1–0) / HNC (1–0)	5.6 ± 1.4	≥ 11.9 ± 5.5			^{13}CO (1–0) / HNC (1–0)	4.6 ± 1.2	≥ 8.4 ± 3.1
		^{13}CO (1–0) / HNCO (4–3)	11.3 ± 3.3	≥ 12.4 ± 5.8			^{13}CO (1–0) / HNCO (4–3)	≥ 3.3 ± 0.7	≥ 6.3 ± 2.3
		^{12}CO (2–1) / HCN (1–0)	12.1 ± 0.8	≥ 14.9 ± 16.1					
		^{12}CO (2–1) / HCO$^+$ (1–0)	17.8 ± 1.7	≥ 18.8 ± 7.7					
		^{12}CO (2–1) / HNC (1–0)	25.6 ± 2.8	≥ 22.5 ± 9.2					
		^{12}CO (2–1) / HNCO (4–3)	51.6 ± 9.3	≥ 25.6 ± 10.5					
		^{13}CO (2–1) / HCN (1–0)	1.4 ± 0.3	-					
		^{13}CO (2–1) / HCO$^+$ (1–0)	2.1 ± 0.4	-					
		^{13}CO (2–1) / HNC (1–0)	3.0 ± 0.6	-					
		^{13}CO (2–1) / HNCO (4–3)	6.1 ± 1.6	-					
	6	^{12}CO (1–0) / HCN (1–0)	15.7 ± 0.5	≥ 34.7 ± 11.6		6	^{12}CO (1–0) / HCN (1–0)	17.8 ± 3.2	≥ 38.8 ± 15.3
		^{12}CO (1–0) / HCO$^+$ (1–0)	24.0 ± 1.2	≥ 39.7 ± 13.3			^{12}CO (1–0) / HCO$^+$ (1–0)	32.7 ± 4.0	≥ 51.8 ± 20.4
		^{12}CO (1–0) / HNC (1–0)	29.5 ± 1.9	≥ 39.3 ± 13.2			^{12}CO (1–0) / HNC (1–0)	40.2 ± 6.1	≥ 39.4 ± 15.5
		^{12}CO (1–0) / HNCO (4–3)	66.0 ± 4.9	≥ 45.0 ± 15.1			^{12}CO (1–0) / HNCO (4–3)	78.2 ± 17.9	≥ 42.7 ± 16.8
		^{13}CO (1–0) / HCN (1–0)	2.1 ± 0.4	-			^{13}CO (1–0) / HCN (1–0)	1.7 ± 0.3	≥ 4.0 ± 1.6
		^{13}CO (1–0) / HCO$^+$ (1–0)	3.2 ± 0.6	-			^{13}CO (1–0) / HCO$^+$ (1–0)	3.2 ± 0.4	≥ 5.3 ± 2.1
		^{13}CO (1–0) / HNC (1–0)	3.9 ± 0.7	-			^{13}CO (1–0) / HNC (1–0)	3.9 ± 0.6	≥ 4.1 ± 1.6
		^{13}CO (1–0) / HNCO (4–3)	8.7 ± 1.7	-			^{13}CO (1–0) / HNCO (4–3)	7.7 ± 1.8	≥ 4.4 ± 1.7
		^{12}CO (2–1) / HCN (1–0)	9.6 ± 0.4	≥ 14.9 ± 5.5					
		^{12}CO (2–1) / HCO$^+$ (1–0)	14.6 ± 0.8	≥ 17.1 ± 6.3					
		^{12}CO (2–1) / HNC (1–0)	17.9 ± 1.3	≥ 17.0 ± 6.3					
		^{12}CO (2–1) / HNCO (4–3)	40.2 ± 3.2	≥ 18.4 ± 6.8					
		^{13}CO (2–1) / HCN (1–0)	1.4 ± 0.2	-					
		^{13}CO (2–1) / HCO$^+$ (1–0)	2.2 ± 0.3	-					
		^{13}CO (2–1) / HNC (1–0)	2.7 ± 0.3	-					
		^{13}CO (2–1) / HNCO (4–3)	6.0 ± 0.8	-					
	7	^{12}CO (1–0) / HCN (1–0)	17.6 ± 1.5	≥ 38.7 ± 13.8		7	^{12}CO (1–0) / HCN (1–0)	15.4 ± 4.6	≥ 35.8 ± 16.5
		^{12}CO (1–0) / HCO$^+$ (1–0)	29.2 ± 3.2	≥ 44.2 ± 15.7			^{12}CO (1–0) / HCO$^+$ (1–0)	29.5 ± 8.0	≥ 40.1 ± 18.4
		^{12}CO (1–0) / HNC (1–0)	40.6 ± 6.4	≥ 44.6 ± 15.9			^{12}CO (1–0) / HNC (1–0)	40.0 ± 11.8	≥ 44.4 ± 20.4
		^{12}CO (1–0) / HNCO (4–3)	76.0 ± 16.5	≥ 52.6 ± 18.7			^{12}CO (1–0) / HNCO (4–3)	≥ 45.1 ± 12.6	≥ 45.0 ± 20.7
		^{13}CO (1–0) / HCN (1–0)	2.2 ± 0.4	≥ 8.6 ± 4.3			^{13}CO (1–0) / HCN (1–0)	1.5 ± 0.5	≥ 4.0 ± 2.0
		^{13}CO (1–0) / HCO$^+$ (1–0)	3.6 ± 0.8	≥ 9.8 ± 4.9			^{13}CO (1–0) / HCO$^+$ (1–0)	2.9 ± 0.9	≥ 4.5 ± 2.2
		^{13}CO (1–0) / HNC (1–0)	5.0 ± 1.2	≥ 9.9 ± 4.9			^{13}CO (1–0) / HNC (1–0)	3.9 ± 1.3	≥ 5.0 ± 2.4
		^{13}CO (1–0) / HNCO (4–3)	9.3 ± 2.6	≥ 11.7 ± 5.8			^{13}CO (1–0) / HNCO (4–3)	≥ 3.8 ± 1.4	≥ 5.1 ± 2.5
		^{12}CO (2–1) / HCN (1–0)	9.1 ± 0.8	≥ 14.9 ± 6.0					
		^{12}CO (2–1) / HCO$^+$ (1–0)	15.1 ± 1.7	≥ 17.1 ± 6.8					
		^{12}CO (2–1) / HNC (1–0)	21.1 ± 3.4	≥ 17.2 ± 6.9					
		^{12}CO (2–1) / HNCO (4–3)	39.4 ± 8.6	≥ 20.4 ± 8.1					
		^{13}CO (2–1) / HCN (1–0)	1.4 ± 0.2	-					
		^{13}CO (2–1) / HCO$^+$ (1–0)	2.3 ± 0.4	-					
		^{13}CO (2–1) / HNC (1–0)	3.2 ± 0.6	-					
		^{13}CO (2–1) / HNCO (4–3)	5.9 ± 1.5	-					
	8	^{12}CO (1–0) / HCN (1–0)	≥ 19.0 ± 7.7	≥ 27.1 ± 10.8		8	^{12}CO (1–0) / HCN (1–0)	-	48.7 ± 10.1
		^{12}CO (1–0) / HCO$^+$ (1–0)	≥ 23.4 ± 9.6	≥ 33.4 ± 13.3			^{12}CO (1–0) / HCO$^+$ (1–0)	-	≥ 51.1 ± 17.9
		^{12}CO (1–0) / HNC (1–0)	≥ 25.1 ± 10.3	≥ 36.0 ± 14.3			^{12}CO (1–0) / HNC (1–0)	-	≥ 46.9 ± 16.4
		^{12}CO (1–0) / HNCO (4–3)	≥ 22.9 ± 9.4	≥ 32.7 ± 13.0			^{12}CO (1–0) / HNCO (4–3)	-	≥ 44.6 ± 15.6
		^{13}CO (1–0) / HCN (1–0)	-	≥ 5.8 ± 2.9			^{13}CO (1–0) / HCN (1–0)	-	5.4 ± 1.1
		^{13}CO (1–0) / HCO$^+$ (1–0)	-	≥ 7.2 ± 3.6			^{13}CO (1–0) / HCO$^+$ (1–0)	-	≥ 5.3 ± 1.8
		^{13}CO (1–0) / HNC (1–0)	-	≥ 7.7 ± 3.8			^{13}CO (1–0) / HNC (1–0)	-	≥ 4.9 ± 1.7
		^{13}CO (1–0) / HNCO (4–3)	-	≥ 7.0 ± 3.5			^{13}CO (1–0) / HNCO (4–3)	-	≥ 4.6 ± 1.6
		^{12}CO (2–1) / HCN (1–0)	≥ 9.4 ± 4.1	≥ 9.5 ± 4.4					
		^{12}CO (2–1) / HCO$^+$ (1–0)	≥ 11.6 ± 5.1	≥ 11.7 ± 5.4					
		^{12}CO (2–1) / HNC (1–0)	≥ 12.4 ± 5.5	≥ 12.6 ± 5.8					
		^{12}CO (2–1) / HNCO (4–3)	≥ 11.3 ± 5.0	≥ 11.4 ± 5.3					
	9	^{12}CO (1–0) / HCN (1–0)	-	≥ 35.4 ± 13.9		9	^{12}CO (1–0) / HCN (1–0)	-	59.3 ± 18.1
		^{12}CO (1–0) / HCO$^+$ (1–0)	-	≥ 36.9 ± 14.5			^{12}CO (1–0) / HCO$^+$ (1–0)	-	≥ 64.8 ± 22.7
		^{12}CO (1–0) / HNC (1–0)	-	≥ 36.6 ± 14.4			^{12}CO (1–0) / HNC (1–0)	-	≥ 61.4 ± 21.5
		^{12}CO (1–0) / HNCO (4–3)	-	≥ 24.3 ± 9.6			^{12}CO (1–0) / HNCO (4–3)	-	≥ 62.1 ± 21.7
		^{12}CO (2–1) / HCN (1–0)	-	≥ 15.6 ± 7.5			^{13}CO (1–0) / HCN (1–0)	-	5.9 ± 1.8
		^{12}CO (2–1) / HCO$^+$ (1–0)	-	≥ 16.3 ± 7.8			^{13}CO (1–0) / HCO$^+$ (1–0)	-	≥ 6.2 ± 2.2
		^{12}CO (2–1) / HNC (1–0)	-	≥ 16.2 ± 7.8			^{13}CO (1–0) / HNC (1–0)	-	≥ 5.8 ± 2.1
		^{12}CO (2–1) / HNCO (4–3)	-	≥ 10.7 ± 5.2			^{13}CO (1–0) / HNCO (4–3)	-	≥ 5.9 ± 2.1

Table B.1: Continued.

Galaxy (1)	Position (2)	Ratio (3)	Nuclear disc (4)	Inner ring (5)	Galaxy (6)	Position (7)	Ratio (8)	Nuclear disc (9)	Inner ring (10)
NGC 4710	10	^{12}CO (1–0) / HCN (1–0)	-	$\geq$ 35.1 ± 12.2	NGC 5866	10	^{12}CO (1–0) / HCN (1–0)	-	$\geq$ 46.8 ± 17.9
		^{12}CO (1–0) / HCO$^+$ (1–0)	-	$\geq$ 37.3 ± 13.0			^{12}CO (1–0) / HCO$^+$ (1–0)	-	$\geq$ 47.1 ± 18.1
		^{12}CO (1–0) / HNC (1–0)	-	$\geq$ 29.0 ± 10.1			^{12}CO (1–0) / HNC (1–0)	-	$\geq$ 46.7 ± 17.9
		^{12}CO (1–0) / HNCO (4–3)	-	$\geq$ 30.8 ± 10.7			^{12}CO (1–0) / HNCO (4–3)	-	$\geq$ 51.2 ± 19.6
		^{12}CO (2–1) / HCN (1–0)	-	$\geq$ 20.7 ± 7.3			^{13}CO (1–0) / HCN (1–0)	-	$\geq$ 5.4 ± 2.0
		^{12}CO (2–1) / HCO$^+$ (1–0)	-	$\geq$ 22.0 ± 7.7			^{13}CO (1–0) / HCO$^+$ (1–0)	-	$\geq$ 5.4 ± 2.0
		^{12}CO (2–1) / HNC (1–0)	-	$\geq$ 17.1 ± 6.0			^{13}CO (1–0) / HNC (1–0)	-	$\geq$ 5.4 ± 2.0
		^{12}CO (2–1) / HNCO (4–3)	-	$\geq$ 18.2 ± 6.4			^{13}CO (1–0) / HNCO (4–3)	-	$\geq$ 5.9 ± 2.2
	11	^{12}CO (1–0) / HCN (1–0)	-	$\geq$ 16.0 ± 7.1		11	^{13}CO (1–0) / HCN (1–0)	-	$\geq$ 1.1 ± 0.6
		^{12}CO (1–0) / HCO$^+$ (1–0)	-	$\geq$ 18.3 ± 8.2			^{13}CO (1–0) / HCO$^+$ (1–0)	-	$\geq$ 1.3 ± 0.7
		^{12}CO (1–0) / HNC (1–0)	-	$\geq$ 13.6 ± 6.1			^{13}CO (1–0) / HNC (1–0)	-	$\geq$ 1.2 ± 0.7
		^{12}CO (1–0) / HNCO (4–3)	-	$\geq$ 14.0 ± 6.2			^{13}CO (1–0) / HNCO (4–3)	-	$\geq$ 1.5 ± 0.8
		^{12}CO (2–1) / HCN (1–0)	-	$\geq$ 7.1 ± 3.3					
		^{12}CO (2–1) / HCO$^+$ (1–0)	-	$\geq$ 8.1 ± 3.8					
		^{12}CO (2–1) / HNC (1–0)	-	$\geq$ 6.3 ± 3.0					
		^{12}CO (2–1) / HNCO (4–3)	-	$\geq$ 6.5 ± 3.0					

Table B.2: Ratios of CO to dense gas tracer lines in the intermediate region of NGC 4710.

Galaxy	Position	Ratio	Value
NGC 4710	9	^{12}CO (1–0) / HCN (1–0)	$\geq$ 26.6 ± 10.8
		^{12}CO (1–0) / HCO$^+$ (1–0)	$\geq$ 27.7 ± 11.2
		^{12}CO (1–0) / HNC (1–0)	$\geq$ 27.5 ± 11.1
		^{12}CO (1–0) / HNCO (4–3)	$\geq$ 18.3 ± 7.4
		^{13}CO (1–0) / HCN (1–0)	$\geq$ 5.7 ± 3.1
		^{13}CO (1–0) / HCO$^+$ (1–0)	$\geq$ 6.0 ± 3.3
		^{13}CO (1–0) / HNC (1–0)	$\geq$ 5.9 ± 3.3
		^{13}CO (1–0) / HNCO (4–3)	$\geq$ 3.9 ± 2.2
		^{12}CO (2–1) / HCN (1–0)	$\geq$ 17.0 ± 7.7
		^{12}CO (2–1) / HCO$^+$ (1–0)	$\geq$ 17.7 ± 8.0
		^{12}CO (2–1) / HNC (1–0)	$\geq$ 17.6 ± 8.0
		^{12}CO (2–1) / HNCO (4–3)	$\geq$ 11.7 ± 5.3

Notes: The uncertainties on the line ratios are calculated from the uncertainties on the integrated line intensities using the standard error propagation formula.

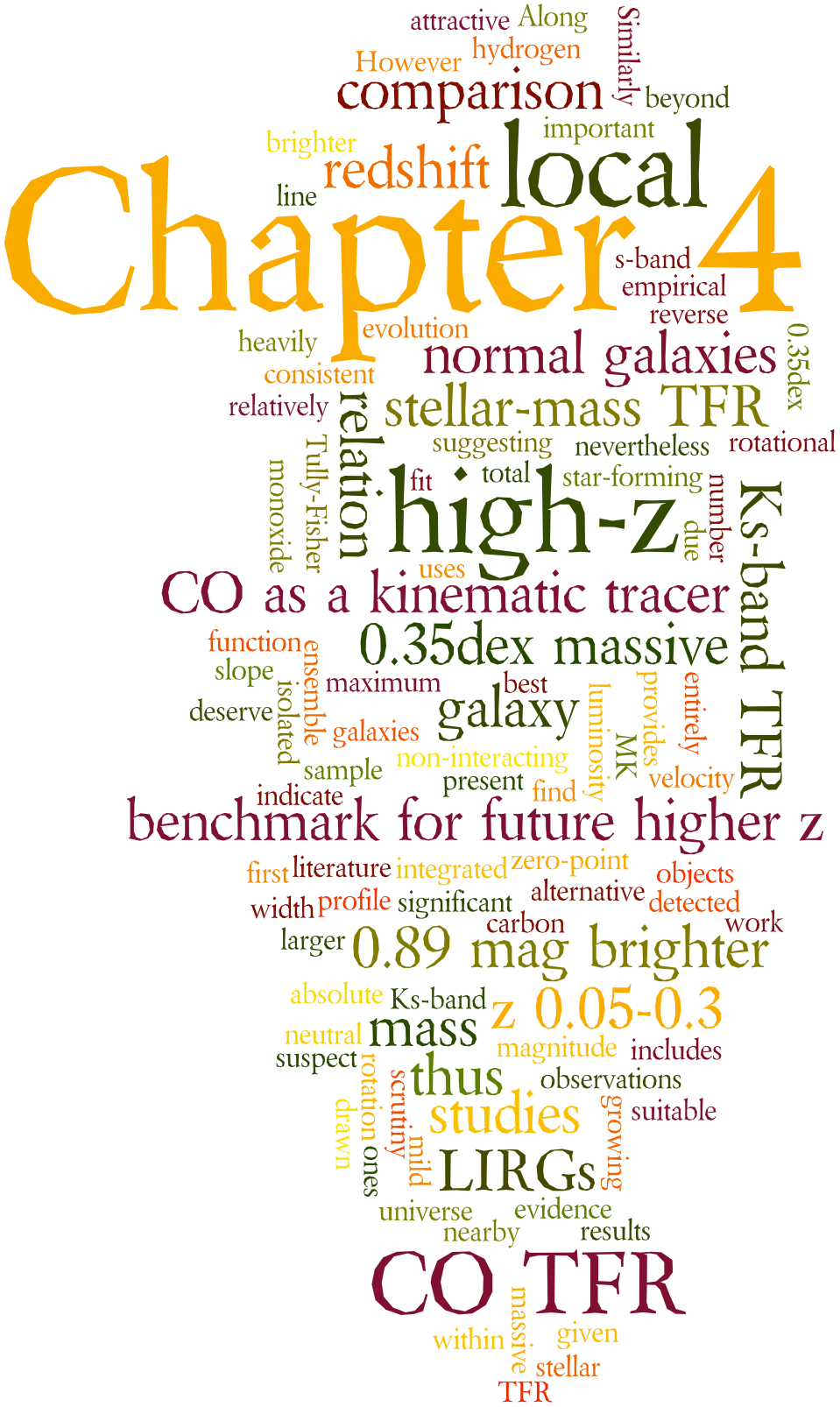
attractive
Along
Similarly
hydrogen
However
comparison
beyond
important
brighter
redshift
local
line
Chapter 4
s-band
empirical
reverse
heavily
evolution
normal galaxies
0.35dex
consistent
relatively
relation
stellar-mass TFR
suggesting
nevertheless
rotational
Tully-Fisher
monoxide
fit
total
star-forming
high-z
number
due
Ks-band TFR
uses
CO as a kinematic tracer
function
ensemble
slope
maximum
best
0.35dex massive
deserve
isolated
galaxy
luminosity
provides
entirely
galaxies
MK
non-interacting
sample
present
find
velocity
indicate
benchmark for future higher z
first
literature
integrated
zero-point
objects
width
profile
significant
alternative
detected
carbon
work
larger
0.89 mag brighter
absolute
Ks-band
z 0.05-0.3
neutral
mass
magnitude
includes
suspect
rotation
thus
observations
scrutiny
studies
growing
suitable
drawn
ones
mild
LIRGs
universe
evidence
nearby
results
CO TFR
within
massive
given
stellar
TFR

4

The CO TFR of Star-forming Galaxies at $z = 0.05 - 0.3$

"When I have a terrible need of - shall I say the word - religion, then I go out and paint the stars."

Vincent Van Gogh

The material in this chapter is to be submitted to MNRAS as "The CO Tully-Fisher Relation of Star-forming Galaxies at $z = 0.05 - 0.3$", Selçuk Topal, Martin Bureau, Alfred A. Tiley, Kazufumi Torii

4.1 Introduction

The Tully-Fisher relation (TFR) is a well-established empirical correlation between the total stellar luminosity of a galaxy (tracing its total stellar mass) and the maximum rotation velocity of a (rotationally-supported) kinematic tracer (tracing the galaxy's total mass). It has been widely studied in the local universe at both optical and near-infrared wavelengths, and it has a relatively small intrinsic scatter. Although the existence of a correlation between the stellar luminosity and the width of the neutral hydrogen (H I) line (roughly twice the maximum rotation velocity) of late-type galaxies (spirals and irregulars) was suggested before [Balkowski et al., 1974], Tully & Fisher [1977a] showed that the relation could be used for distance measurements. It also holds across a wide range of galaxy environments [e.g. Mould et al., 1993; Tully & Pierce, 2000; Willick & Strauss, 1998]. The TFR relation is therefore a useful tool to probe the total mass-to-light ratio (M/L) of galaxies, and when studied as a function of redshift theories of galaxy formation in general [e.g. Steinmetz & Navarro, 1999].

When a suitable kinematic tracer is available, it has been shown that the TFR also holds for early-type galaxies (ETGs, lenticulars and ellipticals; e.g. Davis et al. 2011b; De Rijcke et al. 2007; Gerhard et al. 2001; Magorrian & Ballantyne 2001; Neistein et al. 1999a; Williams et al. 2010). Crucially, if lenticulars are "dead" spirals (i.e. spirals where star formation has ceased), then their masses should remain roughly constant over time while their luminosity decreases. This would lead to an increase of M/L and thus a shift of the TFR zero-point compared to that of spirals. Although some past works were unable to find such an offset [e.g. Dressler & Sandage, 1983; Hinz et al., 2003, 2001; Neistein et al., 1999b], other studies over the last decade or so do indicate one [e.g. Bedregal et al., 2006; Davis et al., 2011b; Mathieu et al., 2002; Williams et al., 2010]. In particular, Bedregal et al. [2006] found that the TFR of lenticular galaxies lies about 1.2 mag below the spiral TFR with a scatter of 1.0 mag at K_s-band, the largest offset found to date.

The H I emission line has been used heavily as the kinematic tracer for TFR studies [e.g. Pizagno et al., 2007; Tully & Fisher, 1977a; Tully & Pierce, 2000]. However, carbon-monoxide (CO) has also been shown to be an excellent kinematic tracer for TFR studies, as long as the CO emission extends beyond the peak of the galaxy rotation curve [Davis et al., 2011b; Dickey & Kazes, 1992; Lavezzi & Dickey, 1998; Schoniger & Sofue, 1994a; Tiley et al., 2015; Torii et al., 2015; Tutui & Sofue, 1997; Tutui et al., 2001].

The CO TFR has so far been studied in nearby galaxies only; to our knowledge there is as yet no CO TFR work beyond the local universe. But probing the TFR in more distant galaxies allows to investigate the evolution of the M/L of galaxies as a function of redshift [e.g. Conselice et al., 2005; Flores et al., 2006; Kassin et al., 2007; Puech et al., 2008]. Our goals in this paper are thus twofold. First, to probe whether there is any evolution of the CO TFR as a function of redshift up to $z = 0.3$, by comparing the TFR of galaxies within our sample and from the literature [Tiley et al., 2015; Torii et al., 2015; Tully & Pierce, 2000]. Second, to provide a local benchmark for future higher redshift CO TFR studies.

This chapter is structured as follows. Section 4.2 describes the data used, while Section 4.3 discusses the sample selection. Section 4.4 presents the velocity measurements and TFR fits. The results are discussed in Section 4.5 and we conclude briefly in Section 4.6.

4.2 Data

4.2.1 EGNoG CO sample

The Evolution of molecular Gas in Normal Galaxies (EGNoG) survey is a CO(1-0) survey of 31 galaxies at $z \approx 0.05$ – 0.5 by Bauermeister et al. [2013]. All galaxies were selected from the Sloan Digitized Sky Survey Data Release 7 (SDSS DR7; Abazajian et al. 2009; Strauss et al. 2002; York et al. 2000) and the Cosmic Evolution Survey (COSMOS; Scoville et al. 2007) to be as representative as possible of the main sequence of star-forming galaxies (a correlation between star formation rate, SFR, and stellar mass, $M_\star$) at the redshifts concerned.

First, only galaxies with a spectroscopic redshift (essential for follow-up CO observations) as well as $4 \leq M_\star \leq 30 \times 10^{10}\ M_\odot$ and $4 \leq \mathrm{SFR} \leq 100\ M_\odot\ \mathrm{yr}^{-1}$ (to restrict the sample to main sequence objects) were selected. SDSS galaxies harbouring an active galactic nucleus (AGN) were then rejected, as diagnosed from standard emission line ratios measured in the SDSS spectra (see Kauffmann et al. 2003 and Section 4.3.2). Interacting galaxies were also excluded via a visual inspection of the SDSS images, although we revisit this issue in Section 4.3.

The galaxies to be observed in CO were selected randomly from all the galaxies meeting the above selection criteria. CO(1-0) observations of all 31 EGNoG galaxies were obtained using the Combined Array for Research in Millimeter-wave Astronomy (CARMA) and were spatially integrated to generate total spectra. The core of our sample is composed of the 24 EGNoG galaxies that were reliably detected according to Bauermeister et al. [2013], all at $z \approx 0.05$ – 0.3 and all from SDSS (i.e. none of the COSMOS galaxies at $z \approx 0.5$ was reliably detected in CO). A few of these galaxies are luminous infrared galaxies (LIRGs, with $10^{11} < L_{\mathrm{IR}} < 10^{12}\ L_\odot$), but none is an ultra-luminous infrared galaxy (ULIRG, with $L_{\mathrm{IR}} > 10^{12}\ L_\odot$). Please see Bauermeister et al. [2013] for more details of the sample selection, observations and data reduction.

4.2.2 Additional CO data

Additional CO data for galaxies within the same redshift range (i.e. $z = 0.05$ – 0.3) were taken from the literature. Tutui et al. [2000] detected 10 LIRGs and 3 ULIRGS at $z = 0.05$ – 0.2. Sanders et al. [1991] published CO line profiles for 52 LIRGs and 8 ULIRGS detections at $z = 0.05$ – 0.1, while Mirabel et al. [1990] conducted complementary observations and detected 19 LIRGs and 9 ULIRGs at $z = 0.01$ – 0.13. See the related papers for more details of the observations and data reduction.

Overall, combining the EGNoG CO detections (24 galaxies) with the additional literature detections (101 galaxies), we obtain a sample of 125 galaxies with integrated CO profiles at

$z = 0$ – 0.3. However, as detailed in Section 4.3, additional selection criteria are applied to construct a more homogenous sample of galaxies appropriate for TFR studies.

4.2.3 Near-infrared photometry

Stellar luminosities are also required to construct TFRs. Near-infrared photometry is superior to that at shorter wavelengths as it is less affected by dust extinction. This is particularly crucial for highly inclined galaxies and dusty high-redshift objects. For example, if left uncorrected dust extinction can cause an error $\gtrsim 1$ mag at optical wavelengths (e.g. B-band or ≈ 440 nm), while the uncertainties at K-band (≈ 2.2 μm) are much less (≈ 0.1 mag; Noordermeer & Verheijen 2007). Longer wavelengths (e.g. mid-infrared) are affected by dust emission and are thus also inappropriate. Partially as a results of these effects, but also because the M/L of stellar populations varies the least at K-band [e.g. Maraston, 2005], the scatter of the TFR is minimised at K-band [Verheijen, 2001]. This thus makes it an optimal choice of passband to measure the galaxy luminosities.

The total apparent K_s-band magnitudes of all sample galaxies were therefore obtained from the Two Micron All Sky Survey (2MASS; Jarrett et al. 2000; Skrutskie et al. 2006b) and are listed in Table 4.1. For most galaxies, we adopted the *k_m_ext* parameter from the 2MASS Extended Source Catalog (XSC; Jarrett et al. 2000). For galaxies that are not extended in 2MASS and thus not in the XSC, we adopted the default K_s-band magnitude (*k_m* parameter) from the 2MASS Point Source Catalog (PSC; Skrutskie et al. 2006b). All magnitudes quoted in this paper are Vega magnitudes.

4.2.4 Inclinations

The inclination of each galaxy is necessary to deproject its measured velocity width. It was calculated using its axial ratio from the SDSS r-band images (specifically the *expAB_r* and *expABErr_r* parameters from the SDSS Data Release 12 catalogue; Alam et al. 2015)

Table 4.1: General galaxy parameters.

Galaxy (1)	SDSS name (2)	z (3)	m_{K_s} (mag) (4)	$\log(M_\star/M_\odot)$ (5)	BPT class (6)	Notes (7)
			Final sample galaxies			
G1	2MASXJ14301041+3112558	0.012	9.2 ± 0.1	7.5 ± 0.2	1	Mirabel et al. [1990]
G2	SDSSJ102219.83+213406.9	0.014	8.9 ± 0.1	10.6 ± 0.1	1	Sanders et al. [1991]
G3	SDSSJ111628.07+291936.1	0.046	11.8 ± 0.1	11.0 ± 0.1	1	Tutui et al. [2000]
G4	SDSSJ233455.23+141731.0	0.062	12.1 ± 0.1	11.0 ± 0.1	1	
G5	SDSSJ141906.70+474514.8	0.072	12.4 ± 0.1	10.9 ± 0.1	1	Tutui et al. [2000]
G6	SDSSJ231332.46+133845.3	0.081	13.3 ± 0.2	11.0 ± 0.1	1	
G7	SDSSJ221938.11+134213.9	0.084	12.6 ± 0.1	11.2 ± 0.1	1	
G8	SDSSJ100518.63+052544.2	0.166	14.7 ± 0.1	10.8 ± 0.1	2	PSC
G9	SDSSJ105527.18+064015.0	0.173	14.5 ± 0.1	11.0 ± 0.1	2	PSC
G10	SDSSJ124252.54+130944.2	0.175	14.8 ± 0.1	10.8 ± 0.2	1	PSC
G11	SDSSJ091426.24+102409.6	0.176	13.2 ± 0.2	11.5 ± 0.1	2	
G12	SDSSJ114649.18+243647.7	0.177	14.7 ± 0.1	11.1 ± 0.1	2	PSC
G13	SDSSJ223528.63+135812.6	0.183	13.5 ± 0.2	11.4 ± 0.1	2	
G14	SDSSJ130529.30+222019.8	0.190	14.4 ± 0.1	11.0 ± 0.1	1	PSC
G15	SDSSJ092831.94+252313.9	0.283	15.1 ± 0.1	11.2 ± 0.2	1	PSC
G16	SDSSJ133849.18+403331.7	0.285	14.0 ± 0.2	11.3 ± 0.2	1	
			Additional initial galaxies			
G17	SDSSJ112731.84+565237.4	0.010	8.7 ± 0.1	10.3 ± 0.1	1	Sanders et al. [1991]
G18	SDSSJ095918.80+521525.4	0.041	11.6 ± 0.1	10.7 ± 0.1	1	Tutui et al. [2000]
G19	SDSSJ141601.21+183434.1	0.055	12.3 ± 0.1	11.1 ± 0.1	2	
G20	SDSSJ100559.89+110919.6	0.076	12.9 ± 0.1	11.0 ± 0.1	1	
G21	SDSSJ105733.59+195154.2	0.077	13.1 ± 0.1	10.7 ± 0.1	1	
G22	SDSSJ085307.26+121900.8	0.081	12.7 ± 0.1	10.9 ± 0.1	1	
G23	SDSSJ211527.81-081234.4	0.091	12.9 ± 0.1	10.6 ± 0.1	1	
G24	SDSSJ234311.26+000524.3	0.097	13.5 ± 0.2	10.7 ± 0.1	1	
G25	SDSSJ135751.77+140527.3	0.099	12.9 ± 0.1	10.8 ± 0.1	1	
G26	SDSSJ134322.28+181114.1	0.178	14.1 ± 0.1	11.3 ± 0.1	2	
G27	SDSSJ115744.35+120750.8	0.183	13.9 ± 0.1	11.2 ± 0.1	1	
G28	SDSSJ002353.97+155947.8	0.192	13.1 ± 0.2	11.3 ± 0.1	1	
G29	SDSSJ090636.69+162807.1	0.301	15.3 ± 0.2	11.2 ± 0.2	1	PSC
G30	SDSSJ132047.13+160643.7	0.312	14.7 ± 0.1	11.5 ± 0.2	1	PSC

*N*otes: Column 3 redshifts were taken from Bauermeister et al. [2013] for EGNoG galaxies and from the original papers otherwise (see Sections 4.2.1 and 4.2.2). Column 4 total Vega apparent magnitudes were taken from the 2MASS PSC survey [Jarrett et al., 2000] for the galaxies so noted in Column 7 and from the 2MASS XSC survey [Skrutskie et al., 2006b] otherwise (see Section 4.2.3). Column 5 stellar masses were taken from MPA-JHU DR8 (see Section 4.2.5). Column 6 BPT classes follow the original Baldwin et al. [1981] classification (see Section 4.3.2). Column 7 lists the source of the data for sample galaxies not belonging to EGNoG, as well as galaxies not found in the 2MASS XSC survey.

and the standard expression [Holmberg, 1958]

$$i_{\rm b/a} = \cos^{-1}\left(\sqrt{\frac{q^2 - q_0^2}{1 - q_0^2}}\right) \ , \tag{4.1}$$

where q is the ratio of the semi-minor (b) to the semi-major (a) axis of the galaxy, q_0 is the intrinsic axial ratio when the galaxy is seen edge-on ($q_0 \equiv c/a$), and we take $q_0 = 0.2$ here as suggested for late-type systems [Pierce & Tully, 1988; Tully & Fisher, 1977a].

4.2.5 Stellar masses

The stellar mass of each galaxy was taken from the Max Planck Institute for Astrophysics-Johns Hopkins University Data Release 8[1] (MPA-JHU DR8). Each mass was derived by fitting the galaxy SDSS *ugriz* photometry to a grid of models from the Bruzual & Charlot [2003] stellar population synthesis code encompassing of a wide range of star formation histories. The mass and its uncertainty are defined as the median of the probability distribution and half the difference between the 16th and 84th percentiles of the distribution (1σ error), respectively. The stellar masses of all galaxies in our sample (both EGNoG and others) have therefore been estimated in a uniform manner. They are listed in Table 4.1.

4.2.6 Absolute magnitudes and K corrections

Because our sample galaxies span the redshift range $z = 0.05$ – 0.3, the portion of their spectra intercepted by the $K_{\rm s}$ filter varies from object to object, and we must correct the apparent magnitudes measured to rest-frame ($z = 0$) measurements. This so-called K correction is fully described in Hogg et al. [2002], and it was applied to our data using the publicly available code *kcorrect*[2] version 4 [Blanton & Roweis, 2007]. Using the spectroscopic redshifts provided (see Table 4.1), *kcorrect* finds the intrinsic spectrum that best represents the observed galaxy spectral energy distribution (SED; here SDSS *ugriz* and 2MASS *JHK*

[1] http://www.sdss3.org/dr10/spectro/galaxy_mpajhu.php
[2] http://howdy.physics.nyu.edu/index.php/Kcorrect

total apparent magnitudes) by fitting templates from the Bruzual & Charlot [2003] stellar population synthesis code. The templates have been optimised to minimise the residuals between the observed and modelled galaxy fluxes.

kcorrect also transforms apparent into absolute magnitudes by calculating the distance modulus for each galaxy, accounting for the angular diameter distance and cosmological surface brightness dimming. we adopt here the cosmological parameters from the latest Planck results [Planck Collaboration et al., 2015]. A Galactic extinction correction is also applied using the extinction maps of Schlegel et al. [1998]. The 2MASS Vega magnitudes are transformed to AB magnitudes to use *kcorrect*, but they were then transformed back to Vega magnitudes for use in this paper. Fully corrected total absolute K_s-band Vega magnitudes for all our sample galaxies were thus generated and are listed in Table 4.2.

4.3 Sample selection

4.3.1 Galaxy interactions

The TFR is only meaningful if the kinematic tracer used is rotationally-supported and in equilibrium. It is thus important to remove from our sample galaxies that are strongly interacting. This was already done based on inspection of SDSS images for the EGNoG sample. For the additional literature data, we first systematically excluded ULIRGs, as ULIRGs at $z \lesssim 0.3$ are dominated by mergers and/or strong interactions [e.g. Armus et al., 1987; Bushouse et al., 2002; Melnick & Mirabel, 1990; Surace et al., 2000]. The original infrared luminosities were also double-checked in the *Infrared Astronomical Satellite* (*IRAS*) Revised Bright Galaxy Sample catalogue [Sanders et al., 2003b], and one additional galaxy now deemed a ULIRG was excluded. This reduced the number of additional galaxies from the literature from 101 to 80 galaxies, all LIRGs by construction.

Second, the morphologies of all remaining sample galaxies were checked. we excluded all galaxies described as interacting in the original papers or in the NASA/IPAC Extragalactic

Table 4.2: TFR galaxy parameters.

Galaxy	M_{K_s} (mag)	W_{50} (km s^{-1})	b/a	$i_{b/a}$ (°)	$W_{50}/\sin i$ (km s^{-1})	Notes
(1)	(2)	(3)	(4)	(5)	(6)	(7)
Final sample galaxies						
G1	-24.5 ± 0.1	304.4 ± 37.0	0.77 ± 0.01	40.92 ± 0.01	464.7 ± 56.6	
G2	-25.1 ± 0.1	225.3 ± 39.1	0.21 ± 0.02	86.25 ± 0.07	225.8 ± 39.2	
G3	-22.9 ± 0.1	177.6 ± 42.3	0.68 ± 0.01	48.72 ± 0.01	278.4 ± 51.1	
G4	-24.7 ± 0.1	422.8 ± 96.2	0.59 ± 0.01	55.27 ± 0.01	514.5 ± 117.1	
G5	-25.1 ± 0.1	230.2 ± 22.4	0.63 ± 0.01	52.10 ± 0.01	291.7 ± 28.5	
G6	-24.5 ± 0.2	231.6 ± 59.1	0.63 ± 0.01	52.72 ± 0.01	291.1 ± 74.3	
G7	-25.3 ± 0.1	485.3 ± 37.2	0.62 ± 0.01	53.57 ± 0.01	603.1 ± 46.4	
G8	-24.5 ± 0.1	302.1 ± 78.5	0.84 ± 0.02	33.34 ± 0.04	549.5 ± 146.0	
G9	-24.7 ± 0.1	419.6 ± 23.0	0.72 ± 0.02	44.88 ± 0.03	594.6 ± 36.6	
G10	-24.5 ± 0.1	254.2 ± 24.0	0.45 ± 0.02	65.85 ± 0.02	278.6 ± 26.4	
G11	-26.3 ± 0.2	463.5 ± 65.8	0.85 ± 0.02	33.08 ± 0.03	849.3 ± 126.1	
G12	-24.7 ± 0.1	363.8 ± 78.9	0.52 ± 0.01	60.98 ± 0.02	416.0 ± 90.3	
G13	-26.1 ± 0.2	586.8 ± 57.9	0.44 ± 0.01	66.40 ± 0.02	640.3 ± 63.4	
G14	-25.2 ± 0.1	195.8 ± 36.6	0.76 ± 0.02	41.40 ± 0.03	296.0 ± 40.7	
G15	-25.5 ± 0.4	539.0 ± 61.6	0.54 ± 0.02	59.26 ± 0.03	627.2 ± 72.3	
G16	-26.5 ± 0.2	265.7 ± 21.7	0.87 ± 0.02	30.27 ± 0.04	527.0 ± 54.2	
Additional initial galaxies						
G17	-23.4 ± 0.1	243.7 ± 28.7	0.39 ± 0.01	69.95 ± 0.01	259.4 ± 30.6	s
G18	-24.6 ± 0.1	73.5 ± 9.3	0.93 ± 0.01	21.68 ± 0.01	198.9 ± 25.9	i
G19	-24.6 ± 0.1	171.6 ± 35.6	0.27 ± 0.01	79.34 ± 0.01	174.6 ± 36.2	s
G20	-24.7 ± 0.1	252.6 ± 58.3	0.57 ± 0.01	56.88 ± 0.01	301.6 ± 69.6	s
G21	-24.5 ± 0.1	405.9 ± 122.9	0.70 ± 0.01	46.57 ± 0.01	559.0 ± 169.3	s
G22	-25.1 ± 0.1	373.9 ± 19.1	0.98 ± 0.01	11.49 ± 0.07	1877.7 ± 637.6	i
G23	-25.1 ± 0.1	181.5 ± 67.2	0.50 ± 0.01	62.16 ± 0.01	205.3 ± 76.0	s
G24	-24.6 ± 0.2	144.7 ± 48.5	0.63 ± 0.01	52.67 ± 0.01	182.0 ± 61.1	s
G25	-25.3 ± 0.1	253.2 ± 131.2	0.73 ± 0.01	43.86 ± 0.01	365.5 ± 189.5	s
G26	-25.4 ± 0.1	355.4 ± 56.7	0.67 ± 0.02	49.08 ± 0.02	470.3 ± 75.7	s
G27	-25.5 ± 0.1	227.3 ± 9.1	0.93 ± 0.02	22.37 ± 0.04	597.3 ± 65.5	i
G28	-26.5 ± 0.2	399.0 ± 49.4	0.54 ± 0.02	59.21 ± 0.02	464.5 ± 57.7	s
G29	-25.3 ± 0.2	142.6 ± 13.8	0.77 ± 0.02	40.53 ± 0.04	219.4 ± 23.2	s
G30	-25.9 ± 0.1	297.6 ± 61.7	0.92 ± 0.03	23.60 ± 0.07	743.4 ± 189.8	s,i

*N*otes: Column 1 lists the galaxies as in Table 4.1. Column 2 corrected total Vega absolute magnitudes were calculated as described in Section 4.2.6. Column 3 velocity widths were calculated as described in Section 4.4.1. Column 4 axial ratios were taken from the SDSS r-band images (see Section 4.2.4). Column 5 inclinations were calculated as described in Section 4.2.4. Column 7 lists the reasons why galaxies were excluded from the final sample: "i" for a galaxy inclination $i < 30°$ and "s" for a single Gaussian integrated profile.

Database[1] (NED), and we removed objects showing signs of interactions in archival *Hubble Space Telescope* (*HST*) images (minor disturbances, bridges, tails, and mergers). These checks resulted in the rejection of a further 43 objects (none from EGNoG), leaving all 24 EGNoG galaxies and 37 additional objects from the literature.

4.3.2 AGN

As the emission from active galactic nuclei (AGN) can contaminate the measured stellar luminosities, we must also remove AGN from our TFR sample. We do this using the MPA-JHU classifications of the galaxies' optical emission line ratios from the SDSS spectra [Brinchmann et al., 2004], inspired by the Baldwin et al. [1981] diagnostic diagrams (BPT diagrams). According to this, 31 of the 37 additional galaxies from the literature harbour an AGN (or are rejected). None of the EGNoG galaxies does by construction, therefore leaving 30 galaxies with BPT class 1 or 2 (i.e. star-forming or low S/N star-forming galaxies) for our TFR analyses, including all 24 ENGoG galaxies and 6 additional objects from the literature. This initial sample of 30 galaxies is listed in Table 4.1.

It is rather disappointing that the number of additional literature galaxies has been reduced so much (from 101 to 6 galaxies), but it is perhaps unsurprising as LIRGs and ULIRGS are often disturbed and the fraction of galaxies with AGN activity increases with increasing infrared luminosity [Veilleux et al., 2002, 1999; Wang et al., 2006]. Nevertheless, the EGNoG sample is increased by 25% by the inclusion of those galaxies.

4.3.3 Inclination

We drew a higher quality sub-sample from our initial sample of 30 galaxies by imposing two additional requirements specific to TFR studies. First, as a galaxy approaches a face-on orientation ($i = 0°$), the uncertainty in the inclination increases. This is particularly problematic as the inclination correction to the velocity width measured is then also large

[1] https://ned.ipac.caltech.edu

($\sin^{-1} i$). To minimise the uncertainties associated with small inclinations, we therefore only retained galaxies with $i \geq 30°$ (a standard cutoff; see e.g. Pierce & Tully 1988; Tiley et al. 2015). 4 of the 30 galaxies in our initial sample have $i < 30°$ and will thus be excluded from our final sample. They are labeled as such in column 7 of Table 4.2.

4.3.4 Integrated profile shape

While this is not a formal proof and the shape of an integrated profile depends on the exact shape of both the circular velocity curve and the surface brightness profile of the kinematic tracer, a kinematic tracer that extends significantly past the turnover of the circular velocity curve will usually yield a double-horned or boxy profile (see e.g. Davis et al. 2011b). Our line profile analysis in Section 4.4.1 indicates that 19 of the 30 galaxies in our initial sample (including three with $i < 30°$) have double-horned or boxy profiles and are thus likely to yield reliable velocity width measurements. The remaining 11 galaxies (including one with $i < 30°$) have line profiles best represented by a single Gaussian and will thus be excluded from our final sample. They are labeled as such in column 7 of Table 4.2.

Overall, our final sample of galaxies with inclination $i \geq 30°$ and a double-horned or boxy integrated profile is thus composed of 16 galaxies (from an initial sample of 30), 12 from EGNoG and 4 additional galaxies from the literature. For our TFR analyses, we shall construct TFR relations and report the results for both the final and initial samples. However, we shall base our discussion on the higher quality final sample only.

4.4 Velocity measurements and Tully-Fisher relations

4.4.1 Velocity widths

The second observable required to construct a TFR is a measurement of the circular velocity, or in the case of integrated spectra (half) the width of the line profile. The line widths at 20% (W_{20}; e.g. Davis et al. 2011b; Tully & Fisher 1977a; Tully & Pierce 2000) and

50% (W_{50}; e.g. Lavezzi & Dickey 1998; Schoniger & Sofue 1994b; Tiley et al. 2015) of the peak intensity are commonly used measures of the maximum rotational velocity, but Lavezzi & Dickey [1997] found that W_{50} has smaller uncertainties and suffers the least bias. we thus adopt W_{50} has our measure of (twice) the rotation velocity.

Tiley et al. [2015] tested four fitting functions when using CO integrated spectra in the context of TFR studies. Using simulated spectra generated from modeled galaxies, they found that the double-horned Gaussian Double Peak function (a quadratic function bordered by half-Gaussians on both sides; see below) was the most appropriate, in the sense that it yielded the most consistent velocity width measures as a function of both amplitude-to-noise ratio (A/N) and inclination, this for a wide range of maximum circular velocities. The only exceptions were at very low inclination and circular velocities, where the single-peaked Gaussian function was unsurprisingly better suited (as even intrinsically double-horned spectra appear single-peaked when spread over only few velocity channels).

Here, we thus fit all our integrated spectra with both the Gaussian Double Peak function and the single Gaussian function, and we adopt the fit with the lowest reduced χ^2 (defined in the standard manner; but see below). The fits were carried out with the package MPFIT [Markwardt, 2009b], that employs a Levenberg-Marquardt minimisation algorithm. To avoid local minima, in each case we ran MPFIT several times with different initial guesses. The fitting parameters with the smallest $|1 - \chi^2_{\rm red}|$ value were taken as the best fit.

The form of the Gaussian Double Peak function is as follows:

$$f(v) = \begin{cases} A_{\rm G} \times \mathrm{e}^{\frac{-[v-(v_0-w)]^2}{2\sigma^2}} & v < v_0 - w \\ A_{\rm C} + a\,(v - v_0)^2 & v_0 - w \leq v \leq v_0 + w \\ A_{\rm G} \times \mathrm{e}^{\frac{-[v-(v_0+w)]^2}{2\sigma^2}} & v > v_0 + w \end{cases} , \tag{4.2}$$

where v is the velocity, $A_{\rm C} > 0$ is the flux at the central velocity v_0, $A_{\rm G} > 0$ is the peak flux of the half Gaussians on both sides (centred at velocities $v_0 \pm w$), $w > 0$ is the half-width of

the central parabola, $\sigma > 0$ is the width of the profile edges, and $a \equiv (A_{\rm G} - A_{\rm C})/w^2$.

The velocity width W_{50} and its uncertainty can then be easily calculated analytically. Defining

$$A_{\rm max} \equiv \begin{cases} A_{\rm C} & \text{if } A_{\rm C} \geq A_{\rm G} \\ A_{\rm G} & \text{if } A_{\rm C} < A_{\rm G} \ , \end{cases} \tag{4.3}$$

then if $A_{\rm G} \geq A_{\rm max}/2$ (i.e. the central parabola is either concave, expected for a standard double-horned profile, or slightly convex) the profile width is determined by the two half-Gaussians and W_{50} and its uncertainty are given by

$$\begin{aligned} W_{50} &= 2\,(w + \sqrt{2\ln 2}\,\sigma) \ , \\ \Delta W_{50} &= 2\,\sqrt{\Delta w^2 + 2\ln 2\,\Delta\sigma^2} \ . \end{aligned} \tag{4.4}$$

If $A_{\rm G} < A_{\rm max}/2$ (i.e. the central parabola is strongly convex) the profile width is determined by the central parabola but the profile is in fact not really double-horned and it is preferable to adopt a single Gaussian fit irrespective of the $\chi^2_{\rm red}$ values.

As can be expected from the parametrisation of the Gaussian Double Peak function above, the single Gaussian function is given by

$$f(v) = A\,{\rm e}^{\frac{-(v-v_0)^2}{2\sigma^2}} \ , \tag{4.5}$$

where $A > 0$ is the flux of the peak at the central (and mean) velocity v_0, and $\sigma > 0$ is the width of the profile (root mean square velocity). The velocity width W_{50} and its uncertainty are then given by

$$\begin{aligned} W_{50} &= 2\,\sqrt{2\ln 2}\,\sigma \ , \\ \Delta W_{50} &= 2\,\sqrt{2\ln 2}\,\Delta\sigma \ , \end{aligned} \tag{4.6}$$

as for the Gaussian Double Peak function with $w = 0$ and $\Delta w = 0$.

We further note here that while $A_{\rm max}/2$ is the mathematically convenient threshold to determine whether one should use the Gaussian Double Peak function or the single Gaussian

function, Tiley et al. [2015] established that $2A_{\rm max}/3$ is a more practical threshold to use. We therefore adopt this convention here, and use the Gaussian Double Peak function (Eqs. 4.2 and 4.4) when $A_{\rm G} \geq 2A_{\rm max}/3$ and the single Gaussian function (Eqs. 4.5 and 4.6) otherwise.

4.4.2 Tully-Fisher relation

We constructed $M_{K_{\rm s}}$ and $M_\star$ TFRs for the galaxies in both our initial and final samples. We used a standard form for the TFR,

$$M_{K_{\rm s}} = a \left[\log \left(\frac{W_{50}/\sin i}{\text{km s}^{-1}} \right) - 2.5 \right] + b \ , \tag{4.7}$$

similarly with $\log(M_\star/M_\odot)$ on the left-hand side, where a is the slope and b the zero-point of the relation. We fit this linear relationship to the data using the MPFITEXY routine [Williams et al., 2010], that uses the MPFIT package. The intrinsic scatter ($\sigma_{\rm int}$) in the relation was estimated by adjusting its value to ensure $\chi^2_{\rm red} = 1$. A fuller description of the fitting procedure can be found in Williams et al. [2010] and Tiley et al. [2015].

Since there is a significant bias in the slope of the forward fit [Willick, 1994], we also fit the inverse of Equation 4.7 (similarly to Davis et al. 2011b; Tiley et al. 2015; Williams et al. 2010). In addition, we fit a number of TFRs with the slope fixed to that of past studies [Davis et al., 2011b; Tiley et al., 2015; Torii et al., 2015; Tully & Pierce, 2000]. The $K_{\rm s}$-band and $M_\star$ TFRs for both the initial and the final sample are shown in Figure 4.1 along with fixed slope fits, and the fits parameters are listed in Tables 4.3 and 4.4. While we list the results of both the forward and reverse fits in the tables, we shall restrict our discussion to the more reliable reverse fits.

We note here that our work is the first attempt to construct a TFR for galaxies beyond the local universe using CO emission as the kinematic tracer.

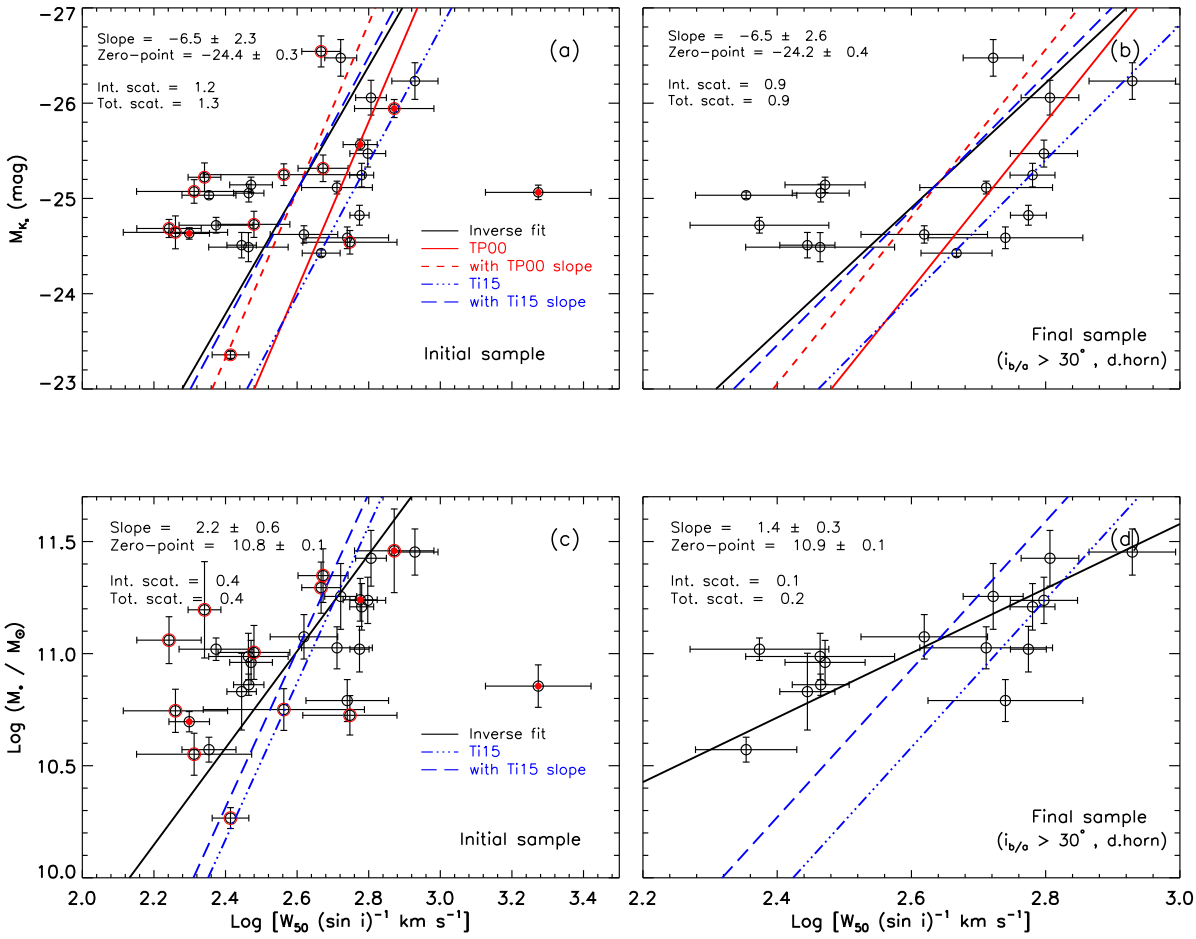

Figure 4.1: **Top**: K_s-band CO TFR for the initial (left) and final (right) samples. The black solid lines show the reverse fits, while the red dashed (respectively blue long dashed) lines show the reverse fit with slope fixed to that of Tully & Pierce [2000] (resp. Tiley et al. 2015). The red solid lines show the H I TFR of local spirals from Tully & Pierce [2000]. The triple dot-dashed lines shows the CO TFR of local spirals [Tiley et al., 2015]. **Bottom**: As for the top panels, but for the $M_\star$ CO TFR. In panels (a) and (c), the data points shown as open red circles represent galaxies with a single Gaussian profile, while those shown as filled red circles represent galaxies with $i_{b/a} < 30°$.

Table 4.3: Best fit parameters for the K_s-band CO TFRs.

Sample	Fit type	Slope	Zero-point (mag)	σ_{int} (mag)	σ_{total} (mag)	Zero-point offset (Our - Their)
Initial	Forward	-1.5 ± 0.5	-24.9 ± 0.1	0.59	0.60	–
	Reverse	-6.5 ± 2.3	-24.4 ± 0.3	1.20	1.28	–
Final	Forward	-2.2 ± 0.8	-24.8 ± 0.2	0.52	0.52	–
	Reverse	-6.5 ± 2.6	-24.2 ± 0.4	0.90	0.94	–
	Fixed (Ti15)	-7.1	-24.2 ± 0.3	0.94	1.03	-0.89 ± 0.29
	Fixed (To15)	-7.7	-24.1 ± 0.3	1.03	1.12	-0.38 ± 3.46
	Fixed (TP00)	-8.8	-23.9 ± 0.3	1.17	1.28	-0.76 ± 0.55

*N*otes: Ti15: Tiley et al. [2015], To15: Torii et al. [2015], TP00: Tully & Pierce [2000].

Table 4.4: Best-fit parameters for the $M_\star$ CO TFRs.

Sample	Fit type	Slope	Zero-point $\log(M_\star/M_\odot)$	σ_{int} $\log(M_\star/M_\odot)$	σ_{total} $\log(M_\star/M_\odot)$	Zero-point offset (Our - Their)
Initial	Forward	0.8 ± 0.2	10.9 ± 0.1	0.23	0.26	–
	Reverse	2.2 ± 0.6	10.8 ± 0.1	0.38	0.42	–
Final	Forward	1.3 ± 0.2	10.9 ± 0.1	0.10	0.15	–
	Reverse	1.4 ± 0.3	10.9 ± 0.1	0.10	0.16	–
	Fixed(Ti15)	3.3	10.6 ± 0.1	0.36	0.43	0.35 ± 0.11

*N*otes: Ti15: Tiley et al. [2015].

4.5 Results & Discussion

Being a relation between luminous and dynamical (i.e. total) mass, the TFR informs us about both the structural and dynamical properties of galaxies, particularly their size and total mass-to-light ratio (and thus all properties affecting this ratio, such as the stellar M/L, gas content, dark matter, etc). Comparing the TFRs measured for different galaxy samples thus reveals differences in those properties, that are however tightly connected to the way the samples were selected. For example, comparing the TFRs of galaxies of different types at a given redshift will inform on differences between those types [e.g. Lagattuta et al., 2013; Russell, 2004; Shen et al., 2009], while comparing the TFRs of galaxies of a given type at different redshifts will inform on the evolution of those galaxies [e.g. Conselice et al., 2005; Flores et al., 2006; Puech et al., 2008]. Similarly, luminosities for a given sample measured in different bands will inform on the stellar M/L. However, when comparing different TFRs, one

must make sure that all the parameters used (e.g. luminosity, rotation velocity, inclination, and any corrections to those) are measured in an identical manner, as otherwise any difference in the zero-points and/or slopes could be due to different systematics between the methods used rather than any intrinsic physical differences between the samples. With those caveats in mind, we compare our results to others in the literature below.

4.5.1 Previous studies

The literature on the TFR is vast, but the number of studies using CO as the kinematic tracer is small. The most recent studies are those of Davis et al. [2011b], Tiley et al. [2015] and Torii et al. [2015]. Davis et al. [2011b] studied ETGs, however, so we will refrain from a comparison here as we would be unable to assign any difference to a redshift evolution rather than structural differences, or vice-versa. Tiley et al. [2015] and Torii et al. [2015] also targeted disc galaxies and measured the velocity widths in a manner identical to us. They are thus best suited for comparison. The sample of Tiley et al. [2015] is composed ≈ 300 disc galaxies from the CO Legacy Database for the GASS survey (COLD GASS; Saintonge et al. 2011) and they used the Wide-Field Infrared Survey Explorer (WISE) Band 1 ($W1$, $\approx 3.4\mu$m) to construct their TFR. Although the $W1$ band is not identical to the 2MASS $K_{\rm s}$ band ($\approx 2.4\mu$m), both filters trace similar stellar populations and $K - W1 \approx 0.0 \pm 0.2$ mag for late-type galaxies [Lagattuta et al., 2013]. Torii et al. [2015] studied ≈ 50 late-type nearby galaxies and also used 2MASS $K_{\rm s}$-band magnitudes.

Despite their use of H I rather than CO, we also discuss the work of Tully & Pierce [2000] below, as it is generally considered the standard reference on the subject. Tully & Pierce measured the velocity width at 20% of the peak (rather than 50% as done here). While the difference is generally small, the velocity width at 20% of the peak is systematically larger.

4.5.2 Evolution with redshift

Some early works suggest an evolution (i.e. a different zero-point) of the B-band TFR at intermediate redshifts, in the sense that higher redshift galaxies are brighter at a given rotational velocity [e.g. Böhm et al., 2004; Milvang-Jensen et al., 2003; Simard & Pritchet, 1998; Vogt et al., 1996; Ziegler et al., 2002], although it may be that only low-mass systems show such an offset [Böhm et al., 2004; Ziegler et al., 2002]. More recent works however seem to indicate that there is no evolution in the K-band relation (e.g. Conselice et al. 2005; Flores et al. 2006; but see Puech et al. 2008 who found that $z \approx 0.6$ galaxies are *fainter* than local galaxies by 0.66 ± 0.14 mag at K-band). On a different note, Ziegler et al. [2002] studied the B-band TFR of 60 late-type galaxies at $z = 0.1$–1.0, and found that the slope is flatter for distant galaxies.

As the galaxies in our samples cover a reasonable range in redshift ($z = 0$–0.3 corresponds to a roughly 3.5 Gyr lookback time), it is possible to probe whether the TFR has evolved during that period by simply breaking down our own samples by redshift. We therefore split our samples into three redshift bins and constructed the CO TFR for each bin separately. Bin A includes galaxies at $z = 0.05$–0.1 (all galaxies in redshift bin A of Bauermeister et al. 2013 and all additional literature galaxies), bin B galaxies at $z = 0.17$–0.20 (redshift bin B of Bauermeister et al. 2013), and bin C galaxies at $z = 0.28$–0.3 (redshift bin C of Bauermeister et al. 2013). We found that the slope and zero-point of the CO TFR for bins A and B are consistent within the uncertainties, although the slope for bin A has a larger uncertainty. There are only two galaxies of the final sample in bin C, not enough for a reliable fit. We therefore conclude that within the redshift range probed in our study, there is no significant evidence for a change of the slope and/or zero-point of the CO TFR.

The other way to test for redshift evolution is to compare our own results with those of other studies of local galaxies, although we then also have to be aware of differences between the samples or methods. Comparing to the TFR studies discussed above (Section 4.5.1),

our results (see Table 4.3) indicate that the slope of the reverse K_s-band CO TFR of the final sample is consistent with that of nearby disc galaxies within the uncertainties (that are however quite large; e.g. Tiley et al. 2015; Torii et al. 2015; Tully & Pierce 2000; see also Ziegler et al. 2002). This therefore reinforces the suggestion that there is no evolution of the slope of the TFR as a function of redshift up to $z \approx 0.3$.

Fixing the slope of the reverse fit to that of the spirals in Tiley et al. [2015], Torii et al. [2015] and Tully & Pierce [2000], we found a zero-point offset (our fit minus their) of -0.89 ± 0.29, -0.38 ± 3.46 mag and -0.76 ± 0.55, respectively. Tiley et al. [2015] being the study most similar to ours, this suggests that, at a given rotation velocity (i.e. dynamical mass), our sample galaxies are brighter than local galaxies by ≈ 0.9 mag (a factor of slightly more than 2 in luminosity).

Now turning our attention to the $M_\star$ CO TFR (see Figure 4.1), we can see from Table 4.4 that the scatter is reduced compared to the K_s-band relation, as expected given that M_{K_s} is only a proxy for stellar mass. The slope of the $M_\star$ CO TFR for our galaxy sample is also significantly flatter than that of Tiley et al. [2015] for local spiral galaxies. Nevertheless, fixing the slope to that of Tiley et al. [2015], we found a zero-point offset (our fit minus their) of 0.35 ± 0.11 dex, suggesting a mild evolution of the $M_\star$ TFR zero-point since $z \approx 0.3$, in the sense that our sample galaxies are slightly more than twice as massive as local galaxies.

At face value, our results for the K_s-band CO and $M_\star$ TFRs are entirely consistent, suggesting that compared to local galaxies our sample galaxies are larger by a factor of slightly more than 2 in both luminosity and mass, exactly what would be expected if all the galaxies in both our and the comparison samples had the same stellar M/L. However, as they were selected to be on the star-formation main sequence at their redshift [Bauermeister et al., 2013], and as the SFR of the main sequence increases with redshift [e.g. Noeske et al., 2007], one would naively expect the higher redshift galaxies to have lower stellar (and thus dynamical) M/L. This would naturally explain the luminosity offset measured at a given rotational velocity, but would not predict a commensurate offset in mass (as the stellar M/L

of our sample galaxies would then be lower than those of the comparison galaxies). Assuming that, like the stellar masses, the dynamical masses ($M_{\rm dyn}$) of our sample galaxies are also larger than those of the comparison sample galaxies, then the offset in mass measured implies that our sample galaxies have a larger characteristic size ($R_{\rm c}$) at a given rotational velocity ($M_{\rm dyn} \propto W_{50}^2 R_{\rm c}$).

Overall, this thus appears consistent with a scenario in which our sample galaxies at higher redshifts are indeed more heavily star-forming than local galaxies, thus appearing more luminous at a given rotation velocity, but they are also intrinsically larger (less compact), thus also appearing more massive at a given velocity. Equivalently, as they evolve into lower redshift galaxies, the stellar populations of our sample galaxies must fade (simple aging of the stellar populations) and their bulges must grow (due to the generally centrally-concentrated enhanced star formation). Our sample galaxies would thus evolve into today's spirals in a manner analogous to how distant spirals evolve into today's ETGs [e.g. Williams et al., 2010].

This scenario is in principle testable, by measuring and comparing the (specific) SFRs and characteristic sizes of both our sample galaxies and the comparison sample galaxies. We shall therefore investigate these issues in a follow-up study in the near future.

4.5.3 Intrinsic scatter

As can be seen from Table 4.3, the intrinsic scatter of the reverse $K_{\rm s}$-band CO TFR for the final sample ($\sigma_{\rm int} = 0.9$) is higher than that of Tiley et al. [2015] ($\sigma_{\rm int} = 0.7$), Torii et al. [2015] ($\sigma_{\rm int} = 0.4$), and also Davis et al. [2011b] ($\sigma_{\rm int} = 0.6$). The reasons for this are unclear, since the final sample only contains galaxies that should yield robust measurements, but we can speculate.

The TFR is known to have a much greater scatter at higher redshifts, this for a variety of reasons such as greater variations of the stellar mass fraction (and thus total M/L ratio) and stellar M/L ratio, and most importantly increased morphological and dynamical anomalies [e.g. Flores et al., 2006; Kannappan et al., 2002; Kassin et al., 2007]. It could thus be that

some of these effects are already significant at $z \lesssim 0.3$.

Our inclinations derived from the stellar axial ratios could also introduce more scatter than superior measurements [e.g Davis et al., 2011b], although as long as the uncertainties are properly quantified then this should only affect the total scatter ($\sigma_{\rm total}$) and not the intrinsic scatter ($\sigma_{\rm int}$). In addition, due to the difficulty of identifying interacting and/or disturbed galaxies at the modest resolution of SDSS, it is possible that despite our best efforts to exclude them some interacting galaxies do remain in the initial and final samples. Overall, however, the main reason behind the large intrinsic scatter measured remains unclear.

4.5.4 Inclinations

In view of the comments in the previous section (Section 4.5.3), it is worth nothing that the accuracy of the TFR fits strongly depends on the accuracy of the inclination measurements, as the circular velocity measurements (here the velocity widths) must be corrected for the inclination of the galaxies. We used here stellar axial ratios to estimate the inclination, as is common in the literature [e.g. Davis et al., 2011b; Tiley et al., 2015; Torii et al., 2015; Tully & Pierce, 2000]. Although these inclinations can lead to a large scatter in the TFR, they do not generally affect its slope and/or zero-point [e.g. Davis et al., 2011b]. For our sample, the slope and zero-point obtained for the initial sample are consistent with those of the final sample within the uncertainties (see Table 4.3 and 4.4), indicating that our results are indeed robust and only minimally affected by inclination uncertainties.

4.5.5 CO as a kinematic tracer

Lastly, it is worth reflecting on the use of CO as a kinematic tracer. There are arguably multiple advantages to using CO for TFR studies rather than the more widely used H I line. First and perhaps most important, we can detect CO to much greater distances than H I, it being routinely detected in normal star-forming galaxies at intermediate redshifts ($z \approx$ 1-3; Genzel et al. 2015; Tacconi et al. 2010) and in star-bursting galaxies up to $z \approx 7$ [Riechers

et al., 2009; Wang et al., 2011]. Second, the beam size of CO observations is typically much smaller than that for H I, both for single-dish and interferometric observations, easily allowing to spatially resolve galaxies (and individual members within clusters of galaxies) even at high redshifts. Third, with its extended distribution the H I in galaxies can easily be disturbed in the outer parts (e.g. by interactions and fly-bys), leading to unreliable line widths. CO on the other hand is less extended radially and more tightly correlated with the stellar component, and thus less affected by interactions [Lavezzi & Dickey, 1998]. Although this is admittedly less of an issue with robust selection criteria seeking to exclude interacting galaxies, Lavezzi & Dickey [1997] analysed simulated CO spectra to measure the maximum rotational velocity for different line shapes. They found that very little CO gas needs to lie in the flat part of the rotation curve to measure the maximum rotational velocity accurately. CO is therefore a useful tracer for TFR studies, even in galaxies in the central regions of clusters or groups where there is a greater possibility of interactions [e.g. Schoniger & Sofue, 1994a; Tutui & Sofue, 1997].

More generally, although H I line profiles are usually very similar among different galaxies, CO line profiles show a greater variety. This is for several reasons: inner velocity field and/or CO distribution differences, beam response along the disc, pointing errors (for single-dish observations), opacity effects, etc [Lavezzi & Dickey, 1997]. Nevertheless, even in ETGs where the radial extent of the molecular gas can be very limited [Davis et al., 2013b], Davis et al. [2011b] have shown that galaxies with a double-horned or boxy integrated CO profile do yield accurate measurements of the maximum circular velocity (see also Tiley et al. 2015), whereas galaxies with a single-peaked profile often do not. This fact underlies our selection of the final sample from the initial sample (see Sections 4.3.3 and 4.3.4).

4.6 Conclusions

We studied the K_s-band CO TFR of 30 galaxies at $z \approx 0.05$ – 0.3 and compared our results to those obtained for similar local disc galaxy samples. This represents the first attempt to construct a TFR for disc galaxies beyond the local universe using CO as a kinematic tracer. The principal results are summarised below.

1. The best-fit reverse TFR is $M_{K_s} = (-6.5 \pm 2.6) \left[\log\left(\frac{W_{50}/\mathrm{km\ s^{-1}}}{\sin i}\right) - 2.5\right] + (-24.2 \pm 0.4)$, where M_{K_s} is the corrected total absolute Vega K_s-band magnitude of the objects and W_{50} is the width of their integrated CO line profile at 50% of the maximum.

2. We do not find significant evidence for an evolution of either the slope or zero-point of the TFR as a function of redshift within our sample. However, when comparing to other TFR studies of local disc galaxies, we find a mild offset of the zero-point in the sense that our sample galaxies are brighter than local spirals by 0.89 ± 0.29 mag at a given rotation velocity.

3. The stellar mass CO TFR also indicates a mild offset in the zero-point, in the sense that our sample galaxies are more massive than local spirals by 0.35 ± 0.11 dex.

4. Similarly to galaxies at much higher redshifts, our sample galaxies show a higher intrinsic scatter around the best-fit TFR than local galaxies. The main drivers of this scatter are also likely analogous, i.e. a higher gas fraction coupled with more intense star formation, and morphological as well as dynamical disturbances.

5. While our results deserve further study, we speculate that the TFR offsets derived imply that our sample galaxies are more heavily star-forming (thus appearing more luminous) and are intrinsically larger (thus appearing more massive) at a given rotation velocity than similar local galaxies.

More generally, our study supports the view that CO is an excellent kinematical tracer for TFR studies. As CO is relatively easily detected even in distant galaxies, our study also provides a useful benchmark for future high-redshift CO TFR studies, themselves a powerful tool to probe the cosmological evolution of the M/L of galaxies.

4.A Integrated CO profiles and best fits

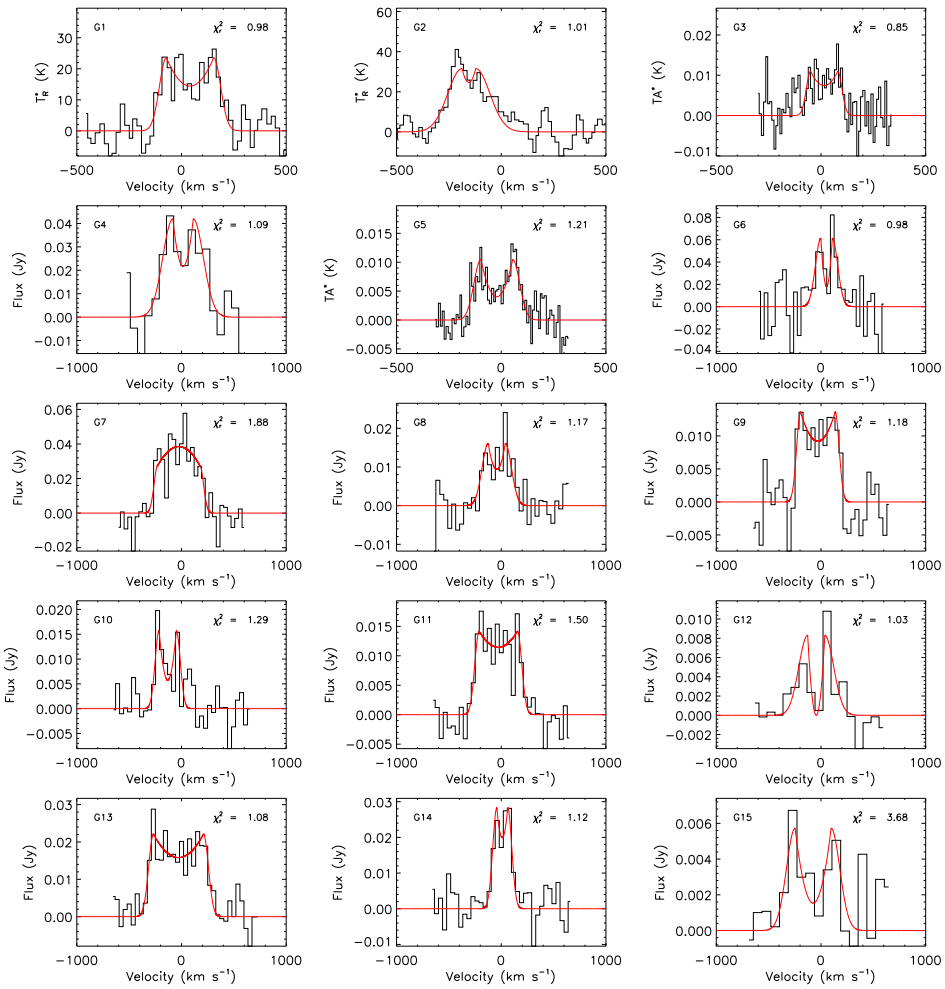

Figure A.1: Integrated CO profiles of the sample galaxies, taken from Bauermeister et al. [2013] and additional literature sources (see Section 4.2.2). For each plot, the red line shows the best parametric fit to the spectrum (see Section 4.4.1). The name of the galaxy as listed in Tables 4.1 and 4.2 is indicated in the top-left corner of each plot, and the reduced χ^2 value of the fit is indicated in the top-right corner.

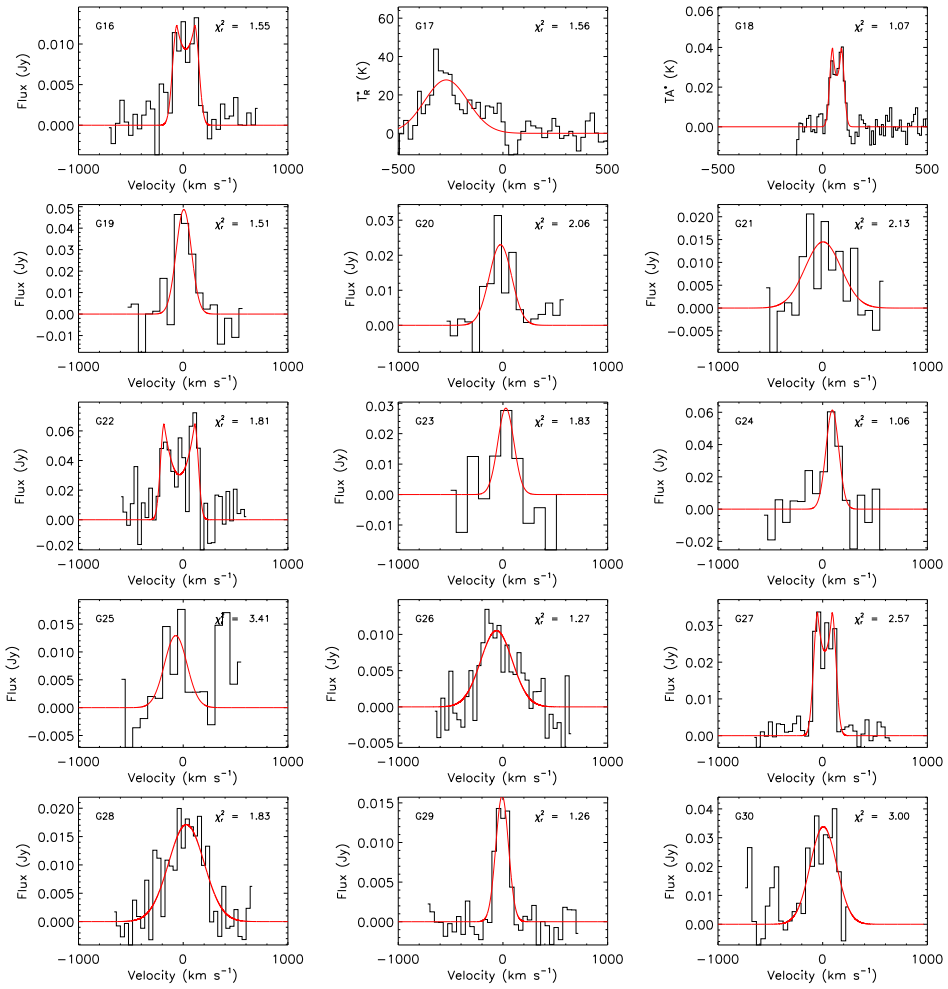

Figure A.1: Continued.

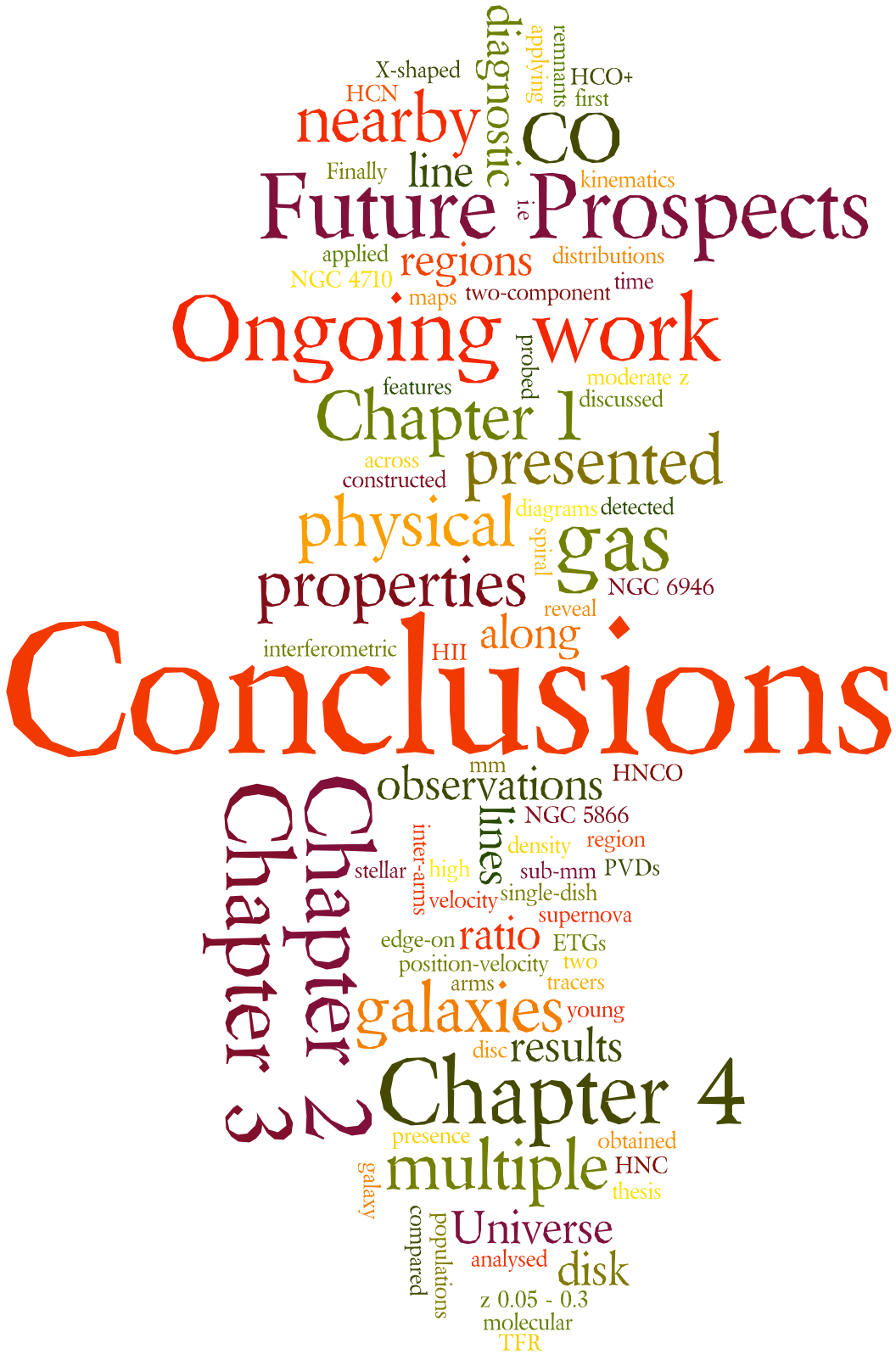
Conclusions
Ongoing work
Future Prospects
Chapter 1
Chapter 2
Chapter 3
Chapter 4
nearby
CO
diagnostic
line
regions
presented
physical
gas
properties
galaxies
multiple
Universe
disk
results
observations
lines
ratio
along
X-shaped
HCN
HCO+
first
remnants
applying
Finally
kinematics
i.e
applied
distributions
NGC 4710
time
maps
two-component
probed
moderate z
features
discussed
across
constructed
diagrams
detected
spiral
NGC 6946
reveal
interferometric
HII
mm
HNCO
NGC 5866
density
region
inter-arms
stellar
high
sub-mm
PVDs
velocity
single-dish
supernova
edge-on
ETGs
position-velocity
two
arms
tracers
young
disc
presence
obtained
HNC
galaxy
thesis
compared
populations
analysed
z 0.05 - 0.3
molecular
TFR

5

Conclusions

"We are the local embodiment of a Cosmos grown to self-awareness. We have begun to contemplate our origins: starstuff pondering the stars; organized assemblages of ten billion billion billion atoms considering the evolution of atoms; tracing the long journey by which, here at least, consciousness arose. Our loyalties are to the species and the planet. We speak for Earth. Our obligation to survive is owed not just to ourselves but also to that Cosmos, ancient and vast, from which we spring."

Carl Sagan (COSMOS, 1980)

In this thesis, we presented (sub-)mm observations of molecular gas and studied the physical properties of this gas in disc galaxies across the Universe (up to $z = 0.3$). In Chapter 2, we presented single-dish observations of multiple lines of CO detected in eight carefully-selected

regions along the arms and inter-arms of the nearby spiral galaxy NGC 6946. We further probed the physical properties of the gas in each region by using line ratio diagnostics and discussed the results in relation to the star-formation activity in each region (as traced by indicators of young stellar populations, such as supernova remnants and H II regions). In Chapter 3, we presented interferometric maps of multiple lines of CO as well as high density tracers (i.e. HCN, HCO^+, HNC and HNCO) in two nearby edge-on ETGs, NGC 4710 and NGC 5866. To reveal the physical properties and kinematics of the gas, we discussed the X-shaped position-velocity diagrams (PVDs) observed (revealing two bar-driven kinematic components) and again applied line ratio diagnostics along the discs, contrasting the physical conditions of the tenuous and dense molecular gas in both kinematic components. Finally, in Chapter 4, we constructed the CO TFR of disc galaxies at $z = 0.05 - 0.3$, the first CO TFR for galaxies beyond the local Universe, and compared our results with those obtained for similar disc galaxies at $z = 0$.

In the next section, we summarise the main results of this thesis, discuss ongoing work, and conclude with some future prospects for the field.

5.1 Summary of the Main Results

5.1.1 Molecular gas in the disc of NGC 6946

In Chapter 2, we aimed to better understand the molecular gas physics and its relation to the presence of young stellar populations (existence of SNe, H II regions, H I holes, young massive stars, etc) and morphological structures (arm and inter-arm regions, galaxy centre) in the spiral galaxy NGC 6946. To achieve this, we analysed multiple CO lines in several regions along and between the arms of the galaxy, and used a radiative transfer code to probe the physical properties of the gas.

We provided the most complete CO ladders ever generated for this galaxy, with observations of ^{12}CO (1–0, 2–1, 3–2, 4–3, 6–5) and ^{13}CO (1–0, 2–1). The main results of this work

are as follows.

A single-dish map obtained from multi-pointing observations of CO (2–1) over the galaxy reveals that the molecular gas extends over the entire disc, with more concentrations along the arms. The radial profiles of multiple lines of CO indicate that the galaxy disc consists of two components: a centrally-concentrated molecular core and a nearly flat lower surface brightness extended disc.

From the spectral line energy distributions (SLEDs) constructed from all the CO transitions available in each region, some of the regions appear to have star-formation activity that is more intense than that at the centre of the Milky Way, while other regions appear to have a similar level. However, although our study attempts to constrain the physical conditions of the gas based on our new CO SLEDs, recent studies have shown that even higher transitions of CO are required to truly reveal the turnover of the SLEDs, and thus the level of star-formation activity.

The eight regions studied along the disc of NGC 6946 can be divided into three different groups based on presence or absence of young stellar population indicators and their location within the galaxy disc. One would therefore have expected to find different beam-averaged physical properties from one group to another. However, the most likely model parameters (i.e. kinetic temperature $T_{\rm K}$, molecular hydrogen number volume density $n(\rm H_2)$ and CO number column density $N(\rm CO)$) do not reflect the empirical results inferred from the observed line ratios. This is at least partially because we have defined robust uncertainties based on the marginalised probability distribution functions (PDFs), that are much larger than usually assumed. The number of CO transitions used is however also limited, and adding higher-J transition should yield more accurate results. If the regions probed have a complex molecular ISM, an analysis combining low-J CO lines and RADEX (that assumes a single component molecular ISM) may not be sufficient to probe the full gas properties. A more sophisticated code exploiting a more complete CO SLED may be required.

5.1.2 Extensive CO and high density gas in early-type galaxies

In Chapter 3, we studied the content, physical properties and kinematics of both tenuous molecular gas traced by CO and dense molecular has traced by HCN, HCO^+, HNC and HNCO, this along the discs of the edge-on ETGs NGC 4710 and NGC 5866. Given the large number of molecular species detected and the relatively high spatial resolution of the observations, this study provides an important step to better understand the kinematics and physical conditions of the molecular gas in "red and dead" ETGs. The main results of this study are summarised below.

The X-shaped PVDs seen in both galaxies indicate the presence of two different (bar-driven) kinematic components in each, a nuclear disc and inner ring. Spectra were thus extracted from the PVDs along the equatorial planes, to obtain line ratios as a function of radius in both components.

The ratios of the CO lines, dense gas tracers, and CO versus dense gas tracers, indicate that the physical conditions along the nuclear discs and inner rings are likely to be different. Most importantly, the nuclear discs appear to contain optically thinner and hotter CO gas with a higher fraction of dense gas, while the inner rings appear to contain optically thicker and colder CO gas with a lower dense gas fraction. In addition, in the nuclear discs, HCN appears to be chemical enhanced with respect to HCO^+, HNC and HNCO, potentially due to UV radiation from young massive stars, while the existence of HCO^+ and HNCO may indicate that cosmic rays (CRs) and shocks are present in the ISM of both galaxies (but are weaker then those in starbursts). However, while the empirical line ratios suggest these differences, our most likely model parameters (T_K, $n(H_2)$ and $N(CO)$) do not support them in a statistically significant manner, because of the large associated uncertainties.

The line ratios measured along the discs of NGC 4710 and NGC 5866 were also compared to those measured in the nuclei of galaxies of different types (normal spirals, starbursts, lenticulars, Seyferts and peculiars) as well as individual GMCs in nearby spirals. The ratios

of CO lines in the disc of NGC 4710 differ from those seen in the nuclei of starbursts, while those of NGC 5866 are similar. Interestingly, the dense gas fraction in the nuclear disc of both galaxies is similar to that seen in the centre of starbursts, while the inner rings have dense gas fractions similar to those in the nuclei of Seyferts and some spirals.

This study is only the first attempt to probe the gas physics along the disc of ETGs using high resolution observations of multiple lines of both CO and dense gas tracers. However, higher transitions observed with larger S/N are still required to better reveal the physical properties of the molecular gas and the dominant energy source(s) driving the physics and chemistry of the molecular medium.

5.1.3 The CO Tully-Fisher Relation of disc galaxies at $z = 0.05 - 0.3$

The aim of the work presented in Chapter 4 was to shed some light on the mass-to-light ratio (M/L) evolution of galaxies as a function of lookback time, and to provide a benchmark CO TFR for comparison with future higher redshift studies. We thus constructed the first ever $K_{\rm s}$-band CO TFR of galaxies beyond the local Universe, using a sample of 30 galaxies at $z = 0.05 - 0.3$. The sample includes relatively isolated (i.e. non-interacting) normal star-forming galaxies and more luminous infrared galaxies (LIRGs) drawn from an initial sample of 125 objects.

We found no evolution of the slope of the $K_{\rm s}$-band and stellar-mass TFRs compared to those of $z = 0$ disc galaxies. However, we did detect a mild evolution of the zero-point of both relations, suggesting that the higher redshift galaxies are both more luminous and more massive (by a factor slightly more than 2) than local galaxies at a given rotation velocity. This seems consistent with higher redshifts galaxies being both more heavily star-forming (and thus intrinsically more luminous) and physically larger (and thus more massive) than comparison sample galaxies.

In keeping with a growing number of CO TFR studies of nearby galaxies, we found that CO is a suitable and attractive alternative to neutral hydrogen (H I) as a kinematic

tracer, particularly at high redshifts. However, more observational data are required to better understand the evolution of the TFR as a function of redshift and galaxy type. With the power of ALMA, CO has already been observed in many galaxies at the edge of the observable universe. In the near future, such observations will thus drastically increase the number of galaxies available for CO TFR studies at distant epochs. The lack of high-quality information on the morphology of the galaxies at higher z will nevertheless remain a stumbling block, although *JWST* should help once operational.

5.2 Ongoing work

5.2.1 Molecular gas in the arms of NGC 0628

This project primarily focuses on molecular gas in the arms of NGC 628 (M74), this for a number of reasons. NGC 0628 is a face-on nearby spiral galaxy (7.3 Mpc; Karachentsev et al. 2004) and is well studied in both Hα and far-ultraviolet (FUV) emission [Adler et al., 1999; Herbert-Fort et al., 2010], both indicating strong star formation activity in the arms. It has been reported to contain as many as 376 H II complexes (see Fig. 5.1), one of the largest numbers in the nearby Universe [Fathi et al., 2007].

An interferometric CO (1–0) map of the central $180'' \times 180''$ region is available in the literature [Helfer et al., 2003]. However, we have acquired new single-dish observations of CO lines that extend much farther out, with higher surface brightness sensitivity on large scales. Together with a central pointing, we defined 10 regions along the northern and southern arms of the galaxy where the FUV emission peaks (see Fig. 5.1). The FUV radiation and stellar winds, coming from young O and B stars, can heat up the gas and dust, increase the molecular gas density, and form H II regions, as seen in the selected regions over the galaxy where H II complexes coincide with FUV peaks (see the right panel in Fig. 5.1).

Another 10 regions along a SE-NW cut were targeted to probe the large-scale molecular gas distribution and kinematics, as well as any radial variation of the molecular gas physical

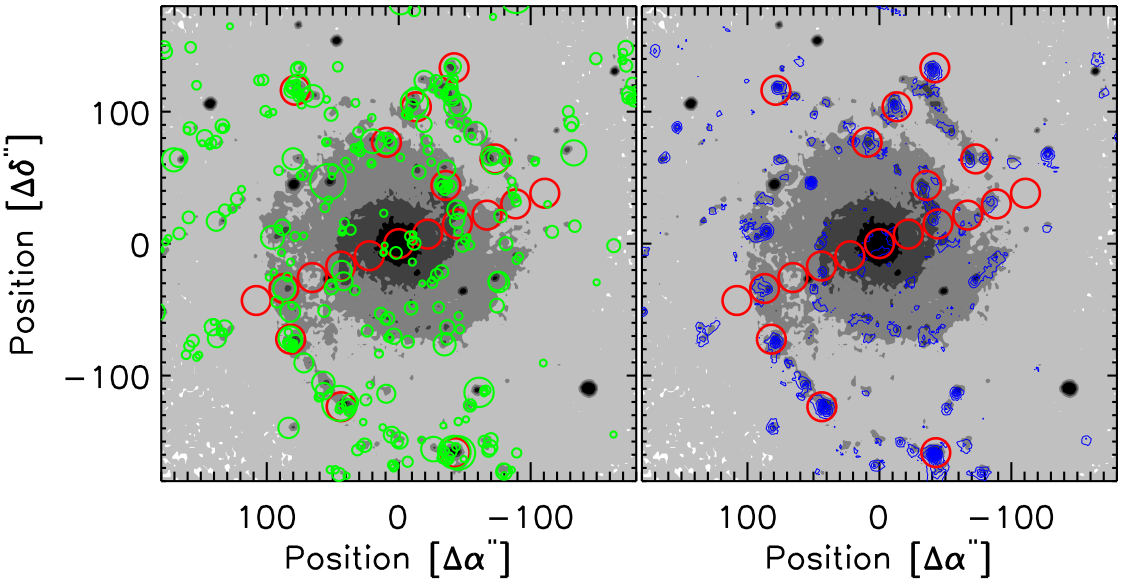

Figure 5.1: **Left**: The targeted regions in the spiral galaxy NGC 628 are overlaid on an optical image of the galaxy (SDSS). The red circles indicate the targeted positions with the IRAM 30m beam of 22 arcsec at 115 GHz, while the green circles indicate the H II regions detected by [Fathi et al., 2007]. **Right**: The targeted regions and the FUV emission are overlaid on the same optical image. Blue contours represent the FUV emission (GALEX). North is up and east to the left in both panels. The offsets are measured with respect to the galaxy centre of $\alpha = 1^{\rm h}36^{\rm m}41.770^{\rm s}$ and $\delta = 15°47'00.40''$

conditions (see Fig. 5.1). Our goals are: i) to increase our understanding of the star formation processes in external spiral galaxies, in particular in spiral arms; ii) to determine for the first time the properties of the molecular gas in the arms of this particular galaxy, this using multiple lines of CO; iii) to probe differences in star formation activity between the spiral arms and the centre of the galaxy (and other galaxies), this by comparing SLEDs; and finally iv) to study the large-scale molecular gas distribution and kinematics.

The CO (1–0) and ^{13}CO (1–0) observations were carried out at the IRAM 30m telescope in July 2012. CO (1–0) was detected in all 20 regions, while ^{13}CO (1–0) was detected in 17 regions. Together with the CO (2–1) data from the HERA CO Line Extragalactic Survey (HERACLES; Leroy et al. 2009b) and CO (3–2) data from the James Clerk Maxwell Telescope (JCMT) Nearby Galaxies Legacy Survey (NGLS; Warren et al. 2010), there are 4

lines detected in 17 out of the 20 regions and 3 lines in the remaining 3 regions (i.e. all lines except the ^{13}CO (1–0) transition).

5.2.2 $M_\bullet$ - $\Delta V_{\rm CO}$ relation in galaxies

Strong correlations between supermassive black hole masses ($M_\bullet$) and the properties of the host galaxies have led us to realise that there is a fundamental connection between the growth of black holes over time and the cosmic evolution of galaxies [e.g., Ferrarese & Merritt, 2000; Gebhardt et al., 2000]. Much work has been carried out during the last decade to study potential drivers of these correlations. For example, do these relations hold for all types of galaxies over a variety of masses? Do the central black holes really play an important role in the evolution of their host galaxies, or are the observed correlations natural outcomes of the hierarchical growth of galaxies (i.e. successive galaxy mergers)? Although tremendous efforts have been made, these and similar questions are still the subject of much debate today [e.g., Jahnke & Macciò, 2011; Shields et al., 2006; Silk & Rees, 1998; Woo et al., 2008].

The tightest correlation between the central black hole and its host galaxy is the so-called $M_\bullet$ - $\sigma_\star$ relation, an empirical correlation between the stellar velocity dispersion of the host galaxy spheroid ($\sigma_\star$) and the black hole mass itself. This relation serves as a tool for calculating $M_\bullet$ in galaxies throughout the Universe. Since CO is generally rotationally supported in disc galaxies, its maximum rotation velocity is related to the total galaxy mass (Tully-Fisher relation) and indeed that of the spheroid (so-called disc-halo conspiracy). A similar correlation should thus hold for $M_\bullet$ - $\Delta V_{\rm CO}$. The inputs that are necessary to study this $M_\bullet$ - $\Delta V_{\rm CO}$ relation are a dynamically calculated $M_\bullet$ (as for all similar relations) and $\Delta V_{\rm CO}$, the width of the CO line from integrated measurements (roughly twice the rotation velocity of the gas; the same measurement as for CO TFRs).

We thus compiled reliably measured supermassive back hole masses from the literature, building a sample of 85 galaxies with different morphological types (50% ellipticals, 25% spirals and 25% lenticulars). We also searched the literature for single-dish CO detections of

all spiral galaxies in the sample, and found that most of the spirals have CO detected at their centres. We must now do a similar search for the lenticulars and ellipticals. After verifying that the CO has reached the flat part of the rotation curve in each object, we will be in a position to probe the $M_\bullet$ - $\Delta V_{\rm CO}$ relation as described above.

5.3 Future Prospects

Since its first detection in the 1970s, the most common molecule used to study the physical properties of the molecular gas and the dense ISM of galaxies has been CO. The discovery and subsequent study of the molecular ISM has dramatically increased our understanding of the Universe on multiple scales, from galaxies to stars, planets and even us. From the perspective of mm/sub-mm astronomy, molecules allow us to track the complex and violent evolution of the ISM and its host galaxies. The more molecules that are detected, the more we know about the physics and chemistry of the star-forming gas, as every molecular transition results from (slightly) different physical conditions. It is therefore particularly important to conduct large molecular line surveys not only in CO, as done for the past decades, but also targeting key molecular diagnostic lines. Key molecules should be studied (e.g. HCN, HCO^+, HNC, HNCO, Si and CS) that are (1) sensitive to the densest parts of the clouds where stars actually form, and (2) good tracers of the chemical evolution of the medium driven by UV radiation, CRs, X-rays, shocks and/or turbulence.

To pursue such goals, we must consider combining the power of both single-dish and interferometric observations. While single-dish observations are an excellent tool to probe large-scale structures with high surface brightness sensitivity, they suffer from poor angular resolution and thus lack the power to spatially resolve small-scale structures. Interferometry, on the other hand, can provide a larger total collecting area and higher sensitivity to small-scale structures.

The improvements in mm/sub-mm astronomy, particularly during the last decade, have shed light on some of the remaining questions concerning star-forming molecular clouds. ALMA currently provides not only an unbeatable resolution and sensitivity, but it also gives the opportunity to combine single-dish and interferometric observations. These improvements will enable us to observe higher redshift galaxies with better sensitivity and resolution, and allow us to better understand the physical characteristics of molecular gas in different types of galaxies across the Universe.

A new generation of ground-based and space-based telescopes that is being built around the globe will further increase our ability to survey large areas of the sky with ever increasing angular resolution and sensitivity (e.g. eVLA, SKA and CCAT; JWST). Synergies between these telescopes and current telescopes (e.g. ALMA) will also enable us to study the star-forming gas in a level of details never achieved before, using multiple lines of several key molecular tracers in different galaxy types, while also allowing us to probe the M/L evolution of different types of galaxy as a function of redshift.

Today's continuously improving technologies, observational techniques, and instruments give us a profound glimpse into a near future full of discoveries. These discoveries will ultimately raise new questions, keeping human curiosity and our quest to understand the Universe very much alive.

References

Abazajian K. N. et al., 2009, The Astrophysical Journal Supplement Series, 182, 543 147

Adler D. S., Knapen J. H., Fanelli M. N., Westpfahl D. J., Wakker B. P., 1999, in Astronomical Society of the Pacific Conference Series, Vol. 182, Galaxy Dynamics - A Rutgers Symposium, Merritt D. R., Valluri M., Sellwood J. A., eds., p. 227 178

Alam S. et al., 2015, ApJS, 219, 12 149

Alatalo K. et al., 2011, ApJ, 735, 88 xxi, 130

Alatalo K. et al., 2015, ArXiv e-prints 75, 116

Alatalo K. et al., 2013, MNRAS, 432, 1796 74, 86, 91, 92, 120

Anders E., Grevesse N., 1989, GeCoA, 53, 197 104

Aragón-Calvo M. A., van de Weygaert R., Jones B. J. T., 2010, MNRAS, 408, 2163 5

Armus L., Heckman T., Miley G., 1987, AJ, 94, 831 152

Arp H., 1966, ApJS, 14, 1 27

Athanassoula E., Bureau M., 1999, ApJ, 522, 699 77, 86, 118

Baan W. A., Henkel C., Loenen A. F., Baudry A., Wiklind T., 2008, A&A, 477, 747 xxi, 77, 130

Baldry I. K., Glazebrook K., Brinkmann J., Ivezić Ž., Lupton R. H., Nichol R. C., Szalay A. S., 2004, ApJ, 600, 681 7

Baldwin J. A., Phillips M. M., Terlevich R., 1981, PASP, 93, 5 150, 154

Balkowski C., Bottinelli L., Chamaraux P., Gouguenheim L., Heidmann J., 1974, A&A, 34, 43 146

Ball R., Sargent A. I., Scoville N. Z., Lo K. Y., Scott S. L., 1985, ApJL, 298, L21 27, 59

Barnes J. E., 1988, ApJ, 331, 699 7

Bauermeister A. et al., 2013, ApJ, 768, 132 xxii, 147, 148, 150, 162, 163, 169

Bayet E., Gerin M., Phillips T. G., Contursi A., 2004, A&A, 427, 45 34, 51

Bayet E., Gerin M., Phillips T. G., Contursi A., 2006, A&A, 460, 467 27, 34, 36, 39, 60

Beck R., Hoernes P., 1996, Nat, 379, 47 42

Bedregal A. G., Aragón-Salamanca A., Merrifield M. R., 2006, MNRAS, 373, 1125 146

Bell E. F. et al., 2004, ApJ, 608, 752 7

Bell T. A., Viti S., Williams D. A., Crawford I. A., Price R. J., 2005, MNRAS, 357, 961 20

Bianchi S., Davies J. I., Alton P. B., Gerin M., Casoli F., 2000, A&A, 353, L13 42

Blake G. A., Sutton E. C., Masson C. R., Phillips T. G., 1987, ApJ, 315, 621 19, 125

Blanton M. R., Roweis S., 2007, AJ, 133, 734 151

Blumenthal G. R., Faber S. M., Primack J. R., Rees M. J., 1984, Nat, 311, 517 4

Böhm A. et al., 2004, A&A, 420, 97 162

Bolatto A. D., Wolfire M., Leroy A. K., 2013, ARA&A, 51, 207 14, 16

Bonnarel F., Boulesteix J., Georgelin Y. P., Lecoarer E., Marcelin M., Bacon R., Monnet G., 1988, A&A, 189, 59 27, 59

Bonnarel F., Boulesteix J., Marcelin M., 1986, A&AS, 66, 149 xv, 28, 55

Boomsma R., 2007, PhD thesis, Kapteyn Astronomical Institute, University of Groningen xv, 28

Boomsma R., Oosterloo T. A., Fraternali F., van der Hulst J. M., Sancisi R., 2008, A&A, 490, 555 28, 55

Braun R., Oosterloo T. A., Morganti R., Klein U., Beck R., 2007, A&A, 461, 455 xv, 28

Brinchmann J., Charlot S., White S. D. M., Tremonti C., Kauffmann G., Heckman T., Brinkmann J., 2004, MNRAS, 351, 1151 154

Brouillet N., Muller S., Herpin F., Braine J., Jacq T., 2005, A&A, 429, 153 xxi, 77, 128, 130

Brown M. J. I., Jannuzi B. T., Floyd D. J. E., Mould J. R., 2011, ApJL, 731, L41 92

Bruzual G., Charlot S., 2003, MNRAS, 344, 1000 151, 152

Buhl D., Snyder L. E., 1970, Nat, 228, 267 13

Bureau M., Athanassoula E., 1999, ApJ, 522, 686 77, 86

Bureau M., Freeman K. C., 1999, AJ, 118, 126 77, 86

Burstein P., Borken R. J., Kraushaar W. L., Sanders W. T., 1977, ApJ, 213, 405 10

Bushouse H. A. et al., 2002, ApJS, 138, 1 152

Caldwell N., 1984, PASP, 96, 287 74

Cappellari M. et al., 2011, MNRAS, 416, 1680 xiv, 6, 8, 74, 76

Cheung A. C., Rank D. M., Townes C. H., Thornton D. D., Welch W. J., 1968, Physical Review Letters, 21, 1701 12

Cheung A. C., Rank D. M., Townes C. H., Thornton D. D., Welch W. J., 1969, Nat, 221, 626 12

Churchwell E., Wood D., Myers P. C., Myers R. V., 1986, ApJ, 305, 405 17

Colín P., Vázquez-Semadeni E., Gómez G. C., 2013, MNRAS, 435, 1701 56

Colless M. et al., 2001, MNRAS, 328, 1039 5

Conselice C. J., Bundy K., Ellis R. S., Brichmann J., Vogt N. P., Phillips A. C., 2005, ApJ, 628, 160 147, 160, 162

Cowan J. J., Sneden C., 2006, Nat, 440, 1151 9

Cox D. P., Smith B. W., 1974, ApJL, 189, L105 10

Crocker A. et al., 2012, MNRAS, 421, 1298 xvii, xxi, 75, 77, 83, 84, 88, 119, 121, 123, 124, 127, 130, 131

Dale D. A. et al., 2005, ApJ, 633, 857 92

Dale D. A. et al., 2007, ApJ, 655, 863 92

Davis T. A. et al., 2013a, MNRAS, 429, 534 74, 82

Davis T. A. et al., 2013b, MNRAS, 429, 534 166

Davis T. A. et al., 2011a, MNRAS, 417, 882 75, 80, 116

Davis T. A., Bayet E., Crocker A., Topal S., Bureau M., 2013c, MNRAS, 433, 1659 75

Davis T. A. et al., 2011b, MNRAS, 414, 968 22, 74, 76, 146, 147, 155, 158, 161, 164, 165, 166

Davis T. A. et al., 2014, MNRAS, 444, 3427 76

de Bernardis P. et al., 2000, Nat, 404, 955 4

de Blok W. J. G., Walter F., Brinks E., Trachternach C., Oh S.-H., Kennicutt, Jr. R. C., 2008, AJ, 136, 2648 27

de Jong T., Dalgarno A., Chu S.-I., 1975, ApJ, 199, 69 29, 37

De Rijcke S., Zeilinger W. W., Hau G. K. T., Prugniel P., Dejonghe H., 2007, ApJ, 659, 1172 146

de Vaucouleurs G., 1974, in IAU Symposium, Vol. 58, The Formation and Dynamics of Galaxies, Shakeshaft J. R., ed., pp. 1–52 5

Degioia-Eastwood K., Grasdalen G. L., Strom S. E., Strom K. M., 1984, ApJ, 278, 564 26

Dickey J. M., Kazes I., 1992, ApJ, 393, 530 147

Dickinson D. F., Rodriguez Kuiper E. N., Dinger A. S. C., Kuiper T. B. H., 1980, ApJL, 237, L43 75

Dobbs C. L., 2008, MNRAS, 391, 844 56

Dobbs C. L., Bonnell I. A., 2008, MNRAS, 385, 1893 56

Doi A., Kameno S., Kohno K., Nakanishi K., Inoue M., 2005, MNRAS, 363, 692 92

Donovan Meyer J. et al., 2012, ApJ, 744, 42 xv, 28, 29, 42, 45, 55

Dressler A., 1980, ApJ, 236, 351 7

Dressler A., Sandage A., 1983, ApJ, 265, 664 146

Duric N., Gordon S. M., Goss W. M., Viallefond F., Lacey C., 1995, ApJ, 445, 173 55

Efstathiou G., Sutherland W. J., Maddox S. J., 1990, Nat, 348, 705 4

Elitzur M., 1983, ApJ, 267, 174 75

Engelbracht C. W., Rieke M. J., Rieke G. H., Latter W. B., 1996, ApJ, 467, 227 27, 59

Epinat B. et al., 2008, MNRAS, 388, 500 27

Ewen H. I., Purcell E. M., 1951, Nat, 168, 356 12

Fathi K., Beckman J. E., Zurita A., Relaño M., Knapen J. H., Daigle O., Hernandez O., Carignan C., 2007, A&A, 466, 905 xxii, 178, 179

Ferland G. J., Korista K. T., Verner D. A., Ferguson J. W., Kingdon J. B., Verner E. M., 1998, PASP, 110, 761 20

Ferrarese L., Merritt D., 2000, ApJL, 539, L9 180

Fixsen D. J., Bennett C. L., Mather J. C., 1999, ApJ, 526, 207 51

Flores H., Hammer F., Puech M., Amram P., Balkowski C., 2006, A&A, 455, 107 147, 160, 162, 164

Flower D. R., Launay J. M., 1985, MNRAS, 214, 271 37

Forman W., Jones C., Tucker W., 1985, ApJ, 293, 102 74

Fridriksson J. K., Homan J., Lewin W. H. G., Kong A. K. H., Pooley D., 2008, ApJS, 177, 465 27

Gao Y., Solomon P. M., 2004a, ApJS, 152, 63 xxi, 130

Gao Y., Solomon P. M., 2004b, ApJ, 606, 271 127, 128

Garnavich P. M. et al., 1998, ApJL, 493, L53 4

Gebhardt K. et al., 2000, ApJL, 539, L13 180

Genzel R. et al., 2015, ApJ, 800, 20 165

Gerhard O., Kronawitter A., Saglia R. P., Bender R., 2001, AJ, 121, 1936 146

Goldreich P., Kwan J., 1974, ApJ, 189, 441 29, 37

Goldsmith P. F., Irvine W. M., Hjalmarson A., Ellder J., 1986, ApJ, 310, 383 104

Goldsmith P. F., Langer W. D., 1999a, ApJ, 517, 209 19

Goldsmith P. F., Langer W. D., 1999b, ApJ, 517, 209 49

Goldsmith P. F., Langer W. D., Ellder J., Kollberg E., Irvine W., 1981, ApJ, 249, 524 17, 104

Green D. A., 2012, in American Institute of Physics Conference Series, Vol. 1505, American Institute of Physics Conference Series, Aharonian F. A., Hofmann W., Rieger F. M., eds., pp. 5–12 56

Green S., Thaddeus P., 1976, ApJ, 205, 766 37

Greve T. R., Papadopoulos P. P., Gao Y., Radford S. J. E., 2009, ApJ, 692, 1432 17

Gribbin J., 2008, Galaxies: A Very Short Introduction 1

Habart E. et al., 2010, A&A, 518, L116 52

Helfer T. T., Blitz L., 1997, ApJ, 478, 233 128

Helfer T. T., Thornley M. D., Regan M. W., Wong T., Sheth K., Vogel S. N., Blitz L., Bock D. C.-J., 2003, ApJS, 145, 259 178

Helmich F. P., Jansen D. J., de Graauw T., Groesbeck T. D., van Dishoeck E. F., 1994, A&A, 283, 626 19

Henkel C., Mauersberger R., 1993a, A&A, 274, 730 39

Henkel C., Mauersberger R., 1993b, A&A, 274, 730 104

Henkel C., Mauersberger R., Wiklind T., Huettemeister S., Lemme C., Millar T. J., 1993, A&A, 268, L17 104

Herbert-Fort S., Zaritsky D., Christlein D., Kannappan S. J., 2010, ApJ, 715, 902 178

Hinz J. L., Rieke G. H., Caldwell N., 2003, AJ, 126, 2622 146

Hinz J. L., Rix H.-W., Bernstein G. M., 2001, AJ, 121, 683 146

Hogerheijde M. R., van der Tak F. F. S., 2000, A&A, 362, 697 20

Hogg D. W., Baldry I. K., Blanton M. R., Eisenstein D. J., 2002, ArXiv Astrophysics e-prints 151

Hollenbach D. J., Tielens A. G. G. M., 1997a, ARA&A, 35, 179 12

Hollenbach D. J., Tielens A. G. G. M., 1997b, ARA&A, 35, 179 13

Hollenbach D. J., Tielens A. G. G. M., 1999, Reviews of Modern Physics, 71, 173 xiv, 12, 13

Holmberg E., 1958, Meddelanden fran Lunds Astronomiska Observatorium Serie II, 136, 1 151

Hubble E., 1929, Proceedings of the National Academy of Science, 15, 168 2

Hubble E. P., 1936, Realm of the Nebulae. "" xiv, 5, 6

Huettemeister S., Henkel C., Mauersberger R., Brouillet N., Wiklind T., Millar T. J., 1995, A&A, 295, 571 75

Ishizuki S., Kawabe R., Ishiguro M., Okumura S. K., Morita K.-I., Chikada Y., Kasuga T., Doi M., 1990, ApJ, 355, 436 27, 59

Israel F. P., Baas F., 2001, A&A, 371, 433 39, 59

Jahnke K., Macciò A. V., 2011, ApJ, 734, 92 180

Jansen D. J., 1995, PhD thesis, Leiden Observatory, Leiden University, P.O. Box 9513, 2300 RA Leiden, The Netherlands 39

Jarrett T. H., Chester T., Cutri R., Schneider S., Skrutskie M., Huchra J. P., 2000, AJ, 119, 2498 149, 150

Jenkins E. B., Meloy D. A., 1974, ApJL, 193, L121 10

Kamenetzky J. et al., 2012, ApJ, 753, 70 52, 56, 57, 112

Kannappan S. J., Fabricant D. G., Franx M., 2002, AJ, 123, 2358 164

Karachentsev I. D., Kajsin S. S., Tsvetanov Z., Ford H., 2005, A&A, 434, 935 26, 27

Karachentsev I. D., Karachentseva V. E., Huchtmeier W. K., Makarov D. I., 2004, AJ, 127, 2031 178

Kassin S. A. et al., 2007, ApJL, 660, L35 147, 164

Kauffmann G. et al., 2003, MNRAS, 346, 1055 148

Kaviraj S., Rey S.-C., Rich R. M., Yoon S.-J., Yi S. K., 2007, MNRAS, 381, L74 42

Kennicutt, Jr. R. C. et al., 2003, PASP, 115, 928 34, 42

Kirk H., 2011, JRASC, 105, 51 26

Knapen J. H., Stedman S., Bramich D. M., Folkes S. L., Bradley T. R., 2004, A&A, 426, 1135 xv, 28, 42

Knapp G. R., Turner E. L., Cunniffe P. E., 1985, AJ, 90, 454 74

Koda J. et al., 2012, ApJ, 761, 41 46

Kormendy J., 1979, ApJ, 227, 714 7

Kormendy J., Bender R., 1996, ApJL, 464, L119 6

Kormendy J., Bender R., 2012, ApJS, 198, 2 xiv, 6, 7

Kormendy J., Kennicutt, Jr. R. C., 2004, ARA&A, 42, 603 124

Kraan-Korteweg R. C., 1982, A&AS, 47, 505 76

Krips M., Crocker A. F., Bureau M., Combes F., Young L. M., 2010, MNRAS, 407, 2261 xxi, 75, 77, 130, 131

Krips M., Neri R., García-Burillo S., Martín S., Combes F., Graciá-Carpio J., Eckart A., 2008, ApJ, 677, 262 125

Lacey C. K., Duric N., 2001, ApJ, 560, 719 xv, 27, 28, 55

Lagattuta D. J., Mould J. R., Staveley-Smith L., Hong T., Springob C. M., Masters K. L., Koribalski B. S., Jones D. H., 2013, ApJ, 771, 88 160, 161

Lavezzi T. E., Dickey J. M., 1997, AJ, 114, 2437 156, 166

Lavezzi T. E., Dickey J. M., 1998, AJ, 116, 2672 22, 147, 156, 166

Le Petit F., Nehmé C., Le Bourlot J., Roueff E., 2006, ApJS, 164, 506 20

Lemaître G., 1927, Annales de la Société Scientifique de Bruxelles, 47, 49 2

Lemaître G., 1931a, MNRAS, 91, 483 2

Lemaître G., 1931b, MNRAS, 91, 490 2

Lepp S., Dalgarno A., 1996, A&A, 306, L21 125

Leroy A. K. et al., 2009a, AJ, 137, 4670 26

Leroy A. K. et al., 2009b, AJ, 137, 4670 179

Levine E. S., Helfer T. T., Meijerink R., Blitz L., 2008, ApJ, 673, 183 27

Mac Low M.-M., McCray R., 1988, ApJ, 324, 776 29

Maddox S. J., Efstathiou G., Sutherland W. J., Loveday J., 1990, MNRAS, 242, 43P 4

Magorrian J., Ballantyne D., 2001, MNRAS, 322, 702 146

Maloney P. R., Hollenbach D. J., Tielens A. G. G. M., 1996, ApJ, 466, 561 125

Maraston C., 2005, MNRAS, 362, 799 149

Markwardt C. B., 2009a, in Astronomical Society of the Pacific Conference Series, Vol. 411, Astronomical Data Analysis Software and Systems XVIII, Bohlender D. A., Durand D., Dowler P., eds., p. 251 98

Markwardt C. B., 2009b, in Astronomical Society of the Pacific Conference Series, Vol. 411, Astronomical Data Analysis Software and Systems XVIII, Bohlender D. A., Durand D., Dowler P., eds., p. 251 156

Martin D. C. et al., 2007, ApJS, 173, 342 7

Martín S., Aladro R., Martín-Pintado J., Mauersberger R., 2010, A&A, 522, A62 104

Mathieu A., Merrifield M. R., Kuijken K., 2002, MNRAS, 330, 251 146

Matonick D. M., Fesen R. A., 1997, ApJS, 112, 49 xv, 27, 28, 55, 56

McCray R., Kafatos M., 1987, ApJ, 317, 190 29

McKee C. F., Hollenbach D. J., 1980, ARA&A, 18, 219 13

Meier D. S., Turner J. L., 2005, ApJ, 618, 259 17, 75

Meier D. S., Turner J. L., 2012, ApJ, 755, 104 17, 75

Meijerink R., Spaans M., 2005a, A&A, 436, 397 17

Meijerink R., Spaans M., 2005b, A&A, 436, 397 20

Meijerink R., Spaans M., Israel F. P., 2007a, A&A, 461, 793 17

Meijerink R., Spaans M., Israel F. P., 2007b, A&A, 461, 793 125, 127

Meijerink R., Spaans M., Loenen A. F., van der Werf P. P., 2011, A&A, 525, A119 56

Melnick J., Mirabel I. F., 1990, A&A, 231, L19 152

Milvang-Jensen B., Aragón-Salamanca A., Hau G. K. T., Jørgensen I., Hjorth J., 2003, MNRAS, 339, L1 162

Mirabel I. F., Booth R. S., Johansson L. E. B., Garay G., Sanders D. B., 1990, A&A, 236, 327 148, 150

Mo H., van den Bosch F. C., White S., 2010, Galaxy Formation and Evolution 10

Mould J. R., Akeson R. L., Bothun G. D., Han M., Huchra J. P., Roth J., Schommer R. A., 1993, ApJ, 409, 14 146

Murphy E. J. et al., 2011, ApJ, 737, 67 58

Murphy E. J. et al., 2010, ApJL, 709, L108 28, 58

Nagar N. M., Wilson A. S., Falcke H., 2001, ApJL, 559, L87 92

Neistein E., Maoz D., Rix H.-W., Tonry J. L., 1999a, AJ, 117, 2666 146

Neistein E., Maoz D., Rix H.-W., Tonry J. L., 1999b, AJ, 117, 2666 146

Nieten C., Dumke M., Beck R., Wielebinski R., 1999, A&A, 347, L5 27

Noeske K. G. et al., 2007, ApJL, 660, L43 163

Noordermeer E., Verheijen M. A. W., 2007, MNRAS, 381, 1463 149

Oka T., Nagai M., Kamegai K., Tanaka K., Kuboi N., 2007, PASJ, 59, 15 46

Ott J., Burton M., Jones P., Meier D. S., 2014, in IAU Symposium, Vol. 303, IAU Symposium, Sjouwerman L. O., Lang C. C., Ott J., eds., pp. 104–105 75

Paglione T. A. D. et al., 2001, ApJS, 135, 183 xxi, 123, 130, 131

Penzias A. A., Jefferts K. B., Wilson R. W., 1971, ApJ, 165, 229 26

Perlmutter S. et al., 1999, ApJ, 517, 565 4

Petitpas G. R., Wilson C. D., 2000, ApJL, 538, L117 56

Phillips T. G. et al., 1987, ApJL, 322, L73 12

Pierce M. J., Tully R. B., 1988, ApJ, 330, 579 151, 155

Pizagno J. et al., 2007, AJ, 134, 945 147

Planck Collaboration et al., 2015, ArXiv:1502.01589 152

Poelman D. R., Spaans M., 2005, A&A, 440, 559 20

Prasad S. S., Huntress, Jr. W. T., 1980, ApJS, 43, 1 15

Puech M. et al., 2008, A&A, 484, 173 147, 160, 162

Rangwala N. et al., 2011, ApJ, 743, 94 52, 56, 57, 112

Rebolledo D., Wong T., Leroy A., Koda J., Donovan Meyer J., 2012, ApJ, 757, 155 xv, 28, 29, 42, 45, 55, 57

Regan M. W., Vogel S. N., 1995, ApJL, 452, L21 27, 59

Rickard L. J., Palmer P., Morris M., Zuckerman B., Turner B. E., 1975, ApJL, 199, L75 12, 74

Riechers D. A. et al., 2009, ApJ, 703, 1338 165

Roberts H., van der Tak F. F. S., Fuller G. A., Plume R., Bayet E., 2011, A&A, 525, A107 104

Rodríguez-Fernández N. J., Tafalla M., Gueth F., Bachiller R., 2010, A&A, 516, A98 75

Röllig M. et al., 2007, A&A, 467, 187 20, 21, 55

Russell D. G., 2004, ApJ, 607, 241 160

Sage L. J., Welch G. A., Young L. M., 2007, ApJ, 657, 232 74

Saintonge A. et al., 2011, MNRAS, 415, 32 161

Sandage A., Bedke J., 1994, The Carnegie Atlas of Galaxies. Volumes I, II. Carnegie Institution of Washington Publ. 76

Sanders D. B., Mazzarella J. M., Kim D.-C., Surace J. A., Soifer B. T., 2003a, AJ, 126, 1607 92

Sanders D. B., Mazzarella J. M., Kim D.-C., Surace J. A., Soifer B. T., 2003b, AJ, 126, 1607 152

Sanders D. B., Scoville N. Z., Soifer B. T., 1991, ApJ, 370, 158 148, 150

Sandstrom K. M. et al., 2013, ApJ, 777, 5 45

Sault R. J., Teuben P. J., Wright M. C. H., 1995, in Astronomical Society of the Pacific Conference Series, Vol. 77, Astronomical Data Analysis Software and Systems IV, Shaw R. A., Payne H. E., Hayes J. J. E., eds., p. 433 80

Sauty S., Gerin M., Casoli F., 1998, A&A, 339, 19 26

Schilke P., Walmsley C. M., Pineau Des Forets G., Roueff E., Flower D. R., Guilloteau S., 1992a, A&A, 256, 595 17

Schilke P., Walmsley C. M., Pineau Des Forets G., Roueff E., Flower D. R., Guilloteau S., 1992b, A&A, 256, 595 104

Schinke R., Engel V., Buck U., Meyer H., Diercksen G. H. F., 1985, ApJ, 299, 939 37

Schirm M. R. P. et al., 2014, ApJ, 781, 101 52, 56

Schlegel D. J., Finkbeiner D. P., Davis M., 1998, ApJ, 500, 525 152

Schlegel E. M., 1994, AJ, 108, 1893 27

Schöier F. L., 2000, PhD thesis, Stockholm Observatory, SE-133 36 Saltsjöbaden, Sweden 20

Schöier F. L., van der Tak F. F. S., van Dishoeck E. F., Black J. H., 2005a, A&A, 432, 369 20

Schöier F. L., van der Tak F. F. S., van Dishoeck E. F., Black J. H., 2005b, A&A, 432, 369 37

Schoniger F., Sofue Y., 1994a, A&A, 283, 21 147, 166

Schoniger F., Sofue Y., 1994b, A&A, 283, 21 156

Scoville N. et al., 2007, ApJS, 172, 1 147

Scoville N. Z., 2012, ArXiv e-prints 127

Scoville N. Z., 2013, Evolution of star formation and gas, p. 491 16

Sellwood J. A., Wilkinson A., 1993, Reports on Progress in Physics, 56, 173 86

Shaw G., Ferland G. J., Abel N. P., Stancil P. C., van Hoof P. A. M., 2005, ApJ, 624, 794 20

Shen S., Wang C., Chang R., Shao Z., Hou J., Shu C., 2009, ApJ, 705, 1496 160

Shields G. A., Menezes K. L., Massart C. A., Vanden Bout P., 2006, ApJ, 641, 683 180

Silk J., Rees M. J., 1998, A&A, 331, L1 180

Simard L., Pritchet C. J., 1998, ApJ, 505, 96 162

Skrutskie M. F. et al., 2006a, AJ, 131, 1163 27

Skrutskie M. F. et al., 2006b, AJ, 131, 1163 149, 150

Snyder L. E., Bhul D., 1971, in Bulletin of the American Astronomical Society, Vol. 3, Bulletin of the American Astronomical Society, p. 388 13

Snyder L. E., Buhl D., 1971, ApJL, 163, L47 13

Snyder L. E., Buhl D., 1972, ApJ, 177, 619 13

Sobolev V. V., 1960, Moving envelopes of stars. Cambridge 16, 18

Solomon P., Jefferts K. B., Penzias A. A., Wilson R. W., 1971, ApJL, 163, L53 26

Solomon P. M., de Zafra R., 1975, ApJL, 199, L79 12, 74

Sorai K., Nakai N., Kuno N., Nishiyama K., 2002, PASJ, 54, 179 77

Steinmetz M., Navarro J. F., 1999, ApJ, 513, 555 146

Strateva I. et al., 2001, AJ, 122, 1861 7

Strauss M. A. et al., 2002, The Astronomical Journal, 124, 1810 147

Surace J. A., Sanders D. B., Evans A. S., 2000, ApJ, 529, 170 152

Swings P., Rosenfeld L., 1937, ApJ, 86, 483 12

Tacconi L. J. et al., 2010, Nat, 463, 781 165

Tacconi L. J., Young J. S., 1989, ApJS, 71, 455 26, 27

Tan Q.-H., Gao Y., Zhang Z.-Y., Xia X.-Y., 2011, Research in Astronomy and Astrophysics, 11, 787 xxi, 123, 130

Tenorio-Tagle G., Bodenheimer P., 1988, ARA&A, 26, 145 29

Tielens A. G. G. M., Hollenbach D., 1985a, ApJ, 291, 747 125

Tielens A. G. G. M., Hollenbach D., 1985b, ApJ, 291, 722 125

Tiley A., Bureau M., Saintonge A., Davis T. A., Topal S., Torii K., 2015, (in prep.) xxii, 22, 147, 155, 156, 158, 159, 160, 161, 163, 164, 165, 166

Tomisaka K., Ikeuchi S., 1986, PASJ, 38, 697 29

Toomre A., 1977, in Evolution of Galaxies and Stellar Populations, Tinsley B. M., Larson D. Campbell R. B. G., eds., p. 401 7

Topal S., Bayet E., Bureau M., Davis T. A., Walsh W., 2014, MNRAS, 437, 1434 xxi, 105, 130

Torii K., Yoshiike S., Shimizu S., Bureau M., Topal S., Ohama A., Fukui Y., 2015, (in prep.) 22, 147, 158, 160, 161, 163, 164, 165

Tully R. B., 1988a, Science, 242, 310 26, 27

Tully R. B., 1988b, Science, 242, 310 76

Tully R. B., Fisher J. R., 1977a, A&A, 54, 661 22, 146, 147, 151, 155

Tully R. B., Fisher J. R., 1977b, A&A, 54, 661 74

Tully R. B., Pierce M. J., 2000, ApJ, 533, 744 xxii, 146, 147, 155, 158, 159, 160, 161, 163, 165

Tutui Y., Sofue Y., 1997, A&A, 326, 915 147, 166

Tutui Y., Sofue Y., Honma M., Ichikawa T., Wakamatsu K.-i., 2000, PASJ, 52, 803 148, 150

Tutui Y., Sofue Y., Honma M., Ichikawa T., Wakamatsu K.-I., 2001, PASJ, 53, 701 147

van der Kruit P. C., Allen R. J., Rots A. H., 1977, A&A, 55, 421 xv, 28, 55

van der Tak F. F. S., Black J. H., Schöier F. L., Jansen D. J., van Dishoeck E. F., 2007a, A&A, 468, 627 xvi, 29, 37, 41, 49, 52

van der Tak F. F. S., Black J. H., Schöier F. L., Jansen D. J., van Dishoeck E. F., 2007b, A&A, 468, 627 xx, 19, 20, 77, 107, 112

van der Tak F. F. S., van Dishoeck E. F., 2000, A&A, 358, L79 17

van der Werf P. P. et al., 2010, A&A, 518, L42 57

van der Werf P. P., Spaans M., 2009, in The Next-Generation Infrared Space Mission: SPICA, Heras A. M., Swinyard B. M., Isaak K. G., Goicoechea J. R., eds., p. 3009 56

van Dishoeck E. F., Black J. H., 1988, ApJ, 334, 771 13

Veilleux S., Kim D.-C., Sanders D. B., 2002, ApJS, 143, 315 154

Veilleux S., Sanders D. B., Kim D.-C., 1999, ApJ, 522, 139 154

Verheijen M. A. W., 2001, ApJ, 563, 694 149

Vogt N. P., Forbes D. A., Phillips A. C., Gronwall C., Faber S. M., Illingworth G. D., Koo D. C., 1996, ApJL, 465, L15 162

Walsh W., Beck R., Thuma G., Weiss A., Wielebinski R., Dumke M., 2002, A&A, 388, 7 26, 27, 32, 33, 34, 36, 56, 60

Wang J. L., Xia X. Y., Mao S., Cao C., Wu H., Deng Z. G., 2006, ApJ, 649, 722 154

Wang R. et al., 2011, AJ, 142, 101 166

Warren B. E. et al., 2010, ApJ, 714, 571 179

Weinreb S., Barrett A. H., Meeks M. L., Henry J. C., 1963, Nat, 200, 829 12

Weiss A., Downes D., Walter F., Henkel C., 2007, in Astronomical Society of the Pacific Conference Series, Vol. 375, From Z-Machines to ALMA: (Sub)Millimeter Spectroscopy of Galaxies, Baker A. J., Glenn J., Harris A. I., Mangum J. G., Yun M. S., eds., p. 25 51

Weiß A., Walter F., Scoville N. Z., 2005a, A&A, 438, 533 51

Weiß A., Walter F., Scoville N. Z., 2005b, A&A, 438, 533 56

Welch G. A., Sage L. J., 2003, ApJ, 584, 260 74, 76, 88

Weliachew L., Casoli F., Combes F., 1988, A&A, 199, 29 27, 59

Wiklind T., Rydbeck G., 1986, A&A, 164, L22 12, 74

Williams J. P., Bergin E. A., Caselli P., Myers P. C., Plume R., 1998, ApJ, 503, 689 17

Williams M. J., Bureau M., Cappellari M., 2010, MNRAS, 409, 1330 146, 158, 164

Willick J. A., 1994, ApJS, 92, 1 158

Willick J. A., Strauss M. A., 1998, ApJ, 507, 64 146

Wilson R. W., Jefferts K. B., Penzias A. A., 1970, ApJL, 161, L43 12, 26

Wilson T. L., Rood R., 1994, ARA&A, 32, 191 104

Wilson T. L., Snyder L. E., Comoretto G., Jewell P. R., Henkel C., 1996, A&A, 314, 909 17

Woo J.-H., Treu T., Malkan M. A., Blandford R. D., 2008, ApJ, 681, 925 180

Wootten A., 1981, ApJ, 245, 105 75

Wootten A., Evans, II N. J., Snell R., vanden Bout P., 1978, ApJL, 225, L143 104

Wrobel J. M., Kenney J. D. P., 1992, ApJ, 399, 94 86

Xilouris E. M., Madden S. C., Galliano F., Vigroux L., Sauvage M., 2004, A&A, 416, 41 116

Yang B., Stancil P. C., Balakrishnan N., Forrey R. C., 2010, ApJ, 718, 1062 20, 37

York D. G. et al., 2000, The Astronomical Journal, 120, 1579 147

Young J. S., Scoville N. Z., 1991, ARA&A, 29, 581 15

Young L. M. et al., 2011, MNRAS, 414, 940 9, 74, 76, 88, 119

Ziegler B. L. et al., 2002, ApJL, 564, L69 162, 163

Zinchenko I., Henkel C., Mao R. Q., 2000, A&A, 361, 1079 17, 75

Zwicky F., 1933, Helvetica Physica Acta, 6, 110 4

Zwicky F., 1937, ApJ, 86, 217 4

Publications

Refereed Papers

(10) S.Topal et al., *CO Tully-Fisher relation of star-forming galaxies at* $z = 0.05 - 0.3$. [in prep. Chapter 4 in this thesis]

(9) Alfred A. Tiley, Martin Bureau, Amelie Saintonge, Timothy A. Davis, **S. Topal**, Kazufumi Torii, *The Tully-Fisher Relation of COLD GASS Galaxies* [in prep.]

(8) K. Torii, S. Yoshiike, S. Shimizu, M. Bureau, **S. Topal**, A. Ohama, and Y. Fukui, Estelle Bayet, Martin Bureau, Timothy A. Davis, Wilfred Walsh, *The first results of the NANTEN2 CO survey of the nearby galaxies* [in prep.]

(7) S. Topal, Martin Bureau, Timothy A. Davis, Melanie Krips, Lisa M. Young, Alison F. Crocker, *Molecular Gas Kinematics and Line Diagnostics in Early-type Galaxies: NGC 4710 & NGC 5866*, 2015, [submitted to MNRAS, Chapter 3 in this thesis]

(6) S. Topal, Estelle Bayet, Martin Bureau, Timothy A. Davis, Wilfred Walsh, *Molecular Gas Properties of the Giant Molecular Cloud Complexes in the Arms and Inter-arms of NGC 6946*, 2014, MNRAS, 437, 1434 [ADS] [Chapter 2 in this thesis]

(5) Timothy A. Davis, Estelle Bayet, Alison Crocker, **S. Topal**, Martin Bureau, *ISM chemistry in metal-rich environments: molecular tracers of metallicity*, 2013, MNRAS, 433, 1659 [ADS]

(4) Fehmi Ekmekçi, **S. Topal**, *2005 Photometric Observations and Multiple Frequencies*

of The δ Scuti Variable V350 Peg, 2009, Astrophysics and Space Sciences, 321:101-107. [ADS]

(3) Fehmi Ekmekçi, **S. Topal**, *2005 Photometric Observations and Multiple Frequencies of The δ Scuti Variable CC And*, , 2008, New Astronomy, 13, 118–123 [ADS]

(2) Fehmi Ekmekçi, **S. Topal**, *δ Scuti Type Variable Stars CC And and V350 Peg : Photoelectric Photometry Observations in 2005*, 2006, Çankaya University, Journal of Arts And Sciences, Number 6, p. 97 [PDF]

(1) Albayrak, B.; Yüce, K.; Selam, S. O.; Tanriverdi, T.; Okan, A.; Çınar, D.; **Topal, S.**; Özgür, E.; Şener, H. T.; Ergün, I; Civelek, E. *Photoelectric Minima of Some Eclipsing Binary Stars*, 2005, Information Bulletin on Variable Stars (IBVS), No. 5649 [ADS]

Conference Proceedings, Abstracts & Others

(10) S. Topal, *Observations and analysis of molecular gas in nearby disc galaxies.*, 2015, National Astronomy Meeting, Ankara/Turkey

(9) Topal, S.,Bureau, Martin; Davis, Timothy A.; Young, Lisa; Krips, Melanie, *Line Ratio Diagnostics Along the Disc of Two Edge-on Lenticular Galaxies, NGC 4710 and NGC 5866*, 2015, Proceedings of the 225th AAS Meeting, Seattle/Washington/USA [ADS]

(8) K. Torii, S. Yoshiike, M. Bureau, **S. Topal** & Y. Fukui , *A new CO Survey of the Nearby Galaxies with NANTEN2*, 2013, National Astronomy Meeting NAM, St. Andrews, Scotland [Poster]

(7) S. Topal, Estelle Bayet, Martin Bureau, Estelle Bayet, Wilfred Walsh, Timothy A. Davis, *Physical Conditions of Molecular Gas in Nearby Disk Galaxies*, 2013, National Astronomy Meeting, NAM, St. Andrews, Scotland[Poster]

(6) S. Topal, Estelle Bayet, Martin Bureau, Wilfred Walsh, Timothy A. Davis, *Revealing the Physical Properties of GMC Complexes in the Spiral Arms of NGC 6946*, 2013, IAUS, 292, 163 [ADS]

(5) ESO Turkey Team, *Journey of Turkey to become a member of ESO (in Turkish)*, 2012, XVIII. National Astronomy Conference proceedings, Turkey

(4) Umut A. Yıldız, İbrahim Küçük, Fahri öztürk, **S. Topal**, Ahmed Akgiray, Elif Beklen, Gülay Gürkan-Uygun, Oktay Ünal, Tülün Ergin, *National Radio Telescope Project (in Turkish)*, 2012, XVIII. National Astronomy Conference proceedings, Turkey

(3) Topal, S. et. al, 2011, ^{12}*CO Lines and LVG Modelling: NGC 6946* National Astronomy Meeting, NAM, Llandudno/Wales, [PDF]

(2) S. Topal, Fehmi Ekmekçi, *Photometric observations of CC And ve V350 Peg in 2005 (in Turkish)* 2007, XV. National Astronomy Conference proceedings, Turkey

(1) Mehmet Fatih Engin, Cavit Burak Uğurluoğlu, **S. Topal**, Güniz Başlangıç,; *Observing meteors using a simple radio-astronomy technique (in Turkish)* ,2005, İstanbul Kültür University, Journal of Istanbul Kültür University, 2005/2 pp 83-91

Popular Articles

(4) S. Topal, *Astronomi, Astroloji ve Gerçekler - Astronomy, Astrology and the Truths (in Turkish)*, Istanbul Art News Magazine / Section: Brain Storm, January 2016 [PDF]

(3) S. Topal, *Nereden Geldik? Nereye Gidiyoruz? Bizler Yıldız Tozuyuz! - Where do we come from? Where do we go? We are stardust! (in Turkish)*, Istanbul Art News Magazine / Section: Brain Storm, September 2015 [PDF]

(2) S. Topal, *Evrende Yalnız mıyız? (Korkma Canım Ben Buradayım!) - Are we alone in the Universe? (Don't Worry Honey I Am Here!) (in Turkish)*, Istanbul Art News Magazine / Section: Brain Storm, June 2015 [PDF]

(1) Topal, S., Yıldız, U. A., *Büyük Veri Kahramanı: Veri Bilimci - The Big Data and Data Scientist (in Turkish)*, Tübitak Bilim ve Teknik Dergisi, Nisan 2015, Sayı: 569 pp64-69. [PDF]

Biography

I was born in 1981, in the north of Turkey in a little town called *Eynesil*. I have 3 sisters and 3 brothers and I am the fourth children in my family. I graduated from the high school with a second rank (GPA of 4.95/5.0). In the same year, 2000, I won the nationwide university entrance examination and went to Ankara University, Department of Astronomy and Space Sciences. I graduated from the university with the third rank among the graduates of the department in that year. I then started my Masters study at the same department in 2004.

In 2006, just after finishing my Masters, I applied for a scholarship to do a PhD abroad. The scholarship is provided by Ministry of National Education in Turkey. My goal was to continue to pursue a career in astronomy. To be eligible for the scholarship I already had the required GPA, but I also had to pass a nationwide exam called ALES (Entrance Examination for Academic Personnel and Postgraduate Education). I passed the ALES and also the final interview afterwards. Finally, I got the scholarship. The scholarship, which supports many disciplines, was providing only one place for studying Astrophysics abroad. It was the happiest day of my life. However, just after a few weeks, the scholarship was cancelled by the Council of State because of a conflict between General Directorate of Higher Education and Turkish government. The court therefore decided to take into account only the ALES score to select the candidates for the scholarship. Since a friend of mine had 2 points more ALES score than I did, he was eligible to go abroad for a PhD in Astrophysics.

It was the saddest day of my life. After this shocking result, I joined the army. After serving 6 months in Turkish army, I was looking for a university to do PhD. I applied to Istanbul University, Department of Astronomy and Space Sciences. However, it did not take me long to realise that the department was split into two groups; old people (ETGs) and young people (Spirals), who do not like each other. I already had an unofficial agreement with one of the 'young' scientists for a PhD position but, unfortunately, there were only three massive ETGs in the interview. During the interview there was no question about my Masters study. Actually there was no scientific question at all. They deliberately failed me without asking any question. I lost the PhD position just because of having 0.5 less point than required score of 70! Sadly, this is the meaning of 'scientific thinking' and 'being professional' at some universities in Turkey. At the time, I was 26 year old young man without a job.

After some unsuccessful attempts to find a job, I again applied for exactly the same scholarship in 2008. I won the scholarship again but this time with a better ALES score. I first chose the Netherlands for my PhD study. I was also planning to take some English course there, but since it was so expensive (yes expensive than the UK), I decided to go the UK for taking English course. During my time in the UK, I also applied to some UK universities for a PhD, including Oxford. At the time, I already got the acceptance from two universities in the Netherlands; Groningen and Utrecht. However, after being accepted by Oxford Astrophysics, I decided to start my DPhil study there. And here I am.

During my Masters, I studied Johnson UBVRI spectra of δ Scuti type variable stars in our own Galaxy. During my bachelor and Masters, I did not take any courses on structure and evolution of galaxies and any wavelength regime other than the optical. I therefore decided to work on something different in Astronomy, something different than what has been done in Turkey for years. I wanted to study observational astronomy similarly to my Masters studies. I therefore chose Galaxies and their observations in (sub)mm wavelength regime. However, frankly, it was not easy to go back to academia after 4 years of break (2006-2010), and especially, to study astrophysics in different wavelength regimes and in much bigger

scales.

During my DPhil in Oxford, I really enjoyed living in this lovely city and country. Oxford also has another important meaning for me that my first ever child, my son Uzay Akay, was born in Oxford. My little family and I will truly miss Oxford. It is maybe the most crazy thing I have ever done in my life that I had a child during my DPhil. However, every second that I spend with my son is priceless. Only drawback would be that I had to extend my DPhil for about a year and a half.

My plan is continue to pursue a career in Astronomy. So, after Oxford, I will start to work at a university in Turkey. However, as soon as I settle down in Turkey, I will apply for a postdoc position. This time I would like to go to the USA. Finger crossed!